

Final Report

Project #2 - The Hip Exoskellie
Group 13



Michael Botros
8327615

Dmytro Lomovtsev
7944601

Yousef Bader
7623716

Philippe Shouldice
7710710

Thursday, December 5th, 2019

Abstract

The goal of this report is to analyze the design of a passive hip exoskeleton device by simulating and analyzing its performance during gait. This includes a summary of design changes since the original working analysis report, a total overview of the system, a model of the kinematics and dynamics of major load bearing components, a fatigue analysis of major system components, an explanation of coding behind the simulation, the method of implementation regarding parametrization, and a complete set of full renders of the device. The system is simulated with real life gait data to ensure accuracy of the analysis and to show device weaknesses during normal usage. The device was simulated with flat, incline and stair ascent gait data as well as some analysis in the frontal plane. Results of simulations and tests showed that the device produces small sagittal plane assist in the stance phase of stair gait and analyzed load bearing components meet the safety factor requirements chosen during the design process. The simulation revealed some weaknesses in the design that must be looked at in depth. These weaknesses include insufficient adaptability of the energy spring to various gait modes, tolerance issues regarding timing components, significant device mass, large casing requirements, and inconsistent energy assistance during flat and incline gait. Future analysis will also need to consider downstairs and incline descent gait as well as a fully developed impact analysis. Future work would involve making the device lighter, smaller and more efficient. Improved energy assistance in flat and incline gait would also need to be considered. Furthermore, future work should also look at meeting requirements that were not met in this design, especially requirements relating to safety features.

Table of Contents

1.	Introduction	1
1.1.	Literature Review Methodology.....	1
1.2.	General problem	1
1.3.	Target users	1
1.4.	User mobility and stability challenges	2
1.5.	Common interventions	3
1.6.	Motivation	4
2.	Literature Review.....	5
2.1.	History of Exoskeletal Devices	5
2.2.	Modern Day Standards and Regulations.....	6
2.3.	Existing Exoskeletal Systems	7
2.4.	Research Systems.....	7
3.	Anatomical Analysis and Design Data	10
3.1.	Functional anatomy.....	10
3.1.1.	Range of motion	10
3.1.2.	Joint stability and force transmission.....	11
3.2.	Gait Analysis	13
3.2.1.	Healthy gait	13
3.2.2.	Elderly gait	14
3.2.3.	Gait Pelvic Obliquity	16
3.3.	Anthropometric Measurements	16
3.3.1.	Kinematic Parameters	16
3.3.2.	Dynamic Parameters	17
3.3.3.	Anthropometric Measurements of Seniors	17
3.3.4.	Stability Measurement	19
4.	Requirements	20
5.	Gait Assist Strategies	21
5.1.	Level Walking Strategy.....	22
5.2.	Uphill Incline Walking Strategy.....	23
5.3.	Stair Ascent Strategy.....	24
5.4.	Assist in the Frontal Plane.....	26
6.	Dynamic Analysis	28

6.1.	Inverse Dynamics of the Lower Limb	28
6.2.	Gait Assist Energy	31
6.3.	Dynamic System Analysis.....	31
7.	System and Subsystem Structure.....	35
8.	Hip Exoskeleton Design Overview.....	37
8.1.	Main Energy Subsystem.....	40
8.2.	Timing Subsystem	43
8.3.	Thigh Subsystem.....	49
8.4.	Waist Subsystem.....	51
9.	Working Analysis	54
9.1.	Compression Spring Analysis	54
9.1.1.	Cam Spring	55
9.1.2.	Disk Lock Spring	57
9.2.	Extension Spring Analysis	57
9.2.1.	Main Energy Extension Spring.....	58
9.2.2.	Pawlever Spring	61
9.3.	Shaft Analysis.....	61
9.3.1.	Main Shaft	61
9.3.2.	Cam Follower Central Pin Arm Shaft.....	66
9.3.3.	Case Hinge Shaft	66
9.3.4.	Timing Pin and Pawl Lever.....	67
9.4.	Gear Analysis	69
9.4.1.	Ratchet Gear	69
9.4.2.	Spring Belt Gear	73
9.4.3.	Thigh Belt Gear	73
9.4.4.	Main Timing Belt Gear	74
9.4.5.	Cam Timing Belt Gear	75
9.5.	Buckling and Non-Circular Section Beam Analysis	76
9.5.1.	Cam Follower Shaft	76
9.5.2.	Pin Arms.....	77
9.5.3.	Thigh bar	77
9.5.4.	Thigh Rigid Support	80
9.5.5.	Thigh Belt Attachment Component	84
9.6.	Bolts	85

9.6.1. Gear Bolts.....	85
9.6.2. Other bolts	87
9.7. Bearings.....	87
9.8. Timing Belts	89
9.9. Finite Element Analysis	91
9.9.1. Case FEA	92
9.9.2. Waist Component FEA.....	95
9.9.3. Ratchet Pawl Lever FEA	97
9.9.4. Thigh Bar Assembly FEA.....	98
9.10. Frontal Plane Damping Pads.....	100
10. Parametrization.....	104
10.1. Workflow	104
10.2. Parametrization Results	108
11. Validation.....	110
11.1. Stability.....	110
11.2. Simulation and Evaluation.....	113
12. Future Work	119
13. Conclusion	119
References	120
Appendix A GUI Instructions.....	126
Appendix B Drawings	132
Appendix C Methodology	150
Appendix D Gait	152
Appendix E Anatomy	155
Appendix F Anthropometry.....	161
Appendix G Kinematic Relations	167
Appendix H Free Body Diagrams.....	170
Appendix I Gears	186
Appendix J Agenda, Minutes, and Gantt	189

List of Figures

Figure 1 Components and of the multi-articular passive exoskeleton developed by Xiong et al. [31] (left). Harvesting and restoring mechanical energy to assist with hip extension [31] (right) ..	8
Figure 2 Diagram showing the basic features of the Honda Walking Assist [33].....	9
Figure 3 Visual representation of the phases and subphases of the gait cycle [46].....	13
Figure 4 Graphs for joint angle vs. stride (left), moment/mass vs. stride (middle), and power/mass vs. stride (right) of elder participants [48].	15
Figure 5 Anthropometric and ergonomic dimensions measured by Kothiyal & Terry [57].....	18
Figure 6 Hip sagittal plane power vs. gait percent for flat surface walking, data from [48].....	22
Figure 7 A visual representation of the proposed gait assist strategy for flat surface walking, modified from [46].....	23
Figure 8 Hip power as a function of incline ascending gait percentage. Generated using data from [62].....	23
Figure 9 The proposed gait assist strategy for upwards incline walking, modified from [46]....	24
Figure 10 Hip power as a function of stair ascending gait percentage, data from [51].	24
Figure 11 The proposed gait assist strategy for stair ascent, modified from [66].	25
Figure 12 Hip frontal plane angle (left) and power (right) as a function of percent gait cycle for flat ground walking [48], high adduction and negative power region boxed in red.	26
Figure 13 Hip frontal plane angle (left) and power (right) as a function of percent gait cycle for inclined walking [68], high adduction and negative power region boxed in red.	26
Figure 14 Hip frontal plane angle (left) and power (right) as a function of percent gait cycle for walking up the stairs [51], high adduction and negative power region boxed in red.	27
Figure 15 Frontal plane gait assist strategy showing damping assist that occurs near maximum adduction that occurs during 0 – 20 % GC (loading response (LR) and mid-stance (MS)).	27
Figure 16 Lower limb model used for Inverse Dynamics.	28
Figure 17 Ground reaction forces (GRFy on the left, GRFx on the right) showing original Winter data, and modified with device weight based on the two approaches.....	30
Figure 18 Inverse dynamics model moments with comparison to Winter’s data.....	30
Figure 19 Thigh bar, thigh belt, and thigh rigid support attachment free body diagrams depicting reference centers as well as all forces.	32
Figure 20 Thigh bar, thigh belt, and thigh rigid support combined to reduce the number of unknowns shown in blue, with knowns shown in orange.	32
Figure 21 Thigh bar, thigh belt, and thigh rigid support partitioned into specific mass regions for computation of L_{CoM} (left) and I_m (right).....	33
Figure 22 Simplified system flow chart graph.....	36
Figure 23 System function flow chart graph.	36
Figure 24 Render of the proposed hip exoskeleton design.....	37
Figure 25 Render of exploded view of the design.	38
Figure 26 Simplified schematic of the main energy subsystem.	40

Figure 27 Simplified schematic of clutch components.....	41
Figure 28 Render of the main energy subsystem inside the device case (left) and the main energy subsystem viewed from the side (right).	42
Figure 29 Exploded view of the main energy subsystem.....	43
Figure 30 Simplified schematic of the timing system clutch control. Schematic B shows how the rotation of the pin disk disengages the pawlever. Schematic C shows the rotation of the pin disk engaging the pawlever.....	44
Figure 31 Standard spring switch design (left) and pawlever spring switch implementation (right).....	45
Figure 32 Render of the paw spring connected to the case (left) and the same render from the side (right).....	45
Figure 33 Simplified schematic of the timing pin location adjustment mechanism.....	46
Figure 34 Simplified schematic of cam height variation mechanism.....	46
Figure 35 Transparent render of the pin disk, timing pins, and the cam follower.....	47
Figure 36 The pin disk with cam follower, pin arms, and timing pins on the left next to the cam disk on the right.	48
Figure 37 Render of the thigh subsystem. Note the thigh belt on the left which connects to the thigh belt gear in the main energy system.	49
Figure 38 Render of the lower components of the thigh subsystem.	50
Figure 39 Simplified schematic of the waist subsystem.	51
Figure 40 A) Insertion of the waist case hinge shaft into waist left. B) Attachment of the left case on waist left.	52
Figure 41 A) Main, timing, and thigh subsystems in the case. B) case attachment to the waist subsystem.	52
Figure 42 A) Male hip exoskeleton, B) Female hip exoskeleton	53
Figure 43 Damping pad placed below the case hinge to provide an assisting hip abduction force.	54
Figure 44 Relevant parameters of spring end hook geometry [70].....	58
Figure 45 Free-body diagram of the main shaft (frontal plane view).	61
Figure 46 Main shaft bending moment (N-m) (A) and torsion (N-m) (B) diagrams as a function of length along the shaft from the left edge at the gait cycle frame corresponding to the maximum hip assist torque.....	63
Figure 47 Points of interest for fatigue stress analysis of the main shaft.	64
Figure 48 The cam follower component. The central pin arm shaft shown in the left of the component, the cam follower shaft shown on the right of component pointing upwards.	66
Figure 49 Thigh bar force transformation for stress analysis as a beam.	78
Figure 50 I-beam section from mechanics definitions [70] (left), and thigh bar parametrization definition in our project (right).	79
Figure 51 Model representation of the thigh rigid support component and associated dimensions (top), and the curved beam theory parameter definitions (bottom).	81

Figure 52 Transformation of coordinates from XY (left) to polar (right) for the curved section to compute beam deflection.....	83
Figure 53 Sketch of bolt loading.....	85
Figure 54 Fitting of the bearings depending on the application [79]	88
Figure 55 Belt section showing fiber reinforcement of belts [82].	90
Figure 56 Optimized case and associated FEA mesh.	93
Figure 57 Von Mises stresses for the case component with maximum stress, and SF25 points marked on the colour legend.....	94
Figure 58 Case wall deflection.	94
Figure 59 Waist attachment component model, forces, and mesh.....	95
Figure 60 Von Mises stresses in the regions with safety factor below 25.	96
Figure 61 Waist component strain (left) and deflection (right).	96
Figure 62 Pawl lever model, mesh, and von Mises stresses.....	97
Figure 63 Pawl tooth transient impact loading.	98
Figure 64 Thigh bar assembly FEA model and analysis mesh with forces and constraints.	99
Figure 65 Von Mises stress (left) and deflection (right) for the optimized thigh bar assembly.	100
Figure 66 A) Case dimensions, B) Compression spring model for the damping pad.....	101
Figure 67 Frontal plane analysis: A) case dimensions and B) case FBD.....	102
Figure 68 Damping pad force as a function of gait cycle.....	103
Figure 69 Assisted and unassisted hip adduction power.....	103
Figure 70 Parametrization workflow.....	104
Figure 71 Parameter Input Screen.....	105
Figure 72 Results Display Screen	107
Figure 73 Difference between male (left) and female (right) devices using identical mass and height parameters.	108
Figure 74 Difference between shortest (left) and tallest (right) settings using identical mass and height parameters.	109
Figure 75 Difference between lightest (left) and heaviest (right) settings using identical mass and height parameters.....	109
Figure 76 Schematics for the BOS and COG of a person [89].....	111
Figure 77 Trajectories of various stability parameters in the frontal plane during gait [91].....	111
Figure 78 GRFy (left) and GRFy (right) with and without the device on, assuming static mass contribution.....	114
Figure 79 Assisted and unassisted hip moment plot (left), and associated gait angles (right)...114	
Figure 80 Power assist of the device throughout the gait cycle.....	115
Figure 81 Stance assist percent and stance assist cost for 1.55m female with varying body mass for flat, incline up, and stair up gait in sagittal plane.	116
Figure 82 Stance assist efficiency for 1.55m female with varying body mass flat, incline up, and stair up gait in sagittal plane.	117

Figure 83 Stance assist percent and stance assist cost for 65kg female with varying height for flat, incline up, and stair up gait in sagittal plane.	118
Figure 84 Stance assist efficiency for 65kg female with varying height for flat, incline up, and stair up gait in sagittal plane.	118
Figure 85 (a) Normal gait, (b) spastic paraparetic gait, (c) cerebellar ataxic gait, (d) parkinsonian gait, and (e) frontal gait [93].....	152
Figure 86 Hip in the frontal plane during gait initiation and regular walking, modified from [95].	153
Figure 87 Hip in the sagittal plane during gait initiation and regular walking, modified from [95].	154
Figure 88 Hip joint structure including ligaments and acetabular structures [41].....	155
Figure 89 Hip joint muscle anatomy [41].....	156
Figure 90 Regression fit for hip flexion and extension rotation angle for female data from [36].	157
Figure 91 Regression fit for hip flexion and extension rotation angle for male data from [36].	158
Figure 92 Stress distribution on the hip bone at a midstance position. [35].....	158
Figure 93 Classical anthropometric model from Drillis & Contini, 1964 - via Winter, 2009 [52].	163
Figure 94 Male anthropometric model from Contini, 1972 [56]	164
Figure 95 Female anthropometric model from Contini, 1972 [56].....	165
Figure 96 Anthropometric mass properties for human segments via Winter, 2009 [52]	166

List of Tables

Table 1 Percentage differences of elderly muscle torques compared to young adult muscle torques.....	12
Table 2 Anthropometric dimensions and relations based on Kothiyal & Terry [57].....	18
Table 3 Updated System Design Restrictions.....	20
Table 4 Updated System Design Criteria	21
Table 5 Part names of labelled parts from Figure 25.	39
Table 6 Definitions of main shaft loads (knowns and unknowns) and their locations.	62
Table 7 Main shaft diameters at different points of interest.	65
Table 8 Gear specific variables to calculate the safety factor.....	69
Table 9 Gear specific variables to calculate the width.	73
Table 10 Gear specific variables to calculate the width.	74
Table 11 Gear specific variables to calculate the width.	74
Table 12 Gear specific variables to calculate the width.	75
Table 13 Keywords used in the different sections of the literature review	150
Table 14 Flexion and extension angles for the elderly, digitized from [38].....	159
Table 15 Comparison of elderly heights between countries [57].	161
Table 16 Comparison between young and old people's heights and weights [57].....	161
Table 17 Elderly waist and hip circumference for different age groups [58].....	161
Table 18 Constant variables and their values. Values sourced from [70]	187

1. Introduction

1.1. Literature Review Methodology

Keywords and research methodology can be found in Appendix C Methodology.

1.2. General problem

Mobility and locomotion play a central role in facilitating daily activities of people throughout their lifespan. Impairments in mobility have a negative impact on all aspects of life, including physical, mental, social, and occupational domains [1]. Mobility issues are a particular challenge in the elderly population due to natural changes in the body as well as the increased incidence of a variety of health conditions [2]. As such, multifaceted interventions to addressing mobility issues are required. Appropriate mobility assist devices are one aspect of these interventions. This review will focus on the merits of application as well as the design of a customizable, passively powered wearable hybrid hip exoskeleton to improve and enhance mobility and stability of a specific population of elderly individuals.

1.3. Target users

Elderly or senior people are generally considered to be those of 65 years of age or older [1]. One in seven Canadians belonged to this age group in 2012, with the peak of one in four expected by 2060 [2]. The growth in the senior age group is largely related to the aging of a large population of “baby boomers” and the following “generation X”, as well as to growing life expectancy [3]. As of the 2016 census, there are 5,935,635 seniors, and over 20% more women than men in this demographic [3]. The sex disparity increases to two women per man in the 80+ age demographic [3], which highlights the importance of accommodating design for both sexes and paying specific attention to the differences.

Labour market participation of people aged 55+ is also expected to increase from 35% to 40% by 2026, particularly those with trades and higher education [4]. Of these, 20% are expected to be over 65 years of age [3]. This is likely a result of lower levels of wealth, higher debt burden, and additional market demand. Over 25% of the senior population lives alone [5]. Those living alone are more likely to have financial difficulties and cope with high shelter costs in the current

housing market [5]. Therefore, the costs of the design should be minimized to accommodate a growing population of productive users facing an increasing financial burden.

A significant care and design challenge is presented by a large variation in physical, cognitive and psychological health and capabilities in this age group [1]. Nevertheless, normal aging results in body system and functional changes. Integumentary, airway, cardiac, musculoskeletal, nervous, sensory, hormonal and immune systems are affected [1]. These changes directly or indirectly alter mobility and locomotion. Furthermore, older adults may deny the changes and expect the same performance from their bodies as if they were younger [1]. Many overestimate their abilities and risk injuring themselves. Mobility device aesthetics and functionality becomes critically important in device acceptance in everyday use.

The daily activities of seniors are similar to younger and middle age adult age groups, especially in light of expected increase in labour force participation [4]. Counter to the common stereotypes, many seniors engage in an active lifestyle, including exercise routines, running, cycling, hiking and other personal and team sports. The breadth of activities and requirements for various exoskeleton designs is staggering and is therefore being limited to activities of daily living (ADLs) shared by the majority of the people in this age group. ADLs include getting in and out of bed, position changes (sitting, standing, lying), bathing, dressing, toileting, shopping, and meal preparation [1]. Different types of motion and positional stabilities (walking, going up or down the stairs, stepping over or avoiding obstacles, balance while bending or turning) are required even under the umbrella of ADLs. Therefore, the design targets are further narrowed down by most common mobility and stability needs.

1.4. User mobility and stability challenges

Analysis of mobility and stability needs of seniors first requires a clear definition of the terms. Mobility is generally defined as the ability to move freely [1]. Mobility in a bipedal locomotion context can be described in terms of gait parameters such as range of motion, step length, cadence, and velocity. Definitions for stability have a larger variation. In general, a stable gait is one that does not result in falls [6], [7]. Static stability definitions center around the idea of balancing the bipedal walker system around the center of mass in relation to the foot support regions [7], [8]. Dynamic stability includes the ability to not fall in the presence of small or large perturbations [6], [7]. Lack of stability can cause gait abnormalities such as limping, or progress

into injuries and occurrence of falls. Specific stability measures will be discussed in later sections of the report.

Both mobility and stability are affected by factors such as disease, disability, injury, pain, developmental age, life changes and medications [1]. Incidence of disabilities increases with age and affects ADL performance. Ninety percent of Canadians over 65 years of age live with at least one chronic disease or condition [2], which can directly or indirectly affect mobility and stability. Chronic degenerative arthritis and acute hip fractures are some of the most common issues affecting mobility and quality of life of seniors, affecting two out of three patients receiving hip replacements [9]. The costs of primary hip surgery were \$11,500 in 2017-18, excluding physicians, rehab costs, lost employment and opportunities, and potential for revision surgeries due to complications [9]. The staggering financial and social costs of hip and knee injuries remain an important motivation for mobility support devices.

Falls remain the largest risk factor of injuries in the elderly. Between 2017 and 2018, 137,500 Canadians aged 65 and older were hospitalized for injuries [10]. Eight-one percent of hospitalizations were related to falls [10]. During walking, 41% of falls may be due to incorrect weight shifting, 21% trip or stumble, 11% hit or bump, 11% loss of support, 11% collapse [11]. More falls were related to center of mass than base-of-support perturbations. Reduced gait stability has been associated with higher risk of falls [12], [13], and can be involved in weight shifting, support loss and collapse problems discussed in the previous study. Gait disorders that can lead to falls are described in Appendix D Gait.

Given the severity of the falls problem and a significant proportion of falls being related to center of mass stability, the design effort will be focused on hip mobility enhancement while prioritizing hip stability. In addition, due to time and data constraints, congenital conditions such as hip dysplasia, knock-knee (genu valgum) and bowleg (genu varum) hip variations will be excluded from this design project. The design ADLs will further be limited to those that are most likely to result in falls, namely walking (leveled and varying inclines), and the use of stairs.

1.5. Common interventions

Currently, the gait stability challenge in the elderly is most widely addressed with relatively inexpensive, lightweight, high-reliability, low-maintenance, long-lasting external assistive devices such as canes, crutches, walkers and orthoses [1]. Canes, crutches, and walkers enhance static

stability and mobility by providing a larger base support and utilizing individual's upper extremities and body to provide extra motive forces. Questions have been raised of whether canes and walkers are actually useful in preventing falls [14]. In the US national health trends study, users and non-users had no differences in fall incidence [14]. Cane users may compensate for fear of falls by limiting activity. More recently it was discovered that 75% of respondents who have such devices fell while not actually using them [15]. Reasons for deciding to skip using the device were related to cognitive, aesthetic, and accessibility concerns.

Lower limb orthoses are commonly used to stabilize lower limb range of motion, provide protection and support following hip, knee, or ankle surgeries [16]. Custom-made bilateral ankle-foot orthoses (AFO) in particular have shown balance improvements in the elderly [17]. The costs of custom orthotics can go as high as \$800 [18]. In comparison, cane costs range from \$18 to \$143, with general options costing below \$40 [19]. Crutches cost from \$35 to \$80 a piece, depending on the configuration [19]. Non-wheeled walkers cost between \$45 and \$77, while wheeled varieties with extra features cost between \$77 and \$550 [19]. Thus, to be truly competitive in the market, the designed device must offer comparable or enhanced benefits while maintaining cost similarity.

1.6. Motivation

Inexpensive gait assistive devices that enhance mobility and stability are required to address the emerging population needs given the growing senior demographic, their increasing participation in the labour force, and the health and financial challenges they face. While current solutions offer relatively low costs and reliability, there is a combined lack of efficacy, flexibility, speed and efficiency that limits device use in meeting the emerging needs. Devices would need to adjust to a variety of daily activities and optimize efficiency via parametric person-specific design. Such devices would be critical in maintaining independence and activity levels required for continued well-being of healthy seniors and seniors facing mobility deficits.

There is currently a lack of literature relating to the benefits of the passive exoskeleton form factor as compared to regular canes or walkers for fall prevention and mobility augmentation for seniors. Comparisons will become viable as this technology matures and becomes more widely available. Nevertheless, the hypothetical benefits of close body integration, efficiency and gait optimization as compared to other devices make this technology worth pursuing.

Our aim is therefore to design a safe and relatively inexpensive lightweight hybrid hip exoskeleton that stabilizes the hip joint to a safe range of motion while providing assistance with locomotion for level and inclined walking, as well as use of stairs. As per project statement, the system would be passively powered and customizable to promote an efficient design.

The following sections will review the existing exoskeleton mobility assist devices, examine their benefits and limitations, analyze data for level, inclined, and stair gait, state the requirements and specifications used for the project, discuss the proposed design of a passively powered hip exoskeleton, analyze and validate the proposed design, and discuss parametrization techniques used to customize the proposed design to individual patients.

2. Literature Review

2.1. History of Exoskeletal Devices

The earliest known record of an exoskeleton system is a patent for a full lower limb exoskeleton by Nicholas Yagn granted by the United States Patent Office in 1890 [20]. Yagn called his device an “apparatus for facilitating walking running and jumping”. It used two leaf springs, one for each leg, to transfer and store the body’s weight to the ground and reduce forces that would act on the stance leg during the running stance period. The leaf springs are attached to stirrups around the feet and a harness around the waist and thighs. The harness has a locking mechanism that allows the user to unlock and detach the leaf springs [21]. There is no record of the device ever being built [20].

In the 1960s [22], General Electric Research led a project sponsored by the Office of Naval Research and the U.S. Natick Laboratories [23] to create an exoskeleton that allows the operator to lift heavy loads up to 1500 lbs, nicknamed the Hardiman. The original concept uses 26 hydraulic servos to maneuver the device, weighed 1500 lbs, had a maximum speed of 0.762 m/s [24]. Intended use-case scenarios included loading bombs into vehicles, underwater construction, and material handling. During development, plans were made to scale up the Hardiman to create a 50 foot tall version for even greater loads [23].

2.2. Modern Day Standards and Regulations

Canada and the United States both use a similar medical classification system in which medical devices are given a classification based on a risk assessment of the usage of the device. In Canada, Health Canada is responsible for defining medical terminology and for classifying medical equipment. Health Canada classifies an “active device” as a device that uses energy sources other than the human body and gravity as long as the harvested energy is not substantially “altered” [25]. A Class I device is exempt from requiring a *Medical Device License*, and if the manufacturer of the device does not sell any Class II or above medical devices within Canada, the manufacturer is also exempt from needing a *Medical Device Establishment License* to do business in Canada while distributing through licensed establishments [26].

The Food and Drug Administration (FDA) is responsible for classifying medical devices in the United States, however unlike the risk classification system Health Canada uses, the FDA has established classifications for around 1700 generic types of medical devices [27]. A passive hip exoskeleton would fall under regulation 890.3475 “Limb orthosis” which specifies a device intended for medical purposes worn on the upper or lower limbs to support, correct, or prevent deformities or to align body structures for functional improvement as a Class I medical device. This exempts the device from the premarket notification procedures and current good manufacturing requirements that apply to Class II and III devices [28].

The International Organization for Standardization has published ISO 22523 in 2006 which specifies the requirements and test methods for external limb prostheses and external orthoses [29]. This document specifies material testing requirements and fatigue analysis requirements. Unfortunately, this document focuses on shoulder and elbow prostheses and orthoses, therefore it is not entirely applicable to lower limb orthotics. The majority of tests require the testing of device components using specialized machinery and stress analysis using gradual loading, i.e. applying a load gradually and then analyzing the reaction of the component. The document does provide fatigue testing guidelines for shoulder and elbow orthotics, which for the purpose of this project and report will also be used as a general guideline for fatigue safety factor calculations for major load bearing components of the proposed hip exoskeleton design. Major load bearing parts within the design must be able to withstand, at the minimum, 300 000 bending loading cycles in order to be considered sufficient for use within the device.

2.3. Existing Exoskeletal Systems

Exoskeletons can be subdivided into four types depending on whether the mechanism is installed in series or in parallel with the human limbs [20].

The first type is series-limb exoskeletons which are wearable devices that increase the effective length of the legs (e.g. placed along instead of adjacent to the limb). Two examples of this type are the PowerSkip and the SpringWalker which augment jumping height, but do not improve metabolic efficiency when running. More work is required at the hip to protract the leg during the aerial phase of running and more energy is required to stabilize movement due to the longer leg length [20].

The second type is the parallel-limb exoskeleton for load transfer (PLELT) which acts in parallel with the human lower limb for load transfer to the ground. In contrast to the series-limb exoskeleton, body weight can be transferred directly through the PLELT to the ground to reduce loads borne on the biological limbs and therefore, reduce metabolic demand. The third type of exoskeleton is a parallel-limb design that provides torque and work augmentation (PLETWA); they do not transfer substantial load to the ground. Boosting torque is provided to augment joint torque and work, resulting in improved walking metabolic economy and increased joint strength in paralyzed/weakened joints. The final type of exoskeleton, which is also a parallel-limb design, increases human endurance by redistributing the cyclic load of anaerobic activity (e.g. sprinting) over a greater number of muscles to delay the fatigue of the main muscles involved in the activity (these main muscles are only a few of the many muscles in the leg) [20].

Since the goal of this project is to design a hybrid hip exoskeleton for stride management and assist, only parallel-limb exoskeletons for torque and work augmentation will be discussed in this report. Recent trends show that robotic lower limb exoskeletons are designed with the goal of reducing the metabolic cost of walking for the user by preserving natural motion kinematics [30].

2.4. Research Systems

Two systems designed to support the hip are discussed in this section: one research system and one commercial system sold on the market.

The research system is a multi-articular passive exoskeleton developed by Xiong et al [31]. This exoskeleton has a waist component, thigh component, and shank component, all of which are connected with strings as shown in Figure 1. A mechanical clutch made up of the ratchet, paw,

and torsion spring near the thigh brace controls the harvest and restoration of energy. The paw engages the clutch when string 3 is not under tension [31].

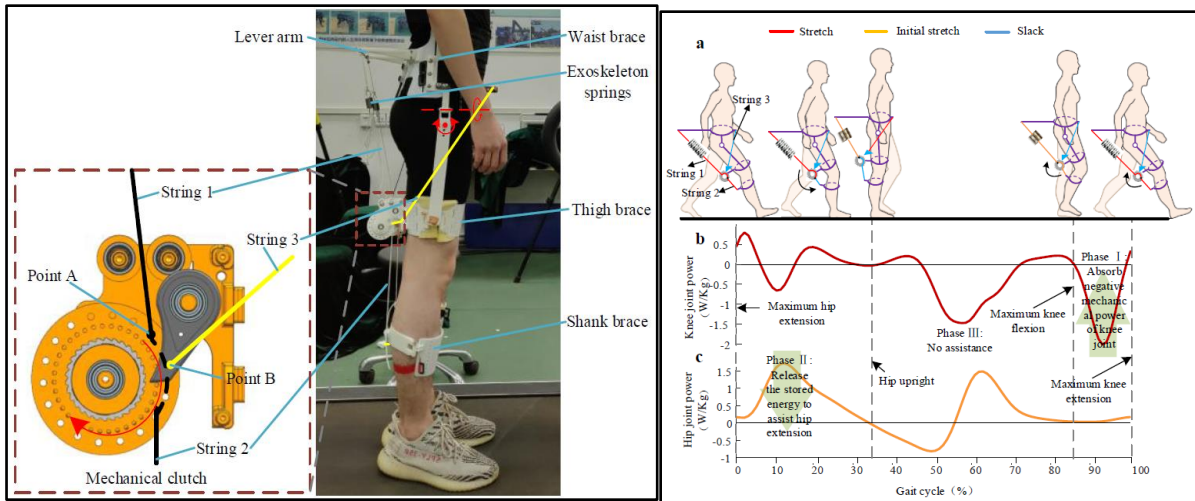


Figure 1 Components and of the multi-articular passive exoskeleton developed by Xiong et al. [31] (left). Harvesting and restoring mechanical energy to assist with hip extension [31] (right)

Hip joint movement in the sagittal plane stretches string 3 to control the engagement/disengagement of the clutch at the appropriate parts of the gait cycle as demonstrated in Figure 1.

The clutch is engaged (can rotate clockwise only) from 85% gait cycle to 30% of the next gait cycle. During Phase I (Figure 1), from 85% to 100% gait cycle (terminal swing phase), knee extension rotates the clutch clockwise, pulling on string 1. When string 1 is pulled, the spring stretches to store negative mechanical knee power, and produce knee flexion torque to assist the hamstring muscles. Extension of the knee joint is slowed during the terminal swing. During Phase II (Figure 1), from 0% to 30% of the gait cycle, the spring holds its potential energy to assist with hip extension because the spring remains stretched (the clutch is still engaged). During Phase III (Figure 1), from 30% to 85% of the gait cycle (terminal stance phase to the end of the mid-swing phase), the hip and knee extend to tighten spring 3 and disengage the clutch so that the clutch can rotate counterclockwise, returning the spring to its initial stretch level of maximum knee flexion (85% gait cycle). Researchers found that metabolic cost would be less when harvesting just the negative mechanical work of the knee rather than both the positive and negative mechanical work of the knee [31].

Ultimately, Xiong et al. designed this exoskeleton with the motivation of reducing metabolic cost. For able-bodied people, their exoskeleton was able to reduce metabolic cost by 7.6% at an average walking speed of 1.38 m/s [31]. This device aids motion in the sagittal plane only; thus, if the device were to also assist in the frontal plane, it would perform better. Furthermore, this device's spring pulls backwards on the leg during the swing phase and therefore, may increase the difficulty of walking for elderly people who struggle to extend their knee as far as they need to during the swing phase. An improved device to enhance mobility in elderly people would need to store the kinetic energy of the swinging leg without hindering its extension.

Today's current market for powered and unpowered exoskeletons remains limited, with few products truly available to the public. Specifically, there appear to be no commercial passively powered hip exoskeleton products on the market today, but some powered exoskeletons do appear to be close to full commercial launch. Honda Walking Assist (Figure 2) is mainly used as a training device with the goal of proficiently supporting walking and striding [32]. It includes four primary segments: a hip frame joining the computer controls with the battery, motors situated on either side of the hip, components that translate the force of the motors to the legs, and a thigh frame guiding the initiation and swing of the lower legs [32].

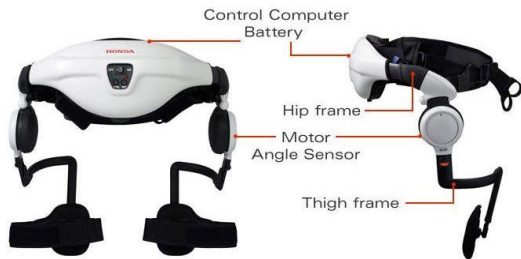


Figure 2 Diagram showing the basic features of the Honda Walking Assist [33].

The device identifies the state of the hip joint while walking by incorporating sensors in each of the motors, and helps swing the lower leg and extend the hip joint with electronic controls [34]. As the individual uses the device, these sensors continue to measure and monitor the left-right symmetry, range of motion, walking speed and other gait characteristics all while cross-checking these attributes against a database of the patient's history [32]. This cross-checking allows the user to create and submit a medical portfolio with real time walking data to a potential medical institution in order to help develop a more successful rehabilitation plan.

3. Anatomical Analysis and Design Data

3.1. Functional anatomy

The hip joint (coxofemoral joint) is a skeletal structure with the primary function of supporting the weight of the head, arms and trunk (HAT) during static and dynamic postures [35]. The joint consists of the articulation of pelvic acetabulum with femoral head, forming a 3-DOF ball-and-socket joint (Appendix E Anatomy, Figure 88). Femoral head and neck form a medially referenced angle of approximately 125° with the femoral shaft [35]. This angle is largest at birth and declines with old age. *Coxa valga* is the pathological increase, while *coxa vara* is the pathological decrease in this angle. Femoral condyles at the knee joint are located at a 15°-20° torsion angle to the head and neck axis. Femoral anteversion and retroversion are pathological conditions with increase or decrease in the torsion angle. Alterations in the femoral angles may have a significant impact on kinematics and dynamics of gait.

3.1.1. Range of motion

The motions supported by the hip joint are flexion/extension in the sagittal plane, abduction/adduction in the frontal plane, and medial/lateral rotation in the transverse plane [35]. The passive hip flexion ranges from 90° to 120° depending on the degree of knee flexion. The largest angle is obtained with the knee flexed, while the smallest angle with the knee extended. Passive hip extension ranges from 10° to 30°. Hip abduction ranges from 45° to 50°, while hip adduction ranges from 20° to 30°. Finally, medial and lateral rotation with hip flexed at 90° are 42° to 50°. Normal gait on level ground requires at least 30° hip flexion, 10° hyperextension, 5° of abduction and adduction, and 5° of medial and lateral rotation [35]. These needs are increased for uneven ground, stairs, or use of chairs.

The range of motion of the elderly group naturally decreases with age and differs by gender. A large cohort comparison study measured hip flexion and extension angles for healthy, community-dwelling individuals up to 69 years of age [36]. While the study described its results in terms of cohorts of the population, the original data was provided. This data could be plotted and regression-fitted in Excel for an equation to parametrically determine hip flexion and extension angles for both genders (Appendix E Anatomy, Figure 90, Figure 91).

In addition, steeper decreases in hip flexion angles could be expected, particularly at later age. A decline of -0.19°/year from 55 to 70 years, and -1.16°/year thereafter was reported for men

[37]. For women, the decline was $-0.66^\circ/\text{year}$ from 55 to 86 years, and $-2.67^\circ/\text{year}$ thereafter. Physical activity was not a significant predictor of better flexibility.

Data for adduction, abduction, internal and external rotation are more elusive. One study examined an exercise program between sedentary and active youth and elders, and measured total ROM for flexo-extension, adduction-abduction, internal-external rotation [38]. Age-related decreases in hip flexion-extension, adduction-abduction, and internal-external rotation were 34%, 29%, and 33%, respectively, between the ages of 19.3 ± 3.2 and 64.3 ± 5.4 . The data plots for total planar movement were digitized using an online WebPlotDigitizer tool [39] (Appendix E Anatomy, Table 14). Adduction-abduction (frontal plane) angle was 54.27 ± 8.95 degrees for sedentary, and 69.93 ± 10.07 degrees for active seniors. Internal-external rotation (transverse plane) was 62.10 ± 11.75 degrees for sedentary, and 71.61 ± 10.63 degrees for active seniors. No gender-divided data was provided, but other studies have shown that young women may have greater active hip internal and external rotation than young men (116.6-118.8% internal, 104.5-105.7% external) [40].

3.1.2. Joint stability and force transmission

Joint stability in the form of range-of-motion restriction and control is important to gait stability where the hip may be loaded by weight that greatly exceeds body weight. Acetabulum, external soft tissues, and ligaments provide passive stability, while local muscles provide active stability [41]. The acetabulum, acetabular labrum, and associated ligaments provide the absolute range of motion limits (Appendix E Anatomy, Figure 88).

Deep local muscles are likely primary contributors to active stability, especially if passive stability structures have developed pathological laxity [41] (Appendix E Anatomy, Figure 89). These muscles typically lack the moment arm necessary to enact a gross anatomical motion. Gluteus minimus provides internal rotation and late stance phase anterior joint support. Deep external rotators (quadratus femoris, gemelli, obturator internus and externus) may stabilize femoral head in the acetabulum by compressing the joint surfaces. Iliocapsularis has extensive attachments to the joint capsule and may provide capsule tightening for stability. Both divisions of iliopsoas (psoas major, iliacus) are active throughout hip flexion, but also provide anterior stability during the late stance phase. Studies have shown that prolonged bed rest and reduced activity of deep muscles can result in their weakening, translating into lower joint stability [41].

Therefore, one of the design goals in managing stability through ROM restriction is to facilitate the action of these muscles without offloading their tasks to the exoskeleton within the normal ROM.

Force transmission at the joint is related to the articulation geometry close to the hip joint as well as the gait cycle discussed in a later section of the report. For both single and double leg support, both tensile and compressive forces are present in the articulating joint structures. Hip joint mobility is enacted by many muscles with large areas of attachment, length and cross-section as required by the need to move and support the HAT [35]. Static stability is maintained via balancing of the HAT weight using abductor muscles, resulting in balance of moments around the joint [35] (Appendix E Anatomy, Figure 92). It is difficult and impractical to describe individual muscle anatomy and contributions. Data can instead be obtained for gross anatomical motions from gait analysis described in another section of this report. Compressive, tensile, bending, and limited shear stresses develop. Design force analysis will need to model this system and the effects of introducing exoskeleton support.

There is a very limited amount of information on hip muscle torques for general population elderly in the literature, as most studies focus on youth and sports. Three relevant studies were found that allow generating the percent decrease data which can potentially be used to adjust young adult gait data to be more representative of the older target users.

One study compared abductor and adductor torques for healthy young (23 ± 1.3 year) and old (74 ± 6.8 year) women, and normalized the data by mass and height [42]. Two studies compared flexor and extensor torques for healthy young and old men and women [43], [44]. The young-old differences are summarized in Table 1. The second study data had to be manually adjusted by given average height and weight of subjects.

Table 1 Percentage differences of elderly muscle torques compared to young adult muscle torques.

Abductor difference	Adductor difference	Flexor difference	Extensor difference
B: -33.3% (0.81 vs 0.54 Nm/kg-m), IM*	B: -22.6% (0.75 vs 0.58 Nm/kg-m), IM*	M: -32.5% (0.716 vs 1.061 Nm/kg-m), IM*	M: -25.8% (0.783 vs 1.055 Nm/kgm), IM*
B: -44.1% (0.93 vs 0.52 Nm/kgm), IK*	B: -53.5% (1.01 vs 0.47 Nm/kgm), IK*	F: -29.5% (0.635 vs 0.901 Nm/kgm), IM*	F: -28.0% (0.700 vs 0.972 Nm/kgm), IM*

*M - elderly male, F - elderly female, B- both genders elderly, IM - isometric, IK - isokinetic

The implication of reduced torque for the design of the current exoskeleton is that the device will need to provide at least 30% additional hip torque in order to enhance elderly gait to the level of young people assuming isometric study values. More torque enhancement will be required the faster a person wants to go based on the single isokinetic study [42].

3.2. Gait Analysis

3.2.1. Healthy gait

Gait is one of the most common human biological functions, in which the center of mass of the body is propelled forward safely and efficiently across level or inclined ground [45]. Winter describes five major functions of gait: generation of mechanical energy to maintain body velocity, shock absorption or stability during motion, support of the upper body, maintenance of posture, and foot-ground clearance [45].

When observing one leg as a reference during the gait cycle, the two primary phases of gait can be identified, each consisting of several sub-phases. A visual representation can be seen in Figure 3.

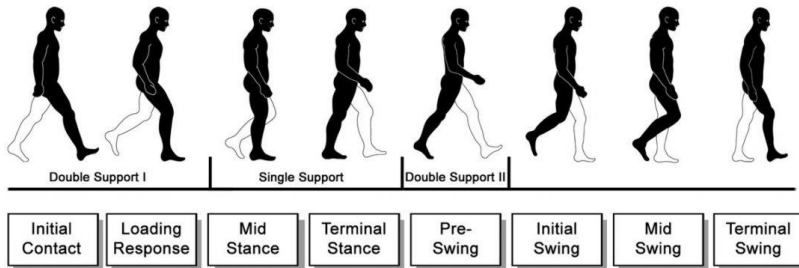


Figure 3 Visual representation of the phases and subphases of the gait cycle [46].

The gait cycle begins at the moment the heel of the reference leg contacts the ground, marking the beginning of the stance phase as well as dual limb support. Following initial contact, loading response begins as weight is transferred from the opposing leg onto the reference leg in preparation for toe-off of the opposing foot. Loading response ends at toe-off of the opposing foot, beginning the mid-stance sub-phase. During this sub-phase, the body is supported entirely by the reference leg while the opposing leg is in swing phase. Terminal stance begins the moment the heel begins to lift, during which body weight is transferred to the front of the reference foot. The

stance phase ends when the opposing foot contacts the ground, marking the beginning of the second phase of gait, the swing phase [46], [47].

The swing phase begins with the pre-swing sub-phase. Load is transferred from the reference leg to the opposing leg until the reference leg reaches toe-off and no longer supports any weight. At toe-off of the reference foot, initial swing begins as the reference leg starts to swing forward and the knee reaches maximum flexion to clear the ground. Initial swing ends at maximum knee flexion and mid-swing begins during which the reference foot continues to clear the ground and move forward. The terminal swing sub-phase begins after the tibia reaches a vertical position. During terminal swing, the knee fully extends in preparation for the start of stance phase of the next cycle [46], [47]. In general, the stance phase is approximately 50%-60% of the gait cycle, and the swing phase varies between 40%-50% of the gait cycle [45]–[47].

3.2.2. Elderly gait

As the human body ages, gait characteristics such as stride length, cadence, walking base, and velocity change. Although some of these changes can be attributed to gait diseases (as discussed in Appendix D Gait), even elders unaffected by gait disorders show differences in their gait when compared to young adults [48].

Winter et al. conducted a study to measure pattern changes between healthy elderly people and healthy young people. Data for 15 elders (10 men, 5 women) with an average age of 68 years was collected using motion capture suits and a specialized motion analysis camera. The collected data was then analyzed to produce angle vs. gait, moment vs. gait, and power vs. gait graphs shown in Figure 4 [48]. Graph data were digitized using an online graph digitizer [39] with an averaging window algorithm at 5 pixel X and 10 pixel Y spacing trigger. The relevant information on the graph relating to the hip was specified using the masking feature to ensure unrelated data for the knee and ankle was not digitized. Manual adjustments were made to fix errors when the data curve intersected the graph axis.

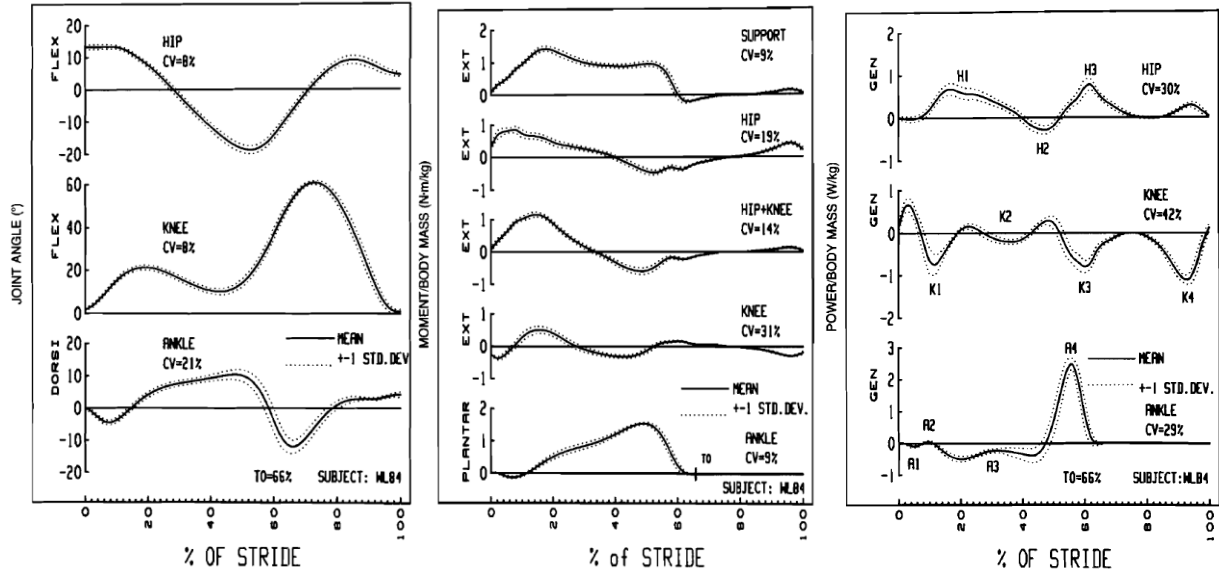


Figure 4 Graphs for joint angle vs. stride (left), moment/mass vs. stride (middle), and power/mass vs. stride (right) of elder participants [48].

Winter et al. also compared the collected elderly data to data collected from 12 healthy young adults (7 men and 5 women, average age of 24.6 years) to identify any changes of gait characteristic that may occur with age. Observed differences between young and elderly gait include: the natural walking velocity of the elders was lower than that of the young adults due to a reduction of stride length, increased double-support stance time, and significant differences in power patterns attributed to differences in toe push-off and flat-footed landing. Winter et al. believe these differences are adaptations that are meant to allow for safer gait strides by increasing stability [48]. Hageman and Blanke compared differences between healthy young women (23.92 ± 3.57 years) and healthy elderly women (66.85 ± 7.60 years) gait from both the frontal and sagittal planes and found similar differences in gait patterns as Winter [49].

Incline walking and stair climbing have also been defined as mobility modes that the proposed hip exoskeleton design will accommodate and support, therefore reference gait data will also be required for these forms of gait.

Vickers et al. [50] conducted a gait motion capture analysis on elderly amputee and able-bodied participants. The able-bodied control data used in their study includes joint angles, joint moments, and joint powers for ascending and descending gait. For the purpose of this project, only ascending incline data for the study's control group was digitized.

Law [51] conducted a gait study to analyze differences in gait between normal, overweight, and obese individuals aged around 60 years old. For the purpose of this project, only data for

normal weight participants will be used. Graphs for hip angle and moment were digitized using the same methodology for the other data sets.

The data sets that were digitized for level, ascending incline, and stair climbing gait only provide data for joint reactions. Vickers et al. provide ground force reaction data however they do not provide motion capture data necessary for accurate calculation of limb velocities and acceleration. They also do not provide limb dimensions which would be required for accurate inverse kinematics. For this reason, Winter's detailed data for level walking gait of a middle-aged man is used for inverse kinematic analysis of the effects of the device on joint reactions [52].

3.2.3. Gait Pelvic Obliquity

Although the major joint actions during the gait cycle are in the sagittal plane, it is important to also consider the movement of the body in the frontal plane. Specifically, hip obliquity during gait should be considered when designing a hip orthotic or exoskeleton to ensure the device does not impede the natural range of motion of the hip while the user is walking. Due to difficulties in finding data for elders, frontal plane gait data for young to middle aged adults will be used instead. The frontal and sagittal pelvic tilt graphs are available in the Appendix D Gait, Figure 86 and Figure 87.

3.3. Anthropometric Measurements

Anthropometric data defines parameters of the segments of the human body necessary for kinematic and dynamic analysis of human locomotion [52]. Anthropometric models combine human measurements into parametric relationships that are easy to apply during design when actual human measurements may not be available. For anthropometric models to be valid, measurements should encompass at least 90% of the target population, emphasizing careful subject selection, positioning and dynamics [53].

3.3.1. Kinematic Parameters

Drillis & Contini produced a lumped-gender average segment length dataset of human segment lengths in 1964 presented in Figure 93 (Appendix F Anthropometry) [54]. This model uses American data with mostly young male subjects with medium to muscular build, and comparative Soviet data includes both male and female subjects young and old [53]–[55]. It is unclear exactly how Drills & Contini averaged the lumped data (age cohorts, gender, racial

makeup) between the studies to obtain the initial approximations. Contini later presented Figure 94 and Figure 95 (Appendix F Anthropometry) for gendered Nordic, Mediterranean, and US data approximations in 1972 [56].

3.3.2. Dynamic Parameters

Segment masses, centers of mass, and radii of gyration are required for dynamic analysis. Anthropometric segment mass and inertial properties are based on body density studies for various somatotypes, or body builds [52]. Body (ponderal) index combining height and weight is used to parametrize density data for various body segments [56]. Density expressions are integrated over the limb volumes to obtain segment masses if empirical methods cannot be used. Centers of mass can also be determined empirically or analytically from mass distribution within the limbs. Figure 96 (Appendix F Anthropometry) shows a snapshot of the table presenting body segment masses, center of mass, and radii of gyration. As with segment length data, subjects are younger Caucasian adults. No gendered distinction is made within the model.

3.3.3. Anthropometric Measurements of Seniors

Body height and weight are usually used as reference values to relate and approximate body segment parameters in anthropometric modeling. The average height is between 1.6 to 1.7m for senior males, and 1.5 to 1.6m for senior females [57], [58]. Table 15 (Appendix F Anthropometry) shows some values from the studies in various countries [57]. The average weight is between 70 and 75kg for senior males, and 60 and 66kg for senior females [57], [58].

The effects of aging introduce changes to the anthropometric measurements for seniors. Height tends to be lower on average (6-8%) at an older age with higher variability [57]. Weight tends to be higher on average (10-22%), but much less variable than for young people Table 16 (Appendix F Anthropometry) [57].

Height and weight changes with age can potentially be parametrized for the design process. A Canadian study tracked elderly (>70 yr old) height and weight changes over 5 years and reported statistically significant decreases for both men and women, regardless of illness status [59]. Height changes were similar between age groups but varied by gender: men at -0.2cm/year, while women at -0.342cm/year. Weight changes were nearly the same for men and women but varied per age

group: age 70-79 at -0.306kg/year, 80-89 at -0.414kg/year, and 90+ at -0.522kg/year. An Italian study reported similar height and weight reduction rates[58].

One of the challenges with the elderly population is that height data does not correlate to other segment data such as the 1977 US air force data from the AMRL data bank [60]. Military selection may introduce a bias for young individuals of similar stature. With elderly, strong correlations ($R^2 > 0.7$) with individual height only occur for eye, elbow, shoulder and knee heights [57]. An additional challenge is that not many studies have attempted extensive measurements of kinematic and dynamic parameters for the general elderly population.

Figure 5 shows the segment dimensions for abled seniors randomly selected from the general population in Australia [57].

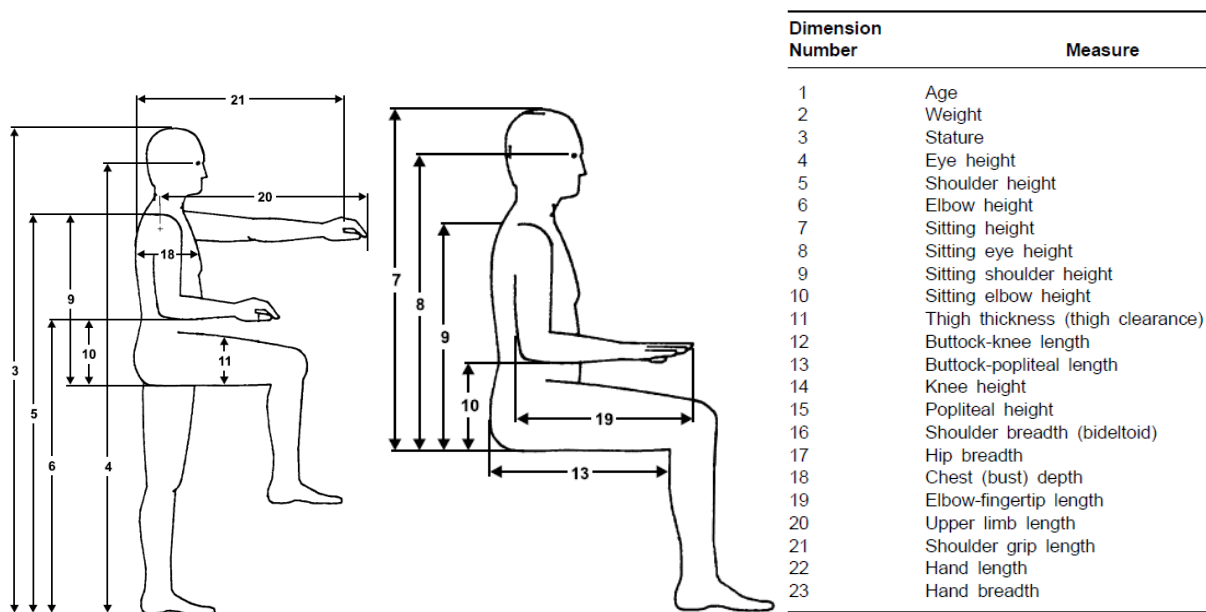


Figure 5 Anthropometric and ergonomic dimensions measured by Kothiyal & Terry [57].

Table 2 shows the segment dimensions relevant to the hip exoskeleton design. Height relations were manually computed from the given stature and segment data. Of note are the coefficients of determination (R^2) for segment dimension and height. Strong relationships are only present for knee ($R^2=0.8$) and popliteal heights ($R^2=0.7$), with moderate to weak relationships for buttocks-popliteal ($R^2=0.4$), buttock-knee ($R^2=0.6$), and thigh clearance ($R^2=0.3$) lengths.

Table 2 Anthropometric dimensions and relations based on Kothiyal & Terry [57].

Parameter	Male \pm SD (Range)	Female \pm SD (Range)	Relation to height H (R^2)
-----------	-----------------------	-------------------------	--------------------------------

14. Knee height, mm	515 ± 31 (462-580)	475 ± 28 (400-570)	M: 0.3106H (0.7992) F: 0.3123H
15. Popliteal height, mm	416 ± 25 (372-468)	379 ± 28 (310-465)	M: 0.2509H (0.6897) F: 0.2492H
12. Buttock-popliteal length, mm	452 ± 38 (357-560)	440 ± 36 (352-536)	M: 0.2726H (0.4326) F: 0.2893H
13. Buttock-knee length, mm	549 ± 38 (443-610)	530 ± 35 (446-620)	M: 0.3311H (0.5962) F: 0.3485H
11. Thigh thickness / clearance, mm	101 ± 23 (65-158)	95 ± 21 (60-157)	M: 0.0609H (0.3436) F: 0.0625H

Parametrized waist and hip circumference data are important for the design of the exoskeleton support sheaths and braces. An Italian longitudinal study on ageing examined these anthropometric indices in men and women [58]. Study results were manually normalized by weight and height in Excel to generate parametric expressions in Table 17 (Appendix F Anthropometry). Across all age categories the waist circumference was 97.5 ± 9.9 cm for males, 96.9 ± 14.1 cm for females. Similarly, hip circumference was 100.2 ± 8.3 cm for males, 103.4 ± 12.1 cm for females. No correlation coefficients between these parameters and height and weight were provided, and no raw data was provided to try to compute in Excel and validate the relations.

3.3.4. Stability Measurement

Anthropometric measures allow for the calculation of parameters required for quantifying a person's stability. Most common static methods include COG% [7] and GCOM [8]. COG% examines the location of the center of gravity in relation to the base of support both of which can be computed using anthropometric data. GCOM examines for the presence of uncompensated moment acting on the base of support. Most common dynamic methods include maximum Lyapunov exponent, maximum Floquet multiplier, variability measures, and long-range correlations [6]. Lyapunov and Floquet methods examine rates of system divergence after perturbation using state-space representation for gait kinematics, while variability and correlational methods use common statistical variability methods such as standard deviation of some parameters, and correlations between them.

4. Requirements

The aim is to design a safe and relatively inexpensive lightweight hip exoskeleton that stabilizes the hip joint to a safe range of motion while providing assistance with locomotion for level and inclined walking, as well as use of stairs. Hip exoskeleton design restrictions were defined early on in the project, however some restrictions had to be redefined during the course of the project due to some restrictions conflicting with gait data used to simulate the design. The updated design restrictions, which are design characteristics that must be respected imperatively, are presented in Table 3. Design criteria, which are design characteristics that can be improved and optimized through design, are presented in Table 4.

Table 3 Updated System Design Restrictions

No.	Restriction.
1	Device supports three modes of locomotion: stair climbing, incline ascent, and flat walking
2	Overall hip joint peak torque 1.4 Nm/kg [61], [62], [51], [43], [44]
3	Subject height range between 1.4m and 1.8m (95% CI) [63]
4	Subject weight range between 38kg and 100kg (95% CI) [63]
5	Subject hip circumference range between 69cm and 124cm (95% CI) [58]
6	Subject waist circumference range between 79cm and 127cm (95% CI) [58]
7	Device provides up to 8% gait energy during gait assist phase [31]
8	Device energy transfer efficiency (applied energy/harvested energy) of at least 70%
9	Sagittal extension is limited to 10° for both genders [36], [51], [64]
10	Sagittal flexion is limited to 70° for both genders. [36], [51], [64]
11	Frontal adduction is limited to 8° for both genders. [36], [51], [64]
12	Frontal abduction is limited to 8° for both genders. [36], [51], [64]
13	Minimum design safety factor of 2
14	Full manual safety disengagement mechanism available while device is worn
15	Meets ISO 22523:2006 testing standards. More specifically, meets or exceeds cyclic testing requirements (300 000 cycles at 0.5 Hz) [29].

Table 4 Updated System Design Criteria

No.	Criterion.	Weight.
A	Minimize device mass	20
B	Maximize device comfort	20
C	Cosmetic Appeal	15
D	Minimize cost	10
E	Maximize energy transfer efficiency	10
F	Minimize number of components	8
G	Ease of maintenance	5
H	Minimize device profile (reduce how far it sticks out from the body)	5
I	Minimize operating noise level	5
J	Parametrize safety factors based on personal needs of the user	2

5. Gait Assist Strategies

Gait assist strategies must be developed in order to design a gait assisting passive hip exoskeleton. A gait assist strategy identifies the appropriate gait phases and durations for energy harvesting and torque application. This information can then be applied to design a timing/controlling device that alternates between collecting and releasing energy. For this hip exoskeleton, three gait assist strategies are envisioned, one for each of the intended use cases: level surface gait, stair ascension, and upwards incline gait. Frontal plane damping functionality consistent across all modes of gait was envisioned in the original project scope as a method of stability assist.

To help create the gait assist strategies, MATLAB code was created to generate power vs. gait graphs using hip joint angle and moment data. First, data is obtained by digitizing literature gait data using the online utility WebPlotDigitizer [39] to create CSV files. Each set of CSV file data is curve fitted using MATLAB polyfit function. Then, the polynomial equation for angle data is differentiated to generate hip angular velocity. Hip angular velocities and moments at equally spaced intervals are then multiplied together and fitted to generate a hip power polynomial and

graph. Power plots are integrated regions between zeroes to evaluate the energy input or dissipation.

5.1. Level Walking Strategy

Winter et al. [48] collected hip angle and moment data in the sagittal plane for 15 healthy and fit elderly participants (average age of 68 years) walking on a flat surface. The power vs. gait graph for the data is shown in Figure 6. Regions coloured in red are positive power phases of gait during which the muscles are acting in the same direction as limb motion. These phases of gait are ideal stages for torque application to reduce required muscle force. Blue regions are negative power phases in which muscle force direction and limb direction are opposite. These phases are ideal for energy harvest since energy is being expended to slow the limb down. Each coloured region of the graph is integrated to obtain the work done during the phase, displayed as numbers near the peaks of each of the regions. Slowing the limb down mechanically harvests energy that can be used during positive power regions to augment movement.

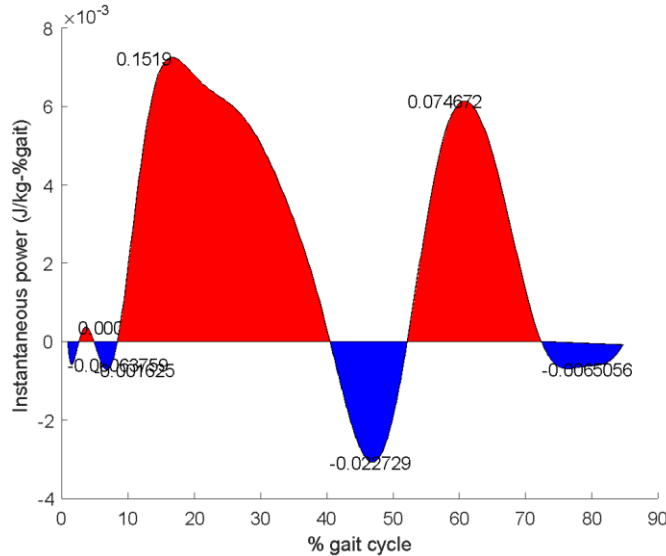


Figure 6 Hip sagittal plane power vs. gait percent for flat surface walking, data from [48].

In the case of a flat surface gait strategy, work done during stance phase is more than double the work done during the swing phase. For this reason, it is proposed that a torque be applied at the hip to assist hip extension from around 10% to 40% of the gait cycle. Energy extraction starts during limb deceleration and continues until terminal swing, from around 40% to 85% of the gait cycle. Figure 7 provides a visual representation of the gait assist strategy.

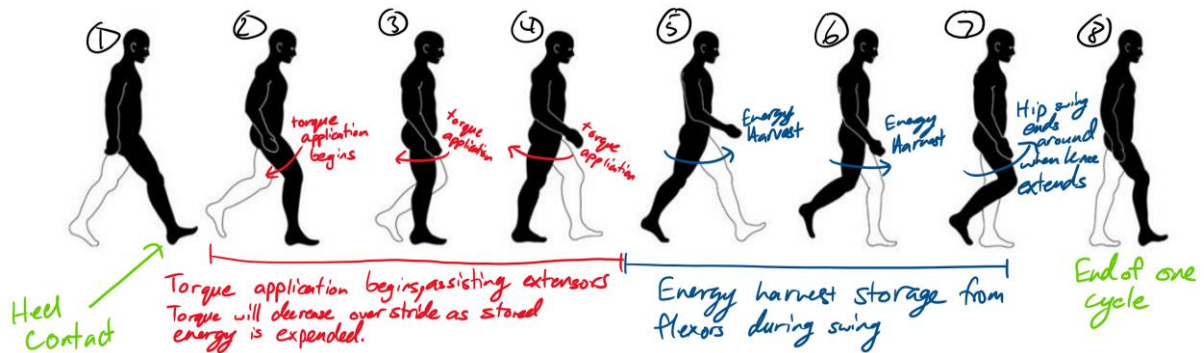


Figure 7 A visual representation of the proposed gait assist strategy for flat surface walking, modified from [46].

This gait assist strategy is similar to Seo et al. [65] proposed gait assist strategy and involves motion extension during assisted walking. However, unlike the device developed by Seo et al., no electric motors will be used. This means that the system is required to extract energy during the swing phase of gait.

5.2. Uphill Incline Walking Strategy

Vickers et al. [62] collected 5% incline walking data from 8 healthy elderly participants (average age of 69.6 years). The hip power vs. gait percent graph is shown in Figure 8.

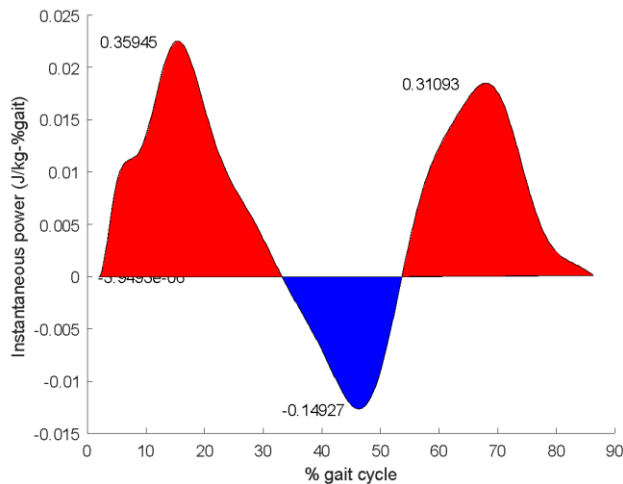


Figure 8 Hip power as a function of incline ascending gait percentage. Generated using data from [62].

The two peaks are fairly similar in magnitude, with the first peak having around 16% more work done than the second peak. The proposed gait assist strategy for upwards incline gait involves applying torque during stance phase, up until terminal stance and extracting energy during terminal

stance and through the swing phase. Since the difference in work done between the two peaks is relatively small, the ideal outcome is to equalize the two regions of positive power. Figure 9 shows a visual representation of the proposed gait assist strategy.

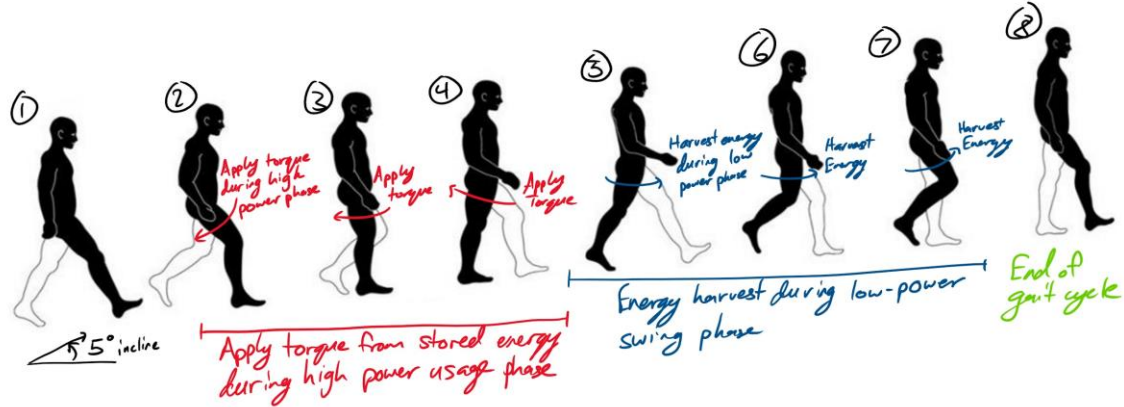


Figure 9 The proposed gait assist strategy for upwards incline walking, modified from [46].

5.3. Stair Ascent Strategy

Kim et al. defined four stages of stair climbing gait: foot contact, pull-up, hip-crossing, and peak joint angle. Foot contact marks the start of stride phase whereas pull-up is the equivalent of load transfer in walking gait, in which load is transferred as the reference leg pushes the center of mass upwards. Hip crossing occurs when the swing leg moves ahead of the reference leg to reach the next step and peak joint angle occurs at maximum hip flexion [66].

Law [51] collected hip angle and moment data for 19 healthy and normal weight (BMI average of 22.1 kg/m^2) participants with an average age of 61.4 years. The MATLAB graph for power is shown in Figure 10.

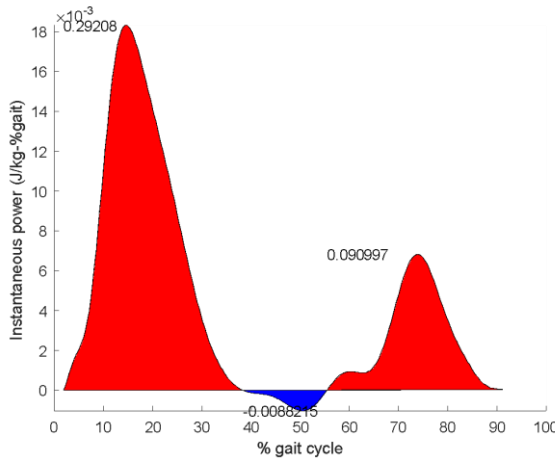


Figure 10 Hip power as a function of stair ascending gait percentage, data from [51].

The generated power graph has two well defined peaks. The first peak, occurring at around 15% of gait, is during the pull-up phase of stair climbing. This phase occurs when load is transferred from the lower leg onto the leg of the next step up. As load is transferred, muscles at the hip, specifically the extensor muscles, must apply a torque to pull the body upwards to the next step. The second peak occurs when the leg enters swing phase and is moved upwards to prepare for foot contact [67].

Observing Figure 10, it is clear that more power is required at the hip during the pull-up phase of gait and therefore the exoskeleton must help facilitate the pull-up phase. Since less power is required during hip-crossing and swing, energy should be harvested during these phases before foot-contact. Figure 11 shows a visual representation of the proposed gait assist strategy for stair ascension.

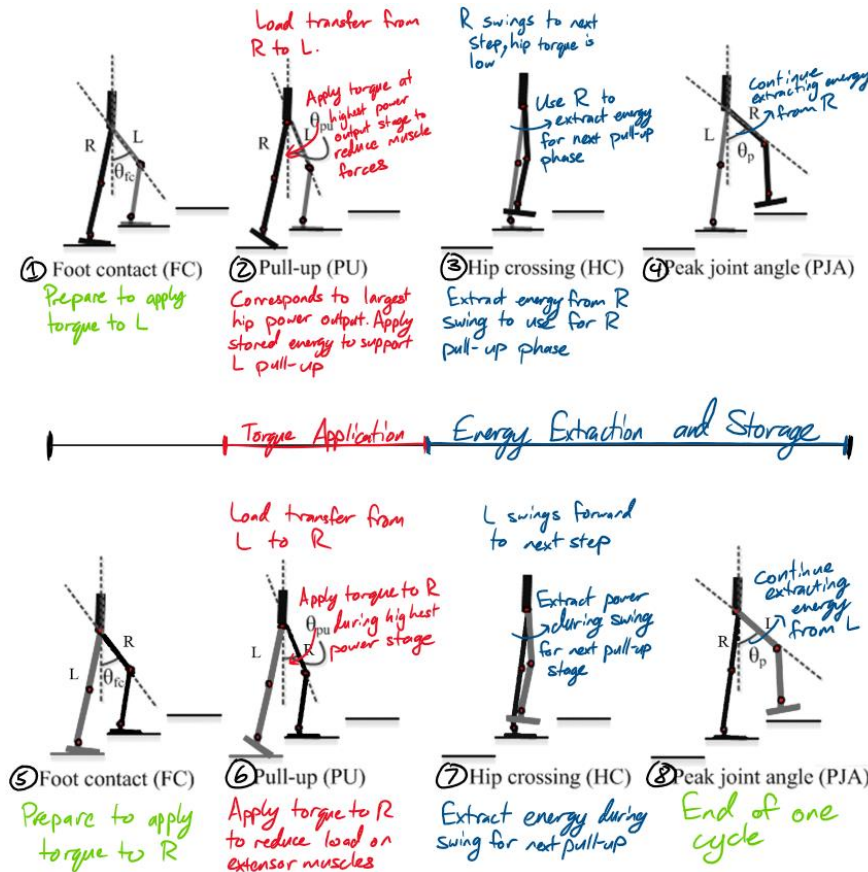


Figure 11 The proposed gait assist strategy for stair ascent, modified from [66].

5.4. Assist in the Frontal Plane

Due to the time constraints of this project, its scope will be limited to analyzing a frontal plane assist strategy for flat walking, inclined walking, walking up the stairs. Figure 12, Figure 13 and Figure 14 show the power expended by the hip adductors to achieve motion in the frontal plane for the three aforementioned walking modes. The data in Figure 12, Figure 13 and Figure 14 are simulated for a male subject with a height of 1.8 m and a mass of 100 kg.

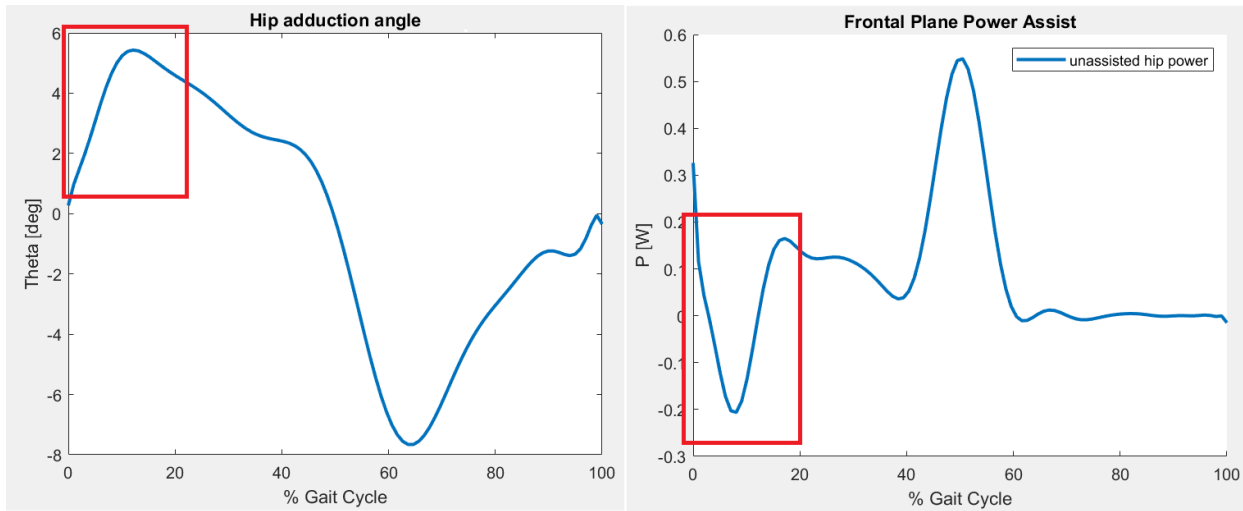


Figure 12 Hip frontal plane angle (left) and power (right) as a function of percent gait cycle for flat ground walking [48], high adduction and negative power region boxed in red.

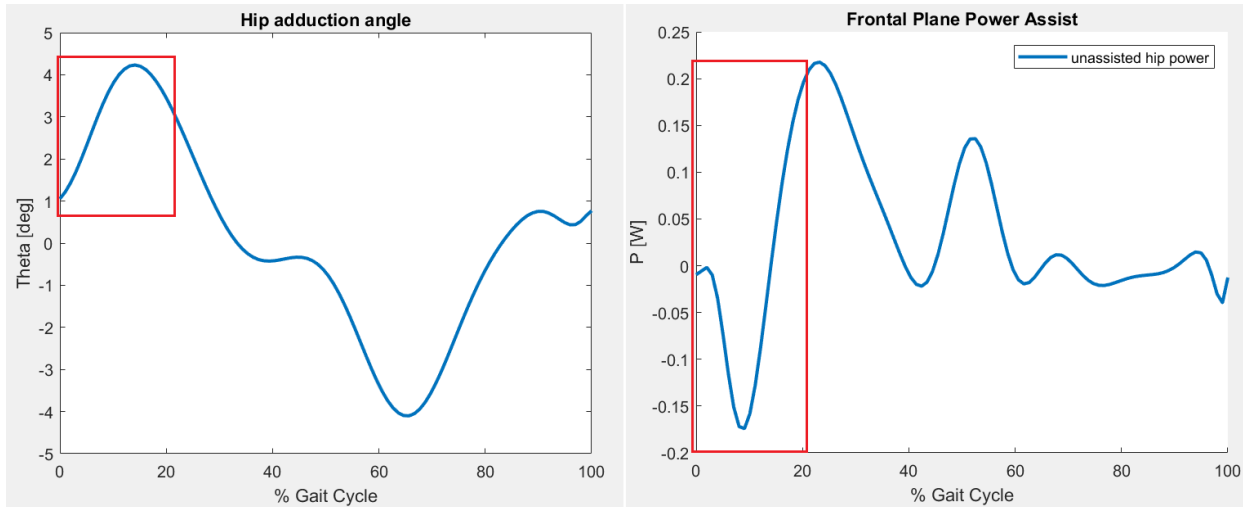


Figure 13 Hip frontal plane angle (left) and power (right) as a function of percent gait cycle for inclined walking [68], high adduction and negative power region boxed in red.

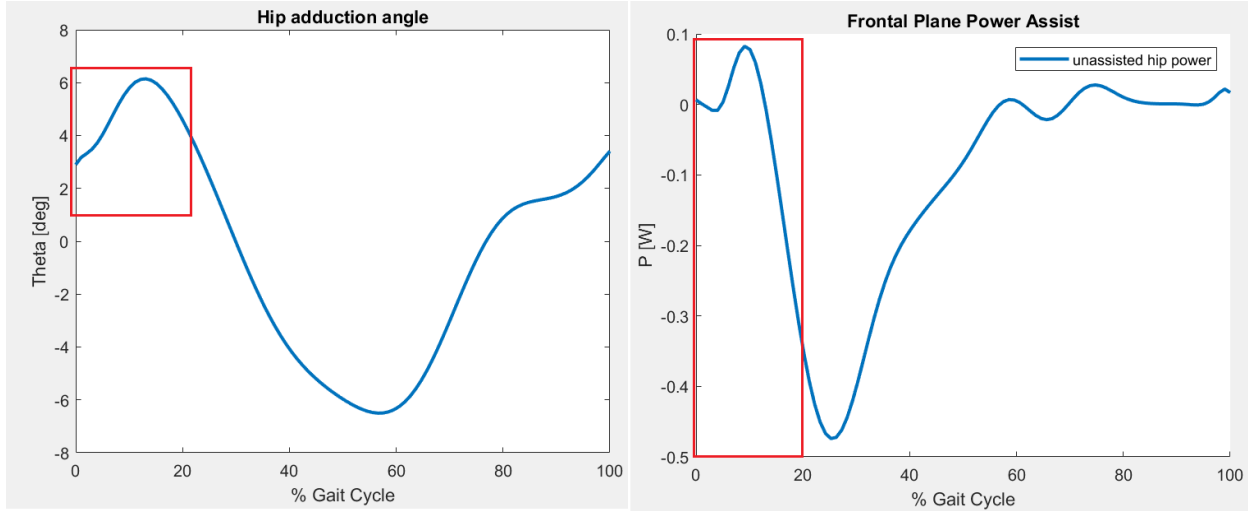


Figure 14 Hip frontal plane angle (left) and power (right) as a function of percent gait cycle for walking up the stairs [51], high adduction and negative power region boxed in red.

For all three gait modes, the hip is abducted at the beginning of stance phase and then is abducted from the mid-stance to late swing phase. In all gait modes, hip adduction (and the maximum hip adduction angle) occurs from 0 – 20% gait cycle (GC) (loading response and half of mid-stance). Moreover, for each walking mode, there is a negative power region that coincides with the adduction that occurs from 0 – 20% GC. Therefore, as demonstrated in Figure 15, a frontal assist strategy is investigated and consists of damping that occurs only at adduction angles that are near the maximum adduction angle for walking.

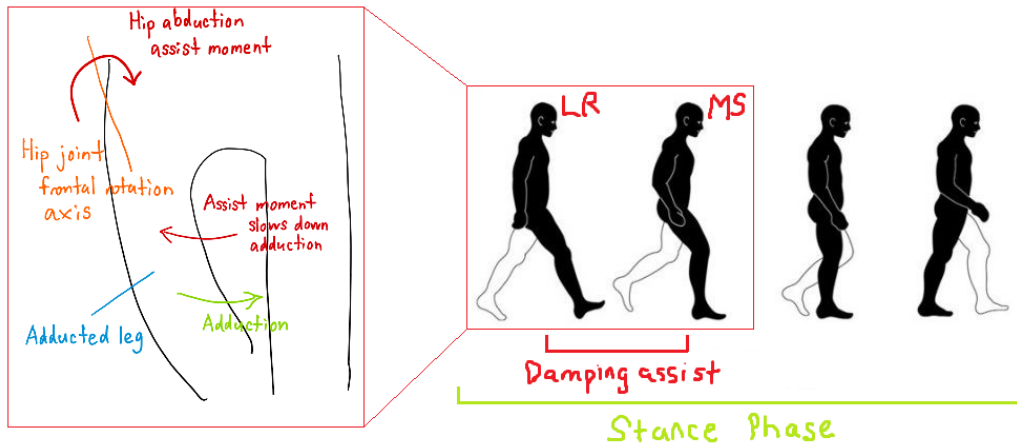


Figure 15 Frontal plane gait assist strategy showing damping assist that occurs near maximum adduction that occurs during 0 – 20 % GC (loading response (LR) and mid-stance (MS)).

During 0 – 20 % GC, the hip abductors are slowing down the adduction of the leg. Thus, the assist strategy reduces the amount of energy that the abductors expend to control the

momentum of the leg as it adducts. Energy harvest and release both occur during 0 – 20 % GC and is discussed in more detail in section 9.10.

6. Dynamic Analysis

6.1. Inverse Dynamics of the Lower Limb

Inverse dynamics (ID) helps in analyzing the effects of the hip exoskeleton device on the gait of a user. Using the ground force reactions from Winter's flat ground gait data [52], knee and hip joint reaction forces can be determined. A simple three-component model of the lower limb was created to analyze joint force reactions, shown in Figure 16.

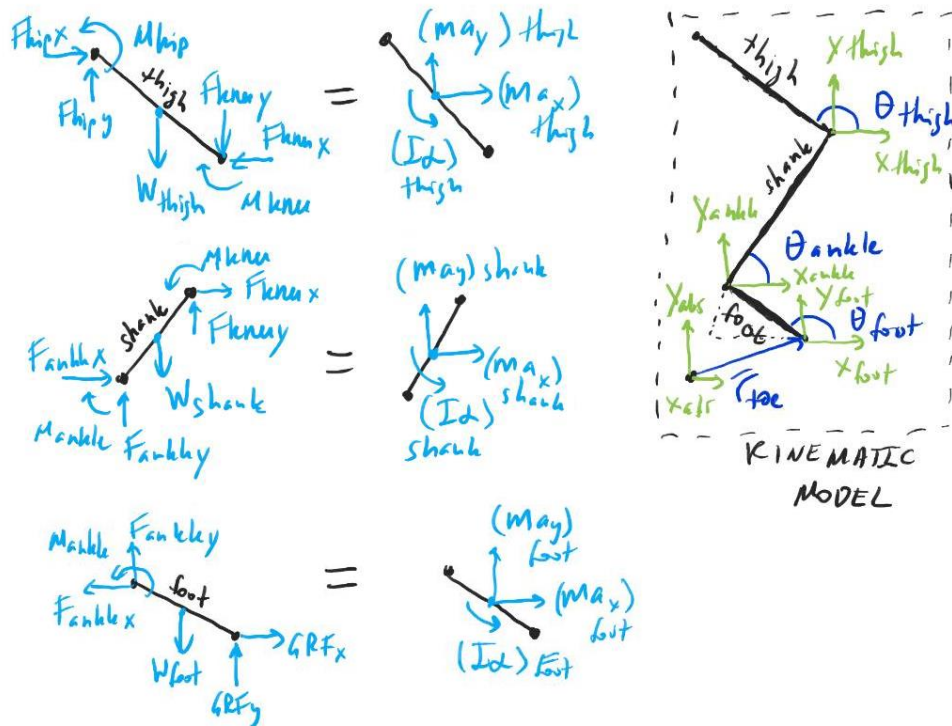


Figure 16 Lower limb model used for Inverse Dynamics.

The simplified model assumes the presence of three rigid links joined by revolute joints that actuate in the sagittal plane. The center of pressure (COP) remains in the same position throughout the gait cycle. Winter's extensive data for non-elderly participants was used to obtain ground reaction forces (GRF) and kinematic parameters for the ID model [8]. Model subject parameters were kept in line with Winter's original parameters for body mass, and thigh and shank

lengths, while Anthropometric model parameters defined link masses, CoM positions and inertial properties [8].

The equilibrium equations for the foot are:

$$\begin{aligned} -F_{anklex} + GRF_x &= m_{foot}a_{footx} \\ -F_{ankley} - m_{foot}g + GRF_y &= m_{foot}a_{footy} \\ M_{ankle} + F_{anklex}\Delta y_{1foot} + F_{ankley}\Delta x_{1foot} + GRF_x\Delta y_{2foot} + GRF_y\Delta x_{2foot} &= I_{foot}\alpha_{foot} \end{aligned}$$

The equilibrium equations for the shank are:

$$\begin{aligned} F_{kneex} + F_{anklex} &= m_{shank}a_{shankx} \\ F_{kneey} - m_{shank}g + F_{ankley} &= m_{shank}a_{shanky} \\ M_{knee} - F_{kneex}\Delta y_{1shank} + F_{kneey}\Delta x_{1shank} - M_{ankle} + F_{anklex}\Delta y_{2shank} - F_{ankley}\Delta x_{2shank} &= I_{shank}\alpha_{shank} \end{aligned}$$

The equilibrium equations for the thigh are:

$$\begin{aligned} F_{hipx} - F_{kneex} &= m_{thigh}a_{thighx} \\ F_{hipy} - m_{thigh}g - F_{kneey} &= m_{thigh}a_{thighy} \\ M_{hip} - F_{hipx}\Delta y_{1thigh} - F_{hipy}\Delta x_{1thigh} - M_{knee} - F_{kneex}\Delta y_{2thigh} - F_{kneey}\Delta x_{2thigh} &= I_{thigh}\alpha_{thigh} \end{aligned}$$

This system of equations was entered into MATLAB and then used to calculate joint reactions at every frame of Winter's flat ground gait data. This provided baseline data of hip reactions without wearing the hip exoskeleton.

Two methods of adding device weight to ID were experimented. The first method assumes a static context and adds device mass to the vertical GRF. A multiplication factor to scale the GRFy data to include the device mass is computed. The new ground force reaction is calculated using the following equation:

$$GFR'_y = GFR_y * \frac{m_{device} + m_{person}}{m_{person}}$$

The second method involves dynamic scaling of both GRFx and GRFy by both the static weight of the device as well as the dynamic weight based on accelerations of the lower torso to which the device is attached. This is done uniquely for each gait frame data and cannot be applied as a single simplified scaling factor.

$$GFRx = GFRx + m_{device} a_{x_waist}$$

$$GFRy = GFRy + m_{device} (g + a_{y_waist})$$

Figure 17 shows the comparison of both approaches. Data analysis will use the dynamic approximation. Moments were obtained using the ID model developed in MATLAB using the derived equations and are shown in Figure 18. Of note are the differences in the first 35% of the gait cycle, likely resulting from the use of Anthropometric model [52] to model limb properties for the ID analysis, as well as constant CoP.

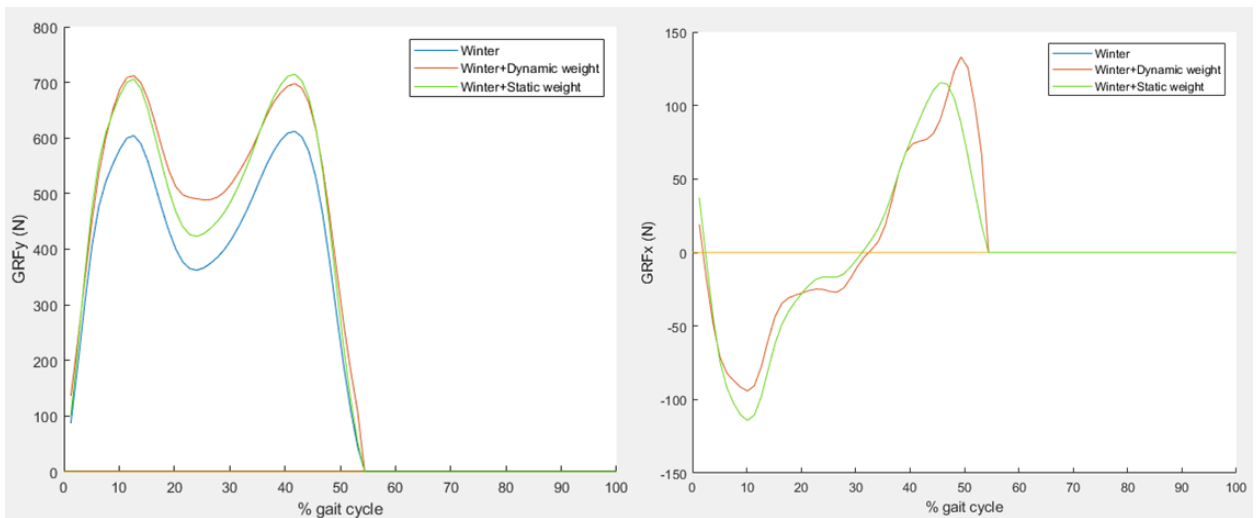


Figure 17 Ground reaction forces (GRFy on the left, GRFx on the right) showing original Winter data, and modified with device weight based on the two approaches.

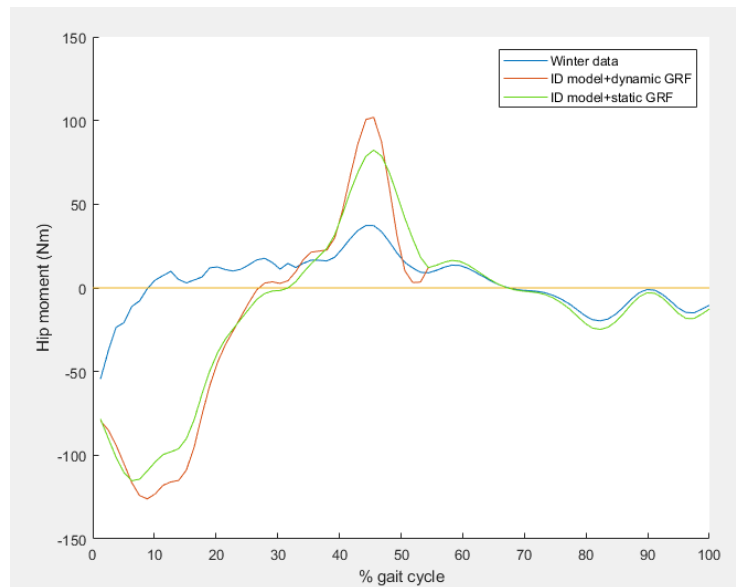


Figure 18 Inverse dynamics model moments with comparison to Winter's data.

6.2. Gait Assist Energy

The 8% maximum stance assist in the sagittal plane was defined in the previous reports based on acceptable amount of energy to harvest from the swing phase of flat and incline gait or pull-up phase of stair climbing in elderly individuals. An extension spring can be used to store energy in extension. Hip rotation angle can be directly related to spring extension via the thigh-belt and spring-belt gear diameter ratio (as derived in Appendix G Kinematic Relations):

$$\Delta x = \frac{r_{tbg}}{R} \theta \quad R = \frac{r_{tbg}}{r_{sbg}}$$

where Δx is the spring extension, r_{tbg} is the thigh belt gear radius, r_{sbg} is the spring belt gear radius. The spring constant can then be derived knowing the maximum hip flexion and extension angles for the gait cycle, the energy based on ID model, and elderly gait data [48], [51], [69]. MATLAB script was written to integrate the power of the stance phase over stance cycle time and take 8% as the maximal energy requirement. Spring constant was then computed for each gait strategy from the energy equation:

$$k = \frac{PE}{0.5(\Delta x)^2}$$

where PE is the spring potential energy, Δx is the spring extension. MATLAB script compares the spring constants and selects the smallest one as related to the extension length to prevent exceeding the 8% limit defined in the requirements. The computed spring constant is 15.60 N/(m*kg), or 1560N/m for a 100kg person, constituting our maximum use case for the analysis.

6.3. Dynamic System Analysis

The first step for the analysis of mechanical components is to model the forces on each component with free-body diagrams (FBDs). The assumptions in force analysis include: forces in sagittal plane only, simple geometry represented by a combination of rigid links or simple shapes, forces represent average forces acting at a point on the geometry, no air resistance, and no bearing friction.

Sample FBDs are presented in Figure 19. The components represent the sagittal view of the thigh bar, thigh belt attachment, and thigh rigid support attachments which transmit thigh rotation and translation to the device main shaft as well as the thigh belt. Thigh belt and rigid

support components are attached to the bottom of the thigh bar. FBDs for other components are presented in Appendix H Free Body Diagrams.

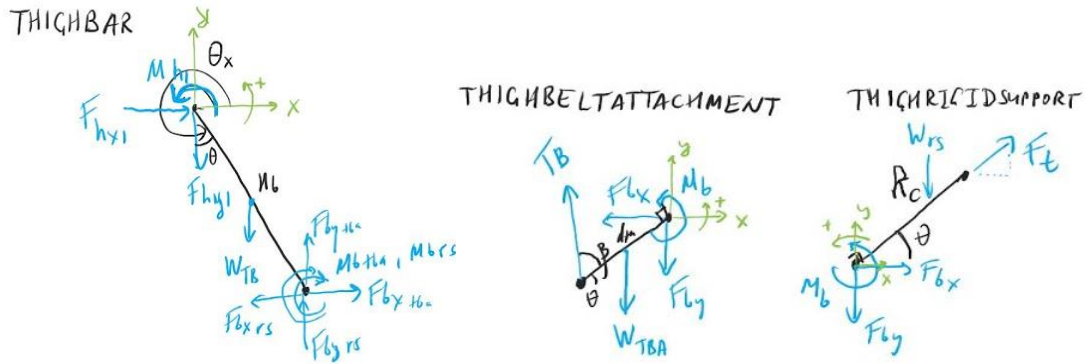


Figure 19 Thigh bar, thigh belt, and thigh rigid support attachment free body diagrams depicting reference centers as well as all forces.

The FBDs in Figure 19 have too many unknowns to solve as is. Therefore, sequential approach to solution is used and programmed into MATLAB. For instance, components are first analyzed as a combination as shown in Figure 20. Unknowns are shown in blue; knowns are shown in orange.

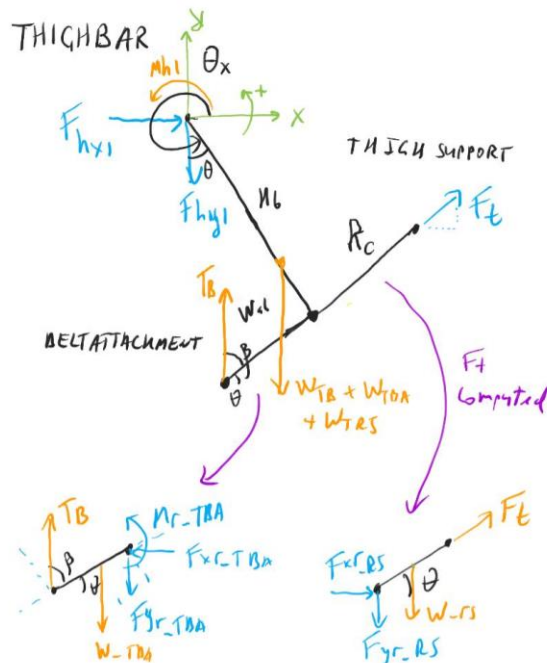


Figure 20 Thigh bar, thigh belt, and thigh rigid support combined to reduce the number of unknowns shown in blue, with knowns shown in orange.

Once the unknowns for the thigh bar assembly have been computed, the internal reaction forces and moments can then be computed for each component. For instance, the moment equation around the coordinate center (shown in green) is solved first to find force F_t , given M_{h1} , T_b , and known kinematic relationships. The reaction forces at the hip (F_{hx1} , F_{hy1}) are computed from the x and y equations. The following equations represent the force and moment relationships:

$$\begin{aligned}\sum F_x &= m_{thighbar} a_{thigh_x} = F_{hx1} + F_t \cos\theta + T_b \cos(\theta + \beta) \\ \sum F_y &= (m_{thighbar} + m_{beltattachment} + m_{thighsupport}) a_{thigh_y} + (W_{thighbar} + W_{beltattachment} \\ &\quad + W_{thighsupport}) = -F_{hy1} + T_b \sin(\theta + \beta) + F_t \sin\theta \\ \sum M_{hipjoint} &= (W_{thighbar} + W_{beltattachment} + W_{thighsupport}) L_{com} \sin\theta + I_{thighbar_hip} \alpha_{hip} \\ &= M_{h1} - W_{ab} T_b \sin\beta + H_b F_t\end{aligned}$$

In order to properly compute moments with gravitational terms and apply dynamic forces at proper locations, the center of mass (L_{CoM}) of the assembly is determined in the sagittal plane. Also, mass moment of inertia (I_m) of the assembly is determined to compute the rotational dynamic contributions of the components during gait. The assembly is assumed as a combination of simple geometry. Figure 21 shows the locations of the L_{CoM} as well as the regions used in computing the parameters.

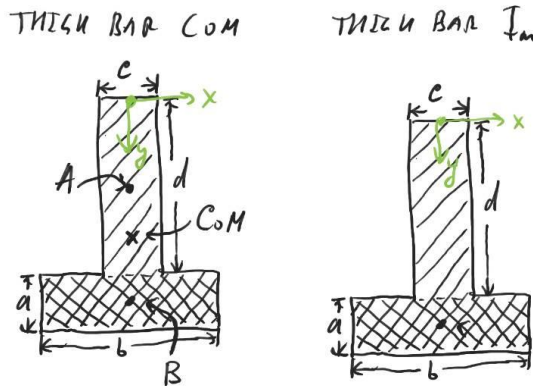


Figure 21 Thigh bar, thigh belt, and thigh rigid support partitioned into specific mass regions for computation of L_{CoM} (left) and I_m (right).

Center of mass is computed as follows [70]:

$$y = \frac{m_A A + m_B B}{m_A + m_B} = \frac{m_{thighbar} * 0.5d + 0.5(m_{beltattachmnt} + m_{thighsupport})(d + 0.5a)}{m_{thighbar} + m_{beltattachmnt} + m_{thighsupport}}$$

where the dimensions a, b, c, d define the lengths as shown in Figure 21, and m_i are the masses of the components.

Sagittal mass moment of inertia is found as follows around the hip attachment coordinate point for the moment equation calculations [70]:

$$\begin{aligned} I_m &= \rho t \iint_A (x^2 + y^2) dA = \rho t \left(\iint_{A1} (x^2 + y^2) dA1 + \iint_{A2} (x^2 + y^2) dA2 \right) \\ &= \rho_A t_A \int_0^d \int_0^c (x^2 + y^2) dx dy + \rho_B t_B \int_d^{d+a} \int_0^b (x^2 + y^2) dx dy \\ &= \frac{1}{3} (\rho_A t_A [c^3 d + d^3 c] + \rho_B t_B [b^3 a + b(d + a)^3 - bd^3]) \end{aligned}$$

where ρ_i is the density of the given region, t_i is the thickness of the given region, and a, b, c, d are the length as shown in Figure 21.

Once the unknowns of the thigh assembly have been computed, the individual thigh belt attachment and thigh rigid support component unknown reaction forces with the thigh bar are computed. The dynamics equations are then reformulated to represent the FBDs in Figure 19.

Thigh bar (tb) dynamics equations are formulated as follows:

$$\begin{aligned} \sum F_x &= m_{thighbar} a_{thigh_x} = F_{hx1} - F_{bxrs} + F_{bxtba} \\ \sum F_y &= m_{thighbar} a_{thigh_y} = -F_{hy1} + F_{byrs} + F_{bytba} - W_{thighbar} \\ \sum M_{hipjoint} &= I_{thighbar_hip} \alpha_{hip} \\ &= M_{h1} - M_{brs} - M_{btba} + Hb \\ &\quad * (\sin(\theta)F_{bytba} + \sin(\theta)F_{byrs} + \cos(\theta)F_{bxtba} - \cos(\theta)F_{bxrs}) - 0.5Hb \\ &\quad * \sin(\theta)W_{thighbar} \end{aligned}$$

Thigh belt attachment (tba) dynamics equations are formulated as follows:

$$\begin{aligned} \sum F_x &= m_{tba} (a_{hip_x} + \alpha_{hip} Hb * \cos(\theta)) = -F_{bx} + T_b \cos(\beta + \theta) \\ \sum F_y &= m_{tba} (a_{hip_y} + \alpha_{hip} Hb * \sin(\theta)) = -F_{by} + T_b \sin(\beta + \theta) - W_{tba} \end{aligned}$$

$$\sum M_{tb} = I_{tba_b} \alpha_{hip} = M_b - d_{ta} \sin(\beta) T_b + 0.5 d_{ta} * \sin(\theta) W_{tba}$$

Rigid support attachment (*rs*) dynamics equations are formulated as follows:

$$\begin{aligned}\sum F_x &= m_{rs} (a_{hip_x} + \alpha_{hip} Hb * \cos(\theta)) = F_{bx} + F_t \cos(\theta) \\ \sum F_y &= m_{rs} (a_{hip_y} + \alpha_{hip} Hb * \sin(\theta)) = -F_{by} + F_t \sin(\theta) - W_{rs} \\ \sum M_{rs} &= I_{rs_tb} \alpha_{hip} = M_b - 0.5 R_c * \cos(\theta) W_{rs}\end{aligned}$$

These equations form a system with shared input and output variables defined via parametrization discussed previously. Mass and section properties are computed using similar methodology. The system including all of the component equations as well as equations linking the shared variables are processed via a MATLAB script containing all of the equations. A matrix representation of the system is created in the form of $Ax = b$, where A is the coefficient matrix, x is the unknown force vector, and b is the known vector containing weight and dynamic terms. The system is solved for 155 unknown forces and force couplings using a MATLAB numerical solver, outputting the force vector in a main loop function for each frame of the gait cycle with given input kinematics obtained from the data. The force results are saved by the MATLAB application to the “Results” folder located in the application directory, as comma separated value files associated with a particular gait data set simulated. Minimum, maximum, amplitude, and average forces across the gait cycle frames are also computed for fatigue stress analyses.

7. System and Subsystem Structure

Four major subsystems combine to create the device, which include the main energy subsystem, the timing subsystem, the thigh subsystem, and the waist subsystem. The main energy subsystem comprises of any component that is directly involved with the transmission of energy from the thigh to the main energy spring used to store and apply energy during gait. The timing subsystem comprises of components used to engage and disengage the main energy spring during gait, or in other words, any component directly involved with implementing gait assist strategies into the device. The timing subsystem also handles switching between different gait strategies (level walking, incline, stair ascent). The thigh subsystem consists of components that interface

the main energy and timing subsystems to the thigh. This includes physical attachments to the thigh as well as parts used to connect thigh attachments to the rest of the device. The waist subsystem consists of components used to attach the device to the trunk of the user. Figure 22 shows a simplified system tree.

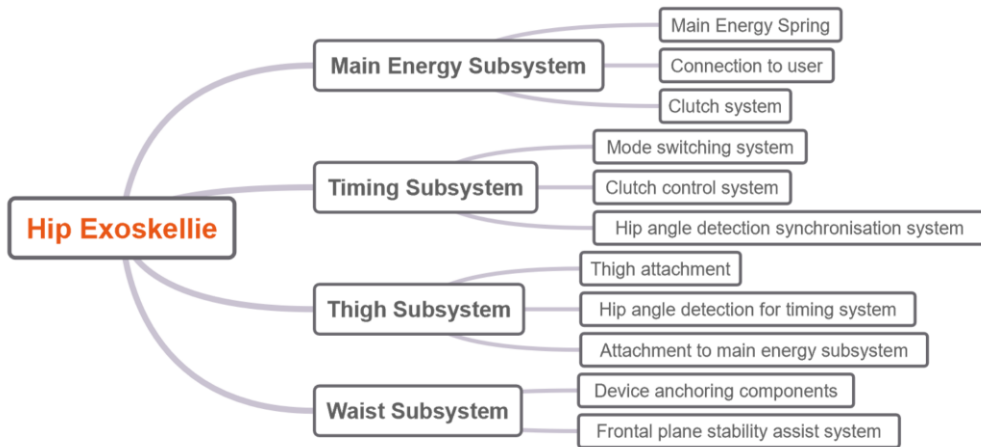


Figure 22 Simplified system flow chart graph.

The described systems are associated with a range of functions, with given inputs and outputs as shown in Figure 23. Energy storage and transfer functions, shown in orange, harvest, transfer, store, and release potential energy. Timing and mode switching functions, shown in green, are responsible for controlling the energy storage and transfer functions to meet the required gait strategy objectives.

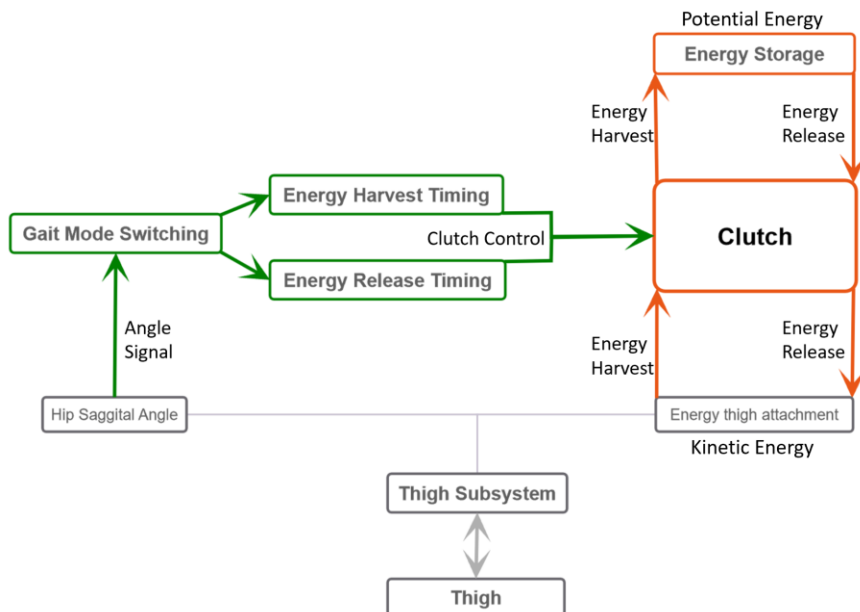


Figure 23 System function flow chart graph.

8. Hip Exoskeleton Design Overview

The proposed design of the passive hip exoskeleton is shown in Figure 24, an exploded view of the design is shown in Figure 25 and names of the labelled parts are shown in Table 5.

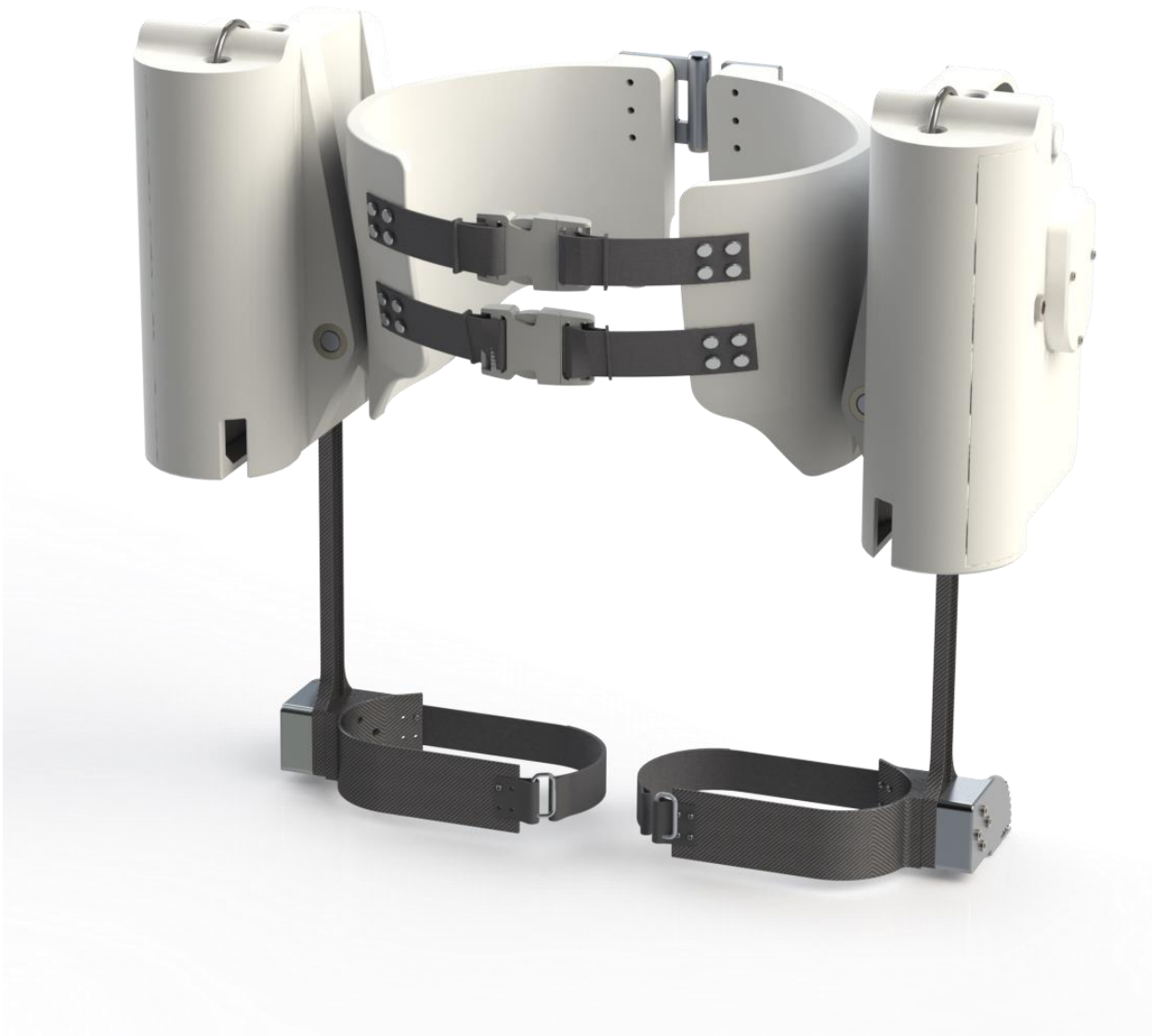


Figure 24 Render of the proposed hip exoskeleton design.

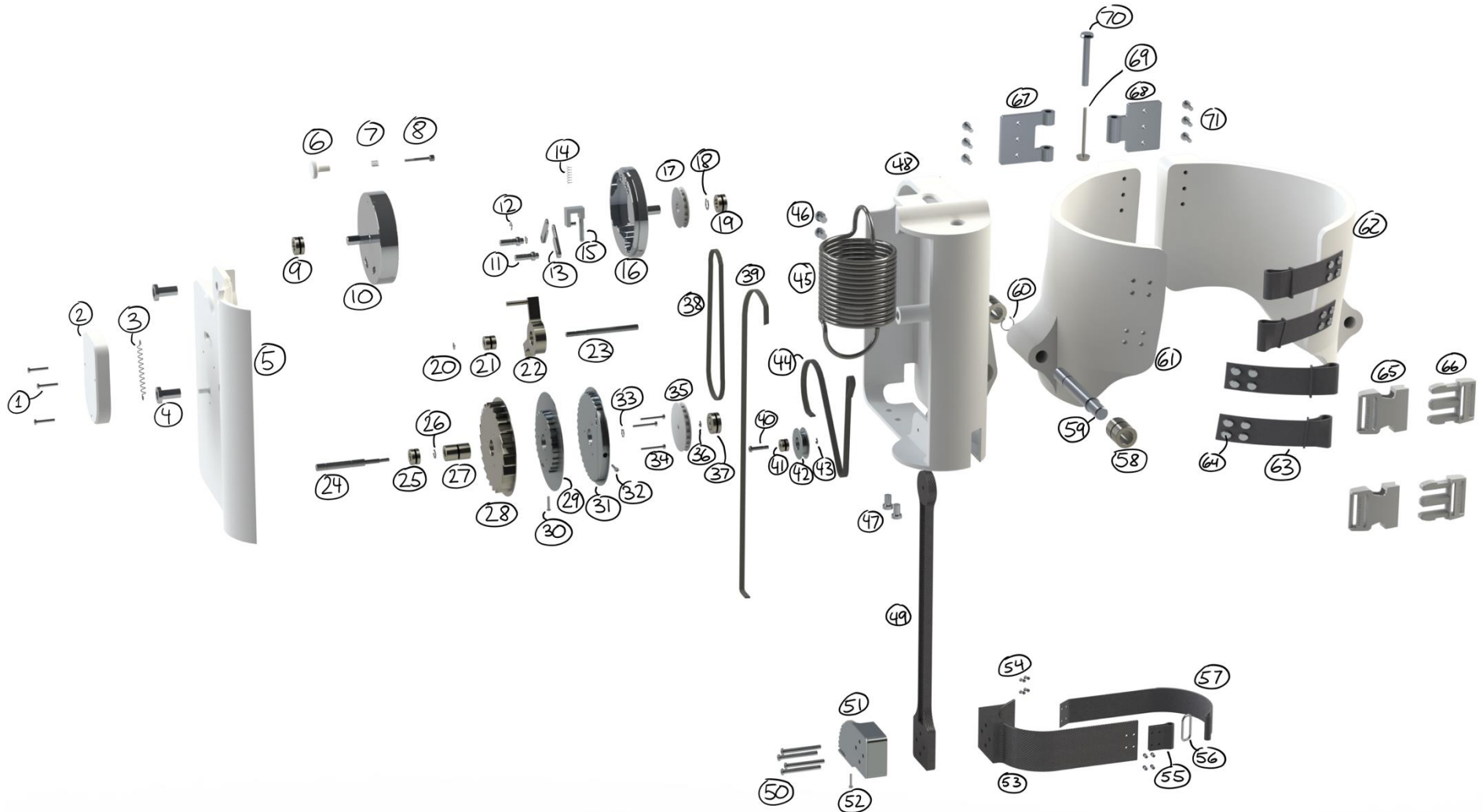


Figure 25 Render of exploded view of the design.

Table 5 Part names of labelled parts from Figure 25.

Label Number	Part Name	Label Number	Part Name
1	Cover 2 Bolts	37	Main Medial Bearing
2	Cover 2	38	Timing Belt
3	Pawl Spring	39	Thigh Belt
4	Cover 1 Bolts	40	Pulley Shaft
5	Cover 1	41	Pulley Bearing
6	Disk Lock Handle	42	Pulley
7	Disk Lock Spring	43	Pulley Circlip
8	Disk Lock Shaft	44	Spring Belt
9	Lateral Timing Bearing	45	Main Energy Spring
10	Pin Disk	46	Side Case Bolts
11	Timing Pin	47	Bottom Case Bolts
12	Timing Pin Circlip	48	Main Case
13	Pin Arm	49	Thigh Bar
14	Cam Spring	50	Thigh Bolts
15	Cam Follower	51	Thigh Belt Attachment
16	Cam Disk	52	Belt Attachment Clamp Bolt
17	Cam Timing Belt Gear	53	Thigh Rigid Support
18	Cam Shaft Circlip	54	Thigh Rivets
19	Medial Timing Bearing	55	Fabric Fastener
20	Pawlever Shaft Circlip	56	Fabric Hoop
21	Pawlever Bearing	57	Thigh Strap
22	Pawlever Bearing	58	Case Hinge Bearing
23	Pawlever Shaft	59	Case Hinge Shaft
24	Main Shaft	60	Case Hinge Circlip
25	Main Lateral Bearing	61	Waist Right
26	Main Shaft Circlip 3	62	Waist Left
27	Main Needle Bearing	63	Front Strap
28	Ratchet Gear	64	Waist Rivet
29	Spring Belt Gear	65*	Buckle Hook
30	Sprint Belt Gear Clamp Bolt	66*	Buckle Insertion
31	Thigh Belt Gear	67	Waist Hinge Right
32	Thigh Belt Gear Clamp Bolt	68	Waist Hinge Left
33	Main Shaft Circlip 2	69	Waist Hinge Bolt
34	Gear Bolts	70	Waist Hinge Rod
35	Main Timing Belt Gear	71	Waist Bolts
36	Main Shaft Circlip 1		

* Buckles are obtained from McMaster-Carr part number 29705T97 [71]

8.1.Main Energy Subsystem

The main energy subsystem is responsible for energy harvesting and release. A simplified schematic of the main energy pathway can be seen in Figure 26. Two toothed timing belts are used to transmit energy from the thigh to the main energy spring. The first belt, named the thigh belt, is fixed onto a belt gear on one, named the thigh belt gear, and the other end is connected to the thigh subsystem. When the hip flexes, the thigh belt is pulled by the thigh, rotating the thigh belt gear. The thigh belt is shown in green in Figure 26. A second belt gear, named the spring belt gear, is fixed to the thigh belt gear such that the two gears rotate together, shown in Figure 26 (B). The spring belt gear acts as an attachment point for a second toothed belt, named the spring belt. The other end of the spring belt is fixed to the main energy spring. The purpose of the spring belt is to redirect the radial motion of the spring belt gear into linear motion to extend the main energy spring. The spring belt is shown in red in Figure 26. A pulley is used to redirect the spring belt to reduce the footprint of the energy subsystem, resulting in a smaller case size.

When the hip flexes, the thigh belt pulls the thigh belt gear in a counterclockwise direction. Since the spring belt gear is fixed to the thigh belt gear, it will also rotate in a counterclockwise direction. The spring belt gear will then pull the spring belt, resulting in energy harvest through linear extension of the main energy spring. This process is shown in Figure 26 (B). When the hip extends, the main energy spring will pull on the spring belt, resulting in clockwise rotation of the two belt gears. This leads to the thigh belt pulling on the thigh and assisting hip extension.

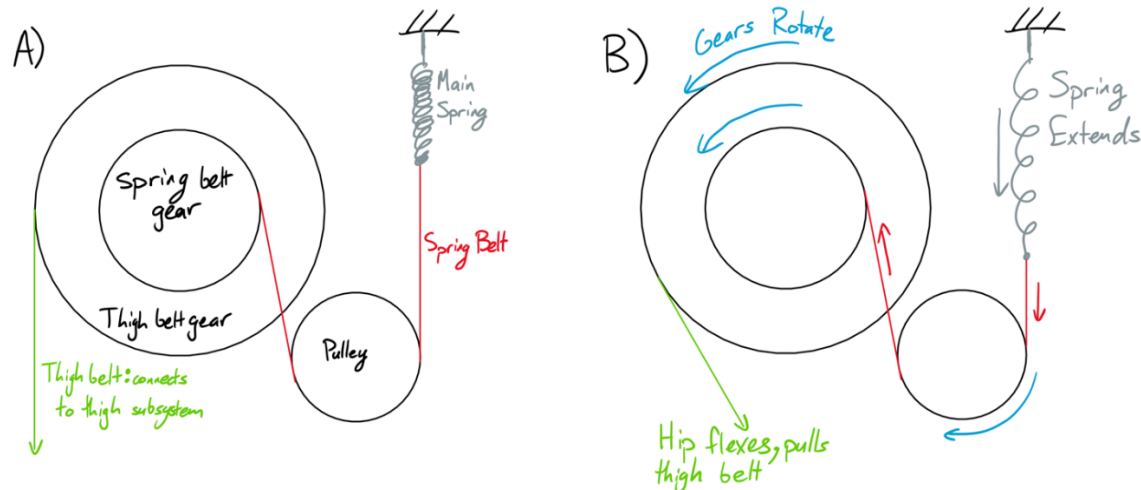


Figure 26 Simplified schematic of the main energy subsystem.

Although this system could have been created with one single belt gear, two were used to function as a gear reducer. The extension of the main energy spring is a function of the diameter

of the spring belt gear. To keep the spring at a reasonable size and mass, its size is limited by reducing the diameter of the spring belt gear, thus reducing spring extension and solid length.

The simplified system shown in Figure 26 needs a clutch to control the engagement of the spring. During the energy harvest phase of gait, the function of the clutch is to stop the spring from contracting but still allow the spring to extend as the hip flexing, therefore storing the kinetic energy of the hip and thigh as potential energy. During the energy release phase of gait, the clutch must allow the spring to actively contract, therefore releasing its potential energy in the form of kinetic energy to assist the hip during gait.

A simplified schematic of the clutch system is shown in Figure 27. The clutch mechanism consists of a ratchet gear and a pawl. The ratchet gear is fixed to the two belt gears discussed previously and will rotate with the belt gears during gait. When the pawl is engaged (Figure 27 (A)), it will constrain the spring belt gear and the thigh belt gear, disallowing them from rotating clockwise, however it still allows them to rotate counterclockwise. This means the energy spring can still be extended (it can still store energy) but it cannot contract and release energy. When the pawl is disengaged (Figure 27 (B)), the ratchet and belt gears are free to rotate in any direction, allowing the energy spring to contract and apply forces onto the thigh.

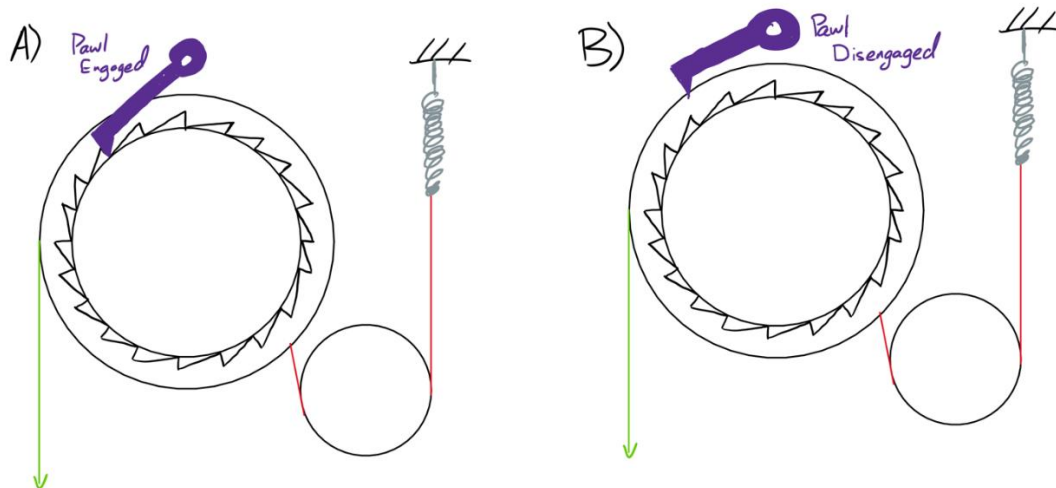


Figure 27 Simplified schematic of clutch components.

It is important to address why a belt is being used to extract and apply energy to and from the thigh subsystem. With the use of a ratchet and pawl clutch system, the motion of the main energy system is being constrained when energy is being extracted. Applying the gait strategies developed in section 5, the pawl would be engaged during the swing phase of gait. If a user of the device were to initiate swing, thus engaging the pawl, and not complete swing phase (for example

the user came to a stop) the pawl would remain engaged. If the connection between the spring belt gear and the thigh subsystem was a rigid beam instead of a belt, the result would be that the user's leg would be constrained with the ratchet gear and spring belt gear, and the user would not be able extend their hip past what the ratchet gear allows. By using a timing belt to connect the energy and thigh subsystems, under the same circumstances discussed previously, the belt would be capable of buckling or folding, therefore the ratchet gear would not constrain the range of motion of the thigh.

A render of the main energy system built into the device case can be seen in Figure 28 (left). Figure 28 (right) shows the spring belt and spring belt gear, as well as the thigh belt and thigh belt gear. Figure 29 shows an exploded view of the main energy gears and shaft. Note that three bolts hold the three gears together, and the three gears are all pressed onto a long needle bearing such that they spin freely on the main shaft.



Figure 28 Render of the main energy subsystem inside the device case (left) and the main energy subsystem viewed from the side (right).

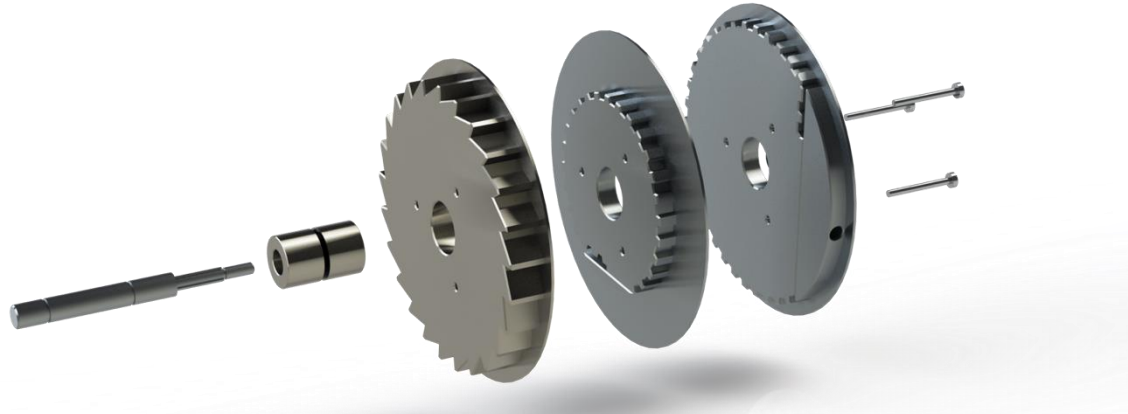


Figure 29 Exploded view of the main energy subsystem.

8.2. Timing Subsystem

The timing subsystem aims to control the clutch system introduced in the energy subsystem. Its main function is to engage and disengage the pawl at specific points of the gait cycles to implement the gait strategies developed in section 5.

The core concept of the timing subsystem is shown in Figure 30. The pawl introduced in the previous section is redesigned to include a lever arm that extends upwards, and the pawl is aptly renamed the pawlever. The redesigned pawlever is shown in Figure 30 (A). A new part is introduced, named the pin disk, which rotates with the hip. The pin disk has two protrusions, named timing pins. The lever portion of the pawlever rests in between the two timing pins. As the pin disk rotates back and forth with the hip, the timing pins will hit the pawlever back and forth, engaging and disengaging the pawl and the clutch system.

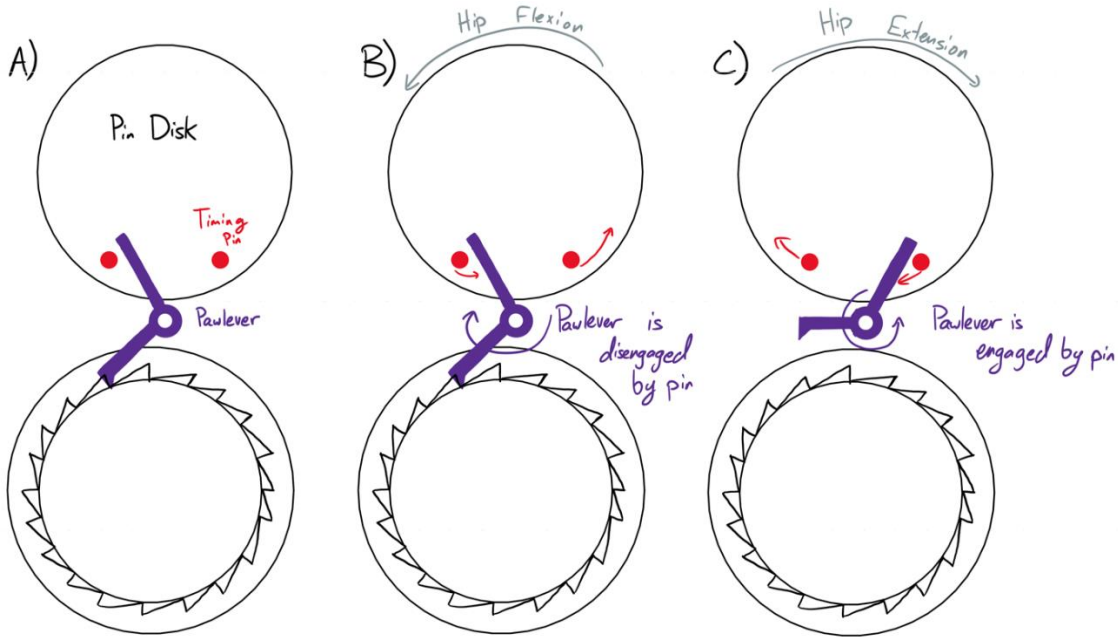


Figure 30 Simplified schematic of the timing system clutch control. Schematic B shows how the rotation of the pin disk disengages the pawlever. Schematic C shows the rotation of the pin disk engaging the pawlever.

Applying the gait strategies from section 5, during the swing phase of gait the pawl will be engaged, and the spring will be harvesting energy. The pin disk will be rotating in a counterclockwise direction as the hip flexes, as shown in Figure 30 (B). As the hip nears maximum flexion, the left-side timing pin on the pin disk will push the pawlever, forcing it to rotate clockwise and disengage the ratchet gear. This engages the energy release as stance phase begins.

During stance phase, the pawlever will be disengaged and the spring will be releasing energy by applying a force on the thigh. The pin disk will be rotating clockwise direction as the hip extends until the end of extension, at which the right-side timing pin will push the pawlever, rotating it counterclockwise and engaging the pawl with the ratchet gear. Thus, energy harvest is initiated as swing phase begins.

To ensure the pawlever does not rotate freely and accidentally engage or disengage due to vibrations during gait, the pawlever implements the functionality of a regular spring switch, shown in Figure 31. A small shaft extends from the top of the pawlever from which a relatively weak extension spring connects to it from the case. This spring switch solution ensures the pawlever state is binary: either it is engaged with the ratchet gear or it is disengaged and being held down by the spring. A render of the implemented design of the pawlever spring is shown in Figure 32.

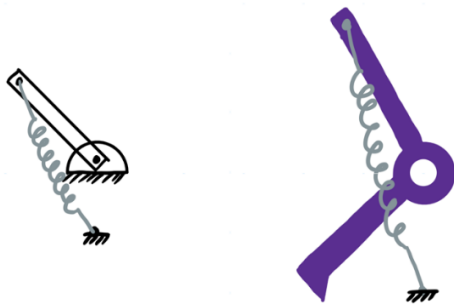


Figure 31 Standard spring switch design (left) and pawlever spring switch implementation (right).



Figure 32 Render of the paw spring connected to the case (left) and the same render from the side (right).

This pin mechanism allows for simple control of the pawlever, and it can be further expanded upon to include mode switching functionality. In its currently described state, the angles of gait in which the pawl is engaged or disengaged are entirely dependent on the position of the timing pins on the timing disk, therefore, to control the angles of engagement and disengagement of the pawlever the timing pin positions needs to be adjustable. This concept is used to create mode switching functionality.

The simplified schematic of the pin adjustment mechanism is shown in Figure 33 (A). The pin disk is modified to add concentric cutouts for the timing pins to move along. Two identical new parts are introduced into the design, called pin arms (shown in purple in Figure 33). Each pin arm connects one of the two pins to a central shaft (shown in grey in Figure 33) which can move freely up and down. When the central shaft moves downwards, it pushes the timing pins apart, as shown in Figure 33 (B). When the central shaft moves upwards, the pins are pulled together.

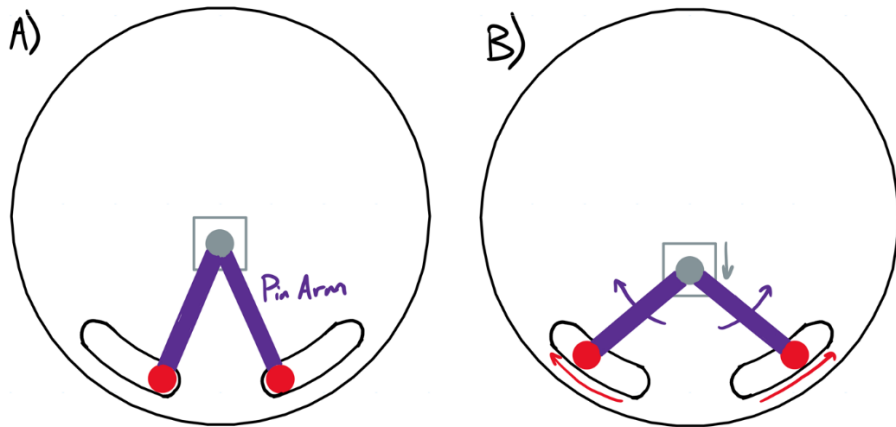


Figure 33 Simplified schematic of the timing pin location adjustment mechanism.

This mechanism relates timing pin radial position to the vertical height of the central shaft; however, it must be further expanded to add mode selection, i.e. add the ability to select discrete vertical positions of the central shaft. Furthermore, this system assumes that maximum extension and flexion angles during gait are equal when in reality the maximum angle of extension during level ground gait is greater than the maximum angle of flexion during the same gait mode. This problem is exasperated when looking at stair ascension, in which the maximum angle of extension is negative (the hip never extends past the vertical plane). To adjust for this problem, the pin disk needs to have an angular offset such that the timing pins are not horizontal to each other and the angle of activation in flexion and extension are not equal.

Both mode selection and angular offset can be solved by using an internal cam system. An exaggerated schematic of the internal cam solution is shown in Figure 34. As the cam follower rotates, it is pushed up and down. If this cam follower is connected to the pin arms, as shown in Figure 33, the pin position will change in relation to the height of the cam.

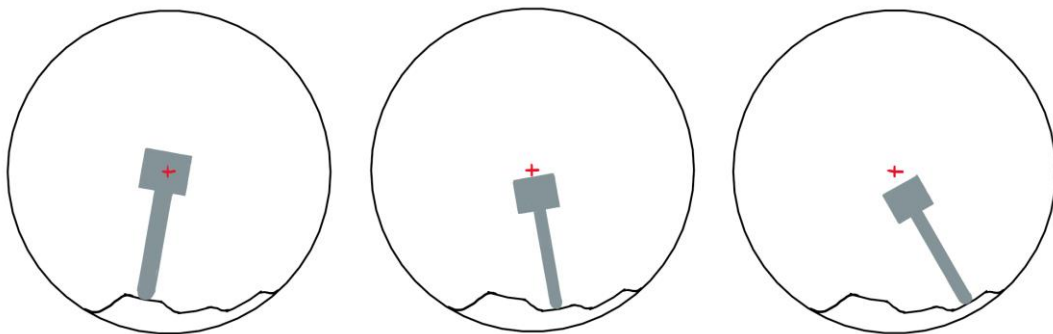


Figure 34 Simplified schematic of cam height variation mechanism.

This proposed solution also solves the issue of positioning the pins for each gait mode separately if the pins are rotated with the cam follower. This is shown more clearly in Figure 35. In both renders of this figure, the timing disk is oriented as if the wearer of the device were standing perfectly straight. The left image shows the pin disk and timing pin orientation for the level ground gait mode in which there is a slight counterclockwise tilt to the pin disk. Due to this rotation, the pin disk must rotate more to engage the right timing pin than the left timing pin, requiring more extension to engage the right timing pin than flexion to engage the left timing pin. This can be seen more clearly in the right image of Figure 35 which shows the timing disk configuration for the stair ascent gait mode. The pin disk is biased counterclockwise, therefore much more flexion is required to disengage the pawlever by hitting the left pin, and much less extension is required to engage the pawlever by hitting the right pin. Also note that in the stair ascent mode, the pins are further apart in their grooves compared to the level ground gait mode due to the cam follower mechanism discussed above.



Figure 35 Transparent render of the pin disk, timing pins, and the cam follower.

The cam follower is connected to the opposite end of the pin arms and the cam follower shaft, seen in between the two timing pins, moves along an internal cam. In Figure 35, the internal cam for the level ground gait mode (left image) pushes the cam follower upwards, pulling the timing pins towards each other. When the pin disk is rotated relative to the internal cam, the cam follower rotates with it, sliding against the internal cam surface. As the internal cam lowers the cam follower, the timing pins are pushed apart. To ensure the cam follower correctly follows the

internal cam, a small compression spring is used. The socket for the spring is seen as a cylinder above the cam follower in both images of Figure 35.

To implement the cam follower concept, a second disk must be added to the design, called the cam disk. The cam disk is placed directly behind the pin disk in order to have the cam follower be as close to the internal cam and the timing pins as possible. The pin disk and cam disk are shown next to each other in Figure 36. The two disks have interlocking lips on their edges to allow them to mesh together smoothly. The cam disk is connected to the thigh subsystem and rotates with the hip. A spring-loaded pull pin, called the disk lock mechanism, is used to lock the pin disk to the cam disk, forcing the pin disk to rotate with the hip. The disk lock mechanism can be seen in Figure 36, in which the pull pin and the handle are visible at the top of the pin disk (left disk in image). Also shown in Figure 36 are the three locking holes at the top of the cam disk, each corresponding to a different gait mode and a different position and height on the internal cam of the cam disk. To change gait modes, the disk lock mechanism is pulled and the pin disk is rotated relative to the cam disk to the required gait mode angle, after which the disk lock mechanism is let go and a spring pushes it into the locking hole of the cam disk for the corresponding gait mode.



Figure 36 The pin disk with cam follower, pin arms, and timing pins on the left next to the cam disk on the right.

This two-disk system provides the necessary mode switching functionality and clutch control to adequately implement the required gait assist strategies. The only remaining challenge is to connect the timing disks to the thigh subsystem without interfering with the main energy system which is positioned in-between the two timing disks and the thigh subsystem.

The following section explains how the timing system is connected to the hip angle.

8.3. Thigh Subsystem

The function of the thigh subsystem is to facilitate the transfer of energy between the thigh/hip and the energy system of the hip exoskeleton. A render of the thigh subsystem is shown in Figure 37. Of note is the thigh belt on the left side of the image, which connects to the thigh belt gear discussed in section 8.1.



Figure 37 Render of the thigh subsystem. Note the thigh belt on the left which connects to the thigh belt gear in the main energy system.

The long carbon fiber I-beam, named the thigh bar, acts as a rigid connection between the thigh subsystem and the other discussed subsystems. The main function of the thigh bar is to transfer the current angle of the hip to the timing subsystem. As discussed in section 8.2, the timing system relies on the current angle of the hip to engage or disengage the clutch mechanism of the main energy subsystem. The main shaft, shown in Figure 28 and Figure 29, has a splined region dedicated to connecting the thigh bar to the timing subsystem. Next to the thigh bar, fitted onto the same spline, is a small timing gear which uses a timing belt to transfer thigh bar rotation to the cam disk of the timing system. The cam disk also has a splined region on its shaft to fit a timing belt gear and receives rotation moment from the thigh bar through the belt gear.

Note that as discussed in section 8.1 and shown in Figure 29, the three gears of the main energy subsystem are mounted on a needle bearing and rotate independently to the main shaft. This allows the main energy system and the timing system to both use the main shaft independently without hindering each other.

The lower region of the thigh subsystem consists of two rigid components attached to the bottom section of the thigh bar. The belt attachment component, shown in Figure 38 (left), attaches laterally to the thigh bar and functions to anchor the thigh belt to the lower thigh using a toothed belt clamp. The second rigid component, the rigid support, is used to transfer forces to and from the thigh and is used as an attachment point for a Velcro belt to wrap around the circumference of the thigh. The rigid support is visible in Figure 38 (left) in which it connects to the thigh bar to the right of the thigh bar. It is also visible in Figure 38 (right) where it is also fitted with a Velcro belt that is revised to the rigid support. In this prototype design, Q-angle is adjusted for by extending the rigid support further medially towards the user.



Figure 38 Render of the lower components of the thigh subsystem.

Due to the chosen gait strategies, during the stance phase of gait the rigid support will be applying a force onto the thigh, pushing the thigh backwards and propelling the user forwards, assisting hip extension. During swing phase, the thigh will be pushing against the rigid support; as a result, energy will be harvested. Under ideal circumstances, little to no forces should be acting on the Velcro belt, other than tension due to belt tightening to secure the thigh subsystem to the user.

8.4.Waist Subsystem

The waist subsystem is the anchor for the case containing the main energy and timing subsystems. A simplified drawing of the waist components is shown in Figure 39.

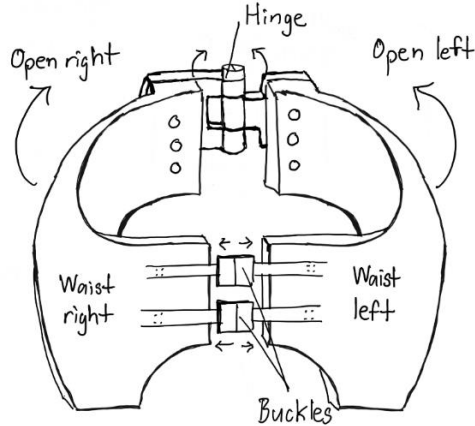


Figure 39 Simplified schematic of the waist subsystem.

In this subsystem, there are two rigid curved components, one named waist right placed on the right side of the waist, and one placed on the left side of the waist. The curvature of both components follows the shape of the human waist and hip. Waist right and waist left are connected to each other through a posterior hinge and through two anterior buckle straps. The hinge allows the waist right and waist left to be separated laterally so that it is easy to put on and take off. Two buckles are used instead of one to adequate support the frontal plane moments acting on the device near and at the medial part of the body.

As demonstrated in Figure 40, on each the right and left sides, there is a shaft named waist case hinge shaft that supports both the casing and internal mechanisms. A shows that this shaft is inserted in a curved protrusion on the side of waist left, for example. B shows how the case is mounted on the shaft.

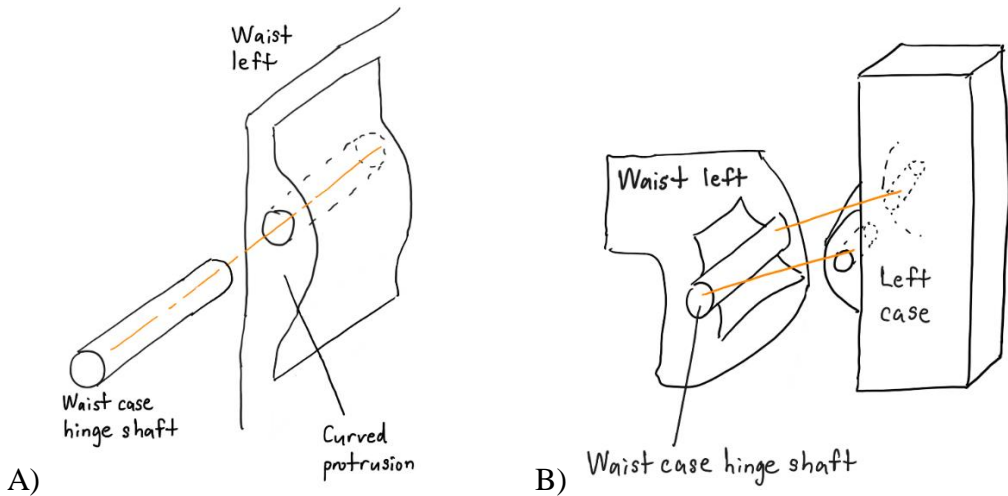


Figure 40 A) Insertion of the waist case hinge shaft into waist left. B) Attachment of the left case on waist left.

This shaft allows the case and its mechanisms to rotate in the frontal plane and thus, not restrict adduction and abduction when within a small flexion or extension angle. For the device to stay stable, the curved protrusions on the sides of each waist right and waist left are rigid and prevent the shaft from rotating in the sagittal and transverse planes.

As demonstrated in Figure 41, the main energy, timing and thigh subsystems are placed in the case; a render of how the case and its components is anchored on the waist subsystem is also shown in Figure 41.

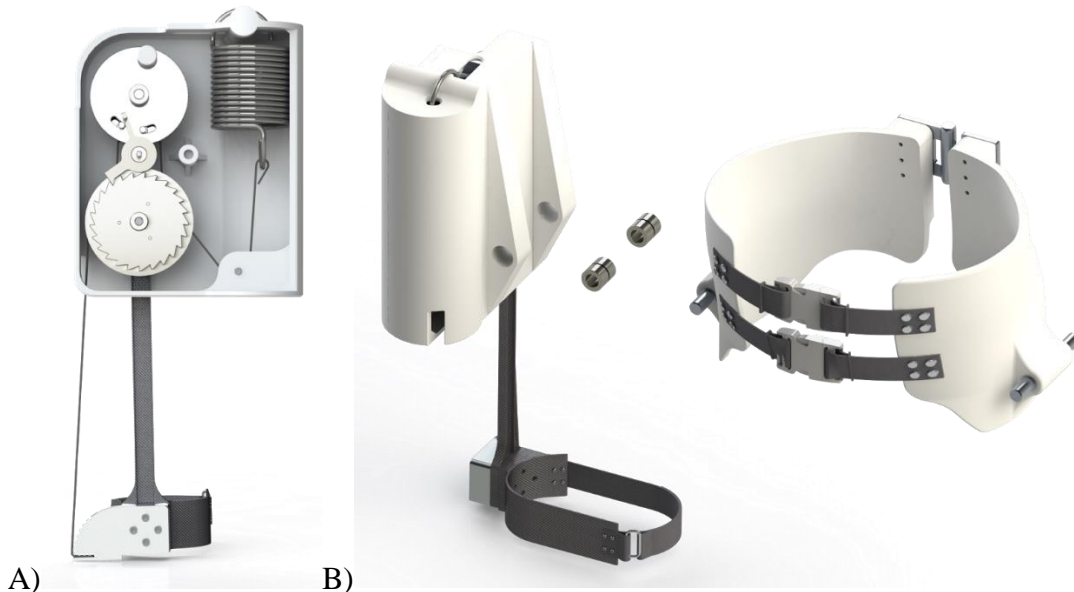


Figure 41 A) Main, timing, and thigh subsystems in the case. B) case attachment to the waist subsystem.

Having the waist parts match human body curvature allows for the weight of the device to be adequately distributed over the body. Additional soft underlayer is not shown, but would normally be placed between the body and the waist component to provide cushioning and help distribute pressure. The graphical user interface gives the option to select between male and female and the curvature for waist right and waist left adjusts based on gender (for example, women typically have a higher hip to waist circumference ratio than men). Renders showing differences in male and female waist and hip curvature are shown in Figure 42.

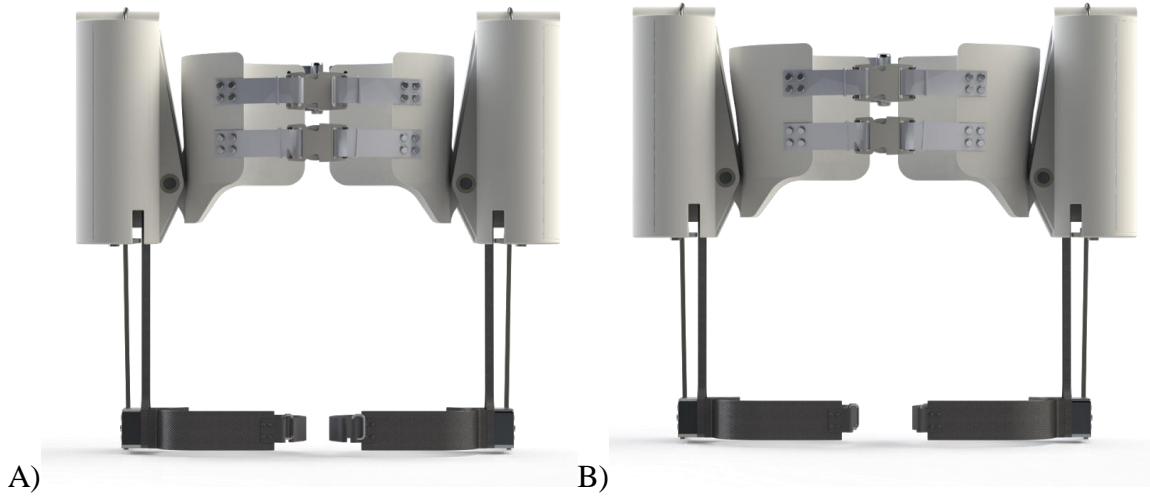


Figure 42 A) Male hip exoskeleton, B) Female hip exoskeleton

Ideally, there should be some degree of freedom in the transverse plane so that waist subsystem does not rotate due to internal and external hip joint rotation that occurs naturally during gait, however it is not implemented in the current iteration of the design. Moreover, the hinge shaft is placed at the same vertical height as the user's natural hip joint so that the device adducts and abducts in unison with the user's leg.

As mentioned in section 5.4, damping assist was envisioned in the frontal plane during adduction from 0 – 20 % GC. As shown in Figure 43, during adduction the bottom corner of the case becomes closer to the rigid waist component. Therefore, a damping pad could be placed below the case hinge. When the pad contacts the rigid waist component, the pad compresses to provide and assist force, acting about a moment arm to produce an assist hip abduction moment. Frontal plane damping has been simulated, but not implemented in Solidworks due to time constraints.

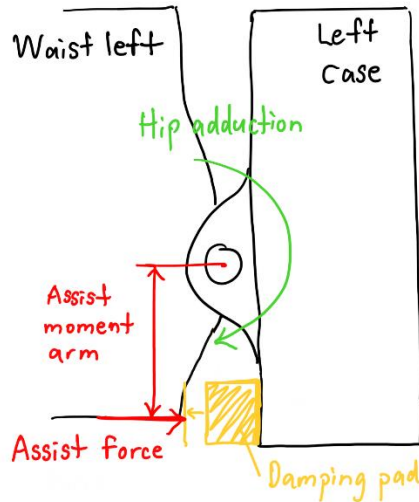


Figure 43 Damping pad placed below the case hinge to provide an assisting hip abduction force.

The damping pad provides an assisting abduction moment about the hinge shaft to help slow down adduction and support initial abduction during gait as discussed in section 5.4. A damping pad is not been placed above the hinge location on the case because an upper damping pad would oppose the desired motion, causing the hip to expend more power than normal to achieve the frontal plane rotation that occurs naturally in gait.

9. Working Analysis

This section introduces the analysis that is be conducted on the components of the device and provides some sample calculations to show how equations are used. The analysis is used for parametrization to determine the appropriate dimensions of the components to meet the minimum safety factor defined by the project requirements in section 4. The components must also pass ISO standard fatigue testing protocol as discussed in section 4, which requires parts to withstand 300 000 cycles of loading under operation. More often, a conservative 10^6 fatigue cycle limit is chosen.

9.1. Compression Spring Analysis

The device has two compression springs. Compression spring analysis involves testing if the spring yields under static loads and testing the fatigue safety factor of a spring that meets the force and extension requirements for operation of the device.

9.1.1. Cam Spring

The cam spring is used to push the timing subsystems cam follower component onto the internal cam of the cam disk. The cam spring must be small enough to fit into the cam disk cutout but does not need to exert large forces to push the cam follower shaft onto the cam disk.

Assuming the use of steel music wire, the maximum allowable shear force applied to the spring can be determined by using the safety factor and the ultimate shear stress of the material. Using an ultimate tensile strength of 758 MPa [70], the ultimate shear strength is calculated as 45% of UTS [72].

$$\tau_{ult} = 0.45 * UTS = 0.45 * 758 \text{ MPa} = 341 \text{ MPa}$$

Using a safety factor of 2.7, the maximum allowable shear force can be calculated as follows:

$$SF = \frac{\tau_{ult}}{\tau_{max}}$$

$$\tau_{max} = \frac{\tau_{ult}}{SF} = \frac{341 \text{ MPa}}{2.5} = 126.4 \text{ MPa}$$

Using an outer diameter D of 7.5 mm, and using a maximum spring force of ~3.1 N (actual number is determined by simulation), the wire diameter d can then be determined using the following equations:

$$\tau_{max} = \frac{K_B 8FD}{\pi d^3}$$

where F is the applied force, D is spring outer diameter, d is spring inner diameter. Max shear force is calculated as follows:

$$\text{Spring index, } C = \frac{D}{d}$$

$$K_b = \frac{4C + 2}{4C - 3}$$

$$\tau_{max} = \frac{K_b * 8 * F * D}{\pi * d^3} = 126.4 \text{ MPa}$$

Given the complexity of isolating the variable d , these equations were solved in MATLAB. The final solution is then checked to ensure the spring index falls between 4 and 12. In this case, the wire diameter is about 0.81 mm.

Given a maximum compression of around 6.2 mm, the spring constant can be determined by dividing the spring force by extension, resulting in a k of nearly 500 N/m. Using a shear modulus of spring steel, 79.9 GPa, the required number of active coils N is calculated as follows:

$$\Delta x = \frac{8FD^3N}{d^4G} \left(1 + \frac{1}{2C^2}\right), N \approx 4 \text{ active coils}$$

Assuming ground, squared spring ends the total number of coils the spring will have is 6. The solid length of the spring can then be calculated as follows:

$$L_s = N_t * d = 6 * 0.81mm = 4.9 mm$$

Assuming a floating length of 2.3 cm, shear due to compression of the string to its solid length can be calculated as follows:

$$K_s = \frac{2C + 1}{2C} = 1.0543$$

$$F_s = k(free\ length - L_s) = 500 * 0.0181 = 9.05 N$$

$$\tau_s = \frac{K_s * 8 * F_s * D}{\pi * d^3} = 338.3 MPa$$

This shear force is less than the ultimate shear force determined above, therefore the spring will not yield if compressed to its maximum, which should not occur under normal operation of the device.

The safety factor of the spring during fatigue can be calculated using the Modified Goodman Criterion. Using Table 10.4 from [72] ultimate stress S_u can be calculated. Ultimate shear stress, S_{su} , of steel can be determined by taking 80% of the ultimate stress [70], and the fatigue max torsion stress for 1,000,000 cycles can be determined to be 32% of ultimate stress using Figure 12.15 from [70].

$$A = 2211 MPa * mm^m \quad \text{from Table 10.4}$$

$$m = 0.145 \quad \text{from Table 10.4}$$

$$S_u = \frac{A}{d^m} = 2.3 GPa$$

$$S_{su} = 0.8S_u = 1.94 GPa$$

$$S_{sn} = 0.32S_u = 729 MPa$$

The Wahl factor K_w and can then be calculated as follows:

$$K_w = \frac{4C - 1}{4C - 4} + \frac{0.615}{C} = 1.1580$$

Using a maximum force of 3.1 N and minimum force of 2.5 N, maximum and minimum shear stresses can be calculated as shown below:

$$\tau_{min} = \frac{K_s * 8 * F_{min} * D}{\pi * d^3} = 102.5 \text{ MPa}$$

$$\tau_{max} = \frac{K_s * 8 * F_{max} * D}{\pi * d^3} = 127.5 \text{ MPa}$$

Shear amplitude and mean can then be calculated:

$$\tau_a = \frac{\tau_{max} + \tau_{min}}{2} = 12.5 \text{ MPa}$$

$$\tau_m = \frac{\tau_{max} - \tau_{min}}{2} = 115.0 \text{ MPa}$$

Using the Modified Goodman Criterion, the safety factor of the spring given the mean and amplitude shears and all the previously determined spring characteristics, the fatigue safety factor is calculated:

$$\frac{\tau_a}{S_{sn}} + \frac{\tau_m}{S_{su}} = \frac{1}{n}$$

$$\frac{12.5}{729} + \frac{115}{1940} = \frac{1}{n}$$

$$n = 13.0$$

This safety factor is higher than the minimum required safety factor of 2.

9.1.2. Disk Lock Spring

The disk lock spring is used to push the disk lock shaft into the cam disk of the timing subsystem to lock the pin and cam disks together into a specified gait mode. The spring does not have to be stiff as it does not resist any forces under normal circumstances. Using the same methodology as section 9.1.1, the safety factors of the spring can be determined.

Using a static safety factor of 3.0, max extension of 2.5 mm with a force of 0.75 N, and using the same material properties of spring steel as in section 9.1.1, a wire diameter of 0.48 mm is calculated. The spring constant k is also calculated to be 300 N/m. A spring index of 12.4 is calculated, and the total number of coils is 10. The fatigue safety factor is 10.

9.2. Extension Spring Analysis

There are two extension springs in the proposed design which are analyzed to ensure they do not fail under load or fatigue. Similar to compression springs, the extension springs must not yield under static loading and must not fail due to fatigue. Additionally, the spring hook ends must be tested to ensure they do not yield or fail due to fatigue.

9.2.1. Main Energy Extension Spring

The main energy spring must not fail under ISO suggested cyclic load testing. Following the same procedure as compression springs as well as the same material properties, the spring geometry can be determined. From a MATLAB simulation, spring constant of 1035 N/m from max spring extension of 54.98 mm are obtained. From assumed design constraints, an 8 cm outer spring diameter is used. For the purpose of balancing all safety factors, a static loading safety factor of 4 was used to calculate the maximum allowable shear force. A high safety factor is chosen for this spring due to the large forces it is expected to handle. A failure of the main energy spring would be catastrophic and would likely lead to injury. The resultant wire diameter is 5.3 mm, with 14 active coils, making the spring solid length 74 mm.

The fatigue safety factor for torsion acting on the active coils can be determined using the same methodology as the compression spring. This safety factor is calculated as 9.4.

The safety factors for cyclic loading on the spring hook end must now be determined. Relevant parameters of the hook are the radii of curvature, shown in Figure 44. It is assumed that r_1 and r_3 are equal, and r_2 and r_4 are equal.

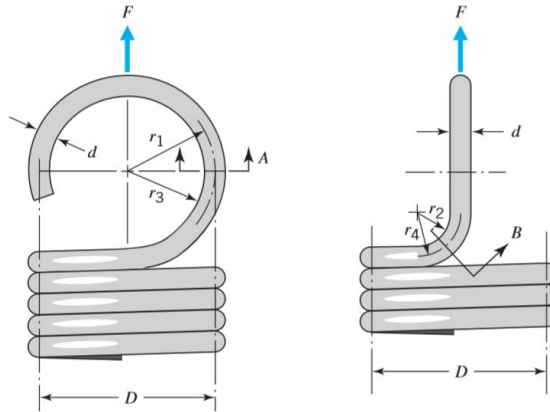


Figure 44 Relevant parameters of spring end hook geometry [70].

The radius r_1 is chosen to be 3 cm, to match the diameter of the spring. The radius r_2 should be around twice the wire diameter, therefore a value of 1 cm was chosen. When a force is applied to the hook end, axial and bending forces occur at point A in Figure 44, and torsional stress occurs at point B (shown in the same figure). For this reason, three different fatigue safety factors are now necessary. The first fatigue safety factor involves the bending stress that occurs at point A in the hook. The equations used to calculate this bending stress are:

$$C_1 = \frac{2r_1}{d}$$

$$K_A = \frac{4C_1^2 - C_1 - 1}{4C_1(C_1 - 1)}$$

$$\sigma_B = \frac{FK_A * 16 * D}{\pi * d^3}$$

Using the bending stress equation with a minimum applied force of 0 N and a maximum force of 56.92 N, the minimum and maximum cyclic bending stresses are:

$$\sigma_{min} = 0$$

$$\sigma_{max} = 168.0 \text{ MPa}$$

The amplitude and mean stresses are:

$$\sigma_a = \frac{\sigma_{max} + \sigma_{min}}{2} = 84.0 \text{ MPa}$$

$$\sigma_m = \frac{\sigma_{max} - \sigma_{min}}{2} = 84.0 \text{ MPa}$$

Fatigue strength for cyclic bending stress must be determined to use the Modified Goodman Criterion. The fatigue strength is calculated using the following equation:

$$S_n = S'_n C_L C_G C_S C_T C_R$$

Factors shared across all calculations are the temperature factor C_T which is 1.0, the surface factor C_L is 0.75, and the reliability factor C_R for 99% reliability is 0.814. S'_n , calculated as 0.5 * UTS. For bending, using Table 8.1 from [70], the load factor C_L is 1.0, the gradient factor C_G is 1.0. The fatigue strength is therefore:

$$S_n = 0.5 * 758 \text{ MPa} * 1 * 1 * 0.75 * 1 * 0.814$$

$$S_n = 231.5 \text{ MPa}$$

Using the Modified Goodman Criterion, the safety factor is determined:

$$\frac{\sigma_a}{S_n} + \frac{\sigma_m}{S_u} = \frac{1}{n}$$

$$n = 2.111$$

The same methodology is used to determine fatigue safety factor due to the axial force acting at point A of Figure 44. The equation used to calculate axial stress is:

$$\sigma_A = \frac{4F}{\pi * d^2}$$

Minimum and maximum stresses of axial loading are:

$$\sigma_{min} = 0$$

$$\sigma_{max} = 2.59 \text{ MPa}$$

The amplitude and mean stresses of axial loading are:

$$\sigma_a = \frac{\sigma_{max} + \sigma_{min}}{2} = 1.30 \text{ MPa}$$

$$\sigma_m = \frac{\sigma_{max} - \sigma_{min}}{2} = 1.30 \text{ MPa}$$

Similar to bending fatigue, the fatigue strength must also be calculated for axial loading. For axial loading, using Table 8.1 from [70], the load factor C_L is 1.0, the gradient factor C_G is 0.7. The fatigue strength is therefore:

$$\begin{aligned} S_n &= S'_n C_L C_G C_S C_T C_R \\ S_n &= 0.5 * 758 \text{ MPa} * 1 * 0.7 * 0.75 * 1 * 0.814 \\ S_n &= 162.1 \text{ MPa} \end{aligned}$$

Using the Modified Goodman Criterion, the safety factor is determined to be 102.

The last fatigue safety factor that must be considered is fatigue due to torsion at point B of Figure 44. The torsional stress at point B can be determined using the following equations:

$$\begin{aligned} \tau_B &= \frac{K_B * 8FD}{\pi d^3} \\ K_B &= \frac{4C_2 - 1}{4C_2 - 4} \\ C_2 &= \frac{2r_2}{d} \end{aligned}$$

Minimum and maximum stresses of torsional loading are:

$$\begin{aligned} \tau_{min} &= 0 \\ \tau_{max} &= 99.7 \text{ MPa} \end{aligned}$$

The amplitude and mean stresses of torsional loading are:

$$\begin{aligned} \tau_a &= \frac{\tau_{max} + \tau_{min}}{2} = 49.8 \text{ MPa} \\ \tau_m &= \frac{\tau_{max} - \tau_{min}}{2} = 49.8 \text{ MPa} \end{aligned}$$

The fatigue strength for torsional cyclic loading is calculated using the same methodology as bending and axial cyclic loading. For axial loading, using Table 8.1 from [70], the load factor C_L is 0.58, the gradient factor C_G is 1.0. The fatigue strength is therefore:

$$\begin{aligned} S_n &= S'_n C_L C_G C_S C_T C_R \\ S_n &= 0.5 * 758 \text{ MPa} * 0.58 * 1.0 * 0.75 * 1 * 0.814 \\ S_n &= 134.3 \text{ MPa} \end{aligned}$$

Using the Modified Goodman Criterion, the safety factor is determined to be 2.54. The lowest safety factor of the main energy spring is 2.2895, which is higher than the required minimum safety factor of 2.

9.2.2. Pawlever Spring

The pawlever spring is used to make the pawlever a spring switch in order to have it act as a binary system: either it is engaged with the ratchet gear or it is not, there is no in-between. The pawlever spring analysis is identical to the main energy spring analysis.

Assuming spring outer diameter of 5 mm, hook r_1 and r_2 of 2.5 mm and 1 mm, a solid length of 50 mm, and a spring constant of 50 N/m, the same methodology used in section 9.2.1 is used to determine paw spring characteristics and safety factors. Wire diameter is calculated to be 0.44 mm, the spring has 57 active coils, the spring has a solid length of 2.5 cm excluding hook ends, the coil fatigue safety factor is 13.5, the hook bending fatigue safety factor is 2.17, the axial fatigue safety factor is 80.0, and the hook transverse shear fatigue safety factor is 2.47.

9.3. Shaft Analysis

9.3.1. Main Shaft

This section shows detailed analysis calculations for the main shaft only since all shafts were analyzed with the same methodology. Subsequent sections for other shafts will show the highlights of the analysis. Figure 45 shows the FBD of the main shaft on which the main bar, main timing gear, main thigh belt gear, spring belt gear, and main ratchet gear are mounted.

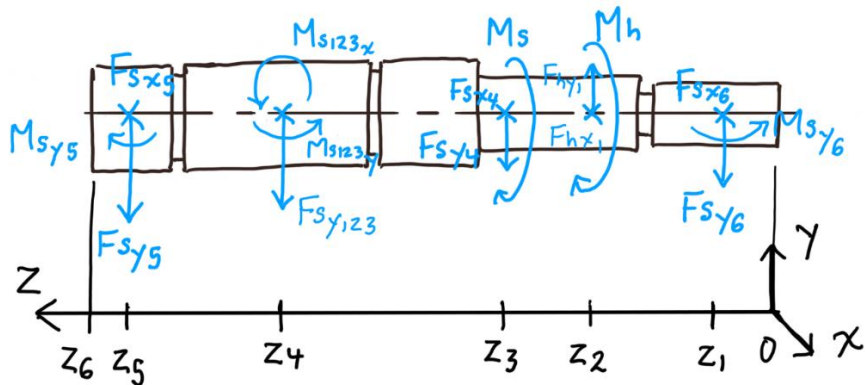


Figure 45 Free-body diagram of the main shaft (frontal plane view).

Table 6 defines each of the loads (knowns and unknowns) acting on the main shaft from right to left and their locations along the main shaft; z_6 represents the total shaft length which is driven by the thicknesses of the gears mounted on the shaft. Loads acting on the gears have been determined before solving for shaft loads. It is assumed that no thrust forces are acting on the bearings.

Table 6 Definitions of main shaft loads (knowns and unknowns) and their locations.

Loads	Descriptions	Locations [m]	Known?
Fsx6, Fsy6, Msy6	Medial bearing x and y reaction forces, and y reaction moment	$z_1 = 0.0125$	No
Fhx1, Fhy1, Mh	Thigh bar x and y reactions forces and reaction moment	$z_2 = 0.0250$	Yes
Fsx4, Fsy4, Ms	Main timing gear x and y reaction forces and reaction moment	$z_3 = 0.0375$	Yes
Fsx123, Fsy123, Ms123x, Ms123y	Resultant reaction loads of the main thigh belt gear, spring belt gear, and main ratchet gear	$z_4 = 0.0735$	Yes
Fsx5, Fsy5, Msy5	Lateral bearing x and y reaction forces and y reaction moment	$z_5 = 0.0970$	No

Gait involves partial cyclical rotations of the hip joint and therefore, for shafts, a fatigue stress analysis was carried out. If bending moments and torques are both present, axial and transverse shear forces are almost always negligible, and thus, will be set to zero for this fatigue stress analysis [70].

First, the bending moment as a function of z was determined as the relationship between bending moment (M) along the shaft and shear (V) along the shaft.

$$\frac{dM}{dz} = V$$

Integrating the above equation and taking each load to be concentrated at a single point, one obtains the following,

$$M(z) = \sum_i F_{i-1}(z_i - z_{i-1}) + F_i(z - z_i) + \sum_i M_i$$

where $M(z)$ is the bending moment about x ($M_x(z)$) or y ($M_y(z)$) and F_i is any concentrated load at point z_i , and M_i is a bending moment acting at point i. Using this equation, piecewise functions for $M_x(z)$ and $M_y(z)$ have been determined for the six intervals (Figure 45) between 0 and z_6 . As an example, $M_x(z)$ for the main shaft is shown below,

$$\begin{aligned}
 0 \leq z < z_1: M_x(z) &= 0 \\
 z_1 \leq z < z_2: M_x(z) &= -F_{sy6}(z - z_1) \\
 z_2 \leq z < z_3: M_x(z) &= -F_{sy6}(z_2 - z_1) + F_{hy1}(z - z_2) \\
 &\dots \\
 z_5 \leq z < z_6: M_x(z) &= -F_{sy6}(z_2 - z_1) + F_{hy1}(z_3 - z_2) - F_{sy4}(z_4 - z_3) - F_{sy123}(z_5 - z_4) - F_{sy5}(z - z_5) \\
 &+ M_{s123x}
 \end{aligned}$$

The piecewise variation of torque along a shaft is expressed below,

$$T(z) = \sum_i T_i, z_i \leq z < z_{i+1}$$

where T_i is a torque applied at point z_i . The equation below shows how it is applied to find torque as a function of z .

$$T(z) = \begin{cases} 0 & 0 \leq z < z_2 \\ -M_h & z_2 \leq z < z_3 \\ -M_h - M_s & z_3 \leq z \leq z_6 \end{cases}$$

A MATLAB script was written to produce piecewise functions for bending moment and torsion based on each shaft's inputted dimensions. Figure 46 shows the bending moment and torsion diagrams for frame 3 out of 100 in the calculation which corresponds to the maximum hip assist torque; these diagrams were constructed using the piecewise equations for bending moment and torsion along the shaft.

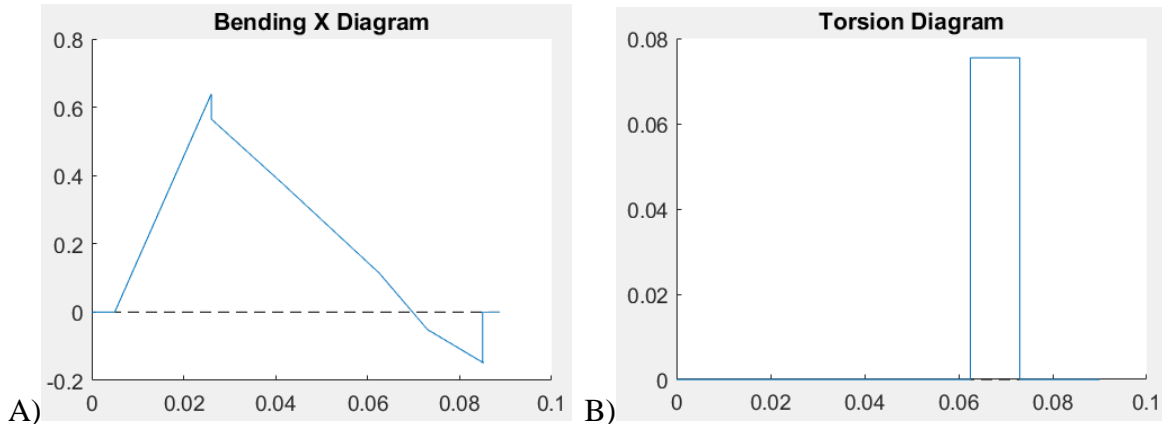


Figure 46 Main shaft bending moment (N-m) (A) and torsion (N-m) (B) diagrams as a function of length along the shaft from the left edge at the gait cycle frame corresponding to the maximum hip assist torque.

During the gait cycle, the hip oscillates, causing cyclic loads around a mean magnitude with a certain amplitude. As demonstrated in Figure 47, points of interest include points of loading along the shaft due to parts mounted on the shaft, and points of stress concentration (circlip gaps and steps). For all points of interest, a set of mean and amplitude loads (bending moment and torque) were calculated. Bending and torsional safety factor were calculated for each point.

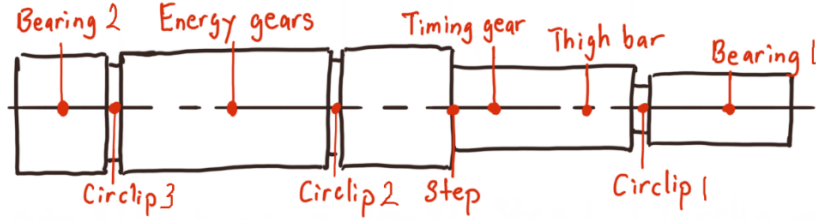


Figure 47 Points of interest for fatigue stress analysis of the main shaft.

Modified Goodman Criterion was used in calculating the safety factors as follows:

$$\frac{\sigma_{ea}}{S_n} + \frac{\sigma_{em}}{S_u} = \frac{1}{n}$$

where σ_{ea} and σ_{em} are the effective alternating (amplitude) stress and effective mean stress respectively, S_n and S_u are the fatigue and ultimate strength of the material respectively, and n is either the bending or torsional safety factor. Constants for stress concentration come from Juvinall et al, and Budynas and Nisbett [70], [73].

For all shafts, Aluminum 2024-T4 with an ultimate strength of $S_u = 448$ MPa was selected. S_n was calculated below, accounting for stress concentrators acting on each shaft,

$$S_n = S'_n C_L C_G C_S C_T C_R$$

where $S'_n = 0.5S_u = 224$ MPa and the C_L , C_G , C_S , C_T , C_R are constants for different modes of stress concentration. These constants are as follows $C_L = 1$ (bending), $C_L = 0.58$ (torsion), $C_G = 1$ (nominal shaft diameter (d) of less than 10 mm), $C_G = 0.9$ (10 mm $< d <$ 50 mm), $C_S = 0.795$ (Al 2024-T4, machined surface), $C_T = 1$ (temperature less always than 840 °F) and $C_R = 0.814$ (99% reliability). S_n is calculated as follows for bending and torsion:

$$S_{n \text{ bending}} = 224 (1)(1)(0.9)(0.795)(1)(0.814) = 130.5 \text{ MPa}$$

$$S_{n \text{ torsion}} = 224 (0.58)(1)(0.9)(0.795)(1)(0.814) = 76.67 \text{ MPa}$$

Stress concentrations associated to changes in geometry (K_f and K_{fs}) (e.g. a circlip gap or a step) can be found for bending with

$$K_f = 1 + (K_t - 1)q$$

and for torsion with,

$$K_{fs} = 1 + (K_{ts} - 1)q_s$$

where K_t and K_{ts} are bending and torsion stress concentration factors corrected with notch sensitivity factors for bending (q) and torsion (q_s) respectively. For all stress concentration regions on all shafts, all K_t and K_{ts} values were selected to conservative. All circlip gaps have $K_t = 2.2$ and

$K_{ts} = 1.65$ and all steps have $K_t = 2.05$ and $K_{ts} = 1.55$. These values were taken assuming the ratio of the notch radius to the shaft nominal diameter to be 0.05. For all circlip gaps, the ratio of the larger shaft diameter to the smaller shaft diameter was set to 1.1. For all steps, this ratio was set to be 1.5 for bending and 1.2 for torsion.

For all stress concentration points, taking the notch radius to be 0.5 mm, $q = 0.425$ and $q_s = 0.575$. For example, at a circlip gap, K_f and K_{fs} are calculated as follows:

$$K_f = 1 + (2.2 - 1)(0.425) = 1.51$$

$$K_{fs} = 1 + (1.65 - 1)(0.575) = 1.37$$

Stresses σ_{ea} and σ_{em} come from the Von Mises stress and maximum principal stress theories respectively; the simplified expressions for these stresses are shown for solid shafts:

$$\sigma_{ea} = \frac{16}{\pi d^3} \sqrt{4(K_f M_a)^2 + 3(K_{fs} T_a)^2}$$

$$\sigma_{em} = \frac{16}{\pi d^3} (K_f M_m + \sqrt{(K_f M_m)^2 + (K_{fs} T_m)^2})$$

These stress equations were substituted in the Modified Goodman Criterion and isolated for the shaft diameter at the point of interest that achieves the given safety factor.

$$d = \sqrt[3]{\frac{16n}{\pi} \left(\frac{A}{S_n} + \frac{B}{S_u} \right)}$$

$$A = \sqrt{4(K_f M_a)^2 + 3(K_{fs} T_a)^2}$$

$$B = K_f M_m + \sqrt{(K_f M_m)^2 + (K_{fs} T_m)^2}$$

For each point of interest, a diameter corresponding to the bending moment safety factor and a diameter corresponding to the torsional safety factor was calculated. The larger of these two diameters was taken as the governing diameter. For a male user who weighs 60 kg and is 160 cm tall, Figure 56 shows the required shaft diameters at the points of interest to achieve a safety factor of 2.5.

Table 7 Main shaft diameters at different points of interest.

Point of interest	Diameter (mm)
Bearing 1	0.959
Bearing 2	3.197
Circlip 1	3.374
Circlip 2	4.272
Circlip 3	3.474

Step	2.779
Energy gears	2.655
Timing gear	2.655
Thigh bar	2.781

The maximum diameter of the points of interest to the right of the step was chosen as the uniform diameter (d_1) of the main shaft to the right of the step; d_1 was found to be 3.374 mm. The same was done to the left of the step (d_2), except d_2 was set to 7.374 mm to account for geometric constraints (i.e. the bore diameter of the energy subsystem gears).

9.3.2. Cam Follower Central Pin Arm Shaft

Figure 48 shows the render of the cam follower. The central shaft for the pin arm has been analyzed in fatigue using similar analysis. It was determined to have a diameter of 8.72 mm for a requested safety factor of 2.5.

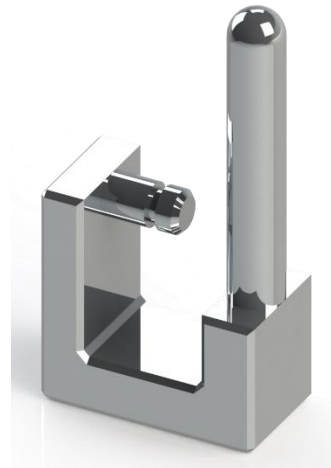


Figure 48 The cam follower component. The central pin arm shaft shown in the left of the component, the cam follower shaft shown on the right of component pointing upwards.

9.3.3. Case Hinge Shaft

The case hinge shaft is the shaft that allows the case to rotate in the frontal plane relative to waist subsystem. Its diameter was similarly determined to be 16.76 mm.

9.3.4. Timing Pin and Pawl Lever

When the ratchet gear is engaged to the paw and the timing pin makes contact with the paw lever, the paw component of the lever starts to disengage from the ratchet. The safety factor for the pin can be computed assuming that only ratchet friction force and lever spring force are resisting the motion of the pin. Impact loading is an important consideration since pin disk rotates and produces a pin impact against the lever at specific angles. Impact loading depends on both the velocity and acceleration of the pin toward the lever, as well as the static counter force of the lever against the pin [70].

Idealized impact analysis represents one impacting structure as a free-falling mass which collides with the second impacting structure represented by a spring. Impact analysis makes several assumptions:

- Mass of structure being impacted is negligible. Dynamic deflection due to impact is represented as static deflection multiplied by some impact factor, ignoring a higher local strain due to impact.
- Deflections in one of the impacting masses are ignored, resulting in elevated deflections in the analyzed mass.
- Damping (via internal friction) is neglected, resulting in stresses and deflections higher than they would actually be.

The derived expression for impact force is as follows:

$$F_{impact} = F * \left(1 + \sqrt{1 + \frac{v^2}{a * \delta_{st}}} \right)$$

where F_{impact} is the impact force resulting from the static force F , given impact speed v , impact acceleration a , and static deflection δ_{st} resulting from force F . The term in brackets is the impact factor. Static deflection is represented as follows:

$$\delta_{st} = \frac{F}{k} = \frac{F}{\frac{3EI}{L^3}}$$

where F is the static force, and k is the spring constant of the mass being impacted. In this case, timing pin spring constant is represented by a cantilever beam with elastic modulus E , moment of area I and length L .

An important consideration is that the impact does not result in an immobile system, therefore the impact speed must be relative between the pin and the lever. It is assumed that impact

results in a perfectly plastic collision where both pin and lever move together until disengagement. Collision equation to approximate the impact speed is constructed:

$$\Delta v = \left(1 - \frac{m_{pd}}{m_{pd} + m_l}\right) * v_i$$

where Δv is the change in speed during impact, v_i is initial speed, and m_{pd} and m_l are masses of colliding objects.

The solution must first obtain a static force in the timing system, then adjust the static force by an impact factor to produce the impact force. An important consideration is the computation time. Proper computation requires an iterative solution that solves the static system and then substitutes the impact force and recomputes the system. Such an iterative system would take too long to compute for each frame of all of the datasets being tested, therefore a pseudo-impact simulation is done where dual iteration is only performed on the timing pin, lever and immediate disk system, and the forces are not propagated to the rest of the device. Simulation results indicate that, at initial impact, the forces can be up to 19 times higher than static forces, necessitating thicker components to ensure a safe design.

The initial impact in the worst-case scenario of end swing stair gait will therefore produce an equivalent transient force of 161.5N (8.5N contact force x 19) at the impact point.

The assumption of ignoring the higher local strain due to impact can be mitigated by applying Hertz stress calculations [70]. For contact between a flat plate and a cylindrical face can be approximated as contact between two cylinders where one has an infinite radius. Contact modulus is first defined between two materials (AISI 1045 steel and Al 2024-T4):

$$\Delta = \frac{1 - v_1^2}{E_1} + \frac{1 - v_2^2}{E_2} = \frac{1 - 0.3^2}{200GPa} + \frac{1 - 0.32^2}{72GPa} = 1.702 * 10^{-11} Pa^{-1}$$

where, v_1 and v_2 are Poisson ratios, and E_1 and E_2 are the elastic moduli of the material obtained from [70] and [74]. AISI 1045 steel yield strength is 310Mpa, Al-2024-T4 yield strength is 280Mpa.

As such the maximum impact stress is:

$$P = 0.564 \sqrt{\frac{F * (\frac{1}{R_1} + \frac{1}{R_2})}{L\Delta}} = 0.564 \sqrt{\frac{161.5 * (\frac{1}{0.01} + \frac{1}{\infty})}{0.02 * 1.702 * 10^{-11}}} = 122.8 MPa$$

The stresses apply to both the pawl lever and the timing pin at the contact location. The safety factor for AISI 1045 steel is 2.52, and for Al-2024-T4 is 2.28. These are considered acceptable in the context of our device. Additional impact consideration for the ratchet pawl is discussed in the finite element analysis section of this report.

9.4. Gear Analysis

There are five gears in our system; one ratchet gear, two belt gears and two timing gears. The assumptions and values for standard and material constants can be found in Appendix I. The ratchet component is the gear that receives the most stress mainly due to the fact that there is always only one tooth that is being engaged at all times. Both belt gears, that is the spring belt gear and thigh belt gear, receive a similar loading force and are therefore treated similarly when it comes to gear variables. Both timing gears receive identical loading and are also treated as being identical when it comes to minimum width calculation.

Note that the source of all the values for Table 8 through Table 12 are taken directly from the code output in MATLAB.

9.4.1. Ratchet Gear

A full comprehensive sample calculation for finding the minimum width is done for the ratchet gear. The equations used to find the width of the ratchet gear would be the same for all the other gears, with the only difference being the input variables. Table 8 outlines the necessary variables specific to the ratchet gear.

Table 8 Gear specific variables to calculate the safety factor.

Symbol	Name	Ratchet Gear	Units
-	Material Type	Steel	-
w	Gear Rotation Speed	0.00813	rad/s
Ft	Force on Teeth	22.7	N
N	Number of Teeth	50	-

N_r	Number of Teeth Engaged	1	
r	Gear Radius	0.05	m
b	Gear Width	0.0134	m
n_s	Surface SF	2.5	-
n_b	Bending SF	2.5	-

To calculate the minimum required width for surface stress safety, the surface fatigue strength must first be found by using the equation in Table 15.5. Surface fatigue strength is defined as the maximum stress the surface element of the gear can withstand without suffering from fatigue failure [70]. Note that the equation outputs ksi units, so a correctional modifier of 6.895 to convert ksi to MPa has been added.

$$S_{fe} = (0.4(Bhn) - 10)6.895$$

$$S_{fe} = (0.4(280) - 10)6.895 = 703.29MPa$$

Next, the surface endurance strength is determined:

$$S_H = S_{fe} C_{Li} C_R$$

$$S_H = (703.29)(1)(1) = 703.29MPa$$

The surface endurance strength is defined as the stress limit the surface element before suffering from fatigue failure. Unlike fatigue strength, this equation modifies the surface fatigue to account for the life cycle and reliability factor of the gear. In order to calculate the surface fatigue stress, the velocity factor has to be calculated. Before finding that however, the pitch line velocity, defined as the linear velocity of the gear teeth, must be determined [70]:

$$V = \frac{\pi d_p n_p}{12}$$

Where the pitch diameter, defined as the diameter of the pitch circle, is [75]:

$$d_p = \frac{N}{P}$$

With N representing the number of teeth and P the pitch of the gear. The pitch is:

$$P = \frac{2\pi r}{N}$$

The gear RPM conversion is:

$$n_p = \frac{30w}{\pi}$$

Note that, unless the gear is a ratchet, the force value must be divided by the number of teeth they are applied onto before using the above equations. Combining equation x, y and z into following:

$$V = \frac{5N^2w}{4\pi r}$$

With the pitch line velocity equation determined, the velocity factor, defined as the severity of impact as successive pairs of teeth engage, can be estimated with the slope formulae for curve D in figure 15.24 [70]:

$$K_v = \left(\frac{1}{960\pi} \right) \left(\frac{N^2 w}{r} \right) + 1$$

$$K_v = \left(\frac{1}{960\pi} \right) \left(\frac{(30^2)0.00813}{0.05} \right) + 1 = 1.0485$$

All variables in this equation are gear dependent, so the velocity factor can vary substantially from gear to gear. The modified geometry factor, defined as a simplification based on the real geometry factor and the elastic coefficient, is [70]:

$$I = \left(\frac{\sin \theta \cos \theta}{2} \right) \left(\frac{R}{R+1} \right)$$

$$I = \left(\frac{\sin 20^\circ \cos 20^\circ}{2} \right) \left(\frac{0.05}{0.05+1} \right) = 0.3726$$

Note that it is assumed the ratio R is 1/r for all gears. The surface stress safety factor is:

$$n_s = \frac{S_H}{\sigma_H} = \frac{703.29}{325.21} = 2.16$$

$$\sigma_H = \frac{S_H}{n_s} = \frac{703.29}{2.5} = 281.3 \text{ MPa}$$

The minimum width of the gear is:

$$\sigma_H = C_P \sqrt{\frac{F_t}{bd_p I} K_V K_o K_m}$$

$$b = \left(\frac{C_P}{\sigma_H}\right)^2 \left(\frac{F_t}{d_p I} K_V K_o K_m\right)$$

$$b = \left(\frac{191}{281.3}\right)^2 \left(\frac{(22.7)(1.0485)(1)(1.3)(2)(0.05)\pi}{(0.3726)(30^2)}\right) = 0.0134m$$

The bending stress safety factor requires less involved computation as it borrows a few equations from the surface stress safety factor section. First, the standard endurance limit, derived from the R. R. Moore fatigue test, must be determined:

$$S'_n = \left(\frac{Bhn}{4}\right)(6.895) = \frac{(280)(6.895)}{4} = 482.65MPa$$

Next, the bending endurance strength, defined as the maximum stress the bending element of the gear can withstand without suffering from fatigue failure is [70]:

$$S_n = S'_n C_L C_G C_S C_r K_t K_{ms}$$

$$S_n = (482.65)(1)(1)(0.7)(1)(1)(1.4) = 439.21MPa$$

The bending stress safety factor is:

$$n_b = \frac{S_n}{\sigma}$$

$$\sigma = \frac{S_n}{n_b} = \frac{439.21}{2.5} = 175.7$$

The minimum width of the gear is:

$$\sigma = \frac{F_t P}{bJ} K_V K_o K_m$$

$$b = \frac{F_t P}{\sigma J} K_V K_o K_m$$

$$b = \frac{(22.7)(1.0485)(1)(1.3)(2)(0.05)\pi}{(175.7)(0.4)(30)} = 0.0046m$$

Since the width found through the surface safety factor is larger than the one found through the bending safety factor, the final minimum width of the ratchet gear would be 13.4mm. This process is fully automated by a function in the code, taking in the relevant variables and outputting a certain minimum width.

9.4.2. Spring Belt Gear

The spring belt gear, mounted in between the ratchet and thigh belt gear on the same shaft, connects to the spring component via a belt gear. Therefore, an estimate of 1/3 of the teeth will be engaged with the belt gear at all times. Table 9 outlines the necessary variables specific to the spring belt gear.

Table 9 Gear specific variables to calculate the width.

Symbol	Name	Ratchet Gear	Units
-	Material Type	Aluminum	-
w	Gear Rotation Speed	0.00813	rad/s
Ft	Force on Teeth	48.3	N
N	Number of Teeth	28	-
N _r	Number of Teeth Engaged	10	-
r	Gear Radius	0.04	m
b	Gear Width	0.0059	m
n _s	Surface SF	2.5	-
n _b	Bending SF	2.5	-

9.4.3. Thigh Belt Gear

The thigh belt gear, mounted adjacent to the spring belt gear on the same shaft, connects to the thigh component via a belt gear. Therefore, an estimate of 1/3 of the teeth will be engaged

with the belt gear at all times. Table 10 outlines the necessary variables specific to the spring belt gear.

Table 10 Gear specific variables to calculate the width.

Symbol	Name	Ratchet Gear	Units
-	Material Type	Aluminum	-
w	Gear Rotation Speed	0.00813	rad/s
Ft	Force on Teeth	33.9	N
N	Number of Teeth	20	-
N _r	Number of Teeth Engaged	7	-
r	Gear Radius	0.05	m
b	Gear Width	0.014	m
n _s	Surface SF	2.5	-
n _b	Bending SF	2.5	-

9.4.4. Main Timing Belt Gear

The main timing belt gear, mounted adjacent to the thigh belt gear on the same shaft, connects to the cam timing belt gear component via a belt gear. Therefore, an estimate of 1/2 of the teeth will be engaged with the belt gear at all times. Table 11 outlines the necessary variables specific to the spring belt gear.

Table 11 Gear specific variables to calculate the width.

Symbol	Name	Ratchet Gear	Units
-	Material Type	Plastic	-
w	Gear Rotation Speed	0.00813	rad/s

Ft	Force on Teeth	2.66	N
N	Number of Teeth	53	-
N _r	Number of Teeth Engaged	27	-
r	Gear Radius	0.33	m
b	Gear Width	0.0014	m
n _s	Surface SF	2.5	-
n _b	Bending SF	2.5	-

9.4.5. Cam Timing Belt Gear

The cam timing belt gear, mounted adjacent to the timing discs on the same shaft, connects to the main timing belt gear component via a belt gear. Therefore, an estimate of 1/2 of the teeth will be engaged with the belt gear at all times. Table 12 outlines the necessary variables specific to the spring belt gear.

Table 12 Gear specific variables to calculate the width.

Symbol	Name	Ratchet Gear	Units
-	Material Type	Plastic	-
w	Gear Rotation Speed	0.00813	rad/s
Ft	Force on Teeth	2.66	N
N	Number of Teeth	40	-
N _r	Number of Teeth Engaged	20	-
r	Gear Radius	0.25	m
b	Gear Width	0.0017	m
n _s	Surface SF	2.5	-

n _b	Bending SF	2.5	-
----------------	------------	-----	---

9.5. Buckling and Non-Circular Section Beam Analysis

Several critical components of the design undergo axial compression loading and are at possible risk of buckling failure. This section will provide a sample calculation of buckling analysis and prevention and will then discuss the dimensioning of components.

9.5.1. Cam Follower Shaft

The cam follower shaft is the timing subsystem component that follows the internal cam of the cam disk in order to adjust the position of the timing pins for a specified gait mode. This shaft undergoes axial compression due to the cam spring and also resists forces from the timing pins. Due to the complexity of modelling the transmission of impact loading from the timing pins, a static loading force of ~2 N generated by a MATLAB simulation will be used instead.

The goal of this analysis is to determine the minimum allowable shaft diameter to avoid buckling failure of the cam follower shaft, shown in Figure 48. Using an aluminum elastic modulus of 68.9 GPa, a system of equations can be created using the equations for moment of inertia and for maximum allowable force before buckling.

For a cylindrical shaft, the moment of inertia I can be calculated using the following equation:

$$I = \frac{\pi * \left(\frac{d}{2}\right)^4}{4}$$

where d is the diameter of the shaft.

The equation for maximum axial compression load before buckling is:

$$F = \frac{\pi^2 * E * I}{L_e^2}$$

where E is the elastic modulus of the component material, I is the moment of inertia of the component along the weakest axis of the component, and L_e is the effective length of the component along the axis of axial loading.

Using Figure 5.27 from [70], the end conditions of the cam shaft are most similar to the cantilever beam in which one end is fixed and the other end is free to move. The effective length

of the shaft is therefore double its physical length. The length of the shaft is set to 3.95 cm, therefore the effective length is then 7.9 cm. Using MATLAB to solve these equations for diameter d outputs a minimum allowable shaft diameter of 0.78 mm. The cam shaft will experience some impact loading transmitted from the timing pins therefore a large safety factor should be implemented. It is also difficult to implement a 0.78 mm shaft onto a ~1 cm wide cam follower component, therefore the shaft diameter should be increased to a reasonable, manufacturable number. For this reason, a minimum cam follower shaft diameter of 5 mm is used.

9.5.2. Pin Arms

The pin arms that connect the timing pins to the central shaft of the cam follower also experience axial compression loads and should be analyzed for buckling due to their relatively small size. The same equation for maximum force before buckling is used again, however a different moment of inertia equation needs to be used for a rectangular prism:

$$I = \frac{w * h^3}{12}$$

where w is the width of the component and h is the height of the component.

The width of the component is fixed to 1 cm to accommodate the timing pins and central cam follower shaft. The pin arm geometry is complex due to the changing thickness of the beam half way through its length. For the purpose of this analysis, only the thin region will be analyzed as it is more susceptible to buckling than the thick region. Solving the two equation system using MATLAB, a minimum thickness of 0.05 mm is required to avoid buckling. Similar to the cam follower shaft, this component is expected to experience impact loading, therefore it should have a built-in safety factor. For this reason, a minimum thickness of 2 mm is set for the pin arm, with the thicker region being defined as double the thickness of the thin region.

9.5.3. Thigh bar

Thigh bar stresses are determined from beam analysis as previously discussed for shafts. The first step transforms the XY coordinate forces to the forces aligned and perpendicular to the bar as shown in Figure 49.

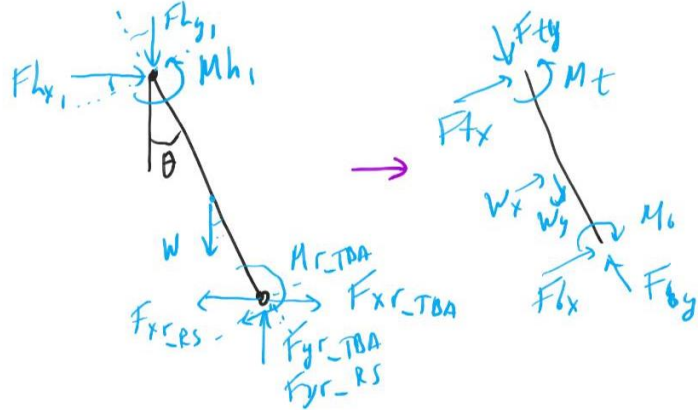


Figure 49 Thigh bar force transformation for stress analysis as a beam.

First transform top forces and moments are transformed:

$$F_{ty} = F_{hy1} \cos\theta - F_{hx1} \sin\theta$$

$$F_{tx} = -F_{hy1} \sin\theta + F_{hx1} \cos\theta$$

$$M_t = M_{h1}$$

Then bottom forces and moments are transformed:

$$F_{yr} = F_{yr_tba} + F_{yr_rs}$$

$$F_{xr} = F_{xr_tba} - F_{xr_rs}$$

$$F_{by} = F_{yr} \cos\theta - F_{hxrs} \sin\theta$$

$$F_{bx} = F_{yr} \sin\theta + F_{xr} \cos\theta$$

$$W_x = -W \sin\theta$$

$$W_y = W \cos\theta$$

$$M_b = M_{r_tba}$$

Axial forces acting on the beam are F_{ty} , F_{by} and W_y , while perpendicular forces are F_{tx} , F_{bx} and W_x . Moments M_t and M_b are also applied at both ends.

Section properties are computed as well to ensure axial, bending, torsional and buckling stresses can be computed. Deflection and angle of twist analysis also requires these properties. The I-beam section is used for the thigh bar to reduce its overall mass while maintaining acceptable bending properties as shown in Figure 50.

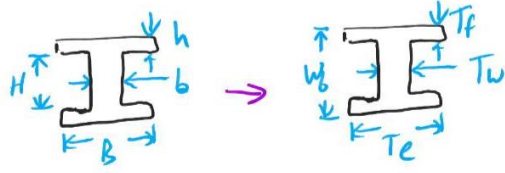


Figure 50 I-beam section from mechanics definitions [70] (left), and thigh bar parametrization definition in our project (right).

I-beam definition of the bar has been transformed to the parametrization used in our models. The section area can then be found as follows:

$$A = 2T_f T_e + (W_b - 2T_f)T_w$$

Moments of area are then transformed from I-beam derivation to parametrization definition as follows:

$$\begin{aligned} I_{xx} &= \frac{H^3 b}{12} + 2 \left(\frac{h^3 B}{12} + \frac{hB(H+h)^2}{4} \right) = \frac{(W_b - 2T_f)^3}{12} + \frac{T_f^3 T_e}{6} + \frac{T_f T_e (W_b - T_f)^3}{2} \\ I_{yy} &= \frac{b^3 H}{12} + 2 \left(\frac{B^3 h}{12} \right) = \frac{T_w^3 (W_b - 2T_f)}{12} + \frac{T_e^3 T_f}{6} \end{aligned}$$

where the equation quantities are dimensions presented in Figure 50.

Unlike shafts discussed previously, torsion of the I-beam cannot use polar moment of inertia J as a sum of I_{xx} and I_{yy} since the section is not circular. Non-uniform sections incur additional twisting deformation of the member, which is analytically complicated to compute. Instead, the polar moment will assume a rectangular section with a length to width ratio (a/b) of 4.0:

$$J \sim \beta ab^3$$

where β is 0.281 factor dependent on the length to width ratio, a is the long side, b is the short side length.

Lastly, material properties the thigh bar are defined. Light composite materials such as glass or carbon fiber reinforced epoxies (GFRE/CFRE) have shown great promise in producing stiff and light components [76]. While more expensive to produce than conventional light metal components, CFRE can reduce component mass by as much as two times compared to similar

geometry aluminum. LY5/4 CFRE [76] consisting of five 0.135mm layer lamina with 0, -35, 0, +35, 0 fiber orientation layers has high tensile (1059MPa) and flexural (996MPa) strength, high impact modulus (5.5J/m), and high tensile (80GPa) and flexural (48Gpa) stiffness. These properties are possible due to the layer angles as compared to other CFRE varieties discussed in the study. No fatigue assessment was provided, and fatigue analysis assumed 10^6 cycle $S_n \sim 0.5 * S_u$ values from experimental charts of another study [77].

Shaft analysis scripts were substituted with the thigh bar I-beam parameters, axial and radial forces, and solved the same way as a regular beam problem. Fatigue safety factor of 2.5 was used for optimization. Deflection of 1mm and angle of twist of $\sim 1^\circ$ (0.0572rad/m) set a further optimization targets. Buckling analysis was also performed using the same generic analysis script as timing pin arms, substituting the forces, support condition for fixed ends, and section properties for the bar.

The resultant safety factor for the thig bar computation for a 60kg male of 160cm height is 230. The safety factor is very large due to the extra cross-sectional area added in order to ensure bending of the long and slender bar is within the 1mm limit, and twist of the bar is within 1° . The actual safety factor is quite smaller given the geometric simplifications taken in this analysis. Finite element analysis is performed and described in Finite Element Analysis section to validate the result.

9.5.4. Thigh Rigid Support

The thigh rigid support component that contacts the thigh was modeled as a curved cantilever beam. Curved beam analysis assumes homogeneous material properties, elastic behaviour described by Hooke's Law, and small deflections [70].

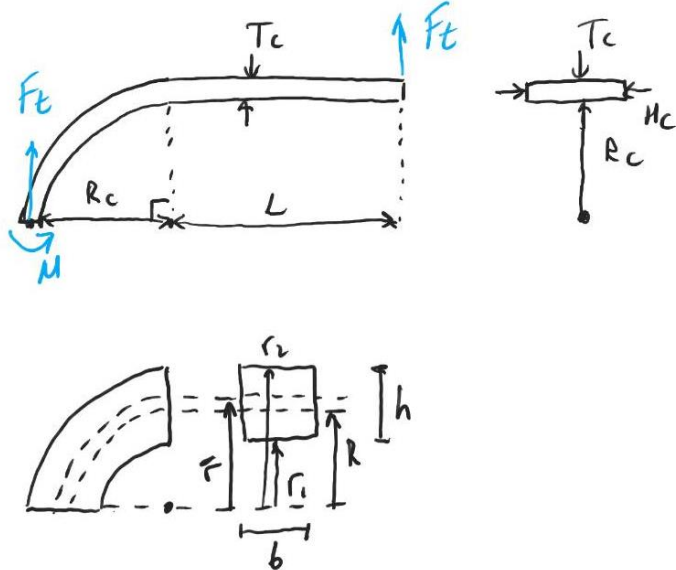


Figure 51 Model representation of the thigh rigid support component and associated dimensions (top), and the curved beam theory parameter definitions (bottom).

Curved beam theory defines pure bending beam stresses as follows:

$$\sigma_b = \frac{M(R - r)}{Ar(\bar{r} - R)}$$

where M is the bending moment applied to the beam, R is the radius of the neutral axis, r is the centroid axis location, A is the section area, and r is the point of interest at which bending stress is assessed [70]. For a rectangular section:

$$R = b * \ln \frac{r_2}{r_1}$$

$$\bar{r} = r_1 + h/2$$

$$A = bh$$

where b is the section width, h is its height, r_1 is the inner radius of curvature, and r_2 is the outer radius of curvature.

The highest stresses in the assembly will be experienced in the curved beam section, at the external surfaces. Combined stresses for the curved beam in the model would also include shear and normal stresses. For example, at the 90° curvature at the top of the beam combined stresses are as follows:

$$\sigma = \sigma_b + \sigma_s = \frac{M(R - r_1)}{Ar(\bar{r} - R)} + \frac{F}{A}$$

Equations are set up for bottom of the beam at 90° , and base of the beam at 0° . Straight beam combined loading equation is also set up for the beam end at the load:

$$\sigma = \sigma_b + \tau_s = \frac{Mc}{I_{xx}} + \frac{F}{A}$$

For the specific beam model shown at the top of Figure 51:

$$\begin{aligned} M &= F_t \left(R_c + \frac{T_c}{2} + L \right) \\ R &= H * \ln \frac{R_c + T_c}{R_c} \\ \bar{r} &= R_c + T_c / 2 \\ A &= H_c T_c \\ r_1 &= R_c \\ r_2 &= R_c + T_c \\ c &= \frac{T_c}{2} \\ I_{xx} &= \frac{H_c T_c^3}{12} \end{aligned}$$

Bending and shear stresses are computed in MATLAB for each frame of the gait cycle for the described points on the beam, and maximum absolute stresses are taken. Amplitude and mean stresses are computed across the gait cycle and combined using von Mises and Mohr criteria [70]:

$$\begin{aligned} \sigma_{ea} &= \sqrt{\sigma_a^2 + 3\tau_a^2} \\ \sigma_{em} &= \frac{\sigma_m}{2} \sqrt{\tau_m^2 + \left(\frac{\sigma_m}{2}\right)^2} \end{aligned}$$

Fatigue analysis for 10^6 cycles similar to the fatigue using Modified Goodman Criterion to compute the safety factor and increment dimensions in the optimization loop:

$$n = \frac{1}{\frac{\sigma_{ea}}{S_n} + \frac{\sigma_{em}}{S_u}}$$

where S_n is the estimated 10^6 cycle fatigue strength of the material, S_u is the ultimate material strength, and n is the fatigue safety factor.

In addition to fatigue safety factor, deflection was computed to further optimize the component. Too much deflection would result in timing problems as transitions between energy storage and release depend on precise definitions of hip flexion and extension angles. Rigid thigh attachment that guarantees small deflection, also guarantees small angle discrepancies in timing disk engagement and disengagement of the ratchet.

Deflection of the complex beam was analyzed using Castigliano's method, which relates strain energy and elastic deflection of the body under any combination of loads [70]. In general, deflection for a straight beam is expressed as follows:

$$\delta = \int M \frac{\partial M}{\partial V} \frac{dx}{EI}$$

where δ is the deflection of the beam, M is the bending moment, V is the force component acting in the y direction, E is the elastic modulus, and I is the section second moment of inertia. Deflection for the straight section of the beam in terms of previously computed properties is therefore:

$$\delta = \int_0^L M \frac{\partial M}{\partial F_t} \frac{dx}{EI} = \frac{F_t L^3}{EI_{xx}}$$

Deflection of the curved section of the beam can be computed by transforming the coordinate system to polar coordinates:

$$\delta = \int M \frac{\partial M}{\partial V} r \frac{d\theta}{EI}$$

$$M = V(r * \sin\theta + L)$$

where θ is the angle along the beam, and extra term L is moment that remains due to the presence of the straight beam at the end of the curved beam, as shown in Figure 52.

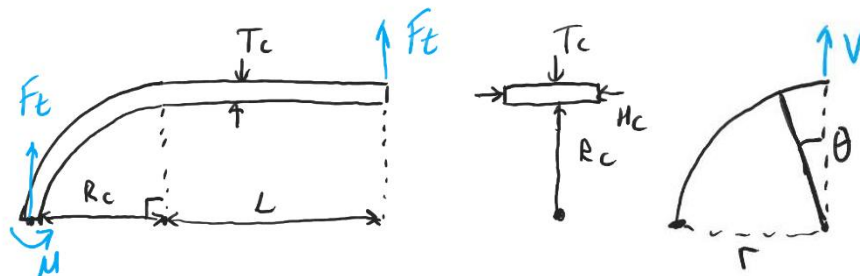


Figure 52 Transformation of coordinates from XY (left) to polar (right) for the curved section to compute beam deflection.

Thus, the deflection expression can be re-written, derived, and substituted for device parameters as follows:

$$\begin{aligned}\delta &= \int M \frac{\partial M}{\partial V} r \frac{d\theta}{EI} = \frac{1}{EI} \int_0^{\frac{\pi}{2}} V(r * \sin\theta + L)^2 r d\theta = \dots = \frac{Vr}{EI} \left(\frac{\pi r^2}{4} + 2rL + \frac{L^2\pi}{2} \right) \\ &= \frac{V * (R_c + T_c/2)}{EI_{xx}} \left(\frac{\pi(R_c + T_c/2)^2}{4} + 2(R_c + T_c/2)L + \frac{L^2\pi}{2} \right)\end{aligned}$$

The deflection optimization algorithm in MATLAB increments beam thickness T_c by two layers of LY5/4 CFRE material thickness (1.35mm), and recomputes deflection until maximum deflection is 2mm. LY5/4 CFRE material has been chosen, similar to the thigh bar, due to light weight and high strength of this large component.

The resultant safety factor for the thigh rigid support component computation for a 60kg male of 160cm height is 13.1. The safety factor is larger than requested optimization value of 2.5 due to the extra thickness added in order to ensure bending is within the 2mm limit. The safety factor is 1.7 times lower than the one computed in the Finite Element Analysis section. This is explained by fatigue loading analysis implemented here which is due to lower fatigue component strength.

The length of the thigh contact section (H_c) is maintained at 5cm producing absolute worst-case pressure of 16kPa for the maximum assist force of 56N for the heaviest person of 100kg during stair gait. This value is higher than the pressure required to collapse tissue capillaries at 4.3kPa, but lower than pressure that results in immediate tissue damage (32kPa) [78]. For an average person of 60kg and 160cm, the pressure expected during routine stair use from assist force of 5.6N is 1.2kPa which is below the capillary collapse pressure with a safety factor of 3.58.

9.5.5. Thigh Belt Attachment Component

Thigh belt attachment is analyzed in MATLAB with the simplification of geometry as a short rectangular beam. Analysis is done similarly to the thigh bar, except the section properties are simpler. Forces shown on the belt attachment component in Figure 19 are transformed to axial and radial forces, section properties are computed with Al 2024-T4 as material, and applied in the fatigue beam analysis script. Aluminum was chosen as material since it supports higher stresses at the belt gear teeth, only 3-4 of which would be engaged by the belt. Stresses at teeth are expected to be similar to the thigh belt gear previously analyzed. The main disadvantage of this choice is the high mass of the component, resulting in lower dynamic efficiency during gait. Additional dimensional equivalences to align belts and gears are applied after the main safety factor

optimization loop, resulting in a much larger component with a safety factor of 62.12 as the gear teeth become wider. FEA analysis from Finite Element Analysis was also applied to the worst-case scenario and validates the safety factor at 62.02.

9.6. Bolts

The following section will discuss analysis completed on bolts in the device. Note that analysis was only completed on bolts considered to be critical to the functioning of the device. Other bolts, such as the bolts of the waist component, are analyzed in finite element analysis.

9.6.1. Gear Bolts

The gear bolts are three bolts that connect the three main energy gears together. To analyze these bolts, forces generated through system simulations will be used. MATLAB dynamic simulation outputs a maximum shear force of 45 N and a minimum of 2 N acting on the bolt. Using the maximum force, maximum moment acting on the bolt can then be calculated. Figure 53 shows a sketch of forces acting on the bolt during max shear scenario. An assumption is made that the spring belt gear force is solely responsible for resisting moment produced by the forces when in reality the resistance to the moment is provided by all three gears. To simplify calculations, the distributed loads are replaced with point loads acting at the center of the bolt sections. There are three bolts resisting the shear, each force having a magnitude of 15 N. It is also assumed the bolts are standard M3 bolts (3 mm diameter).

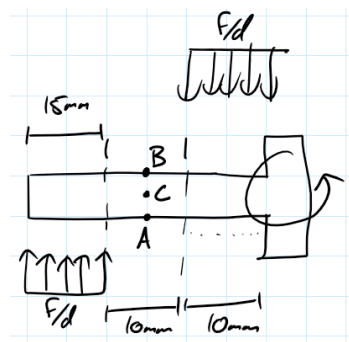


Figure 53 Sketch of bolt loading

Maximum moment can be calculated using the following formula:

$$M_{max} = F_{shear} \frac{7.5 + 10 + 5 \text{ mm}}{2} = 0.1687 \text{ Nm}$$

Assuming the use of stainless steel, material properties are UTS = 600 MPa and Yield Strength = 241 MPa [12]. For steels, the shear yield strength can be approximated as half of yield strength, therefore 120.5 MPa is used.

The Max Shear Stress theory can be used to determine the safety factor of static loading on the bolt. At point A of Figure 53, shear stress is only caused by bending, therefore bending stresses are:

$$\sigma = \frac{32M}{\pi d^3}$$

$$\sigma_{max} = 63.7 \text{ MPa}$$

$$\sigma_{min} = 2.83 \text{ MPa}$$

At point C of Figure 53, there is only transverse shear:

$$\tau_{max} = \frac{4 * V}{3 * A} = 2.83 \text{ MPa}$$

$$\tau_{min} = \frac{4 * V}{3 * A} = 126 \text{ KPa}$$

Using the Max Shear Stress theory, the maximum shear stress acting on the bolt is 31.8 MPa. The safety factor for static loading on the bolt is:

$$SF = \frac{120.5}{31.8} = 3.79$$

Using the Modified Goodman Criterion from previous sections, the fatigue safety factor can be determined. Using the maximum and minimum bending and shear stresses calculated previously, the fatigue safety factors are:

$$S_n = S'_n C_L C_G C_S C_T C_R$$

$$S_n = 0.5 * 600 \text{ MPa} * 1 * 1 * 0.75 * 1 * 0.814 = 183 \text{ MPa for bending}$$

$$S_n = 0.5 * 600 \text{ MPa} * 0.58 * 1 * 0.75 * 1 * 0.814 = 106 \text{ MPa for shear}$$

$$\frac{\tau_a}{S_n} + \frac{\tau_m}{S_u} = \frac{1}{n}$$

n = 4.515 for bending
n = 65.839 for shear

The limiting safety factor is therefore for static loading at 3.79.

9.6.2. Other bolts

Due to the complex geometry of the case and thigh subsystem, analyzing the case bolts and thigh bolts would be time consuming. For this reason, it was decided to analyze these bolts using finite element analysis.

9.7. Bearings

Due to manpower and time restrictions, bearings were not designed from scratch. Shaft bearing design has been relegated to selection of pre-existing components with known parameter data tables providing the bearing sizes and relations. Most of the rotational components, except the medial main shaft bearing, will be composed of needle roller bearings due to their low profile, low inertial forces, high rigidity, and high tolerance for oscillatory stresses [79]. Oscillatory motions are supported for oscillations as low as 30 degrees as required by our design. Minimum oscillatory angle ensures the bearing lubricant is replenished between the needle rollers as they overlap positions during motion. In addition, needle roller bearings provide low friction coefficients on the order of 0.001 to 0.005 [79]. Needle roller bearings have 2-8 times the load-carrying capacity per unit mass than other bearings [79].

KR19 type bearings by NTN have been selected since they have the smallest available form factors for current 8 mm main shaft and timing component shafts. Its dynamic roller load is 460kgf, and track load of 415kgf [79]. The largest expected load for normal gait is 80.7N based on MATLAB force calculations. Static loading on the needle bearings can be computed as follows [80]:

$$S_0 = \frac{C_o}{P} = \frac{460\text{kgf} * 9.81\text{N/kgf}}{80.7\text{N}} = 55.92$$

where S_0 is the static safety factor, C_o is the load rating of the bearing, and P is the static load applied. Track safety factor is 50.45.

Dynamic oscillating loading is most important in the hip exoskeleton. The expected angles of oscillation range from 30 to 70 degrees. Dynamic loading analysis starts with determining the 90% reliability cycles as follows [80]:

$$L_{10} = \left(\frac{C_r}{P}\right)^p * 10^6 \text{cycles} = \left(\frac{460\text{kgf} * 9.81\text{N/kgf}}{80.7\text{N}}\right)^{\frac{10}{3}} * 10^6 \text{cycles} = 6.7 * 10^{11} \text{cycles}$$

where C_r is the radial load rating of the bearing, P is the applied force, and p is the bearing factor which is 10/3 for needle bearings. Additional factors for 99% reliability, environmental and oscillating dynamic loading are applied as follows:

$$L_1 = L_{10} * \Omega * a_1 * a_2 * a_3 = 20 * 10^{12} * 1.2 * 0.21 * 1 * 1 = 5.04 * 10^{12} \text{cycles}$$

where Ω is the oscillating load factor that depends on the oscillation angle (1.2 for 70 degree maximum hip oscillation angle, 2.0 for 30 degree angle), a_1 is the 99% reliability factor, a_2 is the material factor, a_3 is the bearing temperature factor. Bearing temperature rise is not expected to be a concern with low cycling speeds of 30 cycles of gait per minute. The temperature-related changes are expected for above 3000 rpm with significant bearing load of over 250kgf as specified [79]. While the bearing cycle life looks extremely large, it is expected to last less due to potential unpredictable loading situations as well as environmental stresses and shocks.

Rollers will be fit in a rotating inner ring configuration with an ISO 256 K5 tolerance class (+11um, -2um for 20mm shaft diameter) since they support rotating shafts with light and potentially unbalanced loads [79]. The configuration requires a loose fit of the inner ring with a tight fit of the outer ring as shown in Figure 54.

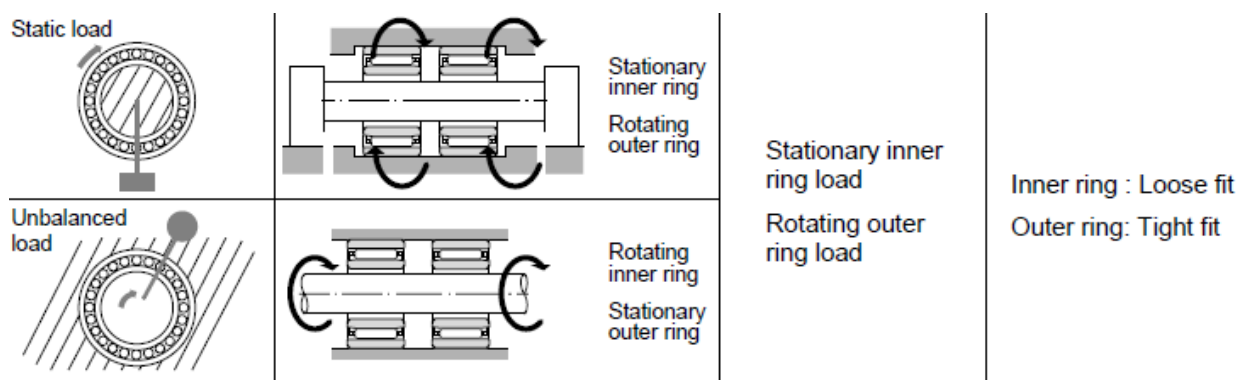


Figure 54 Fitting of the bearings depending on the application [79]

Needle bearings do not carry any axial loads; thus the shafts will require tapered roller bearings on the lateral sides. The calculations for tapered roller bearings involve lateral forces in addition to the analysis for radial forces presented. Since no frontal plane analysis was performed for this report, the lateral forces are not defined. However, given the available components and the relatively low forces involved in the design, the smallest applicable tapered roller bearings in excess of 105kN [81] will more than cover the current application.

9.8. Timing Belts

For this analysis, technical information for timing belts produced by SDP/SI is used as reference. There is a lack of information about timing belt fatigue calculations as well as timing belt impact loading. For this reason, analysis will use constant timing belt operation lifetime and tensile loading. Tooth design of the belt greatly influences the belt lifetime. Trapezoidal tooth designs create stress concentrations at the root of the tooth. Curvilinear tooth design avoids corners at the root of teeth, resulting in better stress distribution within the belt as well as superior load capacities [73].

Timing belt load capacity is dependent on the pitch of the belt teeth. Larger pitches allow for higher loads, however, result in a reduced maximum angular velocity. Angular velocity of belts in this hip exoskeleton design are not expected to exceed 60 rpm. Technical graphs provided by SDP/SI show loading forces for timing belts for velocities as low as 100 rpm, therefore analysis will be done for 100 rpm rotational velocity. The 5mm pitch GT3 belt design can handle loading cases in which the belt gear provides up to 57 Nm torque to the belt. Applying this to the belt gear radius of 50 mm, the allowable tension force is 1140 N, which is significantly higher than the expected maximum force during stair gait of around 60 N.

There is no exact methodology that can be used to determine the fatigue life of a timing belt; instead, there are design methods that can be used to reduce fatigue wear. This includes encasing the belt to keep dust and debris away from the belt teeth, avoiding oil contact with the rubber of the belt, and minimizing contact with water. Increasing diameters of idler pulleys is also recommended to decrease the amount of belt bending wear [73]. As a result, regular maintenance is recommended to visually inspect the belt for cracking and to clean dust and debris off of the teeth.

For the purpose of parametrizing current design, a simplified analysis of timing belts in tension is done assuming composite belt material properties. The belt is represented as a symmetrical composite column with base material and fibers, with linear elastic behavior. It is assumed that fibers are continuous, run along the entire length of the material, and that both materials experience equal strain as a result of tensile loads (Figure 55) [82].

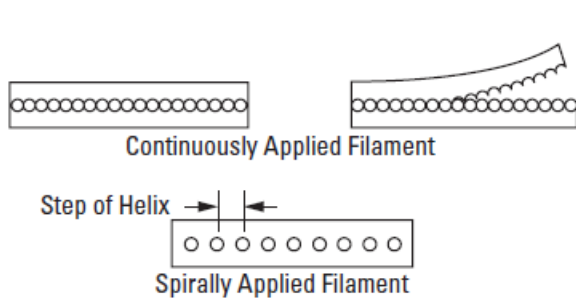


Fig. 15 Belt Cross Section



Fig. 16 Cord Twist

Figure 55 Belt section showing fiber reinforcement of belts [82].

The normal stress for each component j of the material consisting of n materials can be expressed as follows [70]:

$$\sigma_j = \frac{E_j}{\sum_{i=1}^n E_i A_i}$$

where E is the elastic modulus of the material, A is the cross-sectional area of the material. In addition, the area occupied by the fibers can be expressed in terms of the total area. This allows finding the required width of the belt based on analysis of tensile strengths of both materials. Then the width that makes the weakest material safe to use is chosen as the total width of the component. The following expression obtains width of the belt given the loading of each material component:

$$W_{belt} = \frac{E_{base} \times F_{tension} \times SF}{((1 - p_{fiber})E_{base} + p_{fiber} \times E_{fiber}) H_{belt} \times Sy_{base}}$$

$$W_{belt} = \frac{E_{fiber} \times F_{tension} \times SF}{((1 - p_{fiber})E_{base} + p_{fiber} * E_{fiber}) H_{belt} \times Sy_{fiber}}$$

where W_{belt} is the required belt width given safety factor SF , E is the elastic modulus of corresponding material, Sy is its yield strength, H_{belt} is the given height of belt, and p_{fiber} is the

proportion of belt area occupied by the fibers expressed as total area divided by the fiber area. MATLAB script automatically computes the W_{belt} values for each material and picks the largest resultant to meet the safety factor requirement.

Since fibers in the composite material have a larger modulus of elasticity, they take upon greater stress, relieving the more flexible and less strong base material. For example, a longitudinal polyester fiber (5%) with EPDM rubber base thigh belt, connecting the bottom of the thigh component to the thigh belt gear, would have a larger stress on the longitudinal fibers than base. Simulation results show that for the belt of 2mm height the polyester fiber-based width is 5.6mm and rubber base-based width is 0.15mm since fibers take a much larger stress in comparison to the material base.

Belts are typically made with either polyester, Kevlar, fiberglass, or steel reinforcing fibers [82]. Polyester excels at low loads expected in our application since it provides a lower modulus, therefore greater flexibility around small components. Elastic properties dampen shocks and vibration in start-stop operation. One disadvantage of high elasticity is worse belt stretch and dimensional stability as compared to fiberglass or steel.

Base materials include rubber, neoprene, polyurethane, or other polymer compounds such as EPDM rubber [82]. Natural rubber offers a balance of toughness, abrasion and tear resistance, and low compression set which is beneficial for extending component life. However, it suffers from worse environmental performance, including poor weathering and sunlight resistance, which are important considerations for a device that may be used outdoors. EPDM rubber was chosen for its excellent environmental resistance, at the expense of yield strength (<2500lbf/in² vs <3500lbf/in² natural rubber).

9.9.Finite Element Analysis

Finite element methods (FEM/FEA) excel at the analysis of irregular geometry, heterogeneous composition, and unusual boundary condition problems [83]. As such, FEA is well-suited to analyze stresses in some of the device's complex 3D-shaped components.

Multiple approaches to setting up and solving FEA problems exist. SolidWorks 2019 Student Edition implements two main solver types: iterative (FEEPlus) and direct (Direct Sparse Solver) [84]. Iterative solves such as FFEPlus assume an initial solution for each iteration, and calculate associated errors in applying the solution to the equation system. Direct Sparse Solver

uses exact numerical techniques to obtain an exact solution. One of the considerations for the choice of method is the computational resources used. Direct solver uses much more RAM and CPU resources to solve, but generally produces higher accuracy results. Direct solver is also recommended for larger DoF problems with component “no-penetration” contacts and friction applied. Large DoF systems are systems where a detailed mesh is generated in excess of 25,000 nodes. No-penetration contact means that solver ensures adjacent component mesh slide against each other. As such, a Direct Solver is used to ensure accurate solution for the modeled system.

SolidWorks is capable of safety analysis using four criteria: von Mises Stress, Shear Stress, Mohr-Coulomb Stress, and Maximum Normal Stress. Von Mises stress (maximum distortion energy) is most appropriate for ductile materials such as metals and assumes material will not yield if their distortion energy is below the distortion energy that would result in yielding [70]. Shear stress (or Tresca yield) is generally a more conservative criterion for ductile materials and assumes material will not yield below the shear yield limit. Von Mises criterion is recommended due to better correlation with yielding of ductile materials. Mohr-Coulomb stress, an empirical and analytical modification of the shear stress theory, is most used for predicting fracture of brittle materials. Lastly, maximum normal stress is the simplest stress analysis which only looks at material yield uniaxially. Von Mises stress is the most appropriate setting to use for the analysis since ductile materials are used in the design.

Multiple analysis assumptions are made to avoid solving non-linear problems which take a large amount of time and computational resources. Materials are set up as homogeneous, linear elastic, and isotropic. Complete contacts between mating surfaces are assumed with a global friction factor of 0.05. All bolt threads are simplified as cylinders with “bonded” contact which makes the surfaces deform equally and not slide relative to each other. Shaft bearings are assumed to have a sinusoidal force distribution when radial forces are applied. Forces from the MATLAB analytical solution are applied at the appropriate connection surfaces.

9.9.1. Case FEA

Case is modeled as a homogeneous component made from polyetheretherketone (PEEK) plastic. PEEK is a high-performance semi-crystalline thermoplastic with exceptional chemical resistances, mechanical strength, wear, abrasion, and fatigue resistances [85]. Environmental and wear resistances are particularly important properties for everyday use. PEEK mechanical

properties used in the FEA include tensile strength of 95MPa, compressive strength 118MPa, elastic modulus 3.7GPa, Poisson ratio of 0.4, and density of 1310 kg/m³. Von Mises stresses were compared to both tensile strength as well as yield strain since material yields at a strain of >5.2%. PEEK design guide [85] also noted the 10⁶ cycle fatigue limit is 83MPa at 2Hz fatigue cycling. Case is held by AISI 316 annealed stainless steel bolts, size of which was optimized to increase contact surface area with the plastic to reduce stresses.

Several studies were done to optimize the case for stress concentration and load support points for the worst-case use scenarios in frames 1-3 and 95-97 of the stair-up gait cycle for a maximum mass (100kg) and height (180cm) user where energy spring extension forces are greatest. Worst-case scenario performance is critical because failure of the case can result in personal injury if energy components were to fly free while storing full spring energy. Another goal was to minimize case deflection to ensure better alignment of shafts and bearings which is important in dimensional stability and reduced wear of mated gears, and timing components. Figure 56 shows the optimized case design along the FEA mesh.

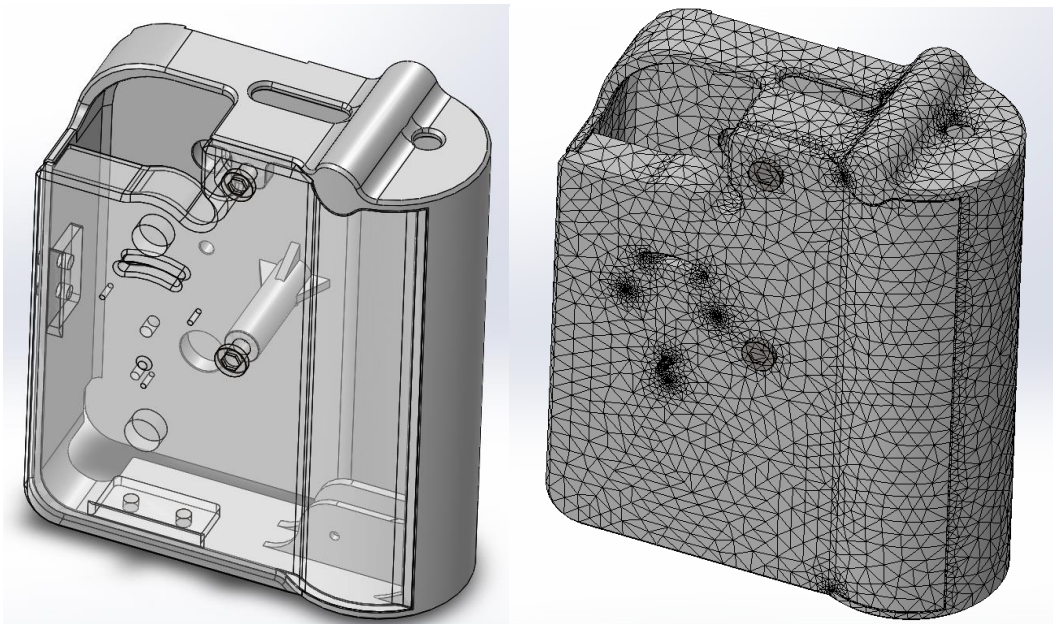


Figure 56 Optimized case and associated FEA mesh.

Von Mises stresses are shown in Figure 57. Greatest stresses were produced at the central bolt attachment as well as the pulley shaft attachment. The maximum stress is just under the edge of the central bolt. Optimization of bolt sizes and locations have yielded a minimum safety factor of 11.48 and maximum deflection around main shaft bearings on the order of 100μm (Figure 58).

The safety factors are improved for smaller and lighter individuals as case width shrinks slightly from parametrization while wall thicknesses are maintained the same to ensure bearings fit fully and securely.

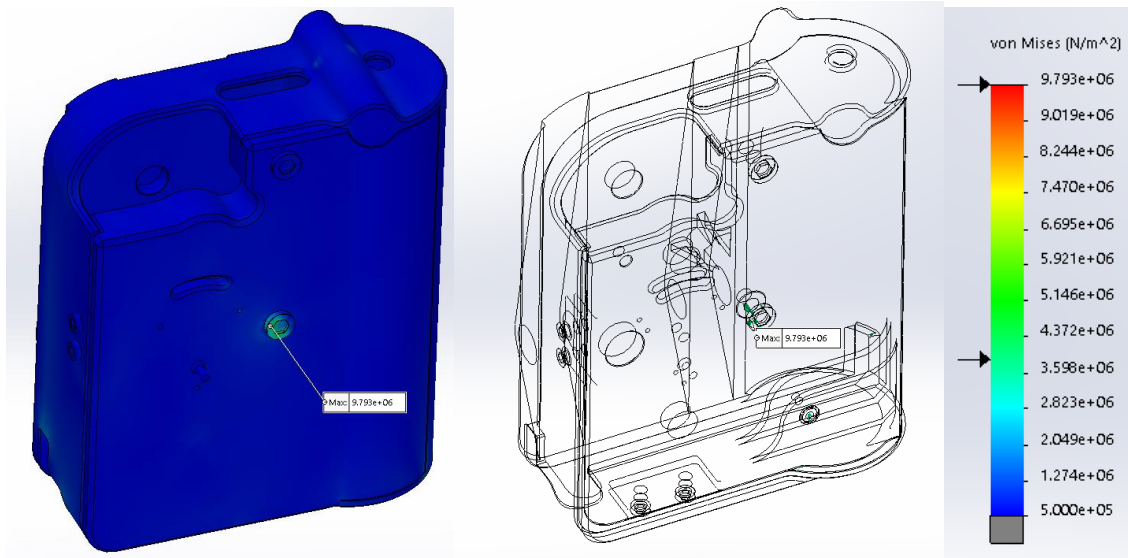


Figure 57 Von Mises stresses for the case component with maximum stress, and SF25 points marked on the colour legend.

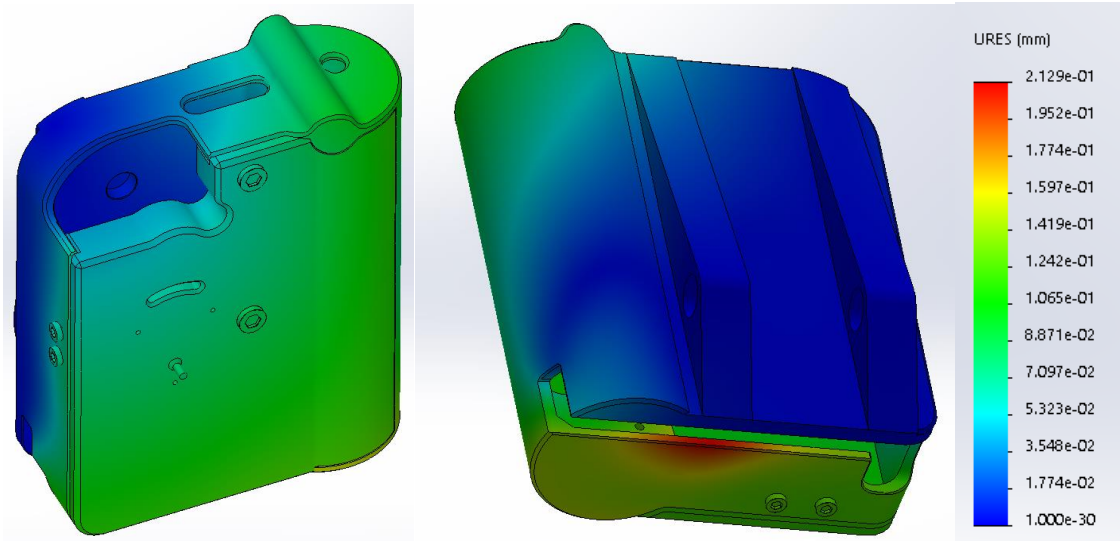


Figure 58 Case wall deflection.

9.9.2. Waist Component FEA

Waist attachment shell is another complex 3D part with multiple forces acting in multiple directions. PEEK was used as material as well. Structural deflections of this component need to be minimized to ensure a more even distribution of forces over larger body regions enclosed by the curvature fit of the attachment. Figure 59 shows the model, applied forces (purple), force reaction locations (green), soft underlayer and body region (dark blue), and study mesh. Body contact face is modeled as elastic support with 20 (N/m)/m^2 stiffness, based on area of 0.08m^2 and skeletal muscle stiffness of $\sim 200\text{N/m}$ for relaxed muscles [86].

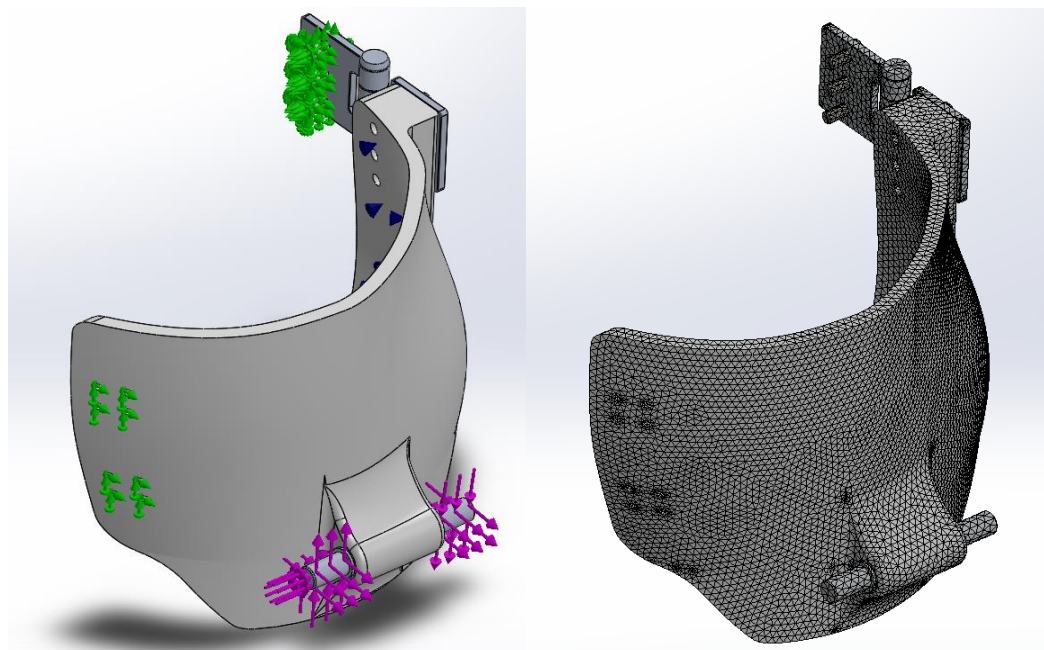


Figure 59 Waist attachment component model, forces, and mesh.

Shaft strength from MATLAB analysis was validated, while shell and hinge components were optimized for the worst-case scenarios as with the device case. Figure 60 shows von Mises stresses in the regions below safety factor of 25. Maximum stress was 38.8MPa at the SS316 steel circlip and Al 2024-T4 shaft mate, resulting in SF 3.56. Circlip is made of relatively soft annealed SS316 which with fatigue is theoretically expected to drop in strength by half over 10^6 cycles with the assumption of $S_n = 0.5S_u$ [70]. This component can be replaced during periodic maintenance after 10^4 cycles to maintain safety factor above 2.

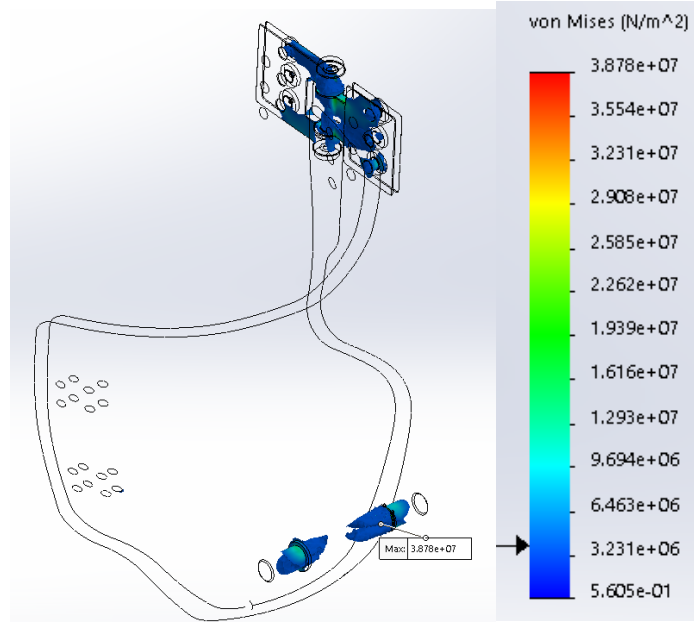


Figure 60 Von Mises stresses in the regions with safety factor below 25.

The von Mises safety factor of the PEEK waist component is >11.99, Al hip case shaft >10.34, SS316 rear hinge bolts >6.01, SS316 hinge rod >5.77, and Al hinge plates >8.53. Softer and more ductile annealed SS316 material is used to ensure no sudden failures and early detection of failure from visible component deformation.

Plastic strain yield safety factor is >42.62 with maximum material strain of 0.122% < 5.2%, as well as low deflection of <0.4mm across the component (Figure 61).

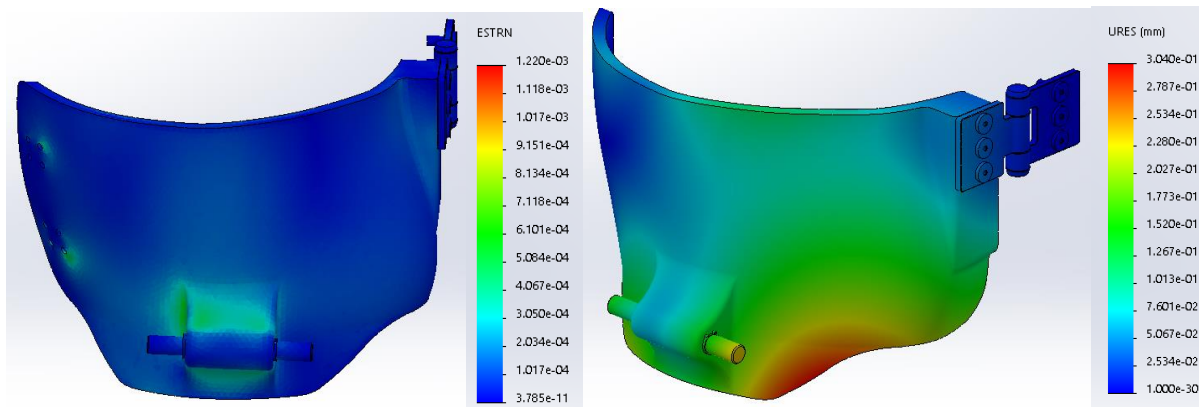


Figure 61 Waist component strain (left) and deflection (right).

9.9.3. Ratchet Pawl Lever FEA

Previous analytic assessment showed that paw lever experiences an impact force from the timing pin. The pawl lever ratchet tooth component may also encounter another impact situation. If the user suddenly stops or reverses hip flexion in swing of the stair gait, the ratchet may be engaged to the pawl via impact. From previous analysis of impact based on component velocities and accelerations, an impact factor of <math><19</math> can be assumed. Figure 62 shows the FEA model set up mesh and non-impact operating von Mises stresses. The AISI 1045 medium carbon steel is used by ratchet and pawl manufacturers due to high tensile strength (310MPa yield, 656MPa ultimate) and hardness (Birnell 163) [74]. As such, the normal operation standard safety factor for worst-case scenario used in previous FEA analyses produces safety factor of 260.

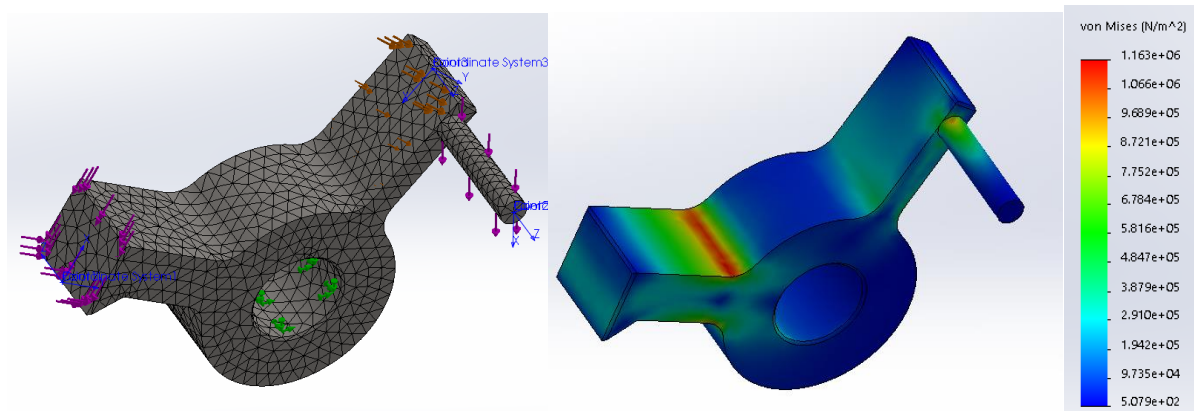


Figure 62 Pawl lever model, mesh, and von Mises stresses.

There is potential to optimize the pawl lever as well as ratchet dimensions to reduce their mass and inertia. However, applying a transient impact multiplication factor of 19 to the ratchet engagement tooth of the pawl reduces the von Mises safety factor to 1.8 (Figure 63).

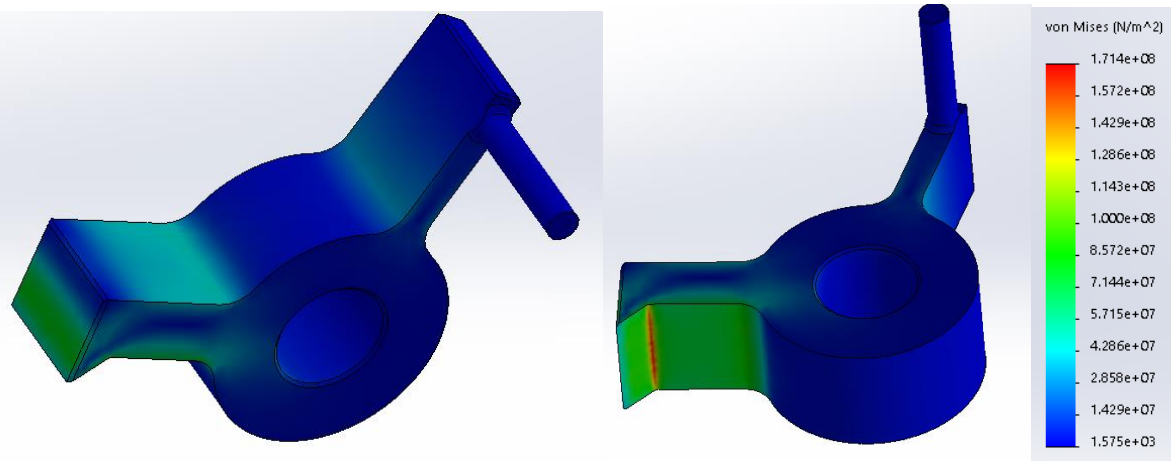


Figure 63 Pawl tooth transient impact loading.

A complete impact analysis of the entire device was beyond the planned scope of this project. Nevertheless, future work should consider the entire assembly for impact loading simulation since impacts are an expected occurrence in everyday use of assistive devices.

9.9.4. Thigh Bar Assembly FEA

Thigh bar assembly, which includes the thigh bar, thigh rigid support attachment, and thigh belt attachment were subjected to FEA analysis to confirm force transfer component deflections against the thigh. Analytic solution equations from classical mechanics used in MATLAB assume small beam deflections, which may not be accurate enough for long members in large deflection. In addition, while axial moments of inertia for I-beam can be exactly computed analytically, the polar moment of inertia of the thigh bar is estimated as a rectangle in the absence of a better approximation. This is an inaccurate approximation of quite complex geometry of the bar, affecting the angle of twist optimization.

As with previous components, maximum height and weight person was modeled to show the maximum deflections with strongest springs and longest components. Thigh bar and thigh contact attachment are assigned the previously described LY5/4 carbon fiber material with homogeneous isotropic material assumption, bolts are assigned annealed SS316, and belt attachment is Al 2024-T4 (Figure 64). Thigh bar splines at the top of the shaft are constrained as force reaction regions in sagittal plane, three of the lowermost belt attachment teeth have the distributed belt force applied, and the end of the thigh contact attachment has thigh reaction applied to it.

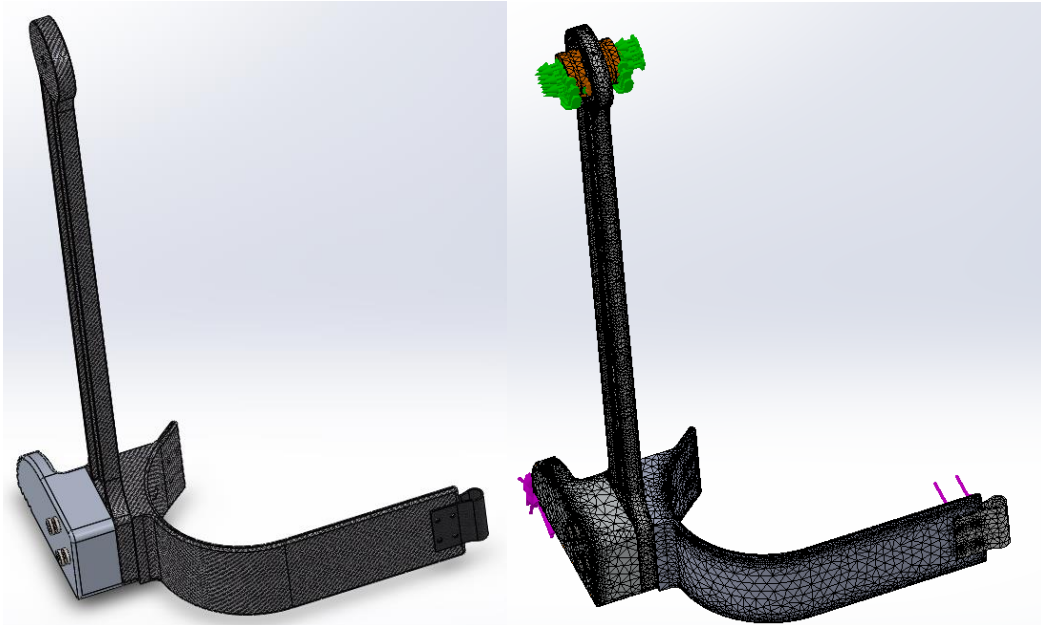


Figure 64 Thigh bar assembly FEA model and analysis mesh with forces and constraints.

The analytic model previously predicted a 4.7mm deflection of the end with the I-beam for a 1° thigh bar angle of twist added to the maximum 2mm deflection of the thigh bar and thigh contact piece as ran by the optimization loop. Larger deflection FEA model instead predicts a ~50mm deflection. In addition, a high stress concentration factor was observed at the top attachment edges with insufficient fillets.

Deflection and stresses have been addressed by thickening both the flanges and the webbing of the I-beam section to 20 layers of LY5/4 carbon fiber epoxy laminate instead of original 10. The resultant deflection of the end beam at thigh contact dropped to ~20mm with a smaller angle of twist of the thigh bar, which is more acceptable without significantly raising the mass of the bar and the attached components (Figure 65). The analytic optimization loop has subsequently been augmented with a post-processing step to include a thickness multiplication factor of 2 to provide a more realistic model.

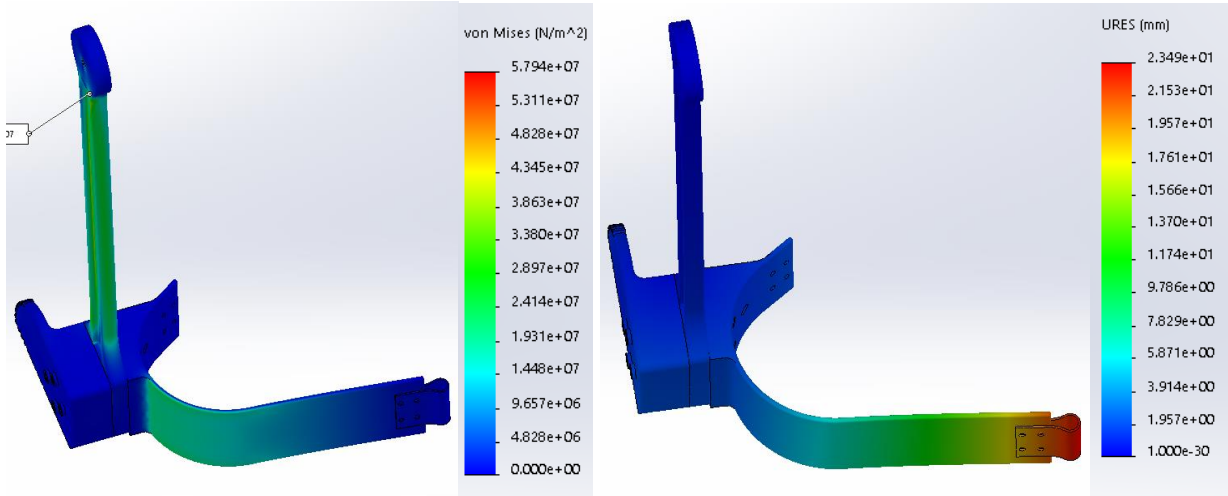


Figure 65 Von Mises stress (left) and deflection (right) for the optimized thigh bar assembly.

The resulting assembly von Mises safety factors are >9.13 for the thigh bar, >18.2 for thighbar splines at main shaft attachment, >9.27 for the connecting bolts, >22.21 for the thigh contact component, and >62.02 for the thigh belt attachment component. Future work should address material change for the thigh belt attachment component from Aluminum to PEEK and assess the strength of its belt teeth while reducing the weight of the component. As was shown in this analysis, single analytic solution using greatly simplified geometric models may be insufficient and adding FEA as an extra modality of verification is recommended.

9.10. Frontal Plane Damping Pads

As described in section 5.4, a damping pad intended to be placed below the case hinge provides an assist moment for hip abduction. When the hip adducts, the damping pad contacts the waist component causing the damping pad to compress to store energy. The pad releases its energy when it decompresses back to its original thickness. Figure 66 shows the case dimensions on the model for the damping pad (a compression damper and a compression spring).

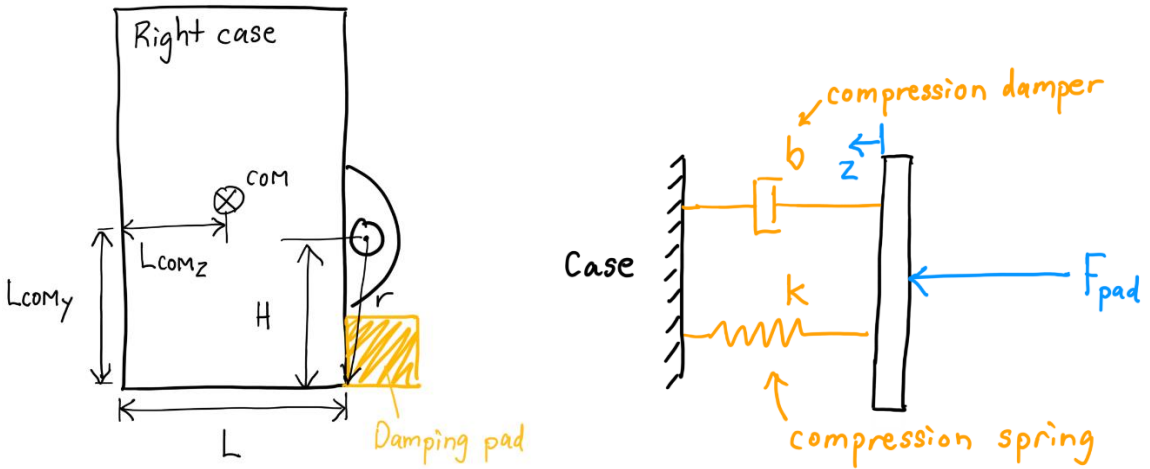


Figure 66 A) Case dimensions, B) Compression spring model for the damping pad.

The force provided by the pad (F_{pad}) is given by,

$$F_{pad} = b|\dot{z}| + k|z|$$

$$b = 2\zeta\sqrt{mk}$$

$$z = rsin\theta_{hipx}$$

$$\dot{z} = r\dot{\theta}_{hipx}cos\theta_{hipx}$$

where b is the damping coefficient, k is the spring coefficient, z is the displacement in the lateral direction and θ_{hipx} is the amount of hip adduction which is assumed to be equal to the amount of case rotation. The pad is chosen to be made of polyurethane with a damping ratio ζ of 0.5. In this model, m is the mass of the case and its components [87].

The pad is a rectangular slab of polyurethane with an equivalent stiffness given by,

$$k = \frac{EA}{t}$$

$$E = \frac{0.0981(56+7.66s)}{0.137505(254-2.54s)} [88]$$

where E is Young's modulus for polyurethane, A is the rectangular area of the pad, t is the thickness of the pad and s is the Shore-A hardness of polyurethane which is taken to be 20.

Figure 67 shows the dimensions of the case and the free-body diagram used in frontal plane analysis.

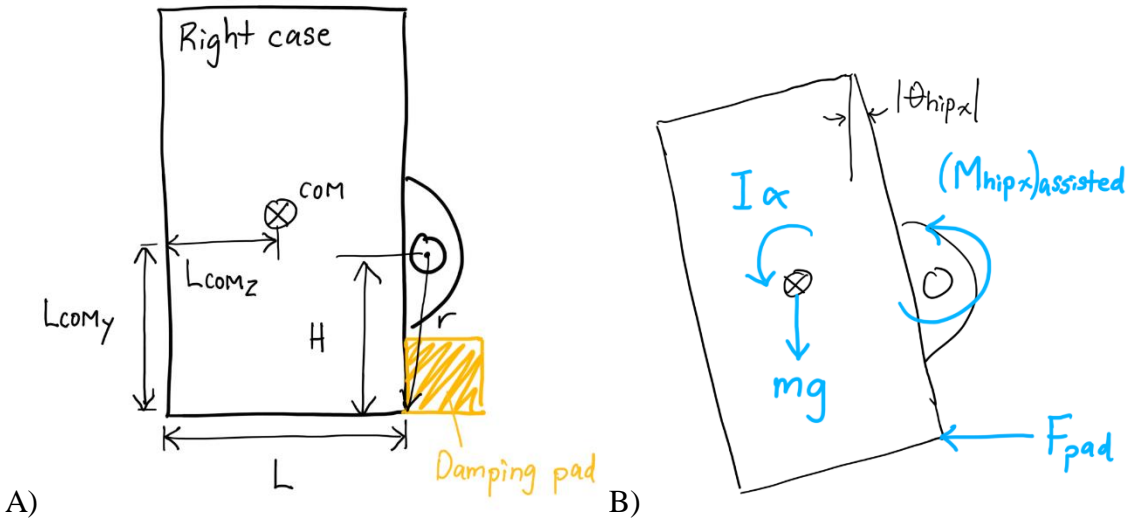


Figure 67 Frontal plane analysis: A) case dimensions and B) case FBD.

The assisted hip moment in the frontal plane (with adduction being positive) is expressed:

$$M_{hipx(\text{assisted})} = M_{hipx(\text{unassisted})} - I\theta_{hipx} - mg(L - L_{COMz})\cos|\theta_{hipx}| - F_{pad}H\cos|\theta_{hipx}|$$

This is the adduction moment that the hip needs to provide during gait while the user is wearing the device in order to reproduce the kinematics of walking without the device on. The unassisted hip adduction moment is that which occurs naturally without the device on. I is the moment of inertia of the case and its components.

Figure 68 shows the pad force as a function of gait cycle. In the model, the pad comes in contact with the waist component when the hip is at 95% adduction. The pad provides a maximum force of approximately 63 N which with $H = 0.076$ m, translates into a hip assist moment of about 4.8 N-m.

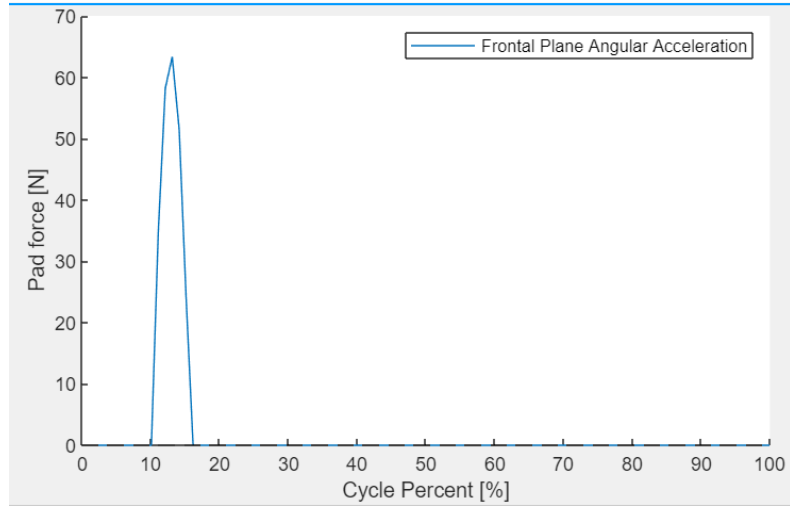


Figure 68 Damping pad force as a function of gait cycle.

Figure 69 shows the contribution of the damping pad and the device's inertia to frontal plane power. Generally, the inertia of the device causes the user to expend more power than he/she would naturally to adduct and abduct the leg. At approximately 12% gait cycle, the pad provides a very small hip abduction assistance to counteract the inertia of the device (the red assist hip power and yellow unassisted hip power lines overlap at around 12% gait cycle). Similar trends were seen for level and incline ascent walking.

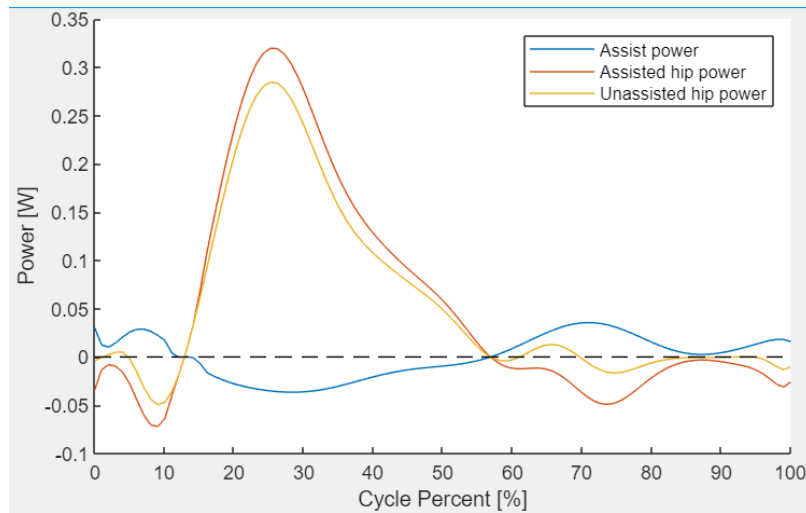


Figure 69 Assisted and unassisted hip adduction power.

10. Parametrization

10.1. Workflow

A parametrization workflow is required to determine how the hip exoskeleton component parameters are going to be calculated. The MATLAB workflow for this project is shown in Figure 70, in which the “START PROGRAM” box acts as an entry into the workflow, rectangles act as discrete steps in the code, and diamonds act as decision branches that can either be user determined or code determined.

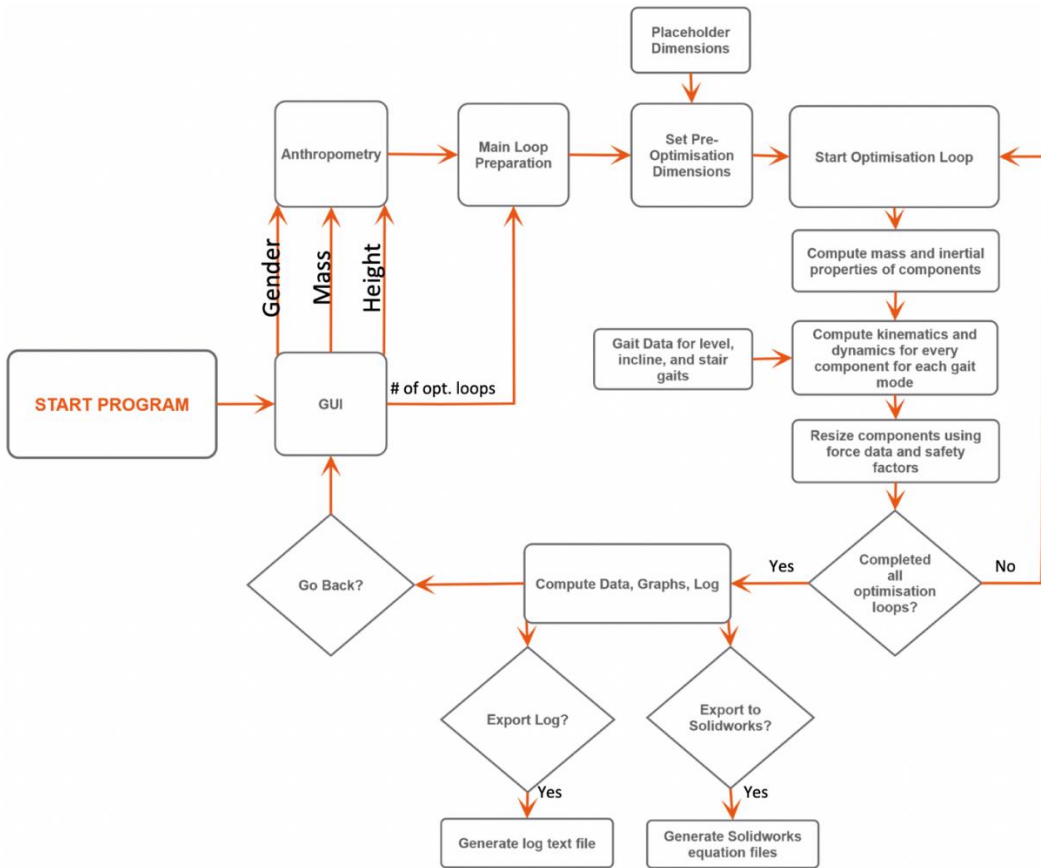


Figure 70 Parametrization workflow.

The Graphical User Interface (GUI) is the first step of the workflow after the program is started. It accepts gender, mass, height, and number of optimization loops. The GUI parameter input screen is shown in Figure 71. The bottom half of the GUI displays some of the generated anthropometric data that will be used if the entered gender, mass, and height parameters are used for calculations.

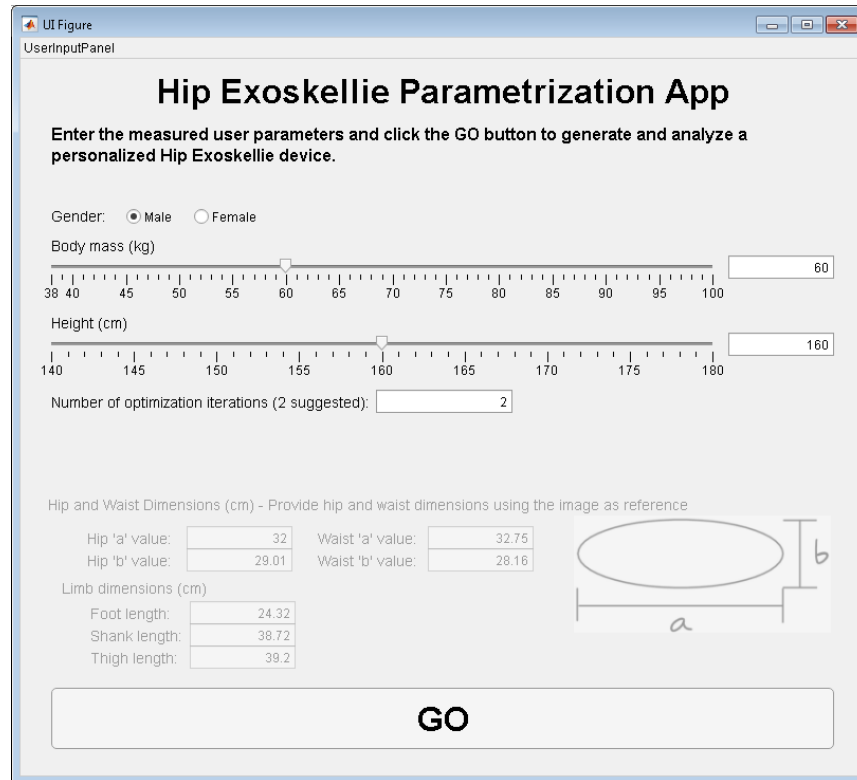


Figure 71 Parameter Input Screen

After the user has selected their input parameters and press the GO button, the gender, mass, and height input parameters are passed to an anthropometric value generation function. This function first uses the chosen gender to choose between two anthropometric data sets, one for male and one for female. It then calculates limb dimensions, waist and hip sizes, and limb masses.

The main loop preparation code receives the anthropometric values from the anthropometric generation function and it also receives the input parameter for number of optimization loops (optimization loops will be explained further down). The main loop preparation makes some initial dimensioning of the design, specifically the thigh, hip, and waist related components. It sizes the thigh bar component as a percentage of thigh length, and it sets the size of the waist components based on anthropometric data.

The main loop preparation code then prepares some default component dimension values. This is required in order to generate preliminary masses and moment of inertia for dynamic analysis of the system. At this point the code also runs a special function named the equivalence function which ensures all components of the design fit into their corresponding mounting points. For example, it resizes bearings to fit generated shaft diameters, and then resizes case holes to fit

generated bearing outer diameters. This equivalence function is used to ensure all default dimension values are consistent and will generate reasonable simulation results.

After all pre-optimization functions are complete, the optimization loop is started. The optimization loop is necessary due to the use of arbitrary default values that have no relation to the input user parameters. Since all the masses and moments of inertia of the components are not accurate for the given user input parameters, iteration must be used to converge to the actual component dimensions and properties. The first optimization loop simulates the system dynamically using the initial masses, moments of inertias, shaft lengths, gear widths, and many other parameters to produce the expected forces on each component. The dynamic simulation uses gait data for all three gait modes (level, incline, and stairs). Each component of the device is simulated and has its forces calculated for every frame of all three gait data sets. The maximum and minimum forces on each component is saved across all simulations, and working analysis is then calculated on each component to determine minimum required dimensions. The equivalence function is then called again to readjust components to fit together into the case.

If more than one optimization loop is selected in the input parameter screen, the code will then redo all calculations starting from recalculating masses and moments of inertia for the new dimensions of all the device components. It will then recalculate all forces again for the newly sized components for the three data sets again and also recalculate component dimensions again. This is repeated until all required optimization loops are completed. The concept behind using an optimization loop is that with enough iterations, the component dimensions will eventually converge to a point where iterating further will produce no difference in component mass, moment of inertia, or size, leading in no difference in calculated forces and stresses between subsequent iterations.

In practice, each optimization loop can take upwards of 2.5 minutes depending on the hardware. The reason for lengthy computation times is due to the sheer amount of calculations required during simulations. For every frame of each gait data set, the code solves a 155 unknown variable system of equations to obtain force data for each component for every frame of the three gait data sets. All testing of the code and Solidworks was done using 1 or two optimization loops due to time constraints, and it is suggested to use a maximum of two optimization loops however the GUI provides the option of using up to five optimization loops.

Once the optimization loop is completed, overall data, such as efficiency and percent assist, is computed for each gait mode. Data sets for graphs are also generated and are returned to the GUI along with the overall system data to be displayed for the user in the results screen, shown in Figure 72. The user can switch between the graphs and data for each gait mode by switching tabs in the top left corner of the GUI. The user can also switch what graph is being displayed for the active gait mode by selecting a different data set from the drop-down list located above the graph. A log file is also generated which details the code progress throughout the optimization loops and the working analysis completed on the components.

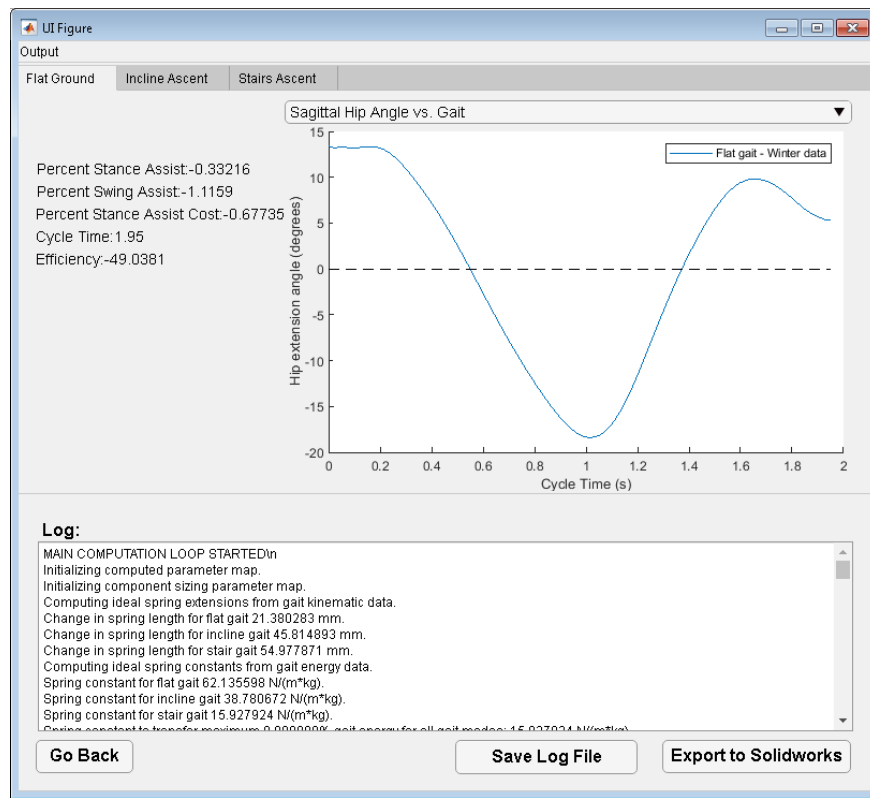


Figure 72 Results Display Screen

The GUI does not automatically output log files and Solidworks. This decision was made mainly due to the lengthy execution time of the code to avoid accidental overwrites of logs or Solidworks files that may still be wanted. When the “Save Log File” button is clicked, the user is given the option to choose file directory and name in order to have the option to save log files from different simulations without overwriting previous log files. Note that the save prompt defaults to the Log folder within the project directory. When the “Export to Solidworks” button is clicked, the code generates equation files for each component and saves them to the equation folder found

within the Solidworks folder. Note that if equation files already exist, they will be overwritten. Save errors may occur if the user tries to overwrite log or equation files that are currently opened or are being used by a different application. The GUI will warn the user if this error occurs and exporting fails.

The workflow ends at this point, and the user is given the option to start again by returning to the parameter input screen and start over.

10.2. Parametrization Results

The goal of parametrization is to optimize component sizes to reduce component sizes and masses to a minimum. Due to the large number of parameters that each component of the device has, some parameters were set as constants to greatly simplify parametrization. Due to this, parametrization focuses on optimizing one or two parameters at most for each component. For example, the main energy gears maintain a constant diameter and number of teeth, however their thickness will change depending on the forces acting on the gear teeth. This section will display some examples of the parametrization of the device working with different user input parameters.

As discussed previously discussed, the GUI allows for the choice between male and female anthropometric data sets. The difference in the results is significant when observing the waist component, as shown in Figure 73. For the same mass and height, the gender setting greatly affects waist and hip circumferences to accommodate the wider hips of females. There is also a slight difference in the length of the thigh components to accommodate statistical differences of limb lengths between genders.



Figure 73 Difference between male (left) and female (right) devices using identical mass and height parameters.

Varying the height input parameter visibly changes the lengths of the thigh components, and it also changes the waist component circumference since anthropometric data shows a relationship between waist circumference and height. Figure 74 shows the difference between the shortest and tallest allowable settings for height of user given the same gender (male) and mass (60 kg).



Figure 74 Difference between shortest (left) and tallest (right) settings using identical mass and height parameters.

Varying the mass input parameter mainly changes the size of load bearing components, including gears, belts, shafts, and the main energy spring. Figure 75 shows the difference between the lightest and heaviest allowable settings for mass given the same gender (male) and height (160 cm). Of note is the size change of the main energy spring.



Figure 75 Difference between lightest (left) and heaviest (right) settings using identical mass and height parameters.

11. Validation

11.1. Stability

Stability is a crucial factor in determining whether a person will fall down during daily activity. This is even more critical when considering that the target user of the hip exoskeleton device are seniors where falls are not only more frequent but also more dangerous to their health. In order to ensure stability, we must define certain parameters. In the paper by H. Razavi, stability is divided into two distinct categories: static stability and dynamic stability. Static stability is defined by its relation between anthropometric data and the center of gravity (COG) and base of support (BOS) among other parameters. Dynamic stability is defined by calculating the Lyapunov exponent from experimental data [89].

The Lyapunov exponent, defined as a measure of the evolution of generic perturbations or more simply, an estimate of a given system's "chaos", relies on a complex mathematical model which exceeds the expectations of this project [90]. Although the H. Razavi paper does attempt to calculate the Lyapunov exponent, it relies on a huge set of experimental anthropometric data as well as a complex MATLAB algorithm [89]. Therefore, only static stability will be used to determine the general stability of a person with the device.

In order to determine whether a person is stable during gait, a general index encompassing all relevant parameters will be determined. This index, given as the center of gravity percentage (COG%), is calculated as:

$$COG\% = \frac{2x}{W_{BOS}}$$

where W_{BOS} is the width of the base of support and x is the relation between the individuals center of gravity height and its anterior sway angle. To find W_{BOS} , the following relation can be used [89]:

$$W_{BOS} = 0.152 \times H$$

Where H is the person's height in cm. A visual of the physical attributes of these equations is shown in Figure 76. Note that the L_{BOS} is not necessary for static stability calculation, only dynamic or for frontal plane analysis.

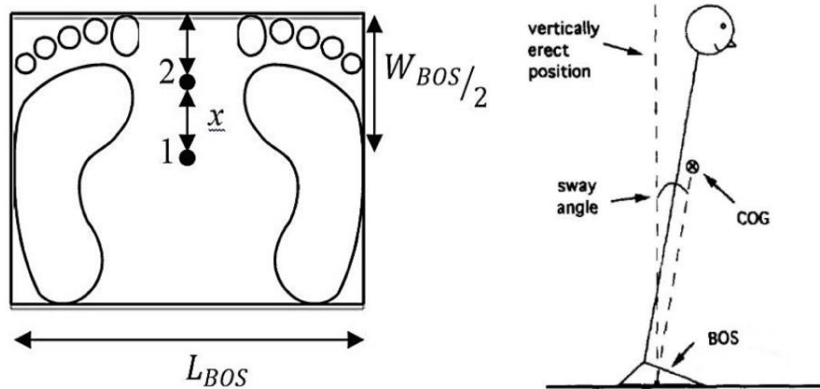


Figure 76 Schematics for the BOS and COG of a person [89].

The relation x can be calculated as follows:

$$x = H_{COG} \times \tan(\theta_{sway})$$

Where the θ_{sway} be visualized in Figure 76 as the sway of the body during gait in the sagittal plane. The difficulty here lies in finding the height of the center of gravity of the person. In order to simplify the calculations, several assumptions must be made. Firstly, it is assumed that the sway of the H_{COG} in the frontal plane is always constant. This is a fairly safe assumption, since by observing experimental data, summarized in Figure 77, we can approximate a linear average due to the rough cyclical nature of change of the GCOM during gait.

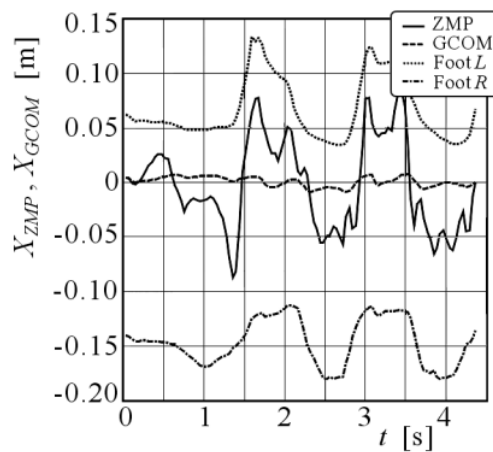


Figure 77 Trajectories of various stability parameters in the frontal plane during gait [91].

Like mentioned before, a second significant assumption would be to neglect the dynamic stability when determining the general stability of a given person. This means that only the variation of the HCOG in the sagittal plane will be considered, and that it will only be based on

the sway angle during the gait cycle as seen in Figure 76. With these assumptions and restrictions in place, a reasonable estimate of HCOG can be made [92].

There are a multitude of ways to find the HCOG, with most using a machine or apparatus to assist the calculations like the balance, suspension or reaction method. However, none of these would directly allow our analysis to include the addition of our device let alone the problem of access to these machines. Instead, the more theoretical segmentation method will be used. This method requires that each major part of the body is separated into segments, such as the head, torso, arms etc. and a moment is found for each one. From there, along with the mass, length and COG of each aforementioned segment, a global HCOG can be found by [92]:

$$\sum M = H_{COG} \times m_p$$

$$H_{COG} = \frac{\sum M}{m_p}$$

Where $\sum M$ is the sum of moments of each segment and m_p the person's total mass. In this case, it is assumed that the device will be one of these segments, with its own estimate of mass, length and COG. These calculations are performed automatically with the MATLAB code by taking in the relevant anthropometric data and outputting the estimated H_{COG} of the given person. With the H_{COG} found, the x values can be determined by using several different sway angles, representing the different phases in the gait cycle, so that several COG% can be determined. By combining the equations above, a sample calculation, with a sway angle of 3, an estimated height of 175cm and an estimated H_{COG} of 100cm, is shown below [92]:

$$COG\% = \frac{2 \times H_{COG} \times \tan(\theta_{sway})}{W_{BOS}}$$

$$COG\% = \frac{2 \times 100 \times \tan(3)}{0.152 \times 175}$$

$$COG\% = 0.394 = 39.4\%$$

From there, an average is taken of all the different COG% to obtain a final number. There is no clear-cut answer to whether a fall will occur based on the COG% since it also relies on a few additional components such as gait type, terrain and a person's physical strength. But, for the purposes of this project, if the given person's COG% exceeds 70%, it is assumed that the gait is unstable.

11.2. Simulation and Evaluation

Device performance was evaluated using four data sets. One data set was Winter's [45] young individual data set which includes ground reaction forces, as well as requisite lower limb kinematic data, allowing the evaluation of additional device mass contribution on gait assistance and the inverse dynamics chain based on anthropometric data as opposed to Winter's man parameters. This validation test also showcases the ability of the MATLAB script to process data and implement inverse dynamics where required from gait experiments in the lab.

The other three digitized data sets for elderly individuals flat [48], incline [69], and stair [51] gait do not provide all of the required parameters to compute inverse dynamics, even if they provide GRF data. Inverse dynamics requires at least the positions of all lower limb components markers (or centers of mass), including foot, shank, and thigh. The positions could then be fitted and numerically differentiated as is actually done in our MATLAB code to obtain hip angular velocity and accelerations where only hip flexion/extension angles are provided. The other data sets are used to approximate the device contribution in various gait modes for elderly individuals specifically as originally envisioned. Of note is the continued use of assumption of superposition where assist or detriment moments provided by the device are directly added to the hip moments to evaluate device performance. This is generally not an accurate assumption and would require live testing of a device prototype to determine true performance.

Winter [45] data set used with anthropometrically parametrized male individual of 60kg mass and 160cm in height is simulated and provides 0.825% flat gait stance phase energy assistance when the device is worn, which is consistent with low assist values in elderly data set simulation for flat gait. The energy storage spring is not strong enough to provide assistance to overcome the inertia of the device, since it is designed to ideally provide at most 8% sagittal assistance in stair-up gait. Spring extends by only 2.1cm in flat gait compared to 5.5cm in stair-up gait, thus work that the spring could provide is smaller by over a factor of 4. GRFy and GRFx plot is shown in Figure 19 with estimated device mass of 8.7kg. The mass of the device is 14.5% of body mass, but needs improvement to be useful for elderly population in daily life. With the device not worn, the elderly person is presently better off in terms of hip moments. It can potentially be used as a weight trainer during flat gait.

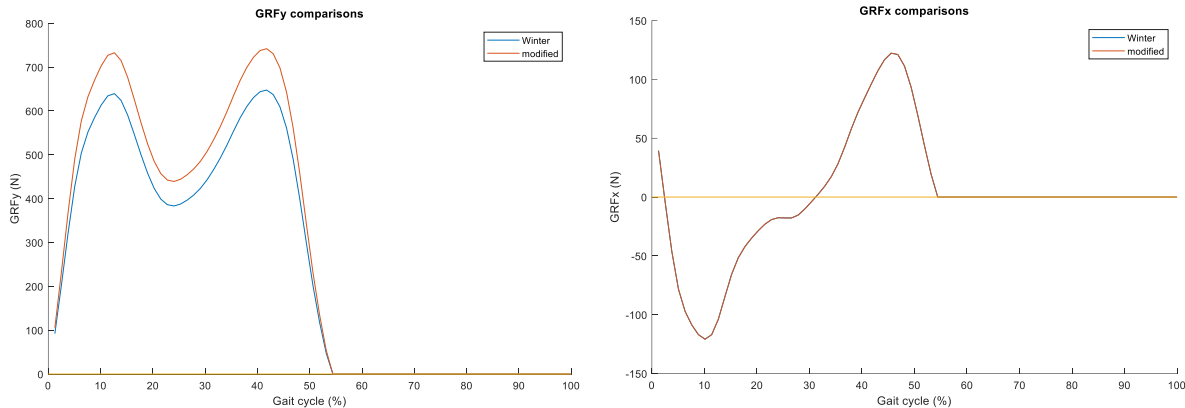
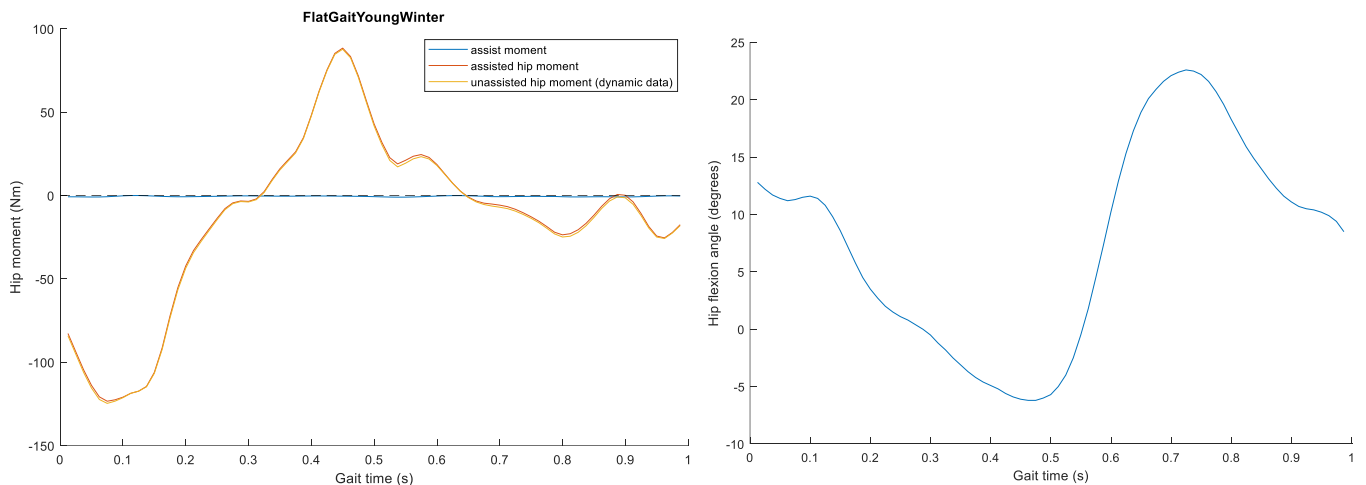


Figure 78 GRFy (left) and GRFx (right) with and without the device on, assuming static mass contribution.

Hip moment plot (Figure 79) show that with the device on, hip moment is shifted (very slightly) in the expected negative direction. Moment is more negative until approximately



halfway point where spring is most discharged and increases again at the 0.7-0.8s region where hip angle is large again at the end of the swing phase.

Figure 79 Assisted and unassisted hip moment plot (left), and associated gait angles (right).

The power assistance of the device can be observed in the power plot Figure 80. Stance phase assistance is minimal. The energy cost is over twice as great, which can also be visualized by the difference in areas occupied by orange regions on the figure between 0.1s and 0.5s, and 0.5s and 0.8s. Assistance is computed as the energy contribution of the assist divided by total stance phase energy in the sagittal plane. Cost is computed as the energy detriment of the device in the swing phase, and expressed as a ratio of this energy to stance phase energy. Cost is always greater

than assist as expected from conservation of energy. The ratio of assist to cost represents device efficiency. Of note, negative efficiency would mean that the device provides a detriment in both stance and swing phase of the gait cycle.

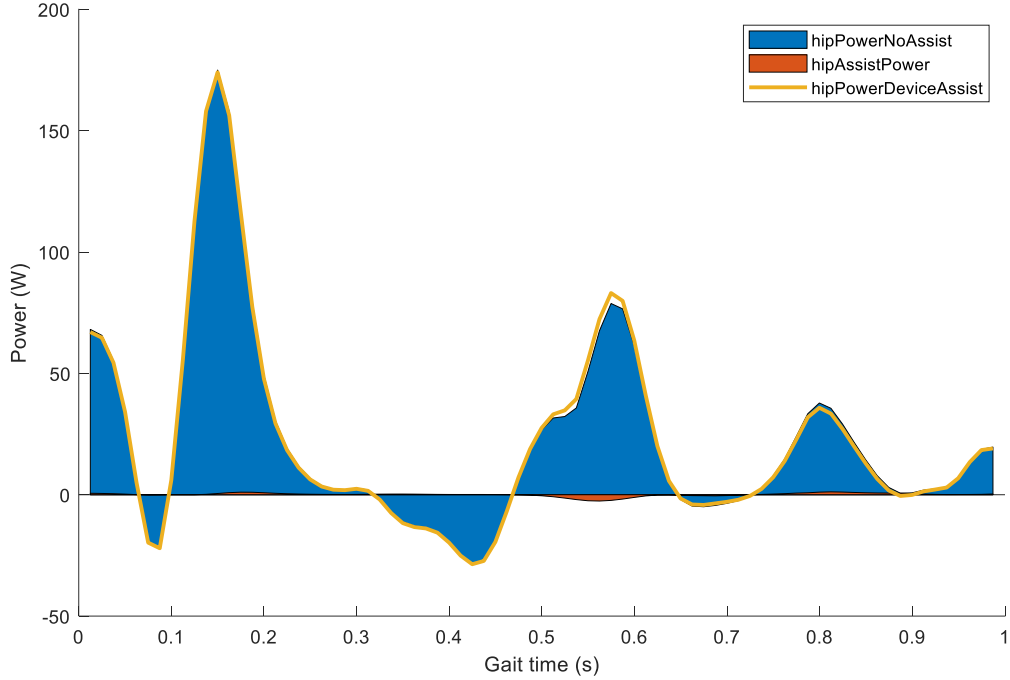


Figure 80 Power assist of the device throughout the gait cycle.

Device performance in different gait modes was evaluated on the flat [48], incline up [69], and stair up [51] digitized datasets to estimate the performance in elderly individuals. These data sets have been implemented in the GUI simulation version of MATLAB code to provide feedback on device performance. Multiple simulations of device assistance were performed to generate plots of assistance in different gait mode dependent on person's mass and height.

First set of simulation examines the effect of increasing body mass alone with constant height. Figure 81 and Figure 82 show gait assists and assist efficiency plots in sagittal plane for a 1.55m female with varying body mass. A 3% assist can be observed across the board for stair gait with a slightly increasing cost between 7 and 7.5%. The results are expected since spring constant computation is parametrized to the gait data presented on a per-mass basis in the literature. Increasing mass proportionally increases assist moments. The increasing costs may be associated with increasing bulkiness and inertia of the device to accommodate the extra safety factors required for greater force transfers.

Of note is the slightly negative performance for flat and incline up gait, where the user would expend extra energy. This issue can only be solved by a stiffer spring, and reduced device inertia and mass. Solutions that would result in not overloading the stair gait energy cost would involve designing a variable-stiffness spring system which is stiffest for flat and incline gait, and less stiff for stair gait.

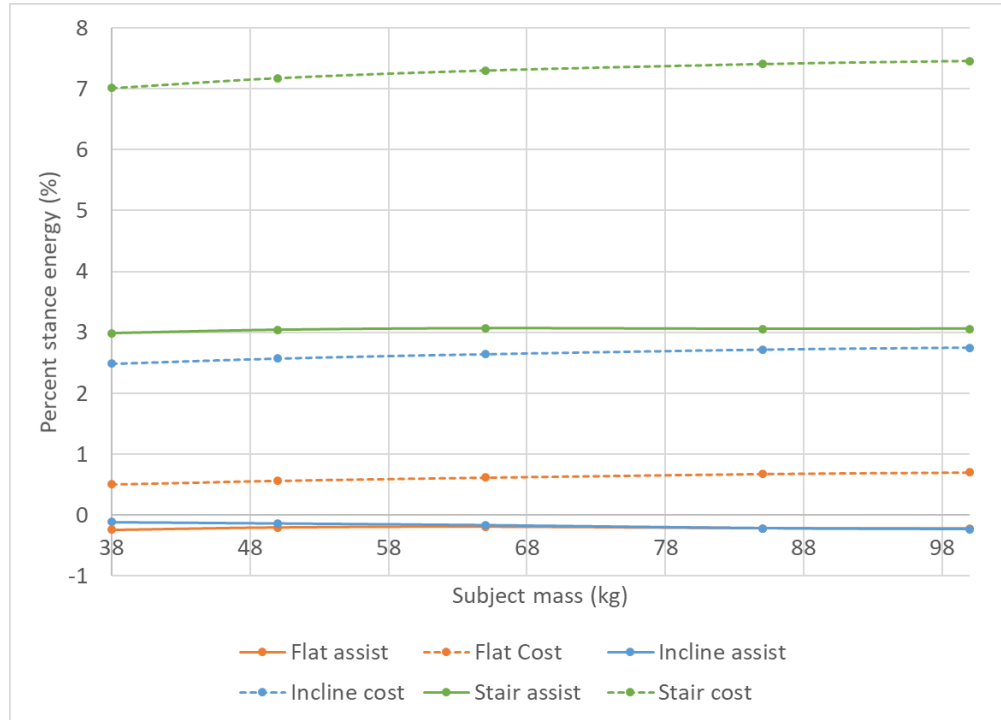


Figure 81 Stance assist percent and stance assist cost for 1.55m female with varying body mass for flat, incline up, and stair up gait in sagittal plane.

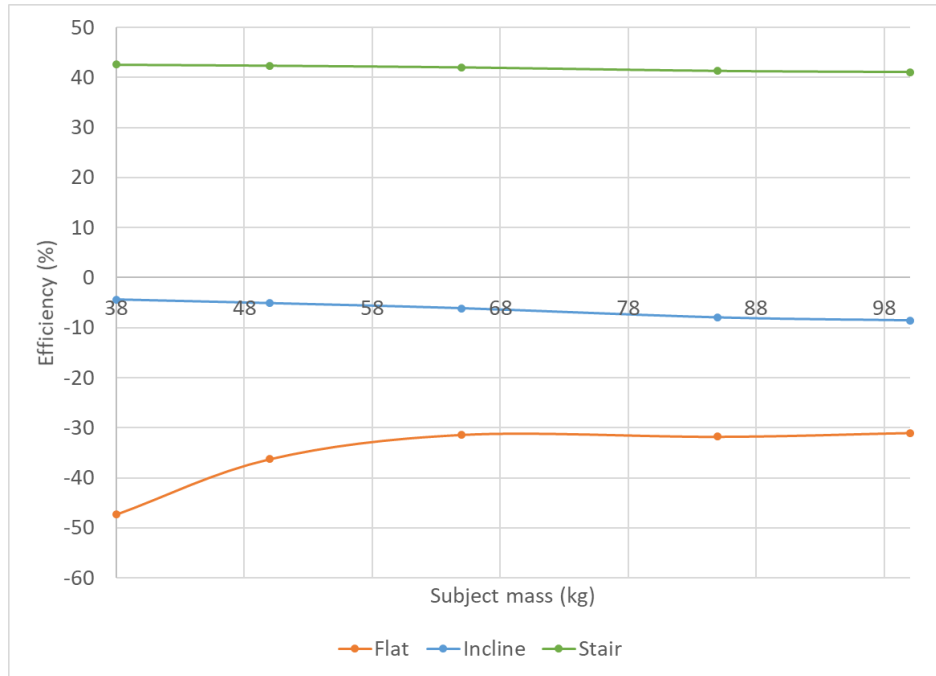


Figure 82 Stance assist efficiency for 1.55m female with varying body mass flat, incline up, and stair up gait in sagittal plane.

Second set of simulation examines the effect of increasing height alone with constant mass.

Figure 83 and Figure 84 show gait assists and assist efficiency plots in sagittal plane for a 65kg female with varying body height. Stair gait assist drops from 3.5 to 2.5% as height increases. The results are expected since the stored spring energy is constant, while device size increases to accommodate larger components for a taller person as generated by the anthropometric model.

Of note is the slightly positive performance of flat and incline gait below a certain height to mass ratio. Spring is stiff due to high body mass parametrization, while device components are small due to body height parametrization. Once again, this provides useful feedback on the device performance, supporting the contention that a variable stiffness spring system would be ideal to tackle the performance and efficiency issues.

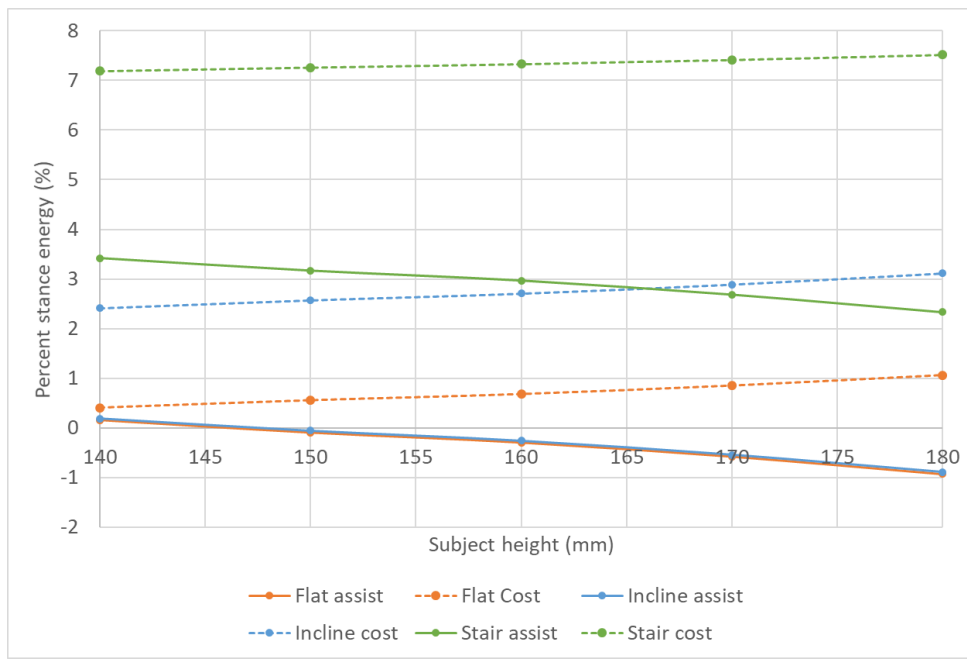


Figure 83 Stance assist percent and stance assist cost for 65kg female with varying height for flat, incline up, and stair up gait in sagittal plane.

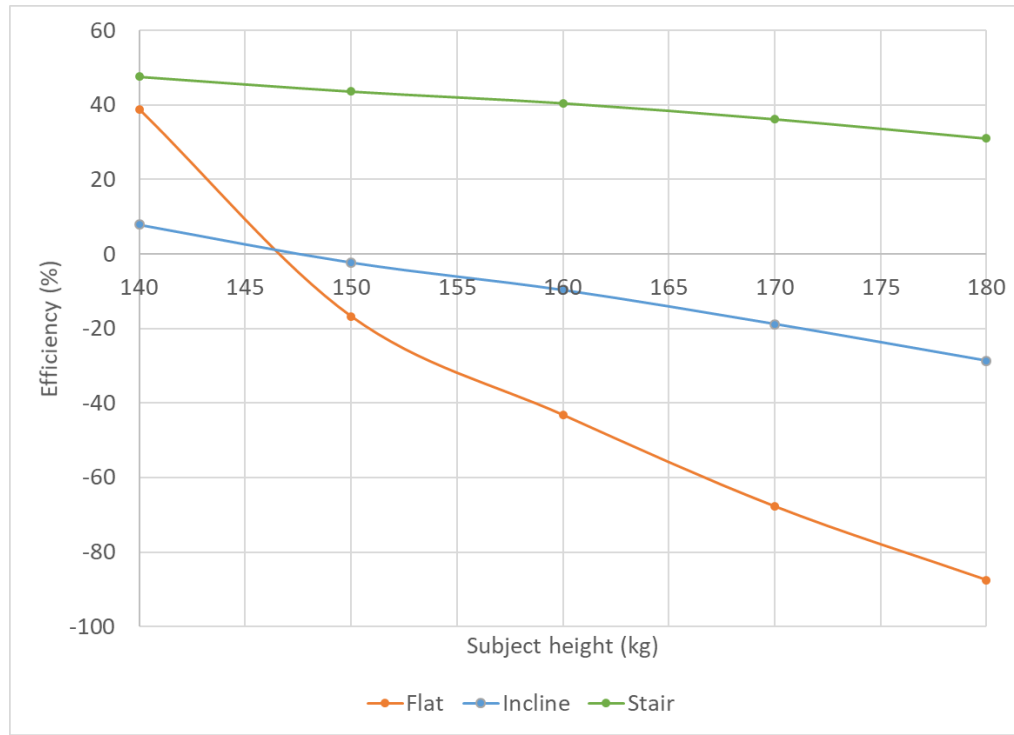


Figure 84 Stance assist efficiency for 65kg female with varying height for flat, incline up, and stair up gait in sagittal plane.

12. Future Work

Future work includes potential improvements of the device:

- Refine the design to meet the defined safety restrictions (safety releases) that are not met in the current design.
- Reduce the overall weight of the device by implementing strategies such as using light and rigid truss-like support structures for the case, enclosed in a thin plastic shell. Add strategic material cutaways to components.
- Reduce the overall size of the device by optimizing component positioning, preventing unnecessary component growth in order to align certain mates.
- Increase the device energy assistance for flat and incline ascent gait by implementing a variable-stiffness spring system in order to allow all gait modes to operate efficiently.
- Reduce the tolerance requirements of the camshaft in the timing discs by reworking components of the mechanism. This would potentially reduce future manufacturing issues and facilitate a more cost-effective design.
- Add the possibility of an incline descent and downstairs gait mode.
- Add another degree of freedom to the hip joint to facilitate thigh attachment that accurately follows the limb motion.

13. Conclusion

The final report provides a comprehensive overview of the final design of a passively powered hip exoskeleton to achieve gait stability and mobility enhancement for elderly people in common activities of daily living. This includes an analysis of all relevant internal mechanisms, the simulation of the device in flat, incline and stair ascent gait, the methods behind the parametrization implementation of relevant parts and a full set of SolidWorks renders of the device. Generally, the simulation analyses of the key components of the system satisfied the global safety factor and modelling criteria. However, it was found that the device mass and dimensions could be reduced or optimized in order to improve device efficiency. The springs, gears, pins, belts and bolts all achieved adequate safety factors while that certain aspects of the device may have been over-engineered. Despite the large weight and size of the device, results from the simulation show that the device provides some assistance in stair ascent gait but performs poorly in flat and incline ascent gait.

References

- [1] P. A. Potter, A. G. Perry, P. A. Stockert, and A. M. Hall, Eds., *Fundamentals of Nursing*, 8th ed. Elsevier, 2013.
- [2] Canada Employment and Social Development, “Government of Canada — Action for Seniors report,” *aem*, 03-Oct-2016. [Online]. Available: <https://www.canada.ca/en/employment-social-development/programs/seniors-action-report.html>. [Accessed: 12-Sep-2019].
- [3] Statistics Canada, “The Daily — Age and sex, and type of dwelling data: Key results from the 2016 Census,” 03-May-2017. [Online]. Available: <https://www150.statcan.gc.ca/n1/daily-quotidien/170503/dq170503a-eng.htm>. [Accessed: 12-Sep-2019].
- [4] Statistics Canada, “The impact of aging on labour market participation rates,” 14-Jun-2017. [Online]. Available: <https://www150.statcan.gc.ca/n1/pub/75-006-x/2017001/article/14826-eng.htm>. [Accessed: 12-Sep-2019].
- [5] Statistics Canada, “Living alone in Canada,” 06-Mar-2019. [Online]. Available: <https://www150.statcan.gc.ca/n1/pub/75-006-x/2019001/article/00003-eng.htm>. [Accessed: 12-Sep-2019].
- [6] S. M. Bruijn, O. G. Meijer, P. J. Beek, and J. H. van Dieën, “Assessing the stability of human locomotion: a review of current measures,” *J R Soc Interface*, vol. 10, no. 83, Jun. 2013.
- [7] H. Razavi, “A Comparison between Static and Dynamic Stability in Postural Sway and Fall Risks,” *J Ergonomics*, vol. 07, no. 01, 2016.
- [8] J. Mrozowski, J. Awrejcewicz, and P. Bamberski, “Analysis of stability of the human gait,” 2015.
- [9] CIHI, “Hip and knee replacements in Canada: CJRR report | CIHI,” 2019. [Online]. Available: <https://www.cihi.ca/en/hip-and-knee-replacements-in-canada-cjrr-report-0>. [Accessed: 12-Sep-2019].
- [10] CIHI, “Falls and vehicle collisions top causes of injury hospitalizations for seniors | CIHI,” 2019. [Online]. Available: <https://www.cihi.ca/en/falls-and-vehicle-collisions-top-causes-of-injury-hospitalizations-for-seniors>. [Accessed: 11-Sep-2019].
- [11] S. N. Robinovitch *et al.*, “Video capture of the circumstances of falls in elderly people residing in long-term care: an observational study,” *The Lancet*, vol. 381, no. 9860, pp. 47–54, 2013.
- [12] D. Hamacher *et al.*, “Gait Stability and Its Influencing Factors in Older Adults,” *Front Physiol*, vol. 9, Jan. 2019.
- [13] B. Salzman, “Gait and Balance Disorders in Older Adults,” *AFP*, vol. 82, no. 1, pp. 61–68, Jul. 2010.
- [14] N. M. Gell, R. B. Wallace, A. Z. LaCroix, T. M. Mroz, and K. V. Patel, “Mobility Device Use Among Older Adults and Incidence of Falls and Worry About Falling: Findings From the 2011–2012 National Health and Aging Trends Study,” *J Am Geriatr Soc*, vol. 63, no. 5, pp. 853–859, May 2015.
- [15] C. Luz, T. Bush, and X. Shen, “Do Canes or Walkers Make Any Difference? NonUse and Fall Injuries,” *Gerontologist*, vol. 57, no. 2, pp. 211–218, Apr. 2017.
- [16] M. M. Lusardi, M. Jorge, and C. C. Nielsen, Eds., *Orthotics & Prosthetics in Rehabilitation*, 3rd ed. Elsevier, 2013.

- [17] C. Wang, R. Goel, H. Rahemi, Q. Zhang, B. Lepow, and B. Najafi, “Effectiveness of Daily Use of Bilateral Custom-Made Ankle-Foot Orthoses on Balance, Fear of Falling, and Physical Activity in Older Adults: A Randomized Controlled Trial,” *GER*, vol. 65, no. 3, pp. 299–307, 2019.
- [18] D. Richie, “How Much Do You Charge For Foot Orthoses?,” *Podiatry Today*, Dec-2009. [Online]. Available: <https://www.podiatrytoday.com/blogged/how-much-do-you-charge-for-foot-orthoses>. [Accessed: 11-Sep-2019].
- [19] “Starkmans Health Care Depot.” [Online]. Available: <https://starkmans.com/>. [Accessed: 12-Sep-2019].
- [20] H. Herr, “Exoskeletons and orthoses: classification, design challenges and future directions,” *Journal of NeuroEngineering and Rehabilitation*, vol. 6, no. 1, p. 21, Jun. 2009.
- [21] “Apparatus for facilitating walking,” US420179A, 28-Jan-1890.
- [22] H. Ali, “Bionic Exoskeleton: History, Development and the Future,” *IOSR Journal of Mechanical and Civil Engineering*, p. 5.
- [23] R. S. Mosher, “Handyman to Hardiman.” Research and Development Center General Electric Company, 1967.
- [24] “Research and Development Prototype for Machine Augmentation of Human Strength and Endurance: Hardiman I Project.” General Electric Company Corporate Research and Development, 1971.
- [25] H. Canada, “Guidance Document - Guidance on the Risk-based Classification System for Non-In Vitro Diagnostic Devices (non-IVDDs),” *aem*, 23-Apr-2015. [Online]. Available: <https://www.canada.ca/en/health-canada/services/drugs-health-products/medical-devices/application-information/guidance-documents/guidance-document-guidance-risk-based-classification-system-non-vitro-diagnostic.html>. [Accessed: 10-Sep-2019].
- [26] H. Canada, “Frequently Asked Questions - Medical Device Establishment Licensing and Fees,” *aem*, 12-Dec-2012. [Online]. Available: <https://www.canada.ca/en/health-canada/services/drugs-health-products/compliance-enforcement/establishment-licences/annual-review-documents/frequently-asked-questions-medical-device-establishment-licensing-fees.html>. [Accessed: 10-Sep-2019].
- [27] C. for D. and R. Health, “Classify Your Medical Device,” *FDA*, 09-Feb-2019. [Online]. Available: <http://www.fda.gov/medical-devices/overview-device-regulation/classify-your-medical-device>. [Accessed: 10-Sep-2019].
- [28] *Title 21: Food and Drugs*, vol. PART 890—PHYSICAL MEDICINE DEVICES. 2019.
- [29] “ISO 22523:2006(en), External limb prostheses and external orthoses — Requirements and test methods.” [Online]. Available: <https://www.iso.org/obp/ui/#iso:std:iso:22523:ed-1:v1:en>. [Accessed: 10-Sep-2019].
- [30] K. Junius, M. Degelaen, N. Lefebvre, E. Swinnen, B. Vanderborght, and D. Lefebvre, “Bilateral, Misalignment-Compensating, Full-DOF Hip Exoskeleton: Design and Kinematic Validation,” *Applied Bionics and Biomechanics*, vol. 2017, 2017.
- [31] C. Xiong, T. Zhou, L. Zhou, T. Wei, and W. Chen, “Multi-articular passive exoskeleton for reducing the metabolic cost during human walking,” in *2019 Wearable Robotics Association Conference (WearRAcon)*, 2019, pp. 63–67.
- [32] “Honda Global | honda walking assist device.” [Online]. Available: <https://global.honda/products/power/walkingassist.html>. [Accessed: 15-Sep-2019].

- [33] “Sales starting of Honda Walking Assist Device,” *Today’s Medical Developments*. [Online]. Available: <https://www.todaysmedicaldevelopments.com/article/medical-device-honda-walking-assist-device-technology-manufacturing-72815/>. [Accessed: 15-Sep-2019].
- [34] “Honda Global | Walking Assist.” [Online]. Available: <https://global.honda/innovation/robotics/WalkingAssist.html>. [Accessed: 15-Sep-2019].
- [35] P. K. Levangie and C. C. Norkin, Eds., *Joint Structure and Function*, 5th ed. F.A. Davis Company, 2011.
- [36] J. M. Soucie *et al.*, “Range of motion measurements: reference values and a database for comparison studies,” *Haemophilia*, vol. 17, no. 3, pp. 500–507, May 2011.
- [37] L. Stathokostas, M. W. McDonald, R. M. D. Little, and D. H. Paterson, “Flexibility of Older Adults Aged 55–86 Years and the Influence of Physical Activity,” *Journal of Aging Research*, 2013. [Online]. Available: <https://www.hindawi.com/journals/jar/2013/743843/>. [Accessed: 14-Sep-2019].
- [38] S. Morini, A. Bassi, C. Cerulli, A. Maranozzi, and M. Ripani, “Hip and knee joints flexibility in young and elderly people: Effect of physical activity in the elderly,” *Biology of Sport*, vol. 21, Nov. 2003.
- [39] “WebPlotDigitizer - Extract data from plots, images, and maps.” [Online]. Available: <https://automeris.io/WebPlotDigitizer/>. [Accessed: 14-Sep-2019].
- [40] G. G. Simoneau, K. J. Hoenig, J. E. Lepley, and P. E. Papanek, “Influence of hip position and gender on active hip internal and external rotation,” *J Orthop Sports Phys Ther*, vol. 28, no. 3, pp. 158–164, Sep. 1998.
- [41] T. H. Retchford, K. M. Crossley, A. Grimaldi, J. L. Kemp, and S. M. Cowan, “Can local muscles augment stability in the hip? A narrative literature review,” *J Musculoskeletal Neuronal Interact*, vol. 13, no. 1, pp. 1–12, Mar. 2013.
- [42] M. E. Johnson, M.-L. Mille, K. M. Martinez, G. Crombie, and M. W. Rogers, “Age-related changes in hip abductor and adductor joint torques,” *Arch Phys Med Rehabil*, vol. 85, no. 4, pp. 593–597, Apr. 2004.
- [43] I. Grunte, G. R. Hunter, B. D. Mccurry, M. S. Bolding, J. L. P. Roy, and J. P. Mccarthy, “Age and Gender Differences in Hip Extension and Flexion Torque Steadiness,” *Gerontology; Basel*, vol. 56, no. 6, pp. 533–41, Oct. 2010.
- [44] D. E. Anderson and M. L. Madigan, “Healthy Older Adults Have Insufficient Hip Range of Motion and Plantar Flexor Strength to Walk Like Healthy Young Adults,” *J Biomech*, vol. 47, no. 5, pp. 1104–1109, Mar. 2014.
- [45] D. A. Winter, *The Biomechanics and Motor Control of Human Gait*. Waterloo, Ontario, Canada: University of Waterloo Press, 1987.
- [46] Protokinetics, “Phases of the Gait Cycle: Gait Analysis » ProtoKinetics,” *ProtoKinetics*, 28-Nov-2018..
- [47] M. Doumit, “Note 2: Gait Analysis.” University of Ottawa, 2019.
- [48] D. A. Winter, A. E. Patla, J. S. Frank, and S. E. Walt, “Biomechanical Walking Pattern Changes in the Fit and Healthy Elderly,” *Journal of the American Physical Therapy Association*, vol. 70, pp. 340–347, 1990.
- [49] P. A. Hageman and D. J. Blanke, “Comparison of gait of young women and elderly women,” *Phys Ther*, vol. 66, no. 9, pp. 1382–1387, Sep. 1986.
- [50] D. R. Vickers, C. Palk, A. S. McIntosh, and K. T. Beatty, “Elderly unilateral transtibial amputee gait on an inclined walkway: A biomechanical analysis,” *Gait & Posture*, vol. 27, no. 3, pp. 518–529, Apr. 2008.

- [51] N.-H. Law, “Kinematics & Kinetics Analysis of the Lower Extremity of Normal Weight, Overweight, and Obese Individuals During Stair Ascent & Descent,” MSc, University of Ottawa, Ottawa, ON, 2013.
- [52] D. A. Winter, Ed., *Biomechanics and Motor Control of Human Movement*, 4th ed. John Wiley & Sons, Inc., 2009.
- [53] W. T. Dempster, “THE ANTHROPOMETRY OF BODY ACTION,” 1955.
- [54] R. Drillis, R. Contini, and M. Bluestein, “BODY SEGMENT PARAMETERS; A SURVEY OF MEASUREMENT TECHNIQUES,” *Artif Limbs*, vol. 8, pp. 44–66, 1964.
- [55] W. T. Dempster, W. C. Gabel, and W. J. L. Felts, “The anthropometry of the manual work space for the seated subject,” *Am. J. Phys. Anthropol.*, vol. 17, no. 4, pp. 289–317, Dec. 1959.
- [56] R. Contini, “Body segment parameters. II,” *Artif Limbs*, vol. 16, no. 1, pp. 1–19, 1972.
- [57] K. Kothiyal and S. Tettey, “Anthropometry for design for the elderly,” *Int J Occup Saf Ergon*, vol. 7, no. 1, pp. 15–34, 2001.
- [58] E. Perissinotto, C. Pisent, G. Sergi, F. Grigoletto, and ILSA Working Group (Italian Longitudinal Study on Ageing), “Anthropometric measurements in the elderly: age and gender differences,” *Br. J. Nutr.*, vol. 87, no. 2, pp. 177–186, Feb. 2002.
- [59] B. Shatenstein, M. J. Kergoat, and S. Nadon, “Anthropometric changes over 5 years in elderly Canadians by age, gender, and cognitive status,” *J. Gerontol. A Biol. Sci. Med. Sci.*, vol. 56, no. 8, pp. M483–488, Aug. 2001.
- [60] E. Churchill, T. Churchill, and P. Kikta, “The AMRL Anthropometric Data Bank Library: Volumes 1-5,” WEBB ASSOCIATES YELLOW SPRINGS OH, Oct. 1977.
- [61] “Winter et al. - Biomechanical Walking Pattern Changes in the Fit a.pdf.” .
- [62] “Vickers et al. - 2008 - Elderly unilateral transtibial amputee gait on an .pdf.” .
- [63] K. Kothiyal and S. Tettey, “Anthropometry for design for the elderly,” *Int J Occup Saf Ergon*, vol. 7, no. 1, pp. 15–34, 2001.
- [64] L. Stathokostas, M. W. McDonald, R. M. D. Little, and D. H. Paterson, “Flexibility of Older Adults Aged 55–86 Years and the Influence of Physical Activity,” *Journal of Aging Research*, 2013. [Online]. Available: <https://www.hindawi.com/journals/jar/2013/743843/>. [Accessed: 14-Sep-2019].
- [65] K. Seo, J. Lee, Y. Lee, T. Ha, and Y. Shim, “Fully autonomous hip exoskeleton saves metabolic cost of walking,” in *2016 IEEE International Conference on Robotics and Automation (ICRA)*, 2016, pp. 4628–4635.
- [66] D.-S. Kim *et al.*, “A wearable hip-assist robot reduces the cardiopulmonary metabolic energy expenditure during stair ascent in elderly adults: a pilot cross-sectional study,” *BMC Geriatrics*, vol. 18, no. 1, p. 230, Sep. 2018.
- [67] P. K. Levangie and C. C. Norkin, Eds., *Joint Structure and Function*, 5th ed. F.A. Davis Company, 2011.
- [68] A. S. McIntosh, K. T. Beatty, L. N. Dwan, and D. R. Vickers, “Gait dynamics on an inclined walkway,” *Journal of Biomechanics*, vol. 39, no. 13, pp. 2491–2502, Jan. 2006.
- [69] D. R. Vickers, C. Palk, A. S. McIntosh, and K. T. Beatty, “Elderly unilateral transtibial amputee gait on an inclined walkway: A biomechanical analysis,” *Gait & Posture*, vol. 27, no. 3, pp. 518–529, Apr. 2008.
- [70] R. C. Juvinall and K. M. Marshek, *Fundamentals of Machine Component Design*, 5th ed. Wiley, 2012.

- [71] “McMaster-Carr,” *Light-Duty Buckles*. [Online]. Available: <https://www.mcmaster.com/29705t87>. [Accessed: 04-Dec-2019].
- [72] J. J. Uicker, G. R. Pennock, and J. E. Shigley, *Theory of machines and mechanisms*, 3rd ed. McGraw-Hill, 2003.
- [73] R. G. Budynas and J. K. Nisbett, *Shigley’s mechanical engineering design*, 9th ed. New York: McGraw-Hill, 2011.
- [74] H. S. Says, “AISI 1045 Medium Carbon Steel,” *AZoM.com*, 02-Jul-2012. [Online]. Available: <https://www.azom.com/article.aspx?ArticleID=6130>. [Accessed: 03-Dec-2019].
- [75] “Pitch Line Velocity: What Is It and Why Is It Important? - Motion Control Tips.” [Online]. Available: <https://www.motioncontroltips.com/pitch-line-velocity/>. [Accessed: 29-Oct-2019].
- [76] H. Rahmani, S. H. M. Najafi, and A. Ashori, “Mechanical performance of epoxy/carbon fiber laminated composites,” *Journal of Reinforced Plastics and Composites*, vol. 33, no. 8, pp. 733–740, Apr. 2014.
- [77] C. Capela, S. E. Oliveira, and J. A. M. Ferreira, “Fatigue behavior of short carbon fiber reinforced epoxy composites,” *Composites Part B: Engineering*, vol. 164, pp. 191–197, May 2019.
- [78] A. F. T. Mak, M. Zhang, and E. W. C. Tam, “Biomechanics of Pressure Ulcer in Body Tissues Interacting with External Forces during Locomotion,” *Annu. Rev. Biomed. Eng.*, vol. 12, no. 1, pp. 29–53, Jul. 2010.
- [79] “NTN Needle Roller Bearing Handbook.” NTN, 2010.
- [80] “NTN Needle Roller Bearings.” NTN, 2010.
- [81] “Double Row Tapered Roller Bearings On NTN Bearing Corp. of America,” *NTN Bearing Corp. of America*. [Online]. Available: <https://bearingfinder.ntnamericas.com/viewitems/metric-iso-series-tapered-roller-bearings/double-row-tapered-roller-bearings>. [Accessed: 28-Oct-2019].
- [82] SDP/SI, “Handbook of Timing Belts, Pulleys, Chains and Sprockets.” SDP/SI, 2017.
- [83] S. C. Chapra and R. P. Canale, *Numerical Methods for Engineers.*, 6th ed. New York, NY: McGraw-Hill, 2010.
- [84] SolidWorks, “2019 SOLIDWORKS Help - Analysis Solvers,” 2019. [Online]. Available: http://help.solidworks.com/2019/english/SOLIDWORKS/cworks/c_Analysis_Solvers.htm?verR=edirect=1. [Accessed: 03-Dec-2019].
- [85] Solvay, “KetaSpire® PEEK Design and Processing Guide.” Solvay, 2014.
- [86] G. Gavronski, A. Veraksits, E. Vasar, and J. Maaroos, “Evaluation of viscoelastic parameters of the skeletal muscles in junior triathletes,” *Physiol Meas*, vol. 28, no. 6, pp. 625–637, Jun. 2007.
- [87] tleto, “Polyurethane Durometer Hardness,” *Gallagher Custom Polyurethane Molding*, 15-Jun-2018. .
- [88] I. M. Meththananda, S. Parker, M. P. Patel, and M. Braden, “The relationship between Shore hardness of elastomeric dental materials and Young’s modulus,” *Dental Materials*, vol. 25, no. 8, pp. 956–959, Aug. 2009.
- [89] H. Razavi, “A Comparison between Static and Dynamic Stability in Postural Sway and Fall Risks,” *J Ergonomics*, vol. 07, no. 01, 2016.
- [90] A. Politi, “Lyapunov exponent,” *Scholarpedia*, vol. 8, no. 3, p. 2722, 2013.
- [91] J. Mrozowski, J. Awrejcewicz, and P. Bamberski, “Analysis of stability of the human gait,” 2015.

- [92] F. Hamandi, “DESIGN A MODEL FOR HUMAN BODY TO DETERMINE THE CENTER OF GRAVITY,” 2012.
- [93] W. Pirker and R. Katzenbach, “Gait disorders in adults and the elderly,” *Wien Klin Wochenschr*, vol. 129, no. 3, pp. 81–95, Feb. 2017.
- [94] P. Mahlknecht *et al.*, “Prevalence and Burden of Gait Disorders in Elderly Men and Women Aged 60–97 Years: A Population-Based Study,” *PLOS ONE*, vol. 8, no. 7, p. e69627, Jul. 2013.
- [95] J.-C. Ceccato, M. de Sèze, C. Azevedo, and J.-R. Cazalets, “Comparison of Trunk Activity during Gait Initiation and Walking in Humans,” *PLoS One*, vol. 4, no. 12, Dec. 2009.

Appendix A GUI Instructions

To make the complex, hard to use MATLAB code easy to use for the intended demographic, a GUI was designed to easily input user parameters and output validation graphs, a log file, and Solidworks equations files.

Compatibility

The GUI was created using MATLAB App Designer using MATLAB 2019a. Due to the use of MATLAB App Designer, the GUI will likely not work on any other version of MATLAB (likely will not work using 2019b). MATLAB App Designer is a default functionality of MATLAB 2019a and does not require extra installation of files or libraries.

Solidworks files were created using Solidworks 2019-2020. The files are not backwards compatible; to guarantee proper function use with the same version of Solidworks.

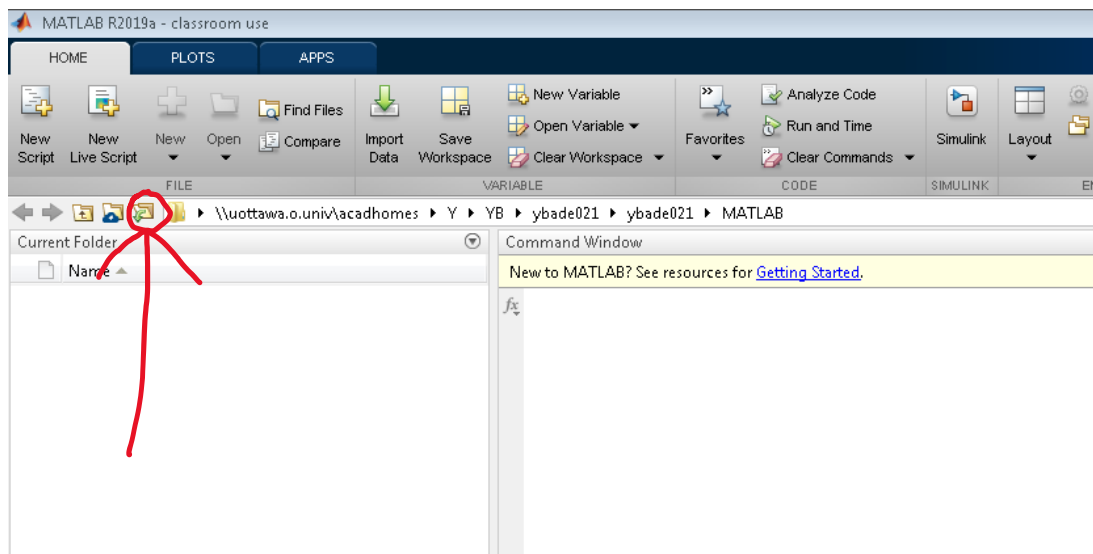
Other Notes

When testing the code on laboratory computers, we ran into the issue where the lab computers were transferring the “Group13” folder extremely slowly. We are unsure if this is due to file structure we used or if it simply because the laboratory computers are very slow. We had to work around this issue by uploading our project folder to Google Drive and download it on the computer rather than use a USB stick to transfer the files.

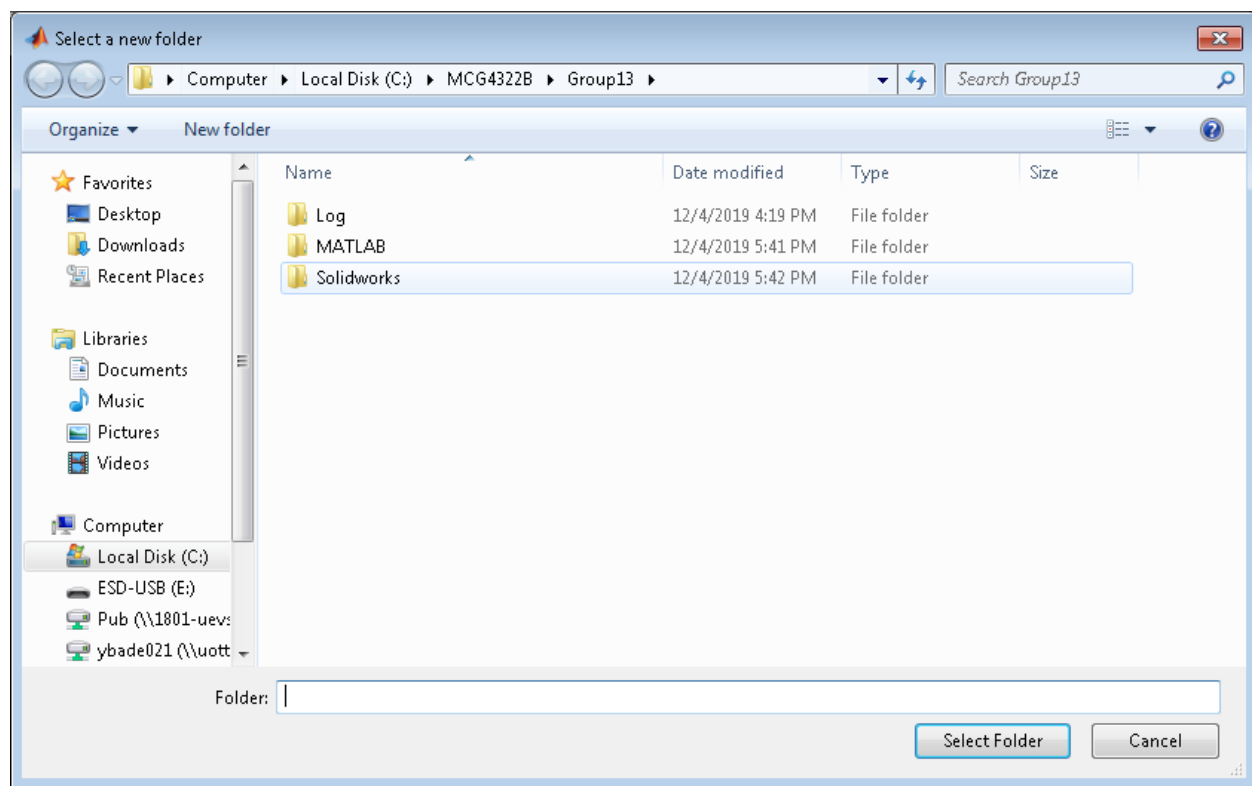
Code Setup

Before using the GUI, some preparations must be completed to ensure MATLAB properly recognizes the file path and can safely start the application. The following steps will explain how to prepare the project folders for use.

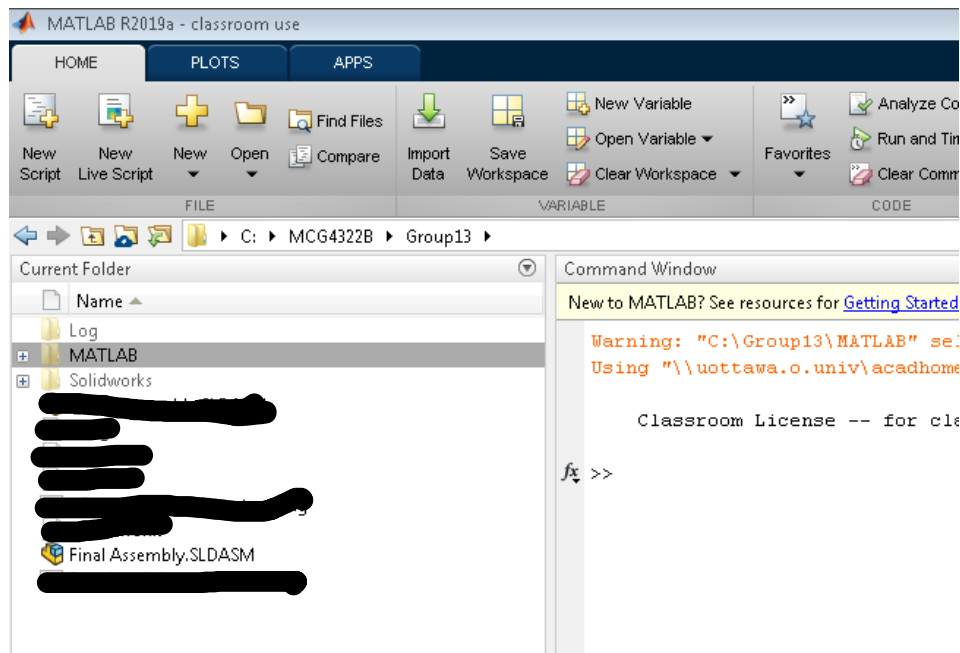
1. Ensure the main folder. are placed under the correct directory. The “Group13” folder should be in the “C:\MCG4322B\” directory.
2. Start MATLAB 2019a.
3. Click the “Browse for Folder” button, shown in the figure below.



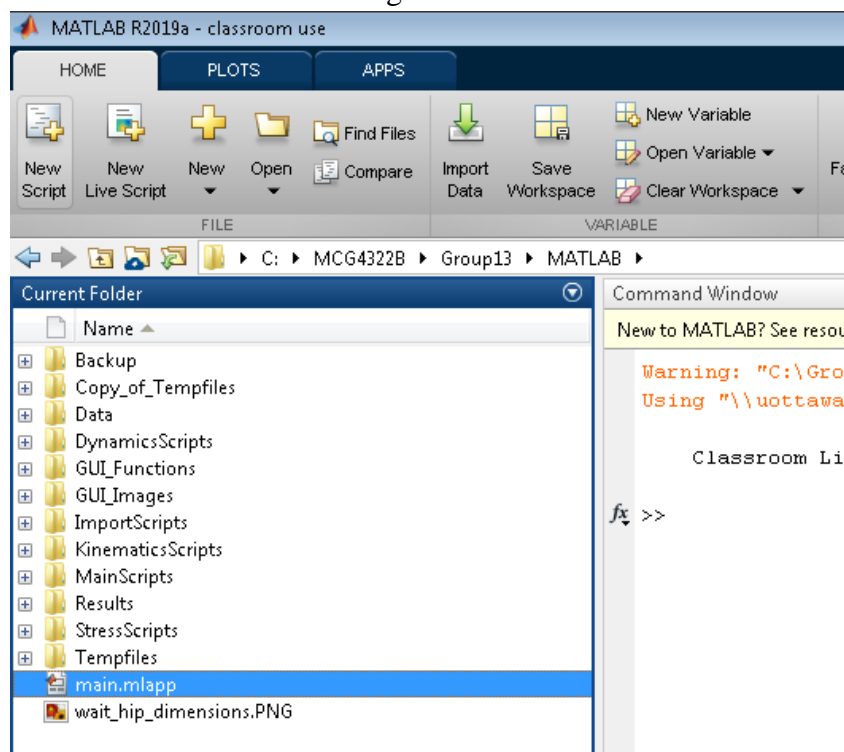
4. Navigate to the “Group13” folder found in the “MCG4322B” folder in the C drive.
5. Enter the “Group13” folder. Your screen should now look like the following screen shot



6. At this screen, click select folder.
7. Your left side folder navigator should now look like the following image



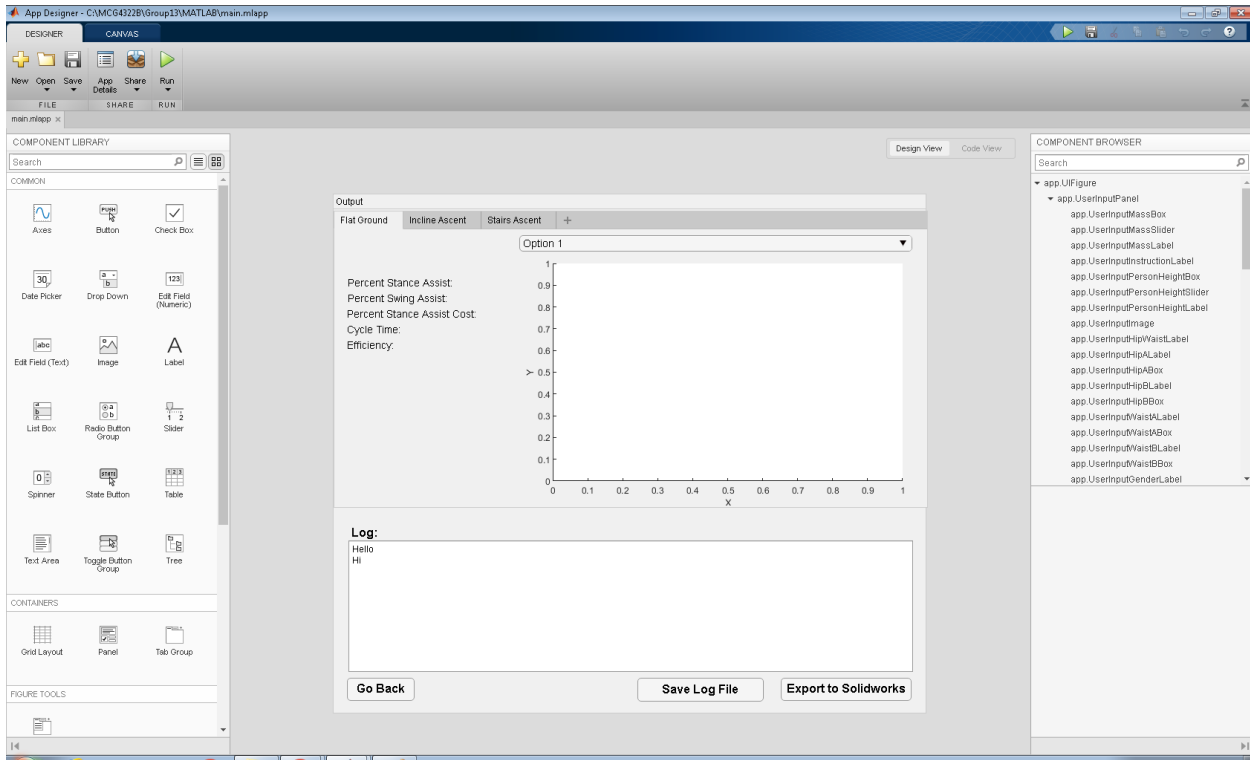
8. Right click the “MATLAB” folder in the left side of the MATLAB program, hover over the option “Add to Path”, click “Selected Folders and Subfolders”.
9. Double click the MATLAB folder to enter the project code. Your “Current Folder” view in MATLAB should look like the image below.



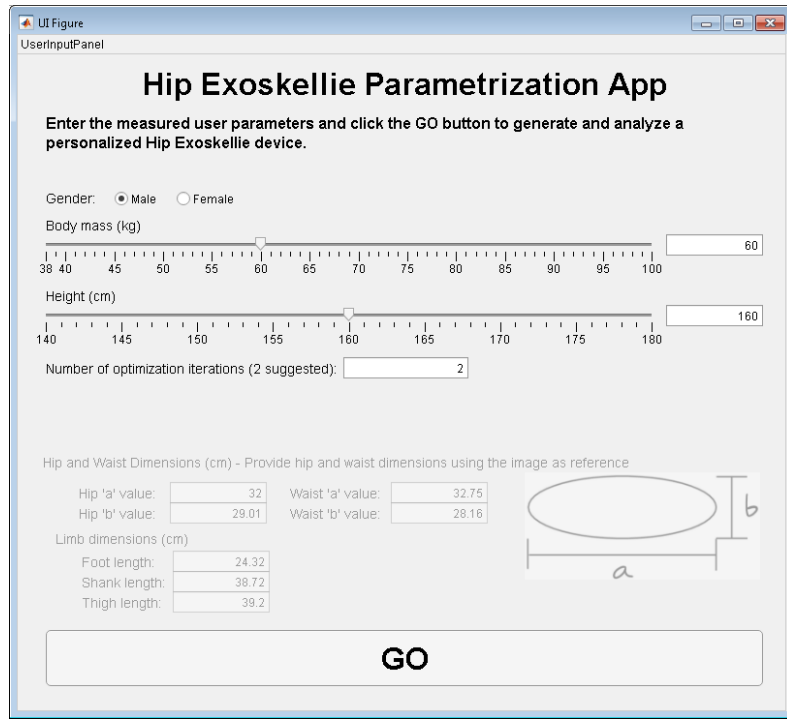
Running the GUI

After completing the code setup, the code should now be ready to run. The following instructions will instruct you on how to operate the GUI:

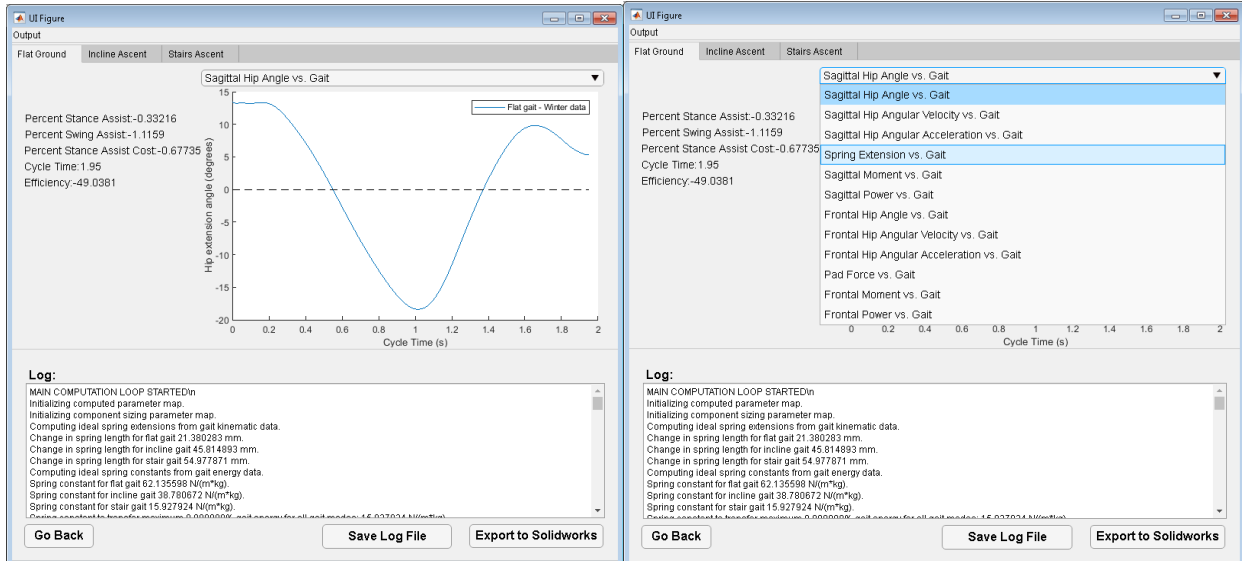
1. Double click the “main.mlapp” file in the “Current Folder” view of the MATLAB program. This will open the App Designer window as shown below.



2. Click the “Run” button at the top left of the App Designer window. Note: it may take a few seconds to appear/become clickable after starting the App Designer window. Once it is ready to run, the button will become clickable.
3. Wait a few seconds for the GUI to pop-up and load. After loading, it should look like the image below.

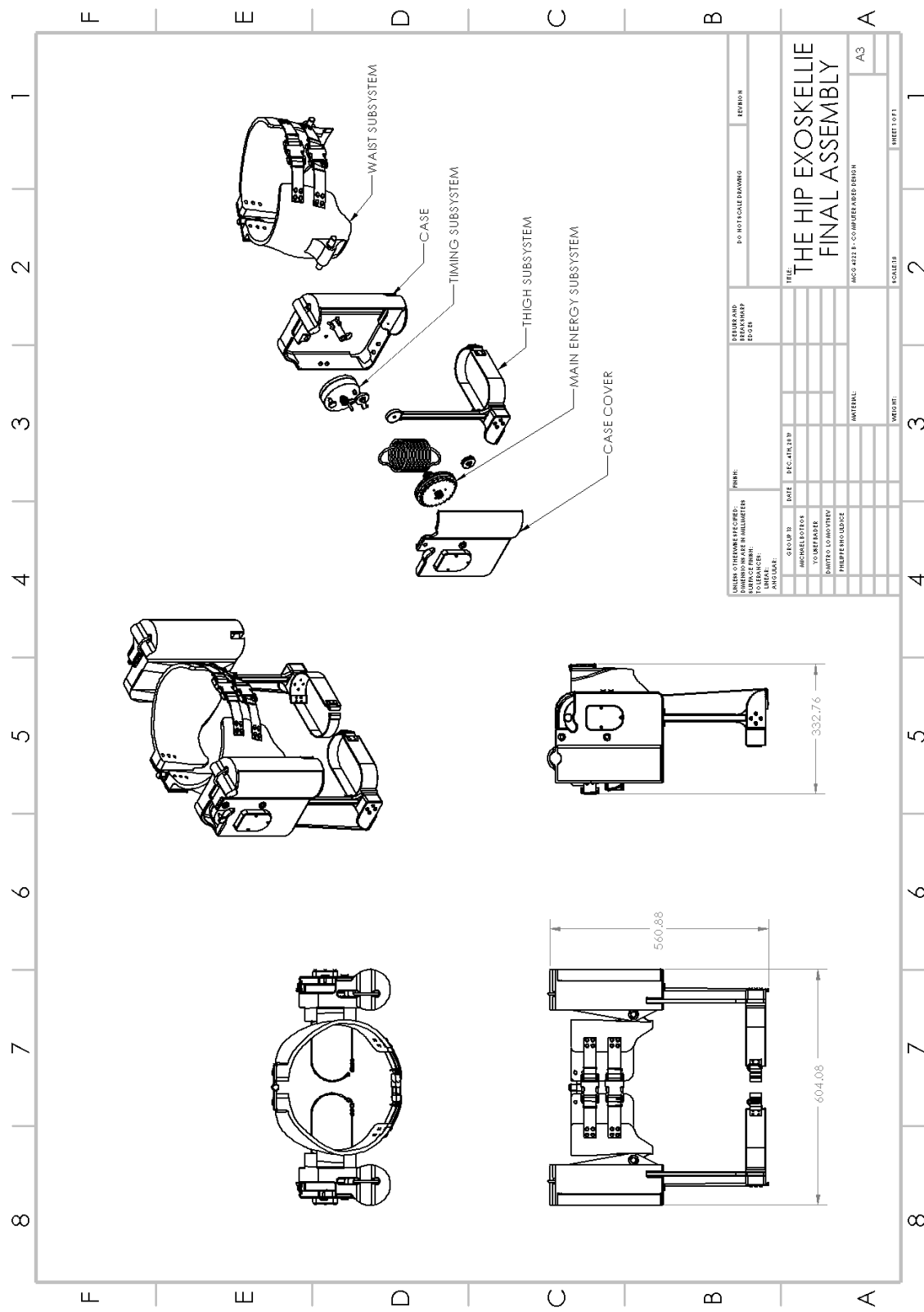


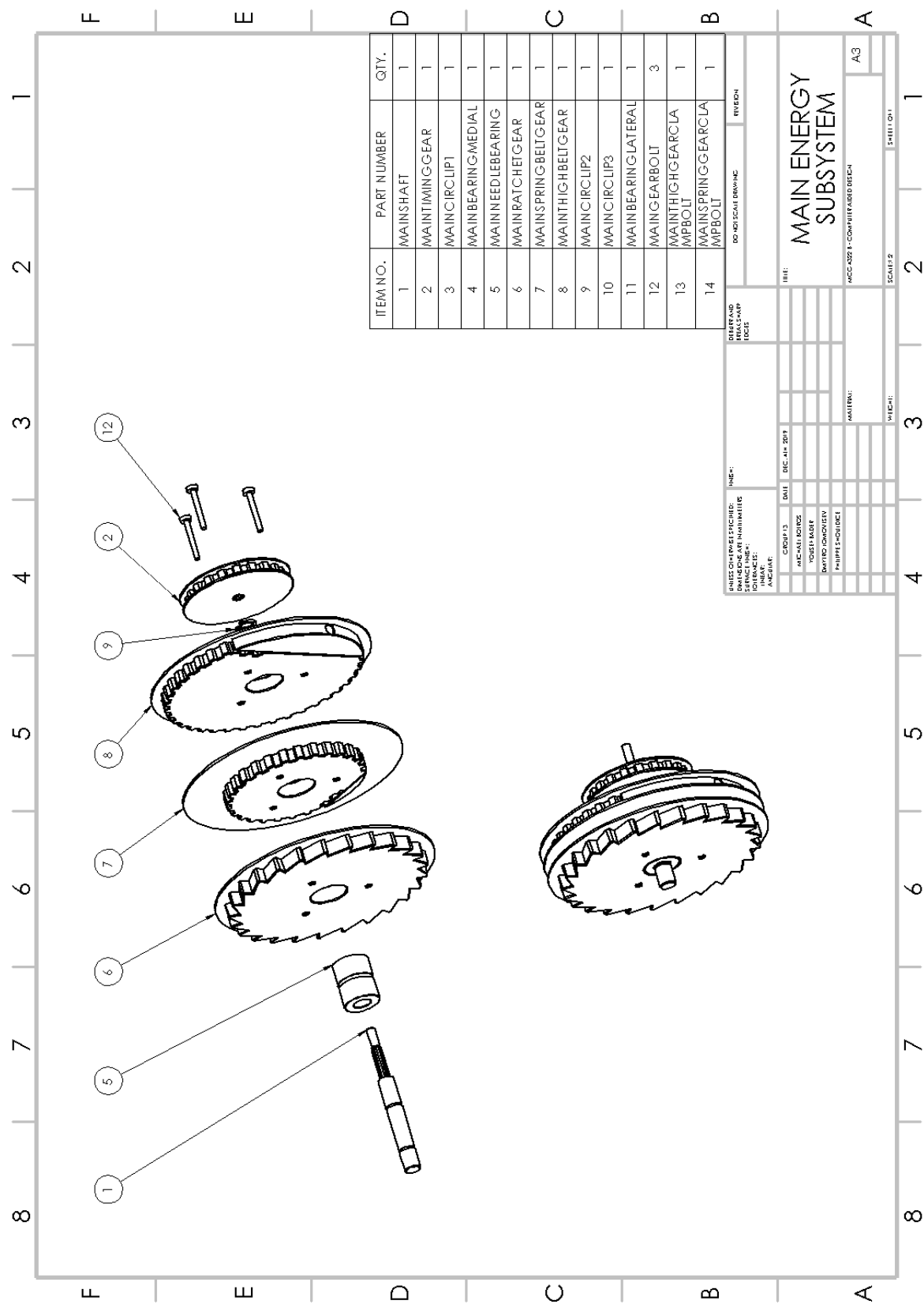
4. Using the sliders or text boxes, enter your desired parameters for body mass and height. Select the desired gender to parametrize for. Select the number of optimization loops to generate data for. Note: it is highly recommended to only use 1 or 2 optimization loops. Testing showed that each loop took around 1.5 - 2 minutes to run on the slow laboratory computers. A loading bar will appear to display current simulation progress.
5. Once computations are completed, the loading bar will disappear, and the results screen will be displayed as shown below in the left image. You can flip between results for different gait modes using the tabs at the top left of the GUI. You can select different graphs to display using the drop-down menu above the graph as shown in the right side image below.

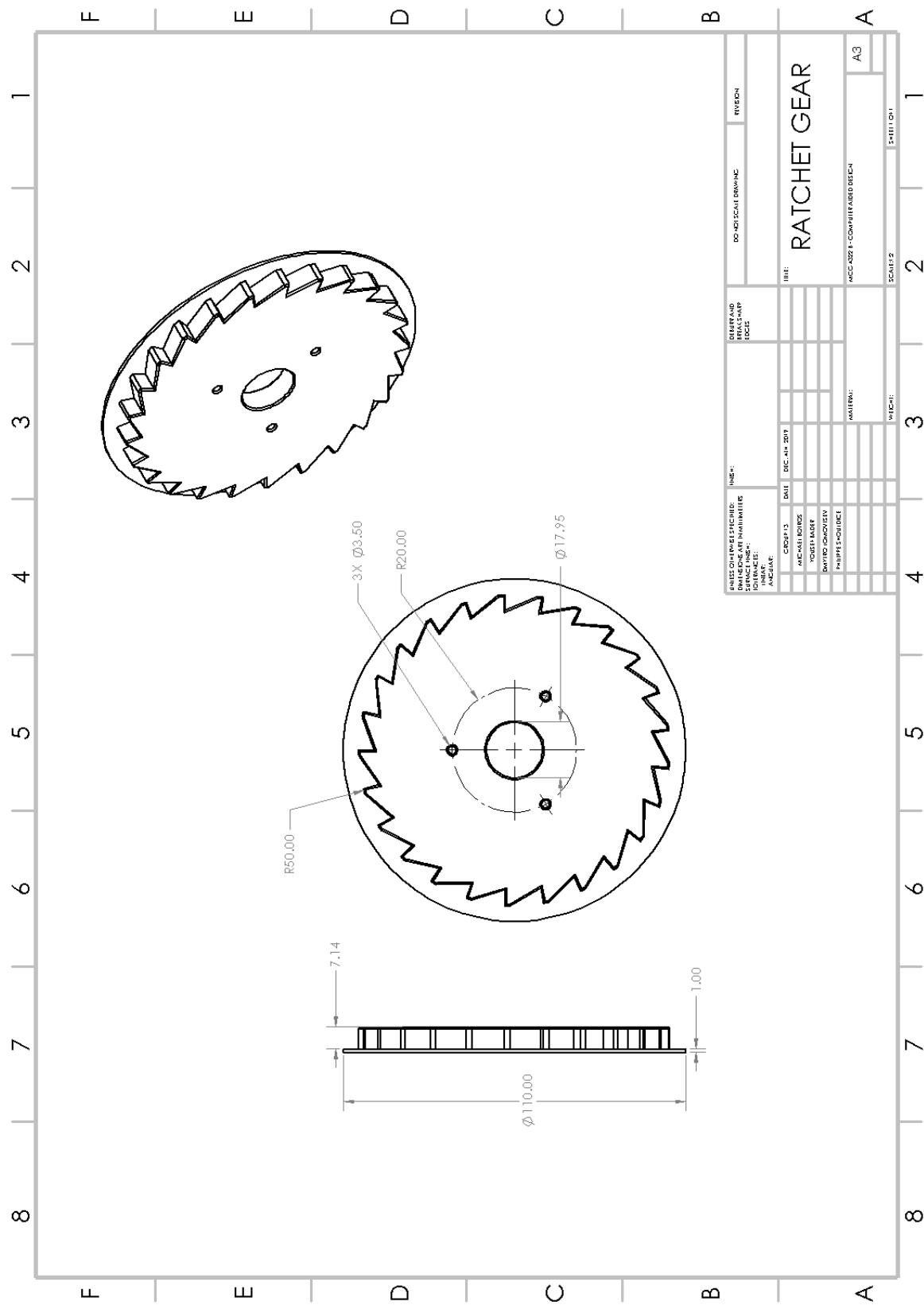


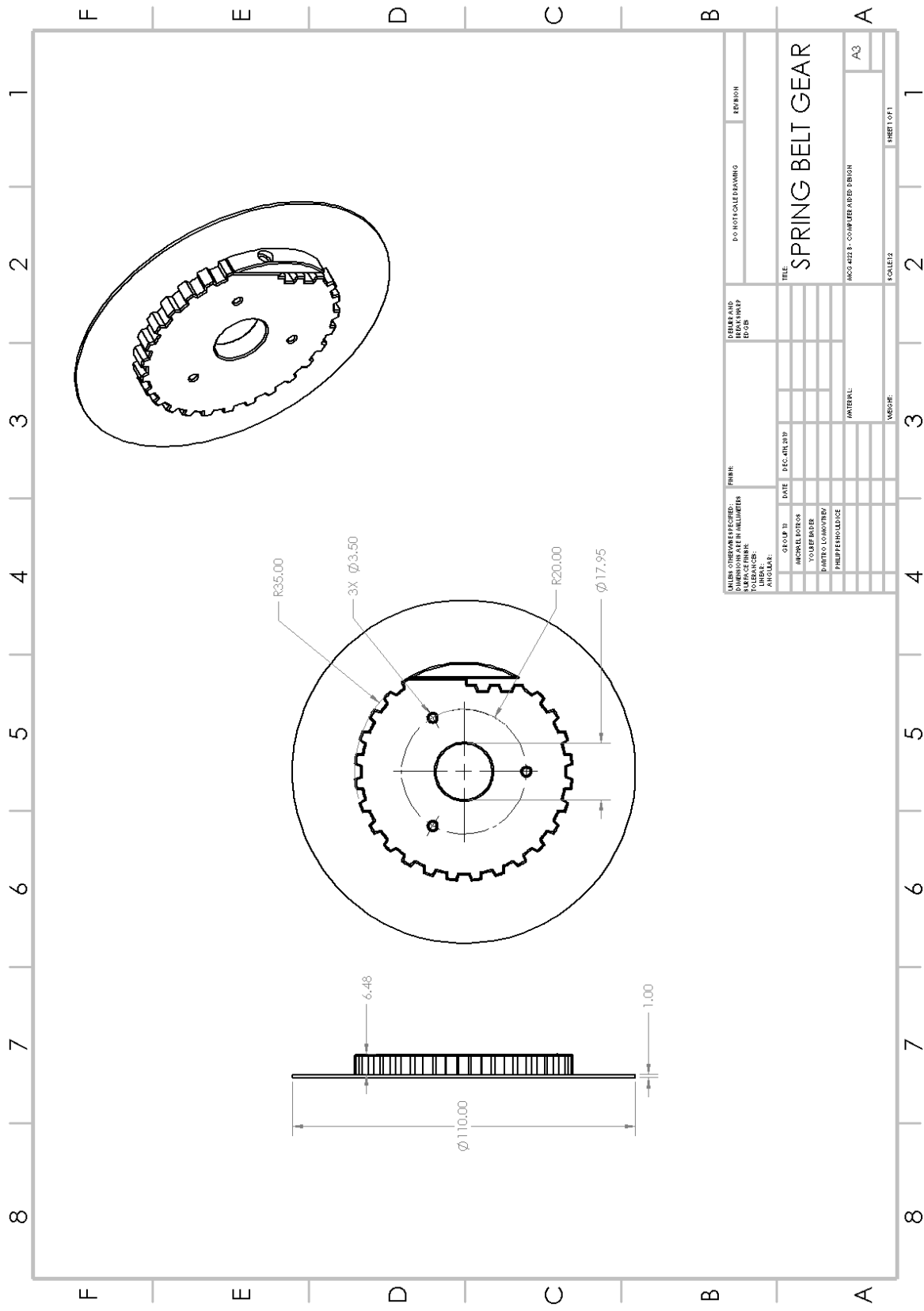
- To export the generated log file, click “Save Log File” button and select a directory and name to save the file.
- To export the equation files to Solidworks, click the “Export to Solidworks” button.
Note: exporting to Solidworks will overwrite existing equation files. If you wish to keep the existing set of equation files, save them to a different location before clicking the “Export to Solidworks” button.
- To return to the parameter selection screen, click the “Go Back” button. Returning to the parameter input screen will delete all calculated dimensions and data. To access the same results again, the simulation must be re-run.
- Open the Solidworks assembly found in the main project folder to view the design. To implement the new component parameters, the assembly must be rebuilt twice due to complex relationships required to form the waist component.

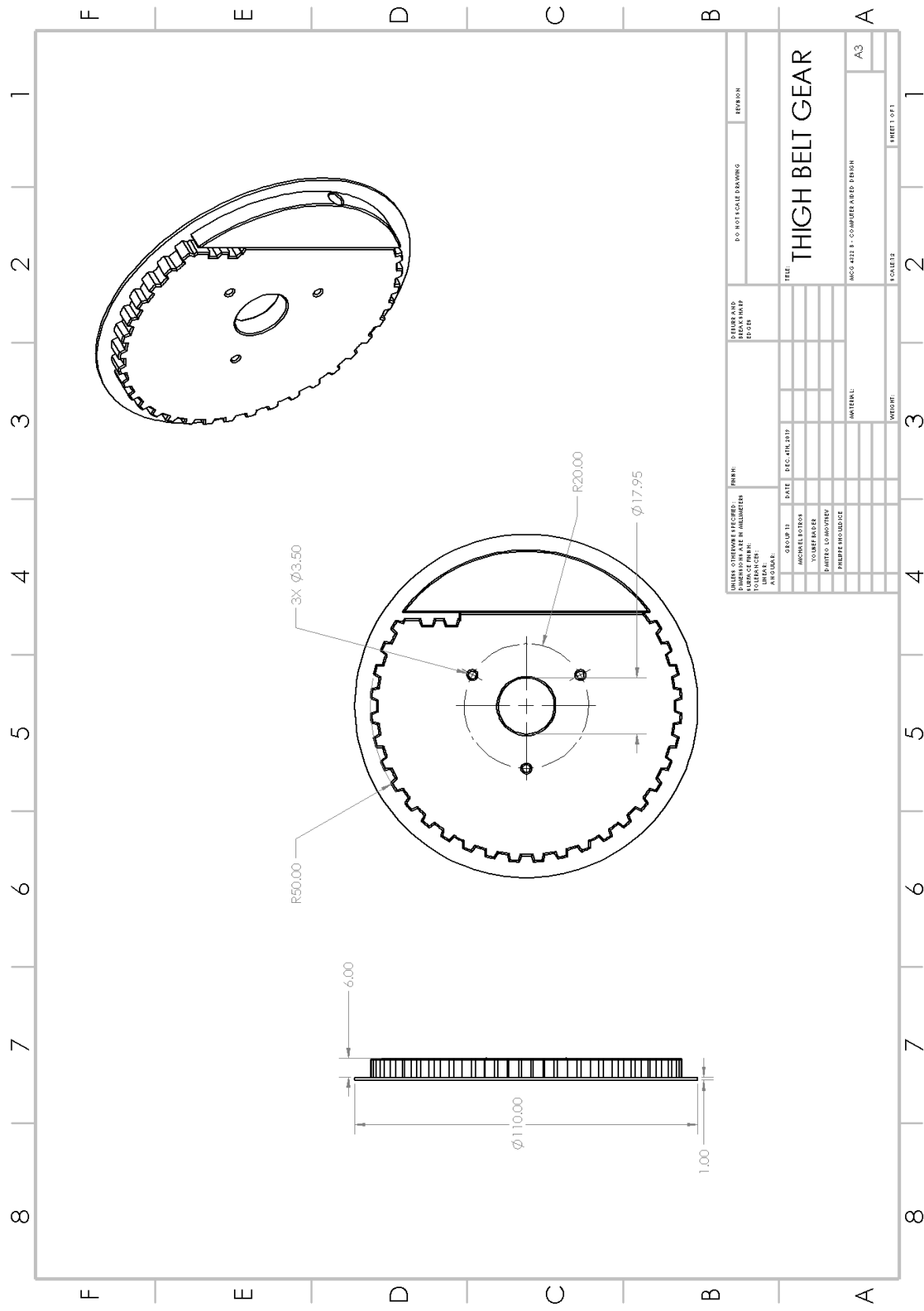
Appendix B Drawings

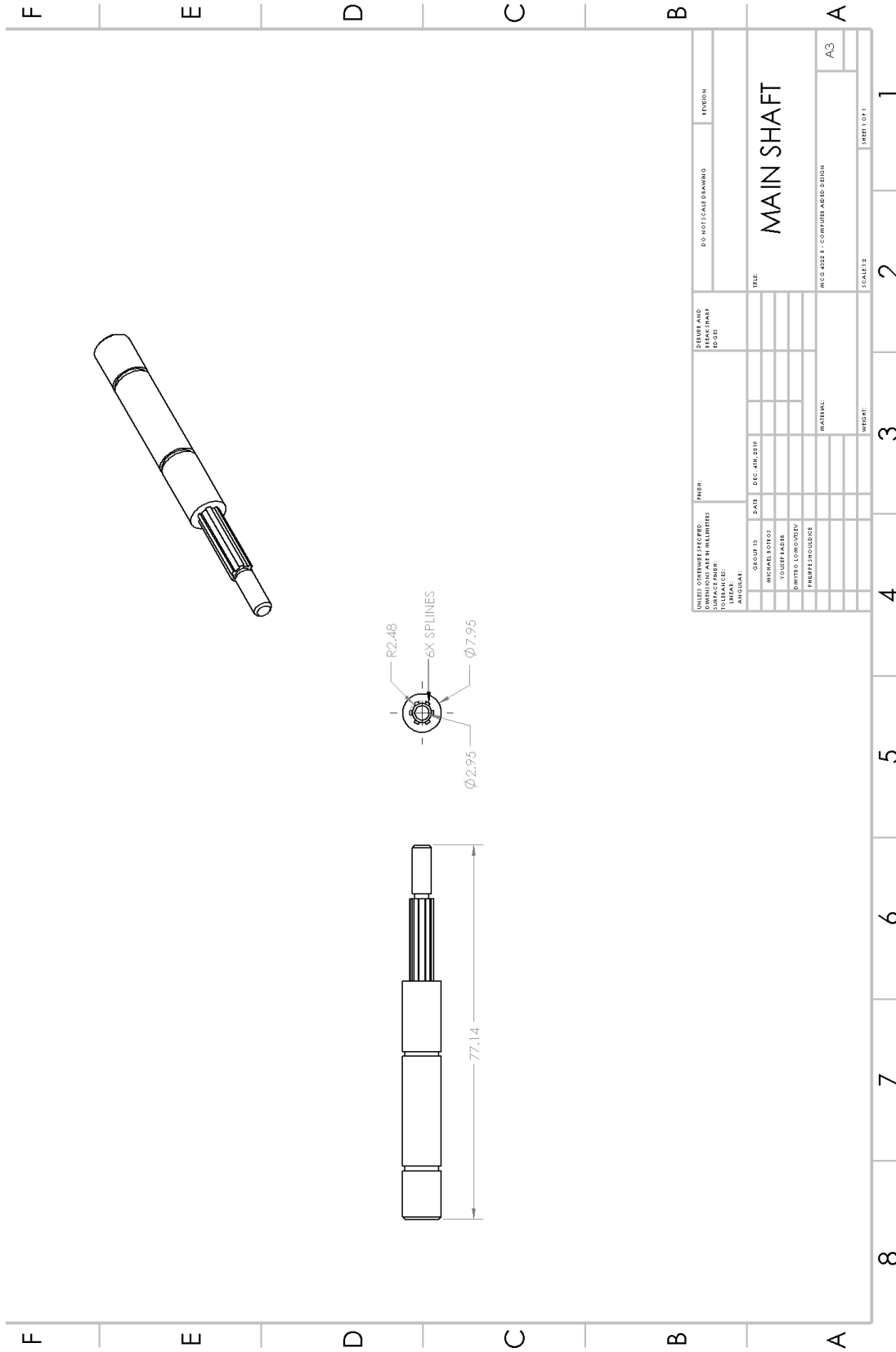


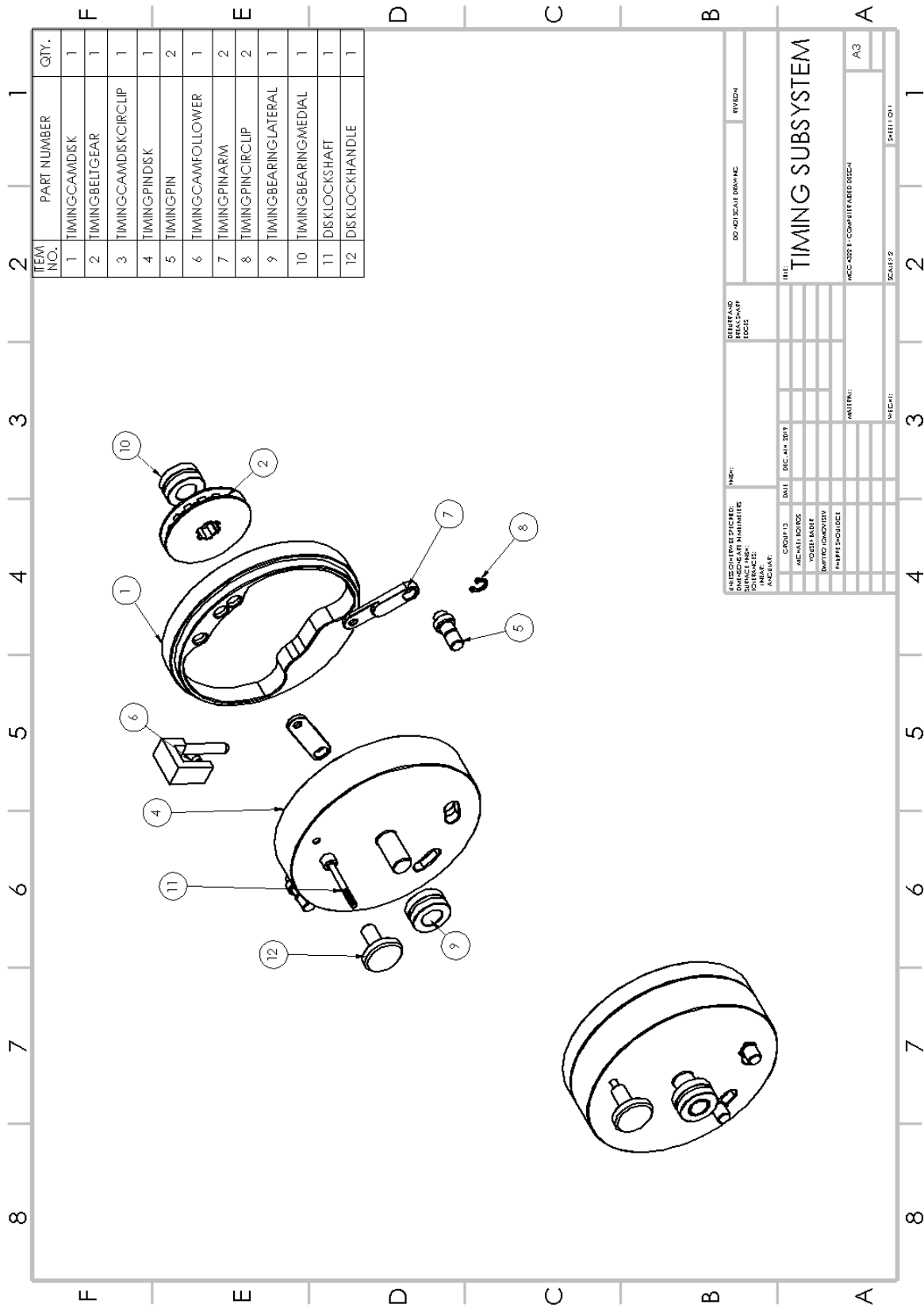


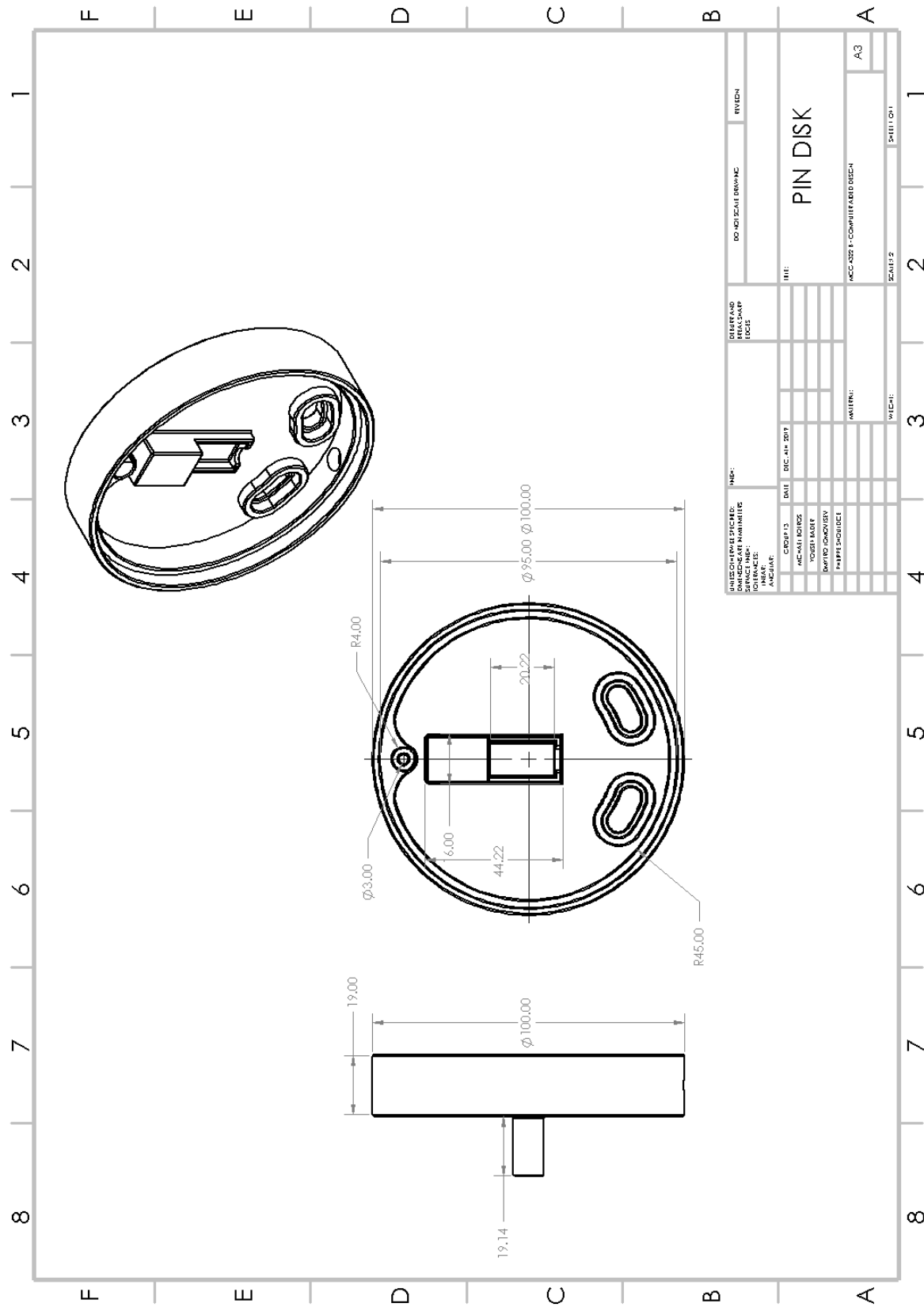


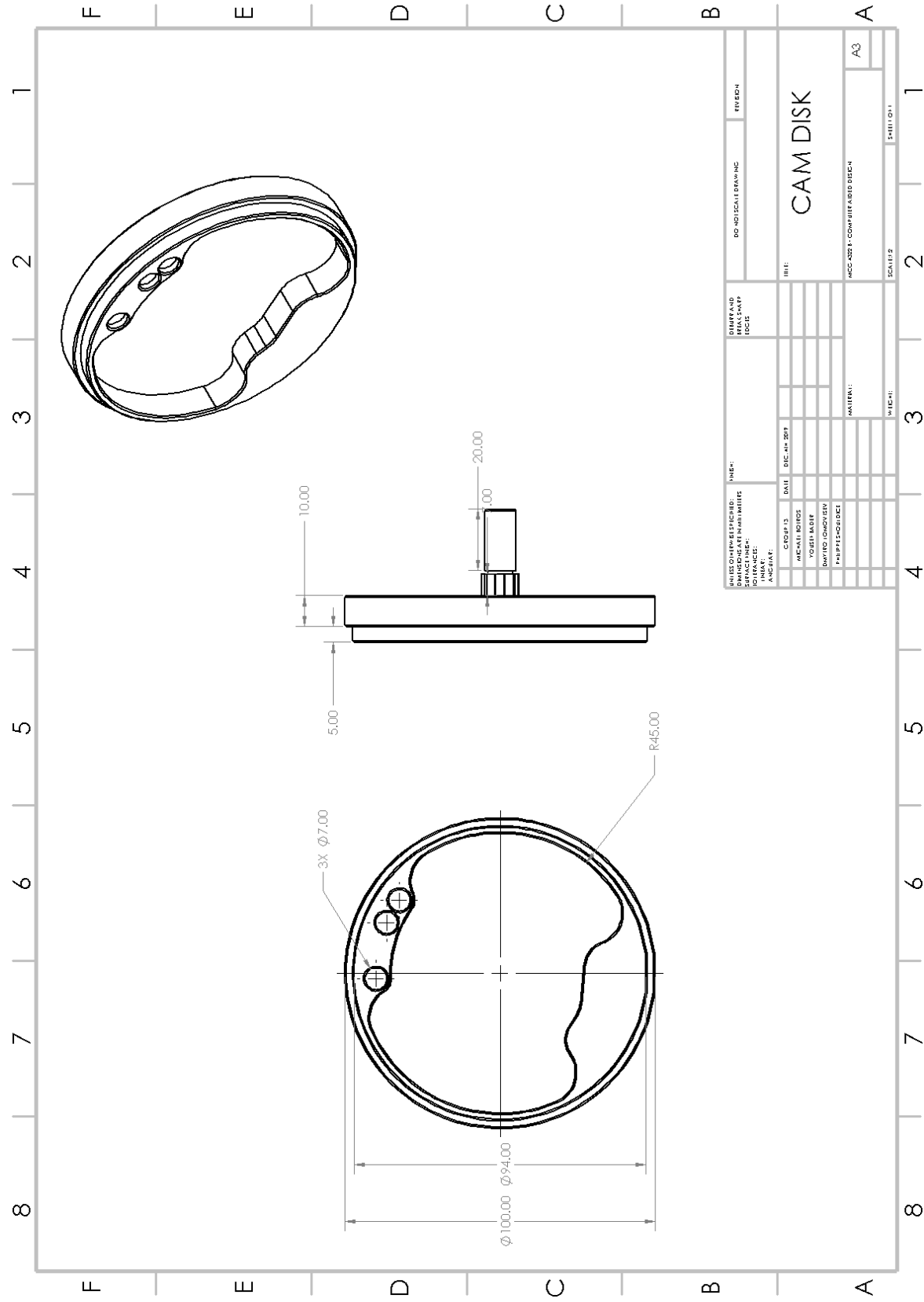


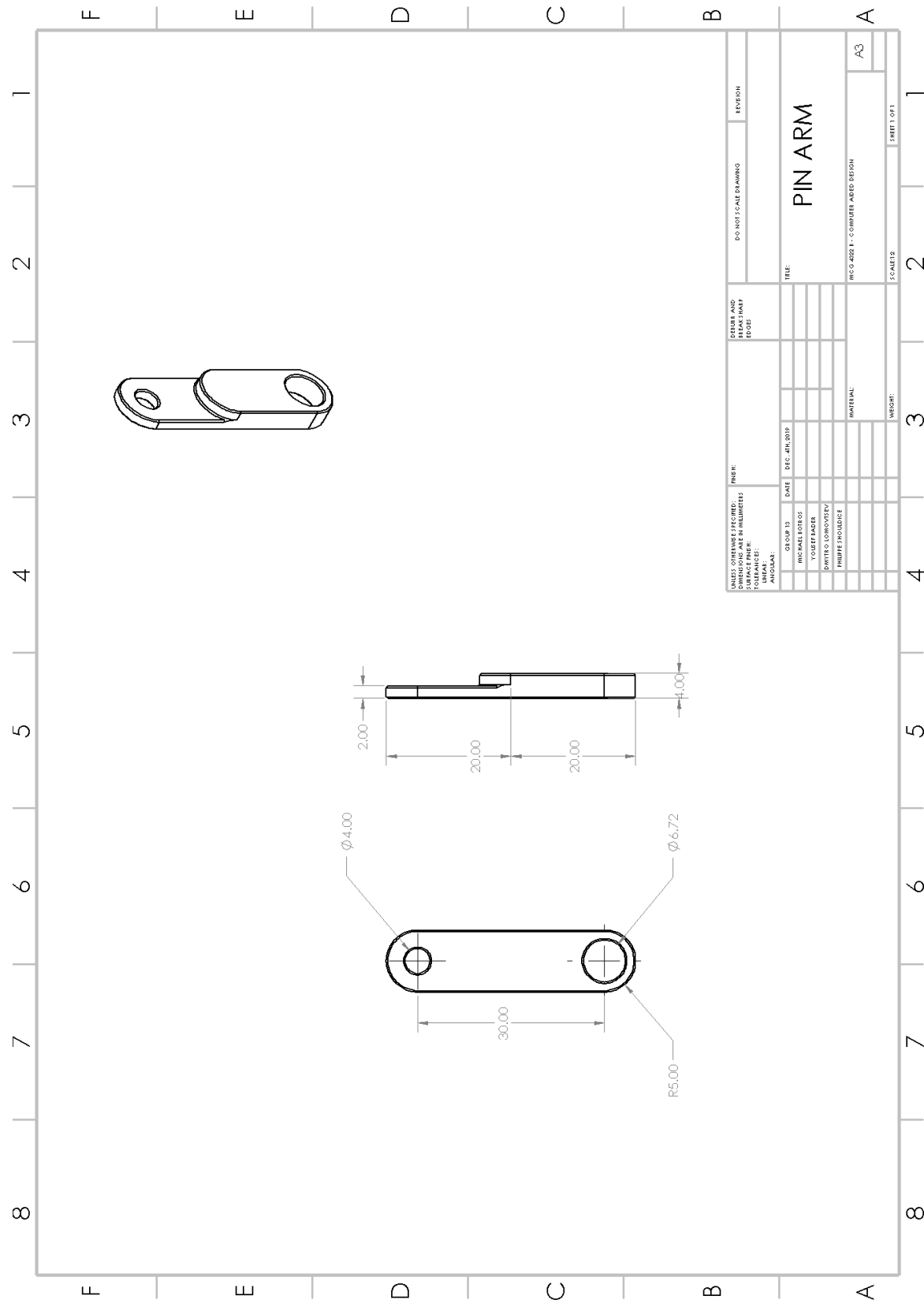


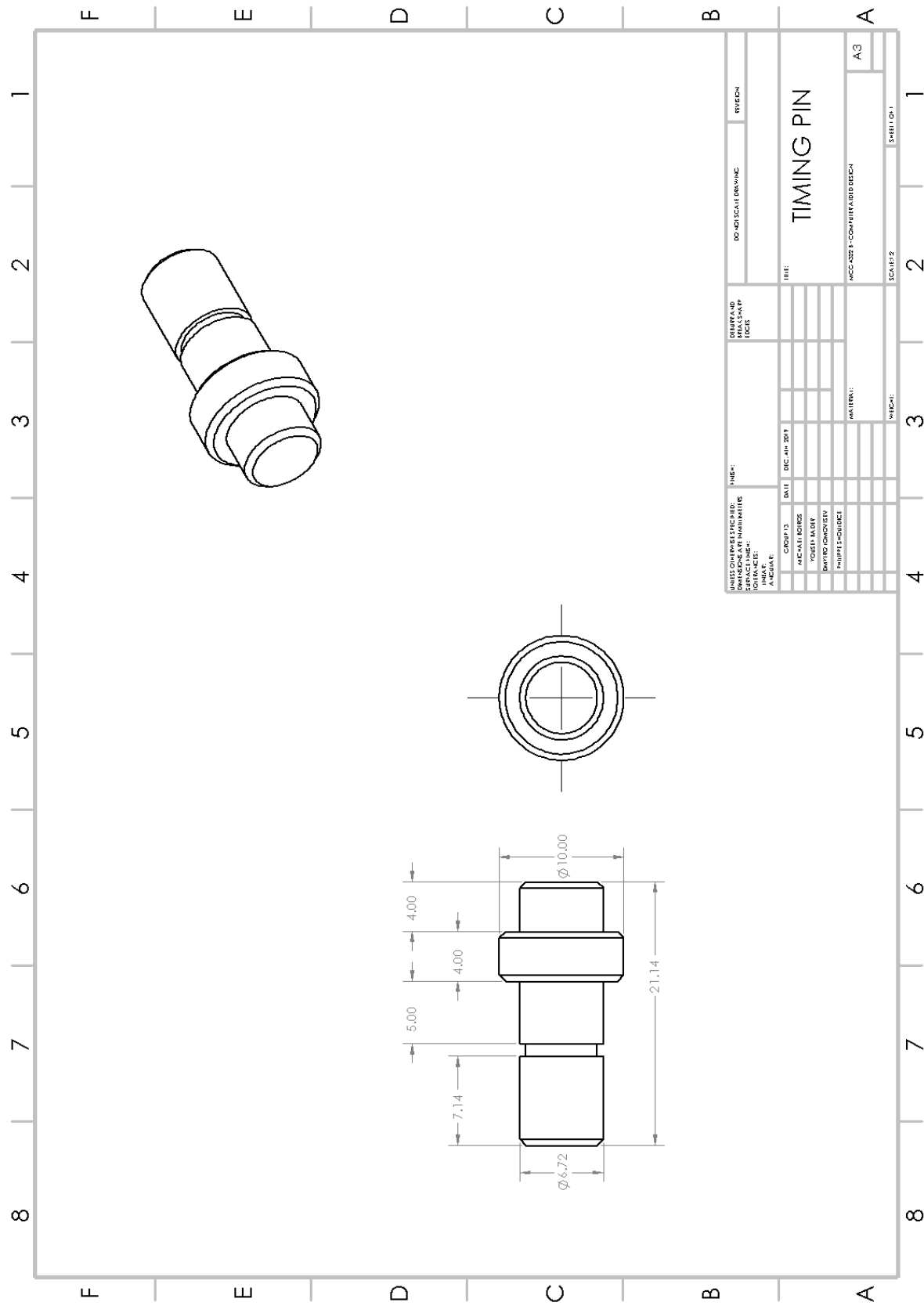


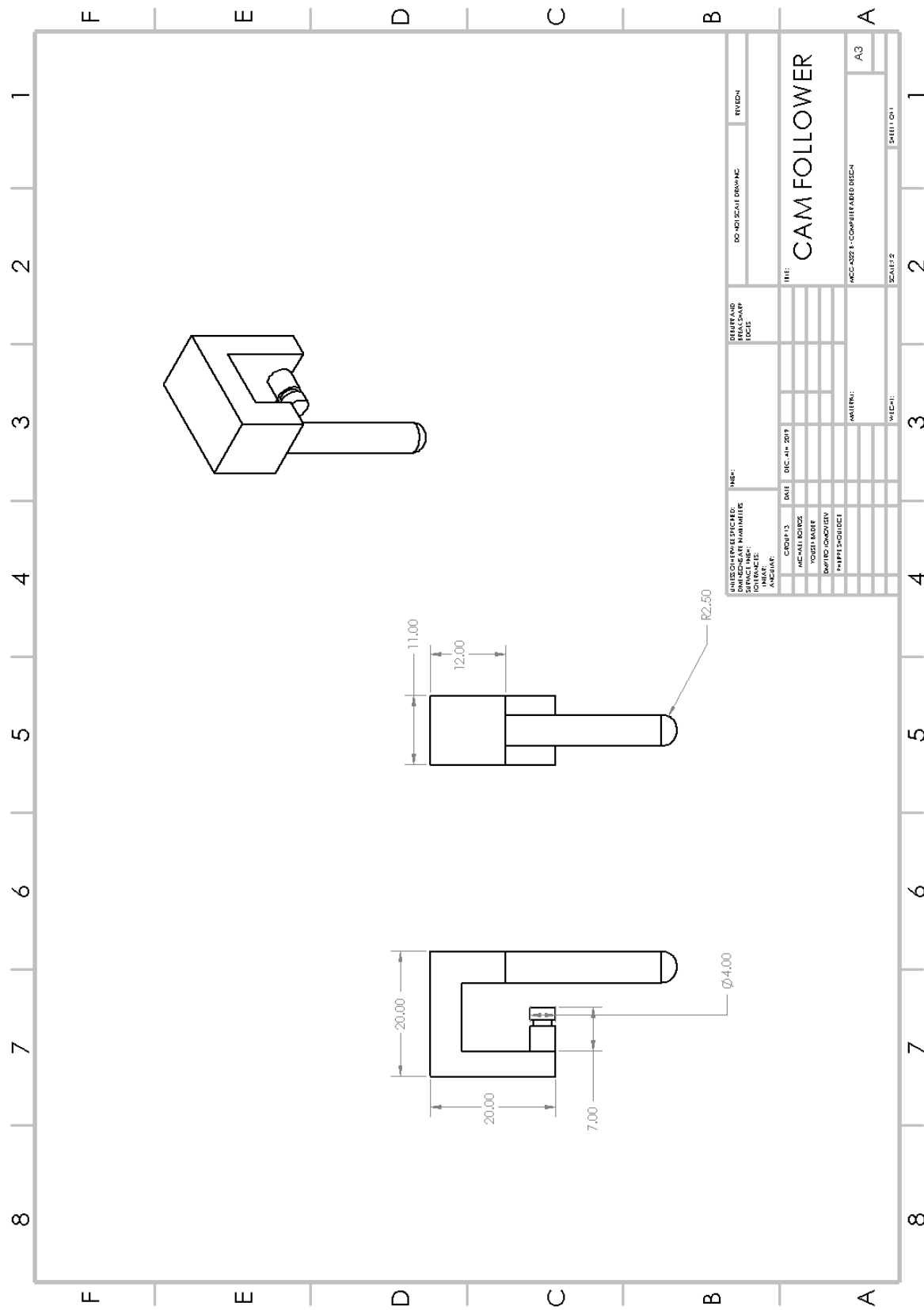


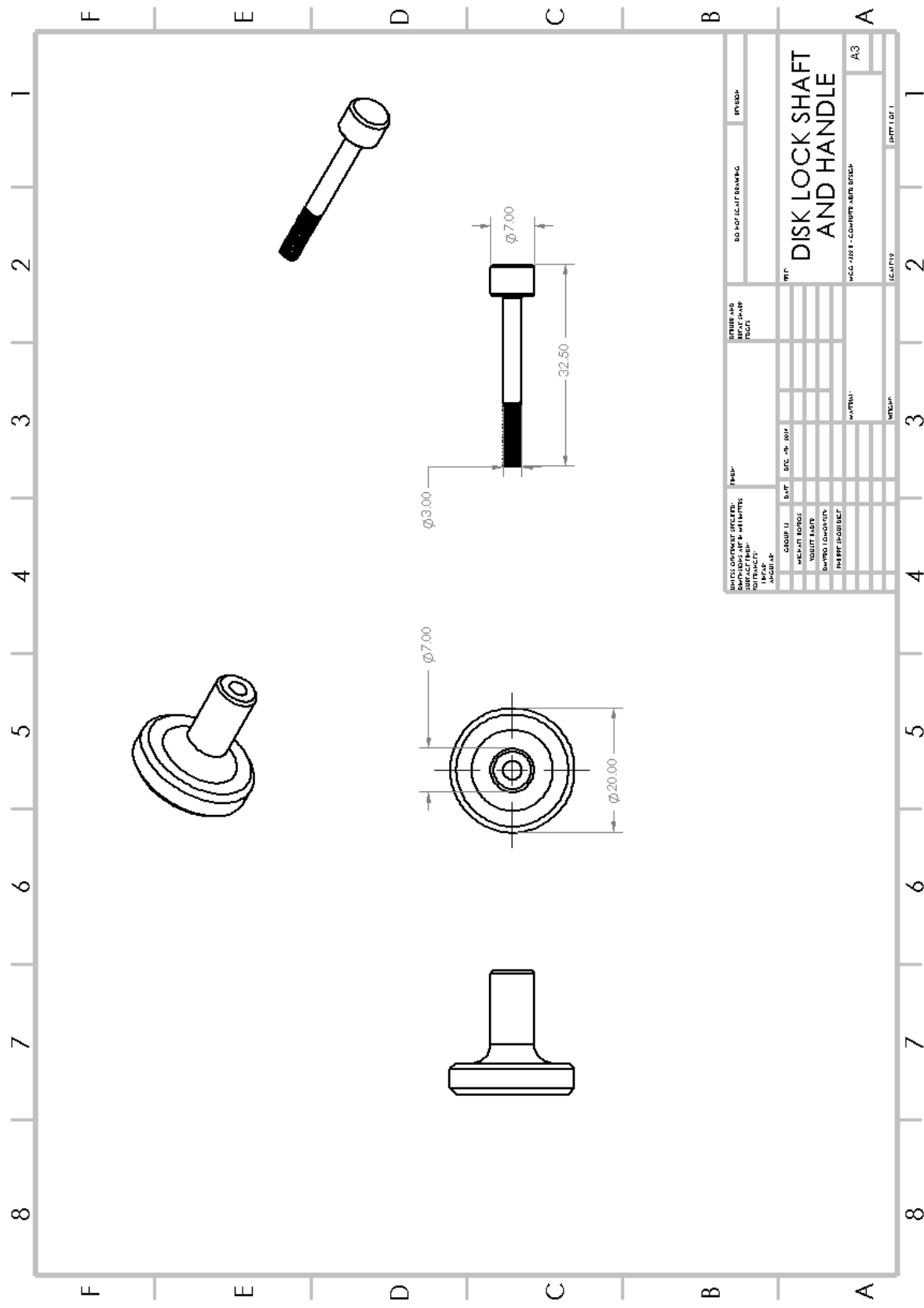


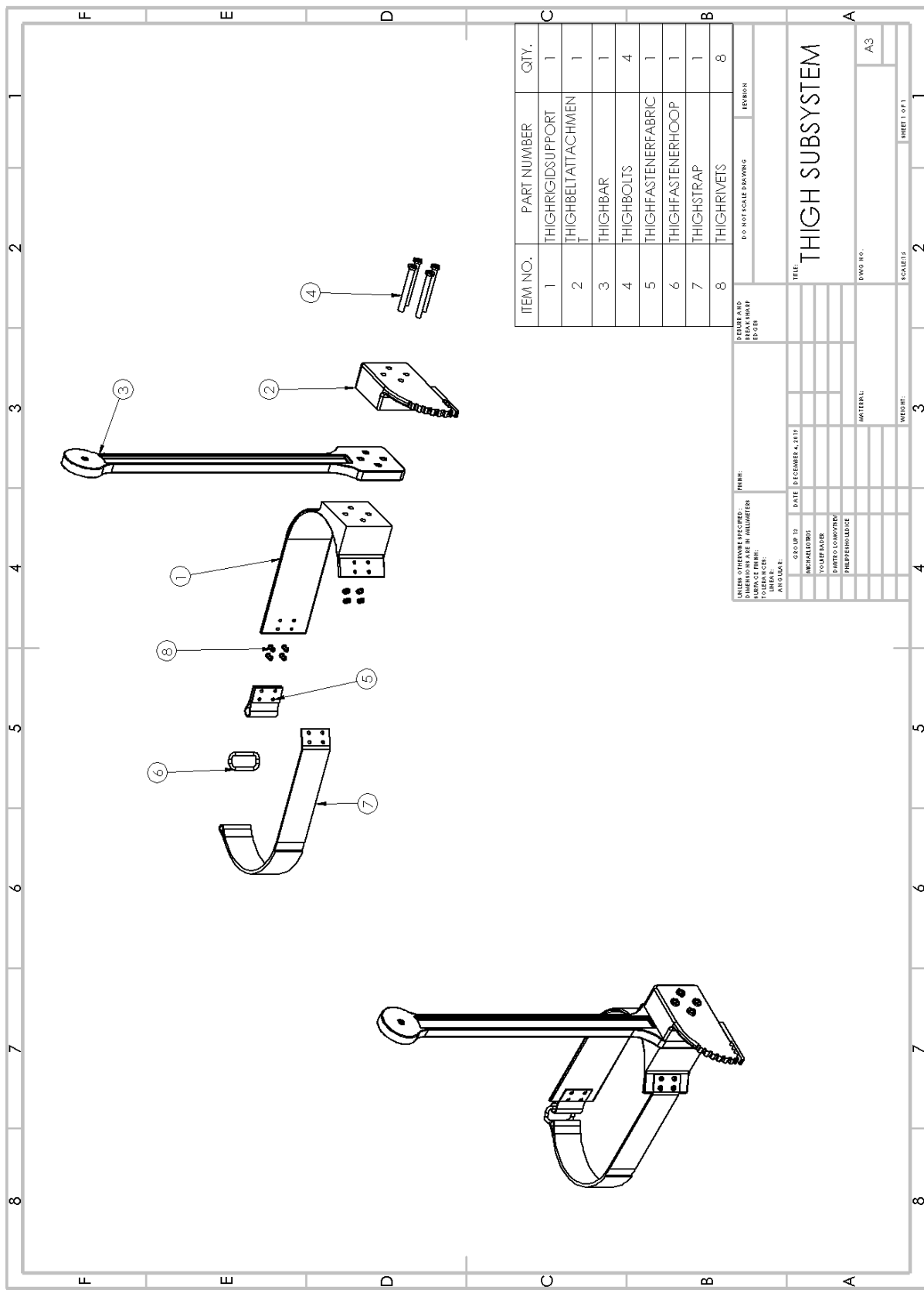


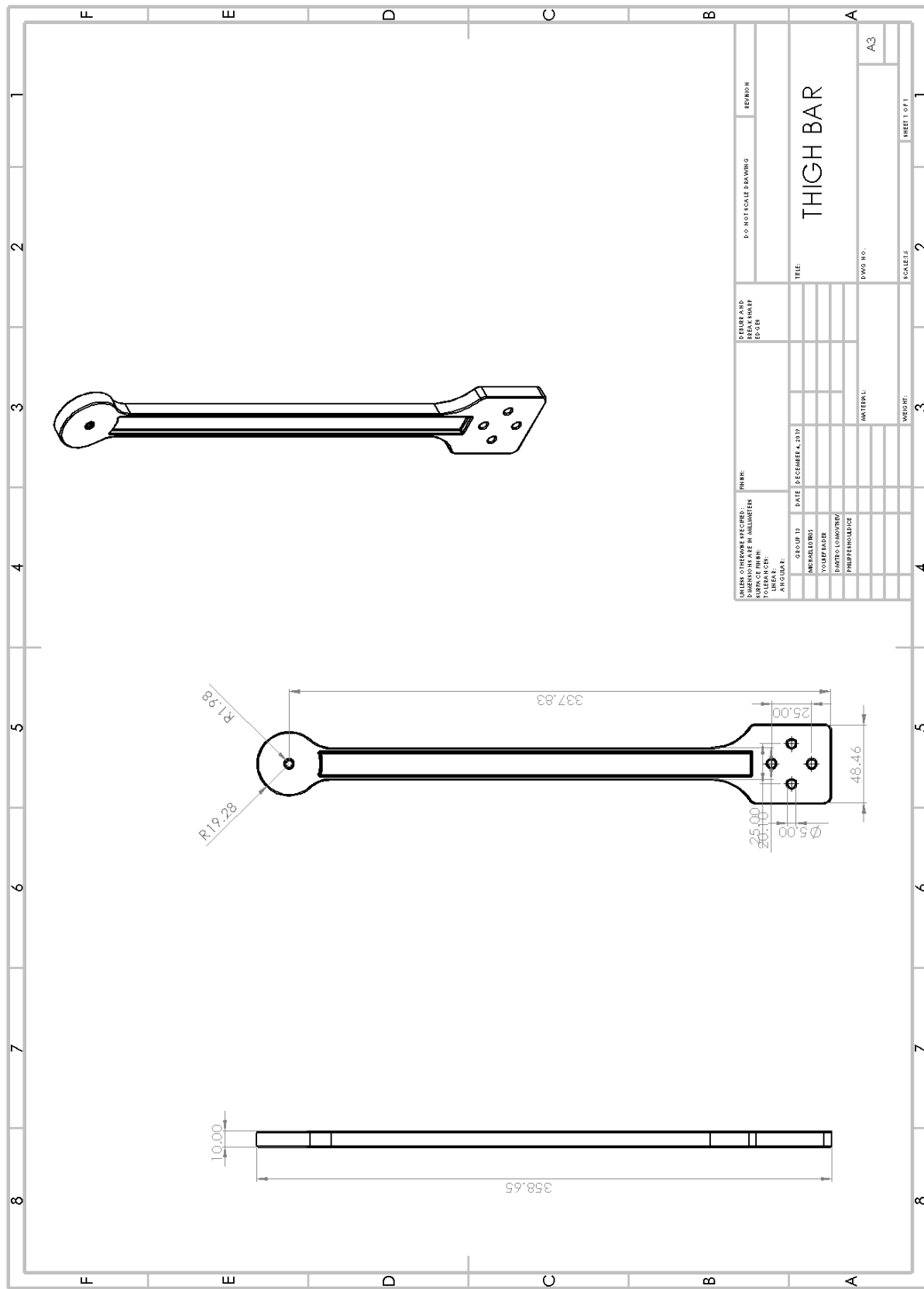


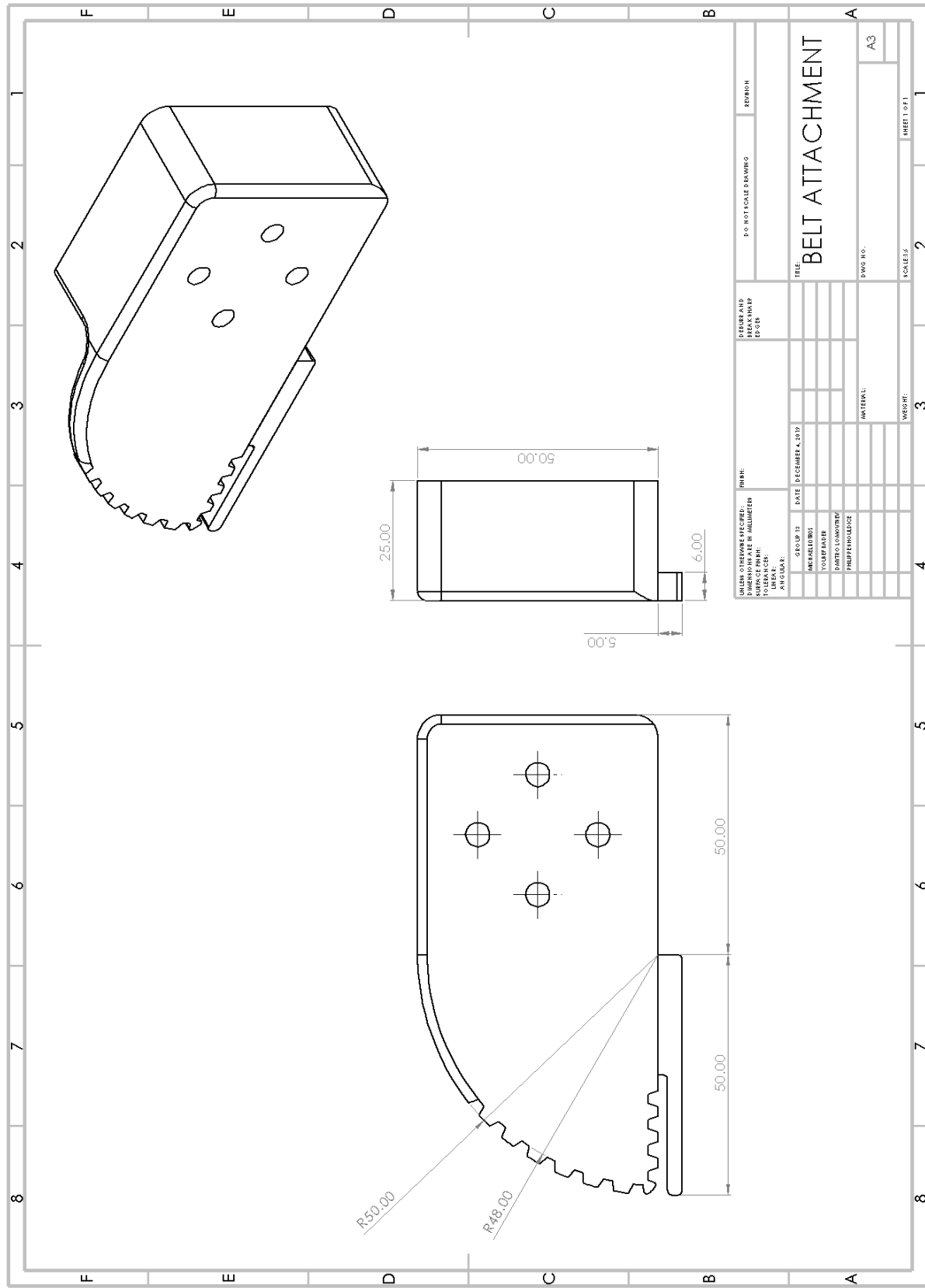


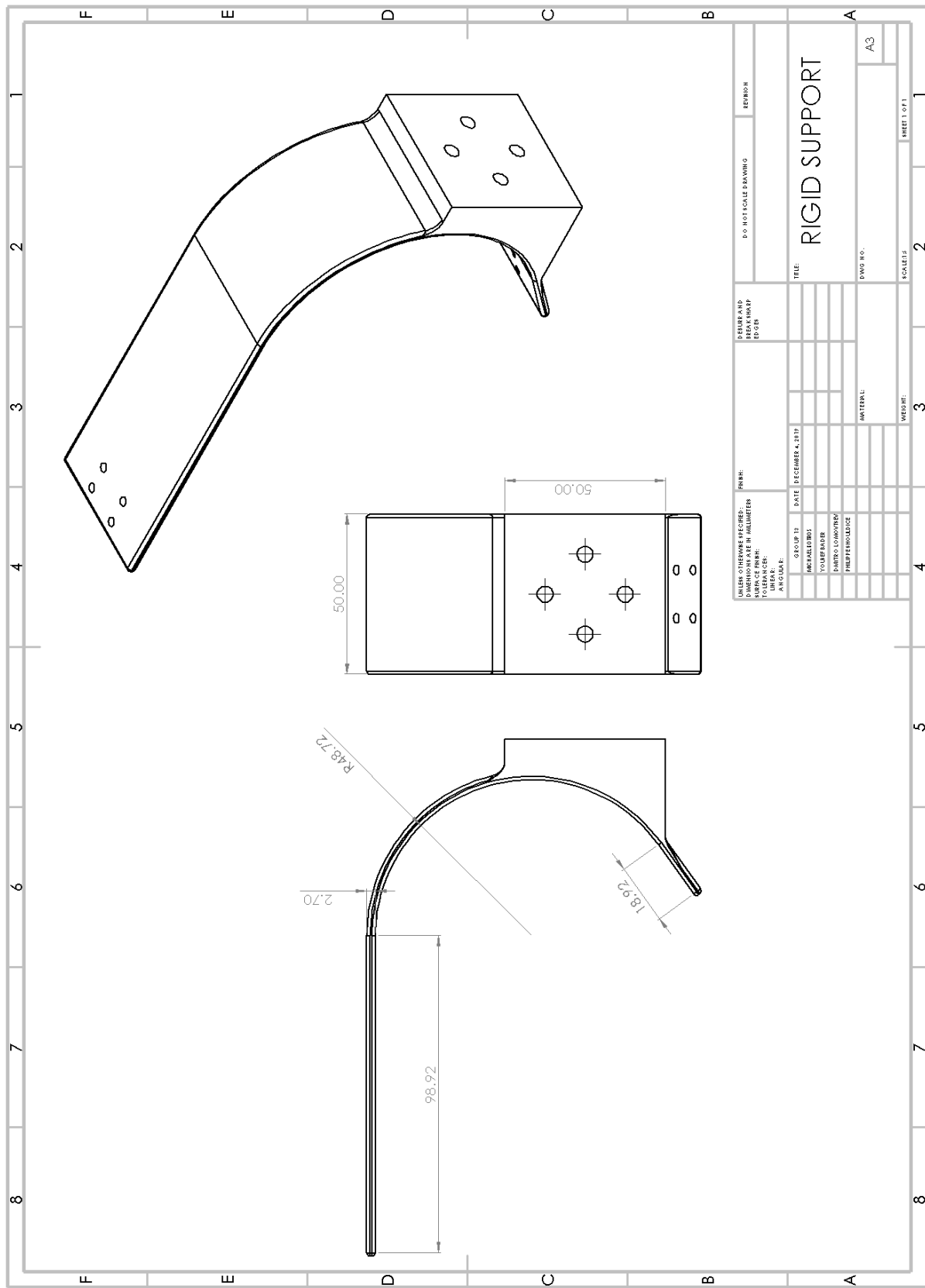


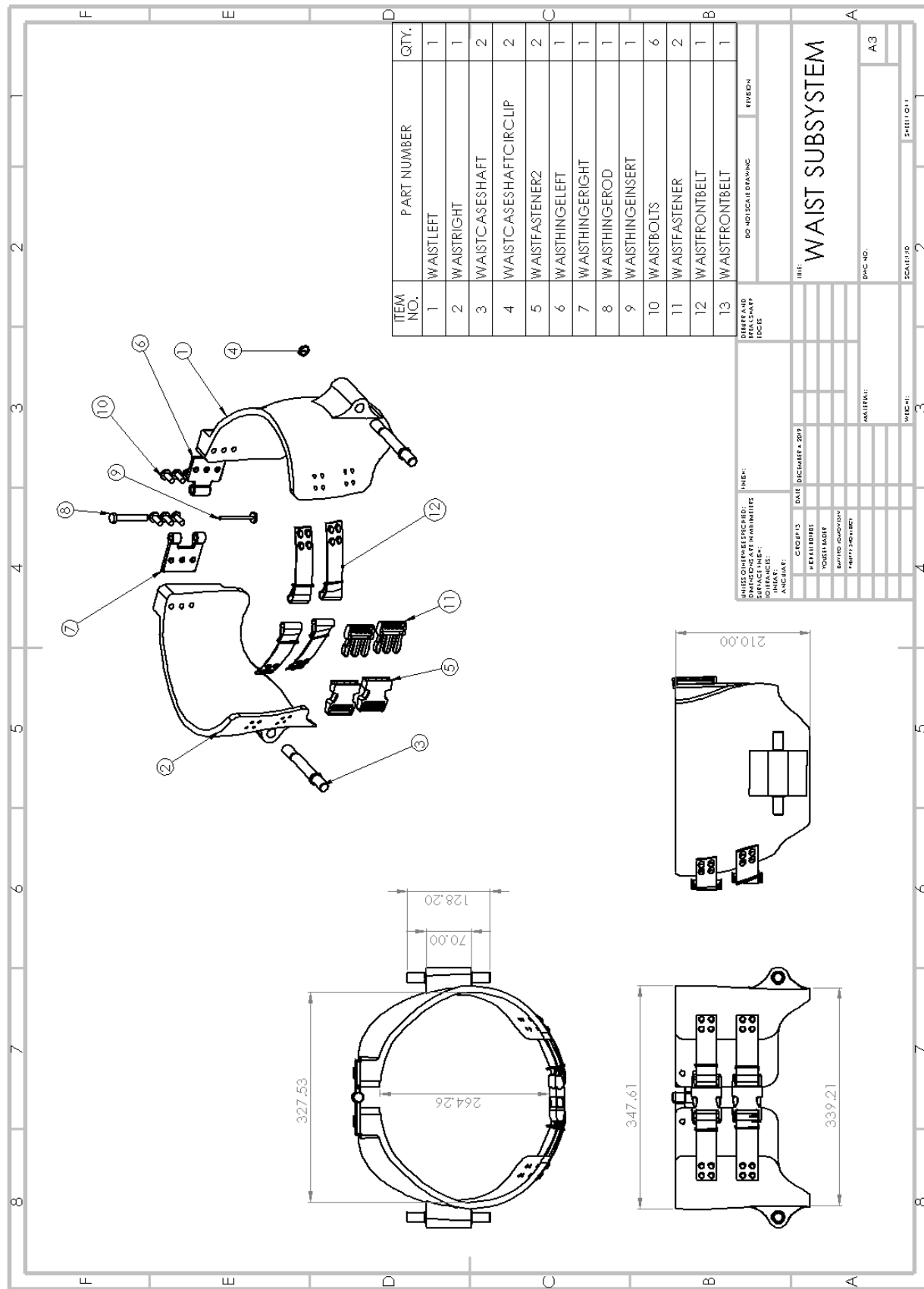












Appendix C Methodology

For this literature review, the following scientific databases were used: Google Scholar, Scopus, PubMed and uOttawa Morisset Library's Search+. In addition, product websites were visited to obtain information for commercially available exoskeletons.

For the sake of brevity, only the main keywords that were used are mentioned. These are the main keywords typed in search engines (e.g. Google) and the aforementioned databases:

Table 13 Keywords used in the different sections of the literature review

Section	Keywords/Sources
Introduction and Motivation	<ul style="list-style-type: none">Common sites providing population data, including Statistics Canada, Canadian Institute of Health Information population, problem incidence and prevalence reports.(older adult) OR (elderly) OR (senior)
Exoskeletal Systems	<ul style="list-style-type: none">exoskeleton AND versus AND orthosispassive AND hip AND exoskeletonfrontal AND plane AND gait AND stability AND elderlypassive AND hip AND exoskeleton AND (coronal OR frontal) AND planehip AND exoskeleton AND transverse AND planequasi-passive AND hip AND exoskeleton
Stability	<ul style="list-style-type: none">(falls) AND (balance) AND (hip)(human) AND (gait) AND (stability) AND (quantification OR models)
Functional Anatomy	<ul style="list-style-type: none">((aging) OR (older adult) OR (elderly) OR (senior)) AND (anatomy OR physiology)(gait disorders)(hip joint) AND (stability) AND (muscles)(hip) AND ((range of motion) OR (flexibility)) AND (reference values)
Anthropometry	<ul style="list-style-type: none">(height OR weight OR waist circumference OR hip circumference) AND ((older adult) OR (elderly) OR (senior))(anthropometry OR ergonomics) AND ((body segments) OR (body action)) AND (quantification OR models)(anthropometric changes)
Gait data	<ul style="list-style-type: none">gait elderly

	<ul style="list-style-type: none"> ● stair climbing hip kinematics elderly ● gait elderly incline
General modifier terms/	<p>Terms narrowed down for elderly population by adding</p> <ul style="list-style-type: none"> ● AND ((older adult) OR (elderly) OR (senior)) <p>Terms adjusted by gender by adding</p> <ul style="list-style-type: none"> ● AND (gender OR sex) <p>Textbook references from Anatomy/Physiology, Medicine and Nursing, Anthropometry/Ergonomics were also used.</p>

To ensure that up-to-date quality information was being obtained, only sources that were dated beyond the year 2000 supported this literature review. The only exceptions were sources dated in the late 1900s that provide historical information and information for scarcely available quantities (e.g. anthropometric limb dimensions, and kinematic and kinetic reference gait data). Furthermore, for research papers, the Scopus prominence score was taken into account. This score shows the moment of a topic and is based on citation count, amount of scopus views and average cite score. The higher the Scopus prominence score, the better the paper was deemed to be. All the obtained literature information is in English.

Appendix D Gait

Gait Disorders

Gait is strongly influenced by age, personality, mood, and lifestyle [93]. The chances of the occurrence of gait and balance disorders increases dramatically with age. A study completed by Mahlknecht et al. showed that people aged between 60-69 have a 10.7% chance of having some form of gait disorder, people aged 70-79 have a 37.4% chance of having a gait disorder, and those aged between 80-97 have a 61.7% chance of having a gait disorder [94]. Causes of gait disorders discussed in this study include: peripheral sensory neuropathy, Parkinson's disease, severe dementia, vascular encephalopathy, as well as several conditions caused by medical history such as ischemic stroke, intracerebral hemorrhage, and surgery. The researchers also found that some participants had gait disorders caused by their fear of falling, which had caused them to modify their gait as an attempt to increase their balance [94]. Figure 85 compares the gait of a healthy person to those who suffer spastic paraparetic gait, cerebellar ataxic gait, parkinsonian gait, and frontal gait.

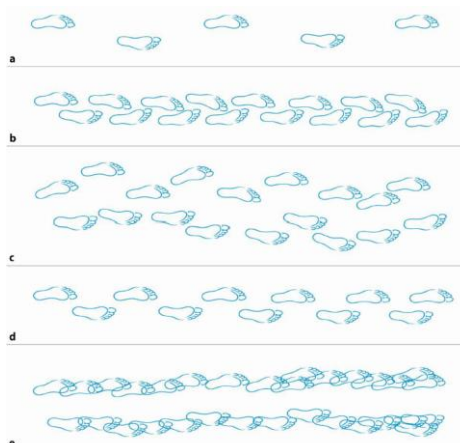


Figure 85 (a) Normal gait, (b) spastic paraparetic gait, (c) cerebellar ataxic gait, (d) parkinsonian gait, and (e) frontal gait [93].

In spastic paraparetic, the person appears to drag both legs forward giving the gait a “stiff” appearance. Figure 85 (b) shows that this form of gait has much shorter step length and walking base when compared to normal gait. Cerebellar ataxic gait occurs when a person develops issues with proprioception, the nervous system function that tracks the position of the body and its limbs. The body attempts to compensate for a lack of proprioception by using visual input; however, gait

is still greatly affected. As shown in Figure 85 (c), step length is inconsistent and walking base varies with each step. Gait issues worsen during turning and walking on inclines and uneven surfaces. Parkinson's gait appears slow, with reduced arm swing while in motion, short step length, and short walking base as shown in Figure 85 (d). As the disease worsens, foot clearance during swing reduces, inconsistency between steps increases, and a change in gait speed results in a change in step frequency without an increase of step length. Patients suffering with frontal gait appear to have "forgotten" how to walk. Patients with frontal gait have wider walking base, very short step length, have difficulties standing up from a sitting position, have trouble with stability in a standing position, and have issues initiating gait. Initiation of gait may result in exaggerated arm movements. Patients with frontal gait are at risk of a backwards fall [93].

Gait obliquity

Ceccato et al. collected 3D optical video data of nine healthy men aged between 23 and 42 years to compare differences in hip, shoulder, and spine movements during gait initiation and during regular walking. Figure 86 is a graph of their results regarding the angles of the shoulders, several vertebrae, and the hips [95].

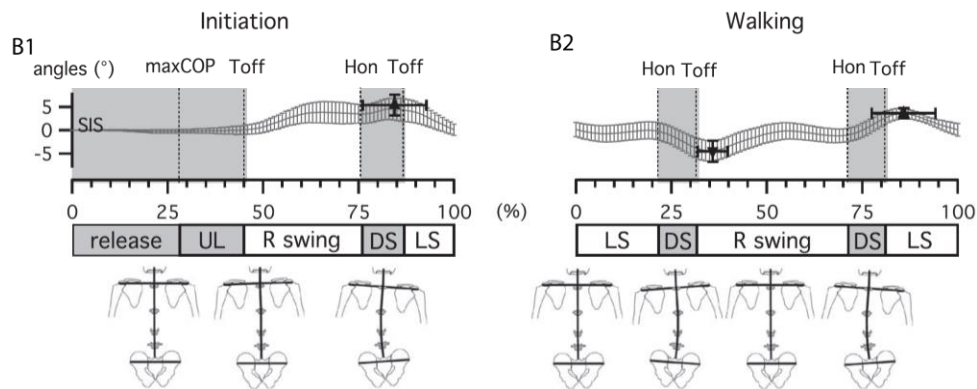


Figure 86 Hip in the frontal plane during gait initiation and regular walking, modified from [95].

Ceccato et al. also recorded angle in the sagittal plane of the thoracic level, several vertebrae, and the pelvis during gait initiation and normal walking shown in Figure 87 [95].

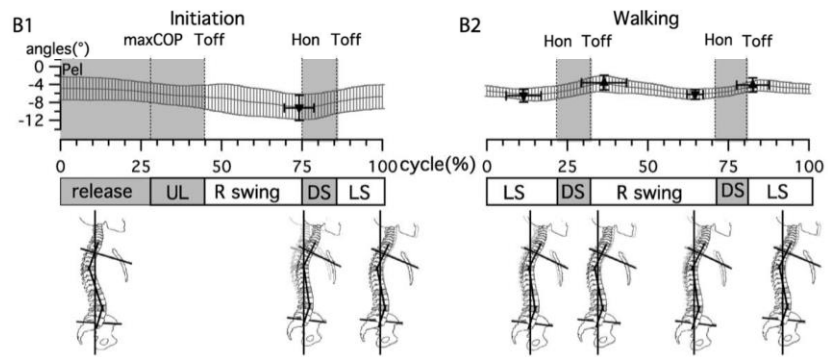


Figure 87 Hip in the sagittal plane during gait initiation and regular walking, modified from [95].

Appendix E Anatomy

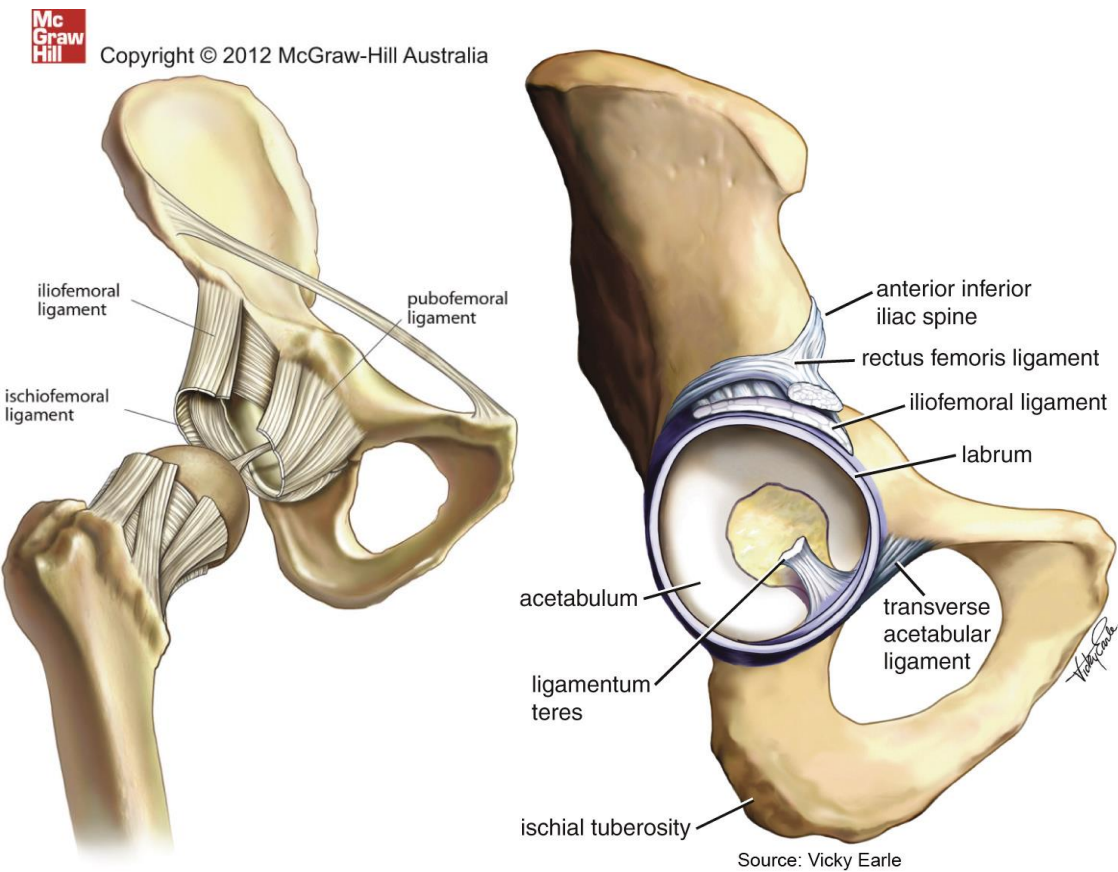


Figure 88 Hip joint structure including ligaments and acetabular structures [41].

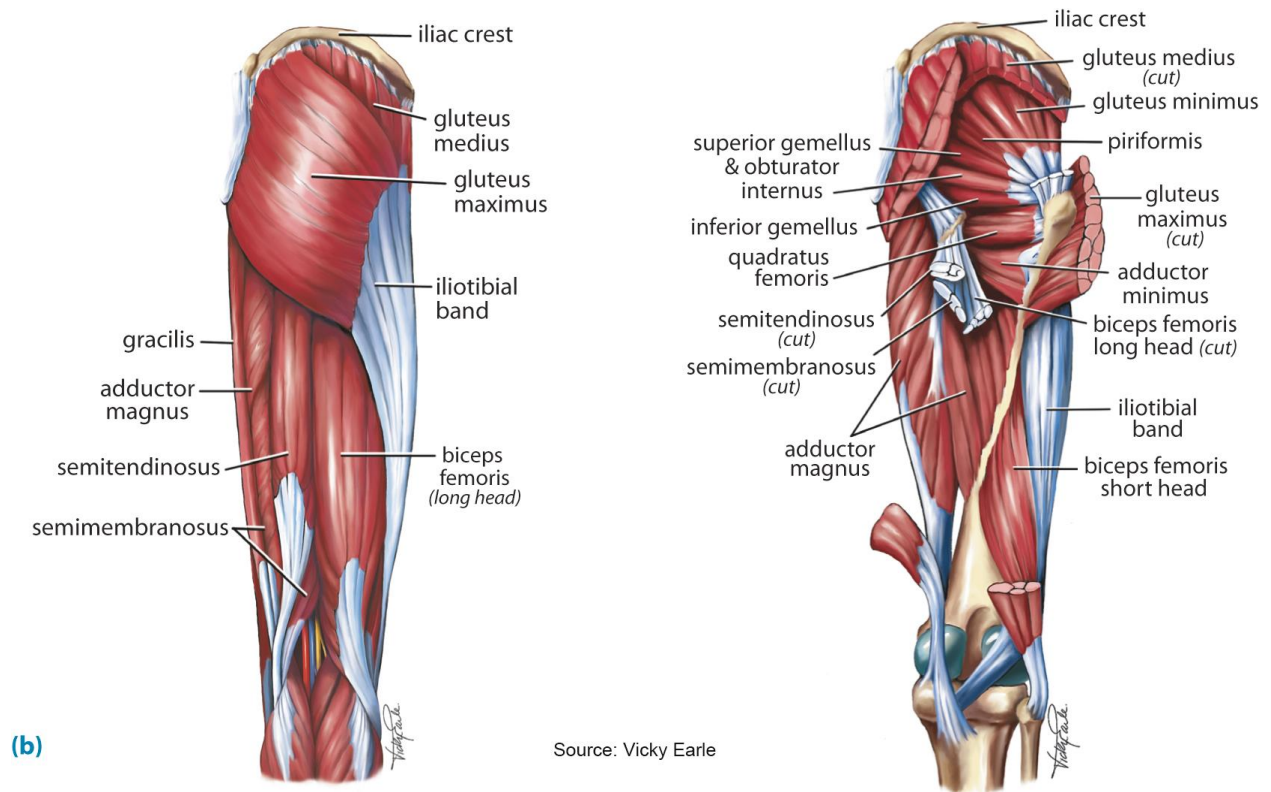


Figure 89 Hip joint muscle anatomy [41].

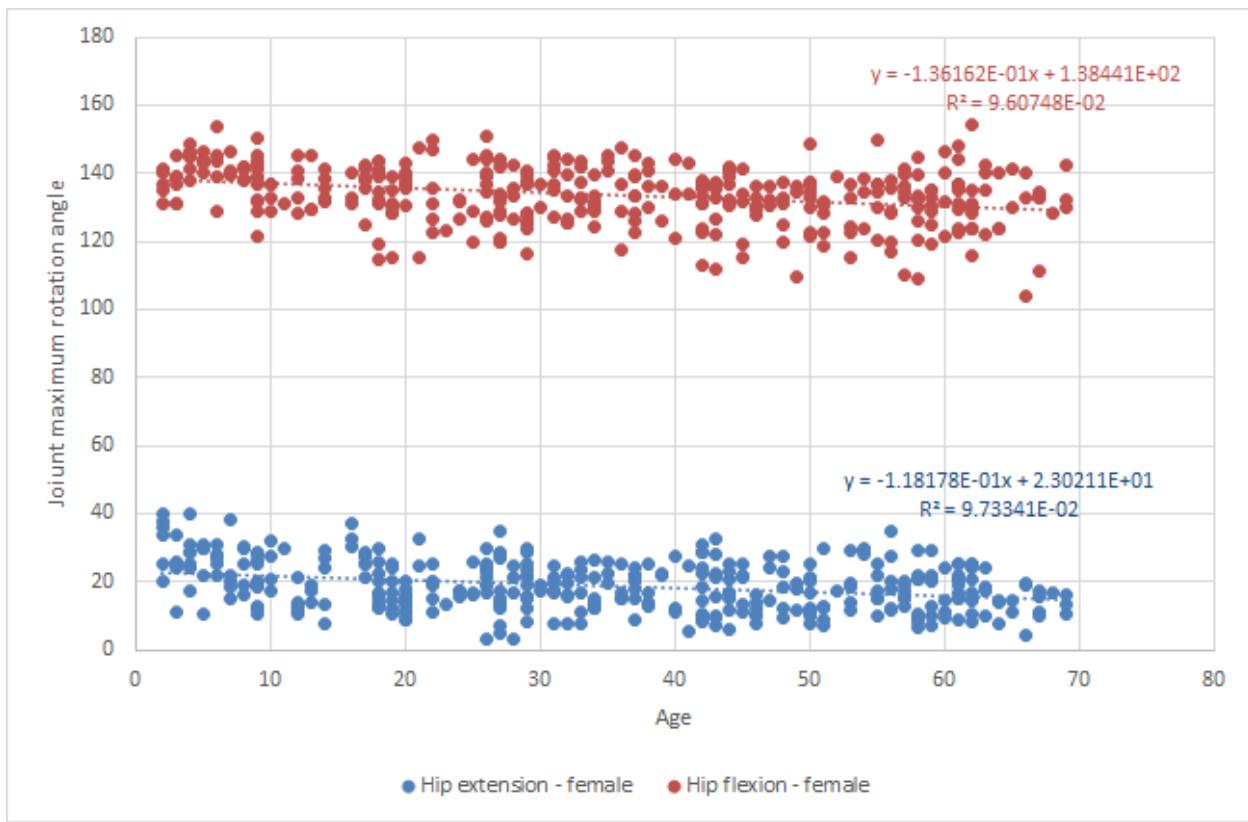


Figure 90 Regression fit for hip flexion and extension rotation angle for female data from [36].

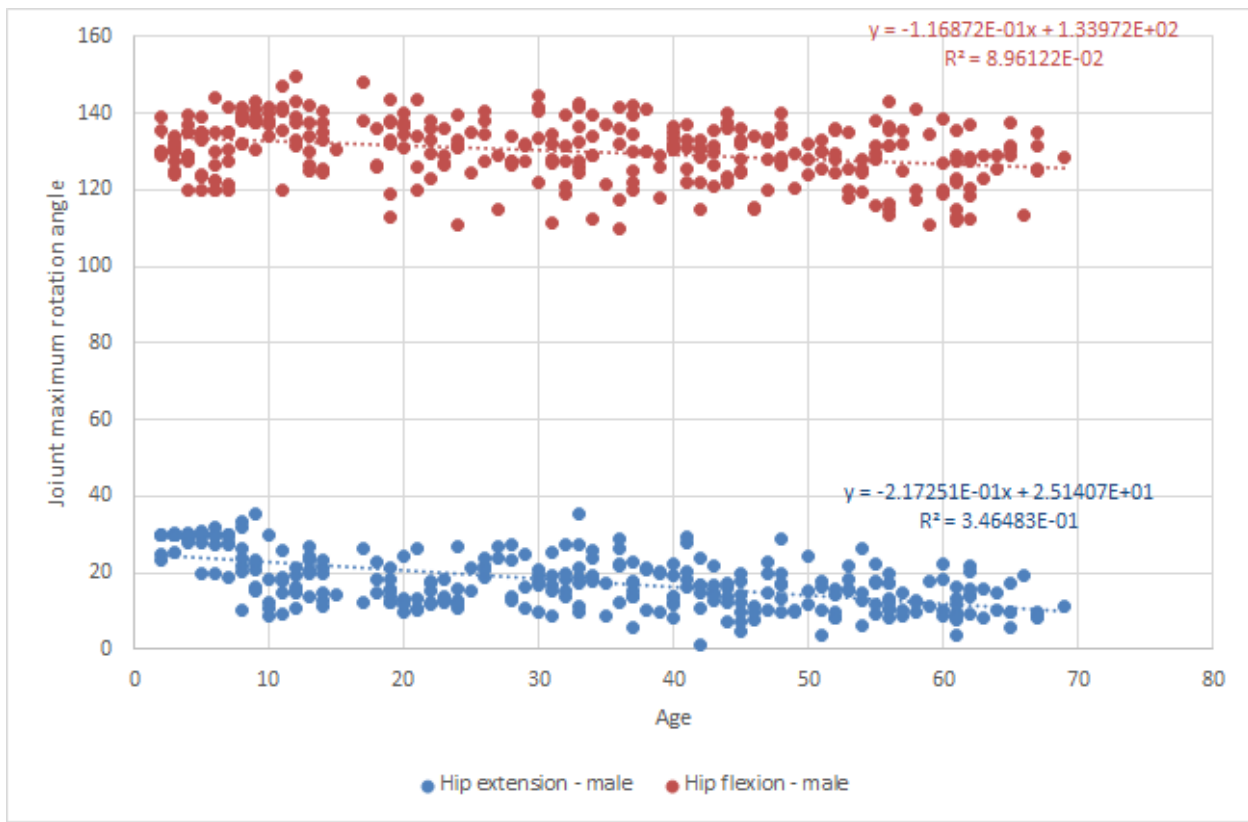


Figure 91 Regression fit for hip flexion and extension rotation angle for male data from [36].

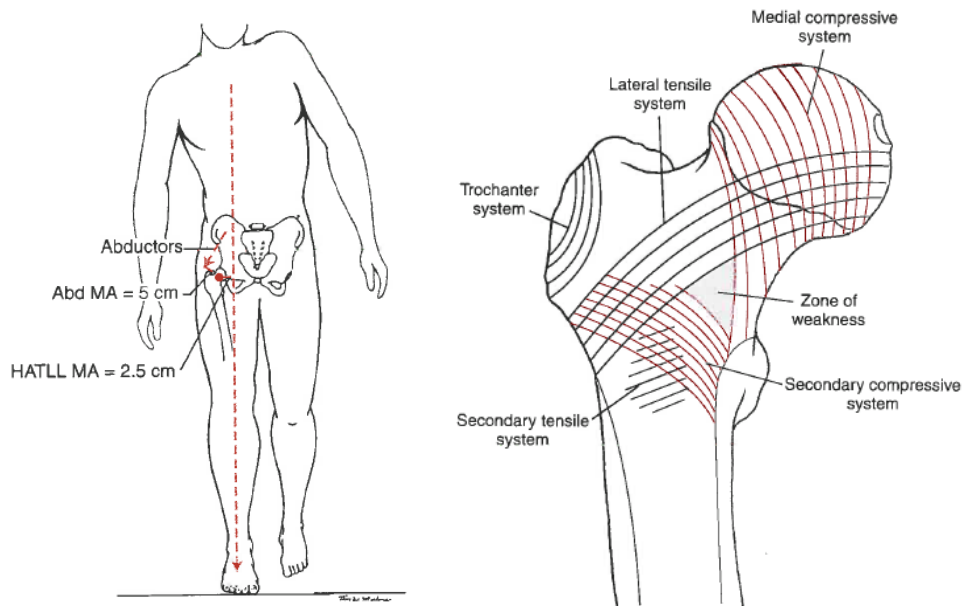


Figure 92 Stress distribution on the hip bone at a midstance position. [35].

Table 14 Flexion and extension angles for the elderly, digitized from [38].

Condition	Angle		Legend
F_E_S	71.04895		F_E = flexion-extension
F_E_A	76.64336		A_A = adduction-abduction
A_A_S	54.26573		E_I = external-internal rotation
A_A_A	69.93007		_A - active
E_I_S	62.0979		_S - sedentary
E_I_A	71.60839		_B - SD error bar top
F_E_S_B	86.15385		_SD - standard deviation
F_E_A_B	92.30769		
A_A_S_B	63.21678		
A_A_A_B	80		
E_I_S_B	73.84615		

E_I_A_B	82.23776		
F_E_S_SD	15.1049		
F_E_A_SD	15.66434		
A_A_S_SD	8.951049		
A_A_A_S_D	10.06993		
E_I_S_SD	11.74825		
E_I_A_SD	10.62937		

The derived equations for hip flexion and extension angles are as follows:

- hip extension in females: $\text{angle}(\circ) = -0.11818 * \text{age(yrs)} + 23.02108$
- hip flexion in females: $\text{angle}(\circ) = -0.13616 * \text{age(yrs)} + 138.44101$
- hip extension in males: $\text{angle}(\circ) = -0.21725 * \text{age(yrs)} + 25.14070$
- hip flexion in males: $\text{angle}(\circ) = -0.11687 * \text{age(yrs)} + 133.97176$

Appendix F Anthropometry

Table 15 Comparison of elderly heights between countries [57].

Population	Age (years) Male/Female		Height (mm) Male/Female	
Australian	76 ± 7 (65–92)	77 ± 8 (65–92)	1658 ± 79	1521 ± 70
British	65+	65+	1640 ± 77	1515 ± 70
Dutch	80.4 ± 7.8 (65–100)	81.5 ± 8.3 (65–100)	1656 ± 82	1543 ± 72
American	(65–74)	(65–74)	1699 ± 38	1562 ± 43

Table 16 Comparison between young and old people's heights and weights [57].

	Young	Old	% difference
Male height, mm	1771±64	1658 ± 79	-6.38
Female height, mm	1657±66	1521 ± 70	-8.21
Male weight, kg	66±102	72±11 kg	+10.00
Female weight, kg	50±61	61±12 kg	+22.00

Table 17 Elderly waist and hip circumference for different age groups [58].

Parameter	Age group	Male ± SD	Female ± SD	Relation to height H (cm) and weight W (kg)
Waist circumference (cm)	65-69	98.1 ± 10.2	97.2 ± 13.2	M: 0.00786961* H*W F: 0.009528085 * H*W
	70-74	98.5 ± 11.1	97.4 ± 12.9	M: 0.007961063 * H*W F: 0.009869248 * H*W
	74-79	96.4 ± 10.7	96.2 ± 12.4	M: 0.008467951* H*W F: 0.010454635 * H*W
	80-84	94.8 ± 11.3	96.5 ± 12.8	M: 0.008735644 * H*W F: 0.010772494 * H*W
	All	97.5 ± 9.9	96.9 ± 14.1	M: 0.008104859 * H*W

				F: 0.009979033 * H*W
Hip circumference (cm)	65-69	100.6 ± 8.4	104.5 ± 11.5	M: 0.00807017 * H*W F: 0.010243672 * H*W
	70-74	101 ± 9.6	104 ± 10.7	M: 0.00816312 * H*W F: 0.010538006 * H*W
	74-79	99.6 ± 8.9	102.3 ± 10.4	M: 0.008749045 * H*W F: 0.011117559 * H*W
	80-84	98.3 ± 9.6	101.5 ± 11.4	M: 0.009058163 * H*W F: 0.011330654 * H*W
	All	100.2 ± 8.3	103.4 ± 12.1	M: 0.008329302 * H*W F: 0.010648421 * H*W

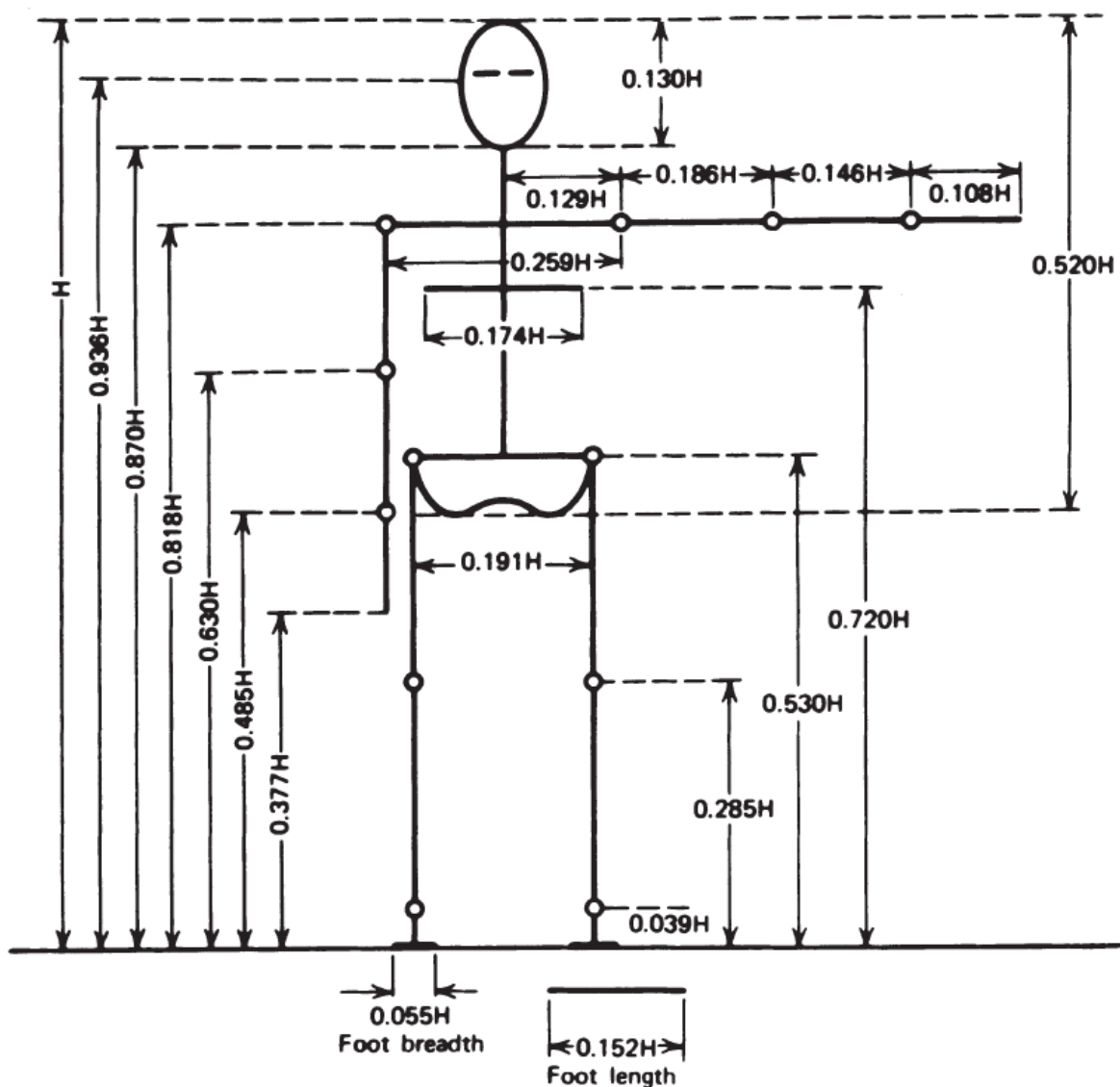


Figure 93 Classical anthropometric model from Drillis & Contini, 1964 - via Winter, 2009 [52].

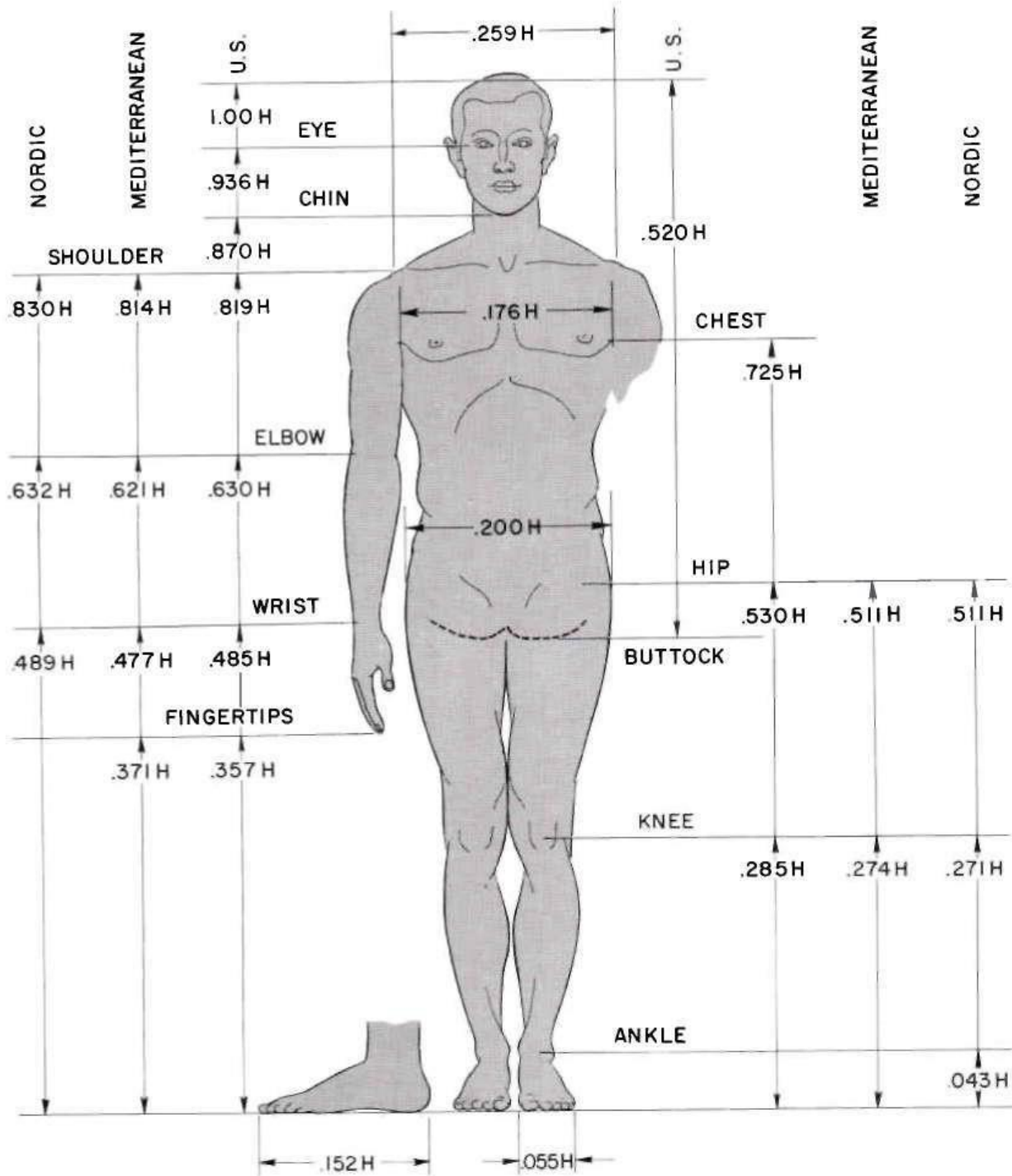


Figure 94 Male anthropometric model from Contini, 1972 [56]

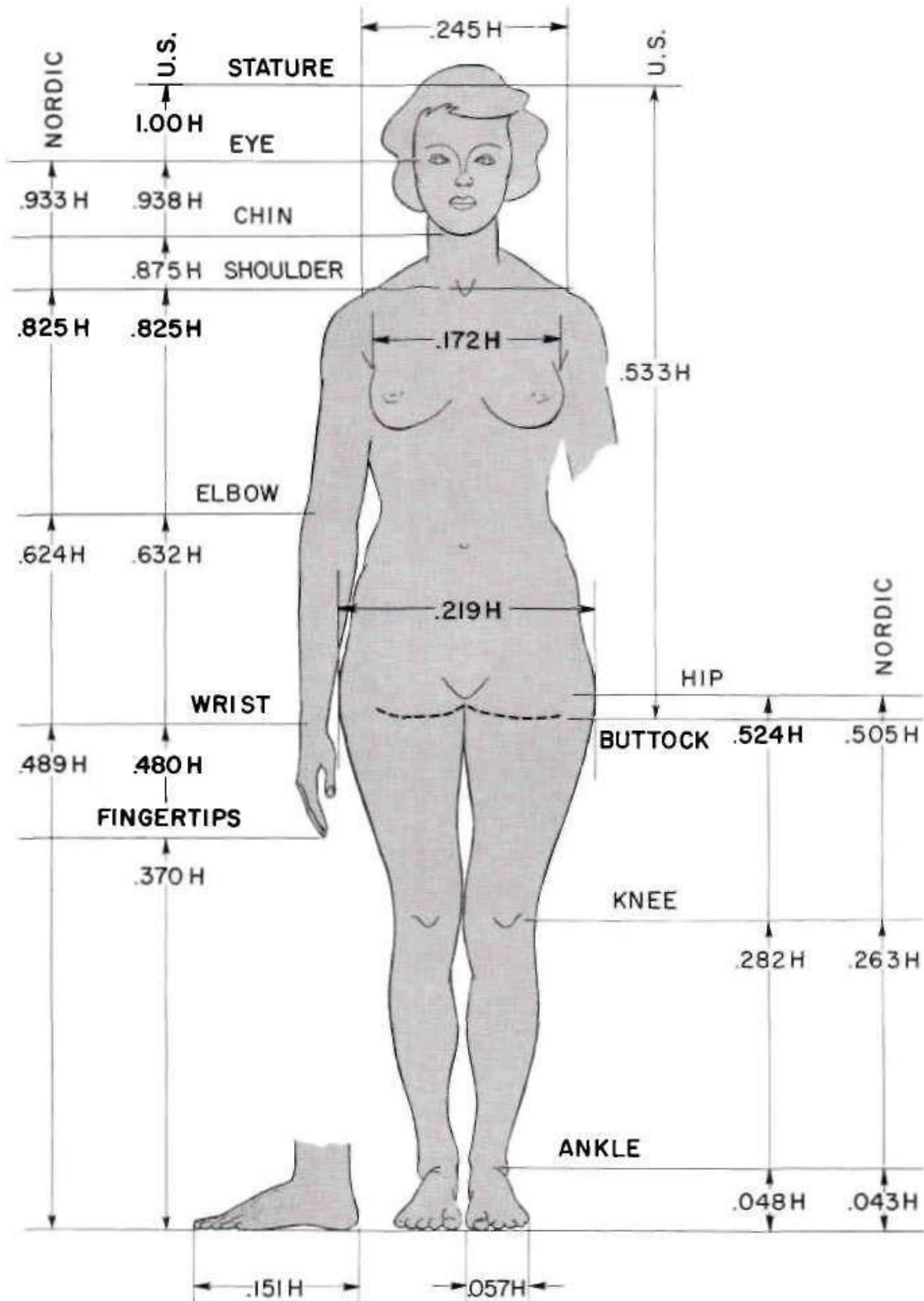


Figure 95 Female anthropometric model from Contini, 1972 [56]

TABLE 4.1 Anthropometric Data

Segment	Definition	Body Weight	Center of Mass/ Segment Length		Radius of Gyration/ Segment Length		
			Weight/Total	Proximal	Distal	C of G	Proximal
Hand	Wrist axis/knuckle II middle finger	0.006 M	0.506	0.494 P	0.297	0.587	0.577 M
Forearm	Elbow axis/ulnar styloid	0.016 M	0.430	0.570 P	0.303	0.526	0.647 M
Upper arm	Glenohumeral axis/elbow axis	0.028 M	0.436	0.564 P	0.322	0.542	0.645 M
Forearm and hand	Elbow axis/ulnar styloid	0.022 M	0.682	0.318 P	0.468	0.827	0.565 P
Total arm	Glenohumeral joint/ulnar styloid	0.050 M	0.530	0.470 P	0.368	0.645	0.596 P
Foot	Lateral malleolus/head metatarsal II	0.0145 M	0.50	0.50 P	0.475	0.690	0.690 P
Leg	Femoral condyles/medial malleolus	0.0465 M	0.433	0.567 P	0.302	0.528	0.643 M
Thigh	Greater trochanter/femoral condyles	0.100 M	0.433	0.567 P	0.323	0.540	0.653 M
Foot and leg	Femoral condyles/medial malleolus	0.061 M	0.606	0.394 P	0.416	0.735	0.572 P
Total leg	Greater trochanter/medial malleolus	0.161 M	0.447	0.553 P	0.326	0.560	0.650 P
Head and neck	C7–T1 and 1st rib/ear canal	0.081 M	1.000	— PC	0.495	0.116	— PC
Shoulder mass	Sternoclavicular joint/glenohumeral axis	—	0.712	0.288	—	—	—
Thorax	C7–T1/T12–L1 and diaphragm*	0.216 PC	0.82	0.18	—	—	—
Abdomen	T12–L1/L4–L5*	0.139 LC	0.44	0.56	—	—	—
Pelvis	L4–L5/greater trochanter*	0.142 LC	0.105	0.895	—	—	—
Thorax and abdomen	C7–T1/L4–L5*	0.355 LC	0.63	0.37	—	—	—
Abdomen and pelvis	T12–L1/greater trochanter*	0.281 PC	0.27	0.73	—	—	—
Trunk	Greater trochanter/glenohumeral joint*	0.497 M	0.50	—	—	—	—
Trunk head neck	Greater trochanter/glenohumeral joint*	0.578 MC	0.66	0.34 P	0.503	0.830	0.607 M
Head, arms, and trunk (HAT)	Greater trochanter/glenohumeral joint*	0.678 MC	0.626	0.374 PC	0.496	0.798	0.621 PC
HAT	Greater trochanter/mid rib	0.678	1.142	—	0.903	1.456	—

*NOTE: These segments are presented relative to the length between the greater trochanter and the glenohumeral joint.

Source Codes: M, Dempster via Miller and Nelson; Biomechanics of Sport, Lea and Febiger, Philadelphia, 1973. P, Dempster via Plagenhoef; Patterns of Human Motion, Prentice-Hall, Inc., Englewood Cliffs, NJ, 1971. L, Dempster via Plagenhoef from living subjects; Patterns of Human Motion, Prentice-Hall, Inc., Englewood Cliffs, NJ, 1971. C, Calculated.

Figure 96 Anthropometric mass properties for human segments via Winter, 2009 [52]

Appendix G Kinematic Relations

Relationship between hip angle and spring extension

$$\Delta X = S_{SLj} = r_{SLj} \theta_{Lj}$$

$$r_{SLj} = r_{SLj} \cdot \left(\frac{r_{Lj}}{S_{Lj}} \right) \rightarrow R$$

$$r_{SLj} = \frac{r_{Lj}}{R}$$

$$\Delta X = \frac{r_{Lj}}{R} \theta_{Lj}$$

$$r_{Lj} = \frac{S_{Lj}}{\theta_{Lj}}$$

$$\ell = \sqrt{d_f^2 + d_m^2}$$

$$S_p = \ell \theta$$

$$S_{Lj} = r_{Lj} \theta$$

$$\therefore \Delta X = \frac{r_{Lj}}{R} \theta$$

$$R = \frac{r_{Lj}}{S_{Lj}}$$

Prove $\theta = \theta_{Lj}$

$$GP = \sqrt{e^2 - O_4^2}$$

$$G'P' = \sqrt{e^2 - O'_4^2}$$

$$\therefore GP = G'P'$$

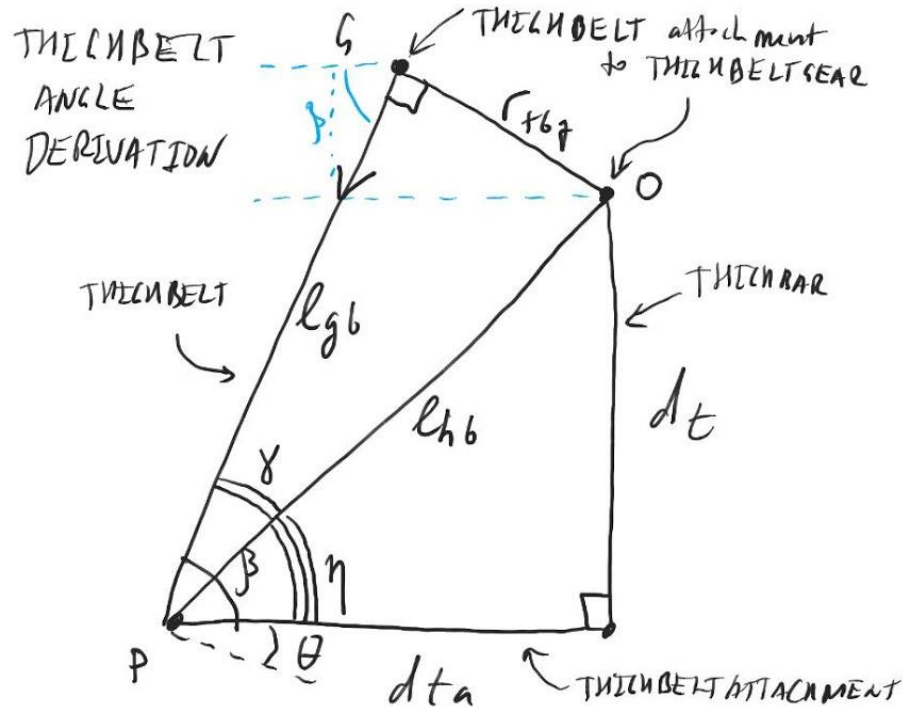
$$\therefore O'G'P' = OG P$$

$$\therefore \angle S' O_4 = \angle P' O P$$

$$\boxed{\theta_{Lj} = \theta}$$

Proof complete

Relationship between hip angle θ , and belt angle β .



$$l_{gb}^2 = d_t^2 + d_{ta}^2 = l_{hb}^2 + r_{tbg}^2$$

$$\eta = \arctan \left(\frac{d_t}{d_{ta}} \right)$$

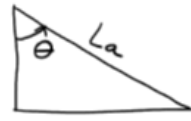
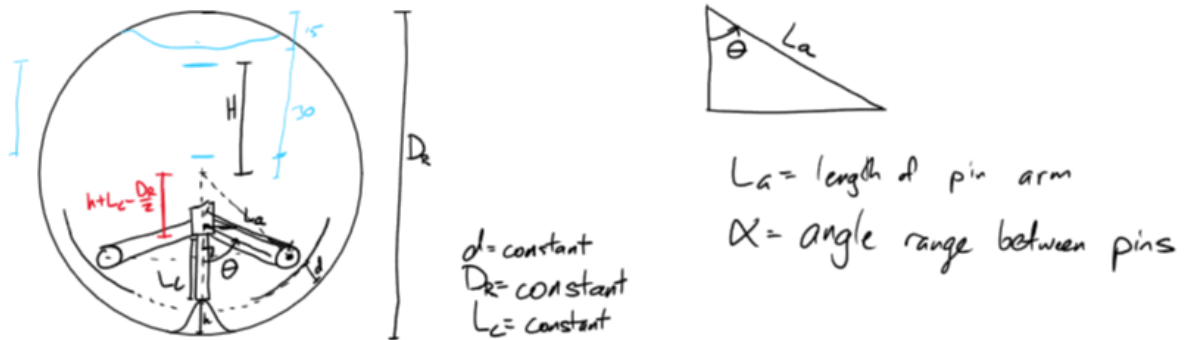
$$l_{gb}^2 = l_{hb}^2 - r_{tbg}^2$$

$$\gamma = \arctan \left(\frac{r_{tbg}}{l_{gb}} \right)$$

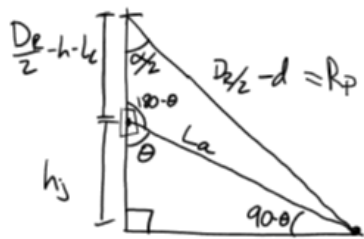
$$= \arctan \left(\frac{r_{tbg}}{\sqrt{d_t^2 + d_{ta}^2 - r_{tbg}^2}} \right)$$

$$\underline{\beta = \eta + \gamma}$$

Relationship between timing pin arm angle to vertical and angular distance between timing pins.



$L_a = \text{length of pin arm}$
 $\alpha = \text{angle range between pins}$



$$\frac{\sin \alpha}{L_a} = \frac{\sin(180-\theta)}{D_c/2 - d}$$

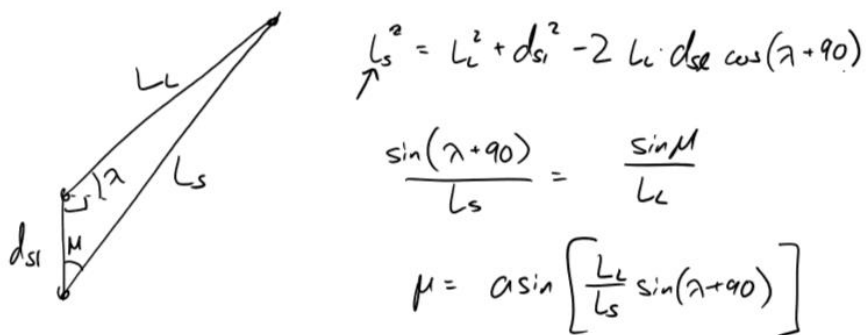
$$\theta = 180 - \arcsin\left(\frac{D_c/2 - d}{L_a} \sin \alpha\right)$$

$$L_a^2 = \left(\frac{D_c}{2} - h - L_c\right)^2 + (D_c/2 - d)^2 - 2\left(\frac{D_c}{2} - h - L_c\right)(D_c/2 - d) \cos \alpha$$

$$-\frac{L_a^2 - \left(\frac{D_c}{2} - h - L_c\right)^2 - (D_c/2 - d)^2}{2\left(\frac{D_c}{2} - h - L_c\right)(D_c/2 - d)} = \cos \alpha$$

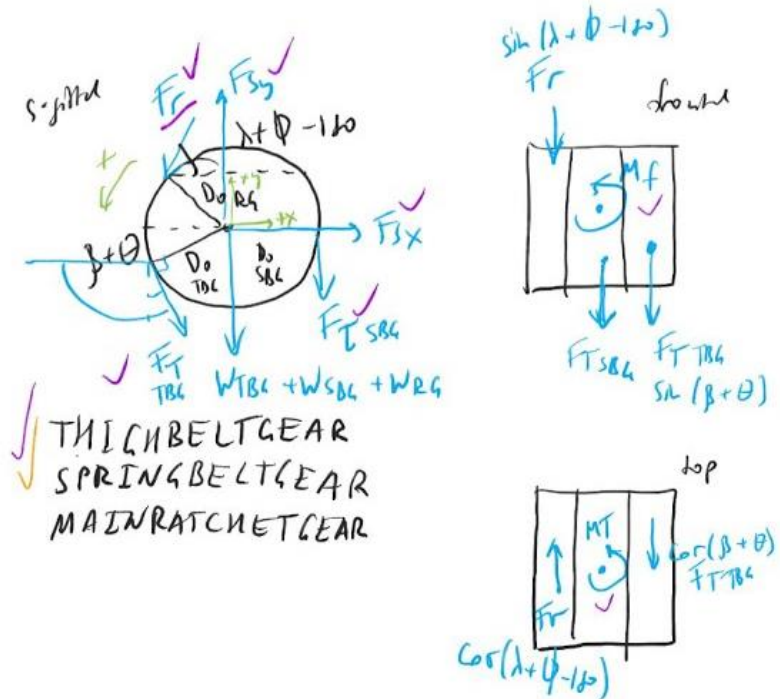
Relationship between timing cam spring angle and extension to angle of timing pawlever.

cosine law $\rightarrow L_s$



Appendix H Free Body Diagrams

Energy system free body diagrams



Symmetries:

$$\checkmark X: F_{T_{B4}} \cos(\theta + \beta) - F_r \cos(\lambda + \phi - 180) = \\ = (m_{TBC} + m_{S84} + m_{rg}) g \times h_{wp}$$

$$\checkmark y: F_{S_y} - F_{T_{B4}} \sin(\theta + \beta) - F_r \sin(\lambda + \phi - 180) = \\ = (w_{TBC} + w_{S84} + w_{rg}) + \\ (m_{TBC} + m_{S84} + m_{rg}) g \times h_{wp}$$

$$\checkmark M: \frac{F_T \cdot D_0}{TBG} - \frac{F_T \cdot D_0}{SBG} + \frac{F_r \cdot D_0}{RG} =$$

$$= (I_{T\Delta G} + I_{S\Delta G} + I_{R\Delta}) \Delta L_p$$

Frontal:

$$\checkmark M: F_r \sin(\lambda + \phi - \omega) \cdot \left(\frac{t_{S\Delta G} + t_r}{2} \right)$$

$$- \frac{F_T}{TBG} \sin(\beta + \theta) \cdot \left(\frac{t_{S\Delta G} + t_{TBG}}{2} \right) + M_f$$

$$= 0$$

$$\checkmark \text{Top: } M: -F_r \cos(\lambda + \psi - \omega) \left(\frac{t_{S\Delta G} + t_r}{2} \right)$$

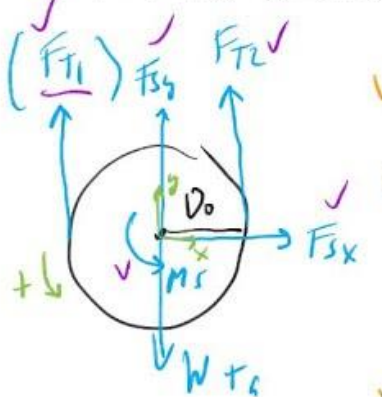
$$-F_t \cos(\beta + \theta) \cdot \left(\frac{t_{\text{back}} + t_{\text{front}}}{2} \right) + M_T = 0$$

✓ MAIN ENERGY SPRING



$$\checkmark y: F_{sy} - F_{sy} = 0$$

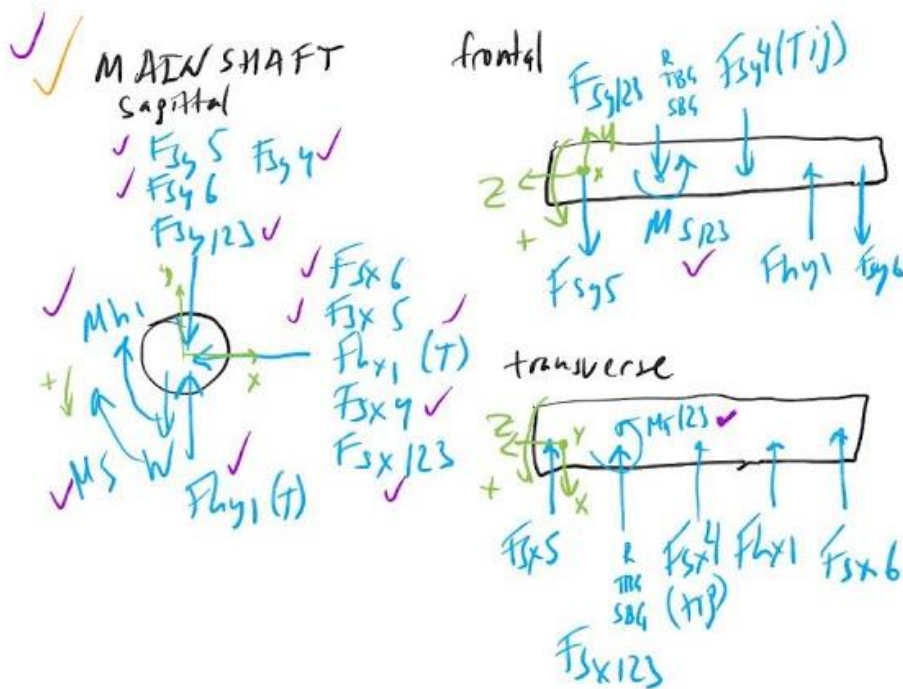
✓ MAIN TIMING GEAR



$$\checkmark x: F_{sx} = M_{TG} a_{x,hp}$$

$$\checkmark y: F_{T2} + F_{sy} = W_{TG} + m_{TG} a_{y,hp}$$

$$\checkmark M: \frac{F_{T2} \cdot D_0}{TG} + M_S = I_{TG} \alpha_{hp}$$



Sagittal:

$$\checkmark x: -F_{sx6} - F_{sx5} - Flx1 - F_{sx4} - F_{sx123} =$$

$$m_s a_x h_p$$

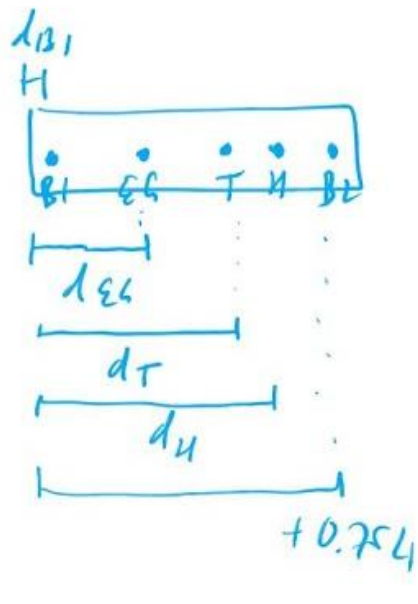
$$\checkmark y: Flx1 - F_{sy5} - F_{sy6} - F_{sy123} - F_{sy4} =$$

$$= m_s a_y h_p$$

$$\checkmark M: -M_s - M_{h1} = I_s \alpha_{h_p}$$

Frontal:

- ✓ $d_{B1} = 0.5L_4$
- ✓ $d_{Ec} = L_4 + T_{C2} + 0.5L_3$
- ✓ $d_T = L_4 + T_{C2} + L_3$
 $+ L_2 + T_{C1} + 0.25L_1$
- ✓ $d_H = L_4 + T_{C2} + L_3 + L_2$
 $+ T_{C1} + 0.5L_1$
- ✓ $d_{B2} = L_4 + T_{C2} + L_3 + L_2$
 $+ T_{C1} + 0.75L_1$



✓ $M_{Fy5}:$ $M_{S123} - F_{Fy123} \cdot d_{Ec}$
 $- F_{Fy4} \cdot d_T + F_{Hg1} \cdot d_H$
 $- F_{Fy6} \cdot d_{B2} = 0$

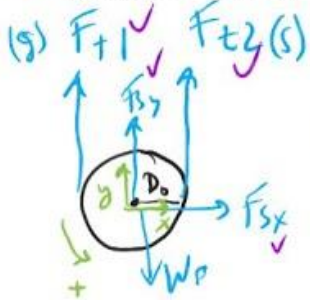
Top:

✓ $M_{Fz5}:$ $M_{T123} + F_{Sx123} \cdot d_{Cr}$

$$+ f_{sx} \cdot d_T + F_{hx1} \cdot d_h$$

$$+ f_{sx} \cdot d_{B2} = 0$$

✓ MAIN PULLEYS

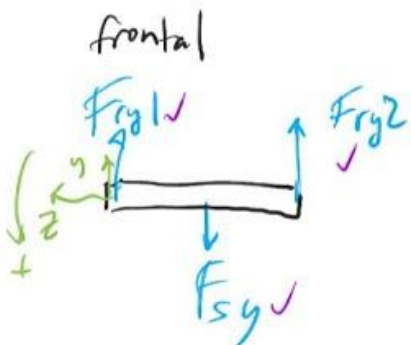


$$\checkmark x: F_{sx} = m_p a_x L_p$$

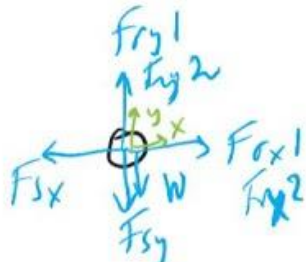
$$\checkmark y: F_{sy} + F_{t1} + F_{t2} \\ = W_p + m_p a_y L_p$$

$$\checkmark M: -F_{t1} \cdot D_o + F_{t2} \cdot D_o \\ = I_p \alpha L_p$$

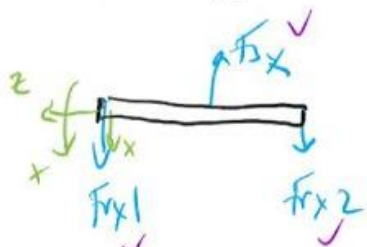
✓ MAIN PULLEY SHAFT



sagittal



transverse



sagittal:

$$\checkmark x: -F_{sx} + F_{rx1} + F_{rx2} \\ = m_{ps} a_x L_p$$

$$\checkmark y: -F_{sy} + F_{ry1} + F_{ry2} \\ = W_{ps} + m_{ps} a_y L_p$$

Frontal:

$$\checkmark d_{B1} = 0.5l_1$$

$$\checkmark d_p = \left(\frac{l_1 + l_2 + l_3}{2} \right)$$

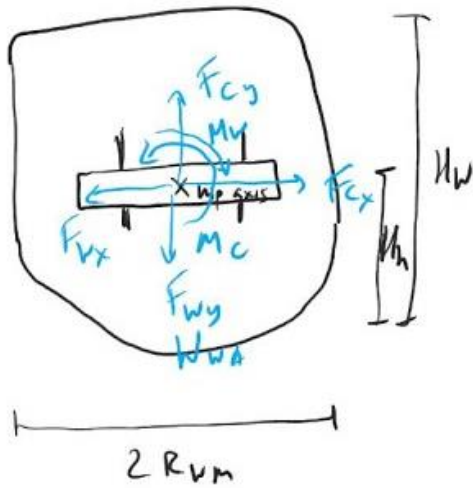
$$\checkmark d_{B2} = l_1 + l_2 + 0.5l_3$$

$$\checkmark M_{Fml}: f_{sy}2 \cdot d_{B2} - f_{sy} \cdot d_p = 0$$

Transverse:

$$\checkmark M_{Fx1}: f_{sx} \cdot d_p - f_{cx}2 \cdot d_{B2} = 0$$

WAIST ATTACHMENT - WAISTR

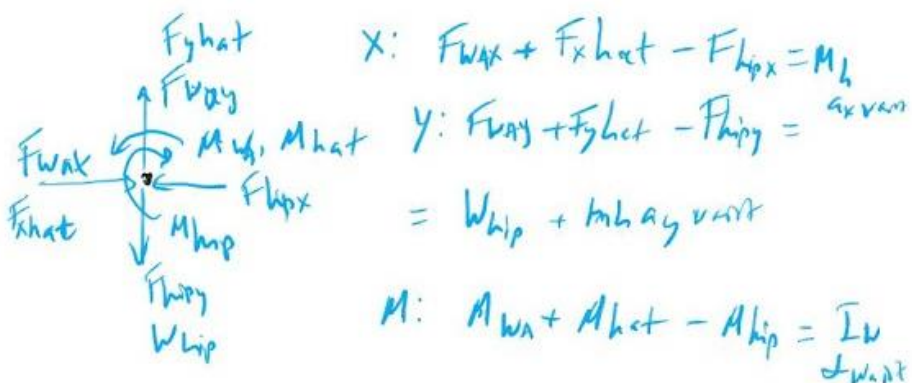


$$X: F_{Cx} - F_{Wx} = m_w a_x v_{wrt}$$

$$Y: F_{Cy} - F_{Wy} = w_{wa} + m_w a_y v_{wrt}$$

$$M: M_C - M_W = I_{Wa} \cdot \alpha_{WADT}$$

WAIST

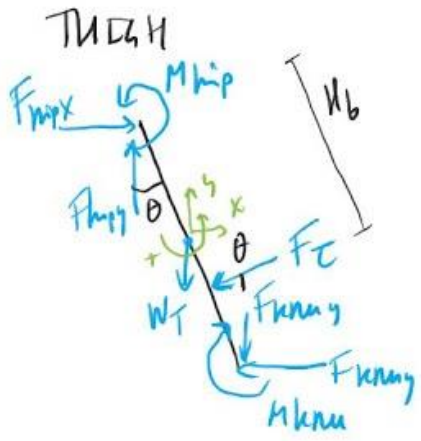


$$X: F_{Wax} + F_{Xhat} - F_{Lipx} = M_b$$

$$Y: F_{Way} + F_{Yhat} - F_{hipy} = a_y v_{wrt}$$

$$= w_{hp} + m_{hay} v_{wrt}$$

$$M: M_{Wa} + M_{hat} - M_{lip} = I_w \cdot \alpha_{WADT}$$



GPR ID reflections

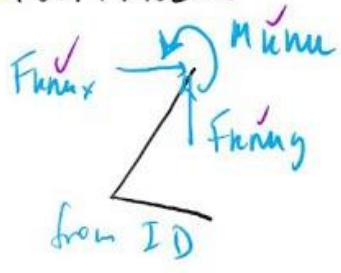
$$X: F_{\text{flap x}} - F_{\text{flap y}} = F_t \cos \theta$$

$$= M_{\text{flap}} L \cdot a_x \text{ flap}$$

$$Y: \text{Flipy} - \text{Fluency} - \text{FeS2H}$$

$$= V_{\text{thyl}} + m_{\text{thyl}} \cdot a_{\text{thyl}}$$

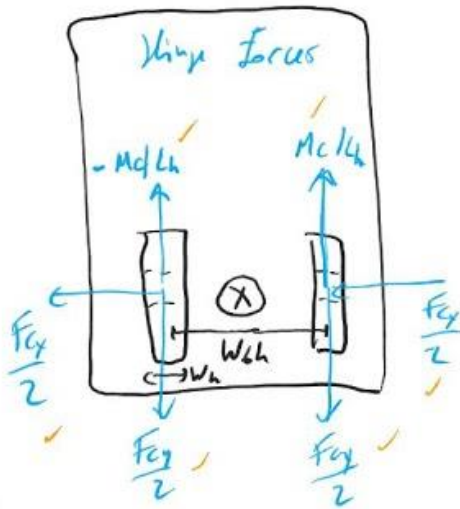
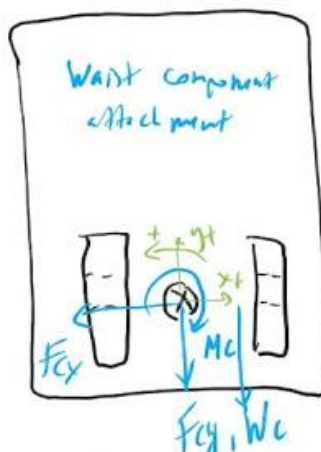
FOOT + KNEE

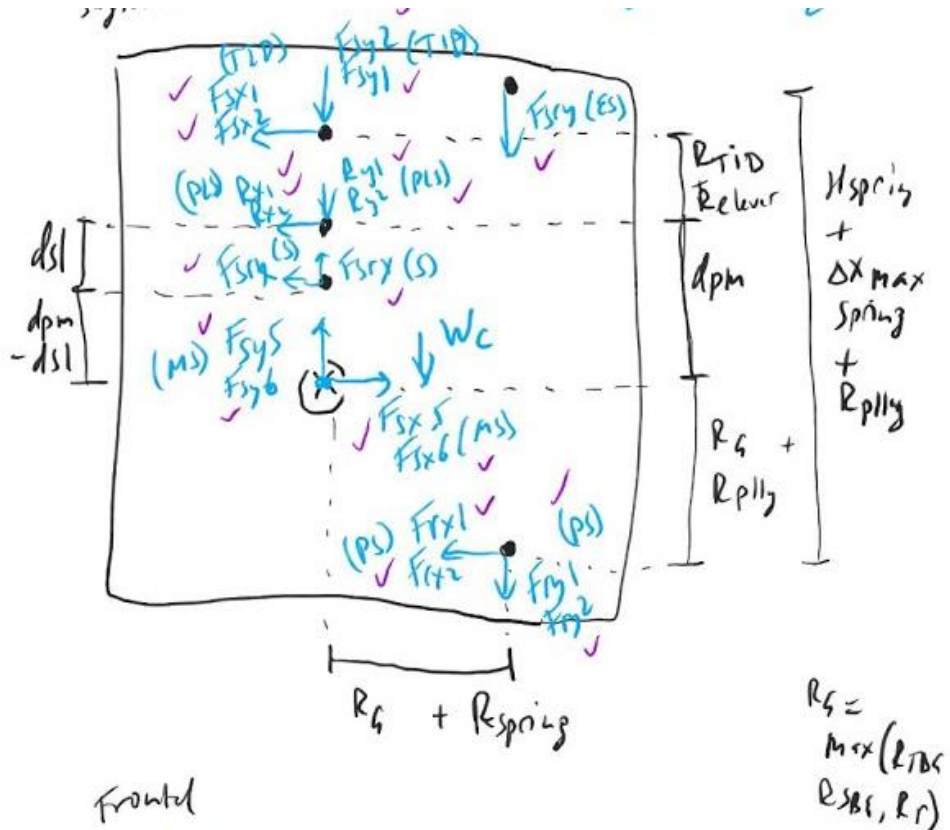


$$H_b = \underline{T h y L . D . S .}$$

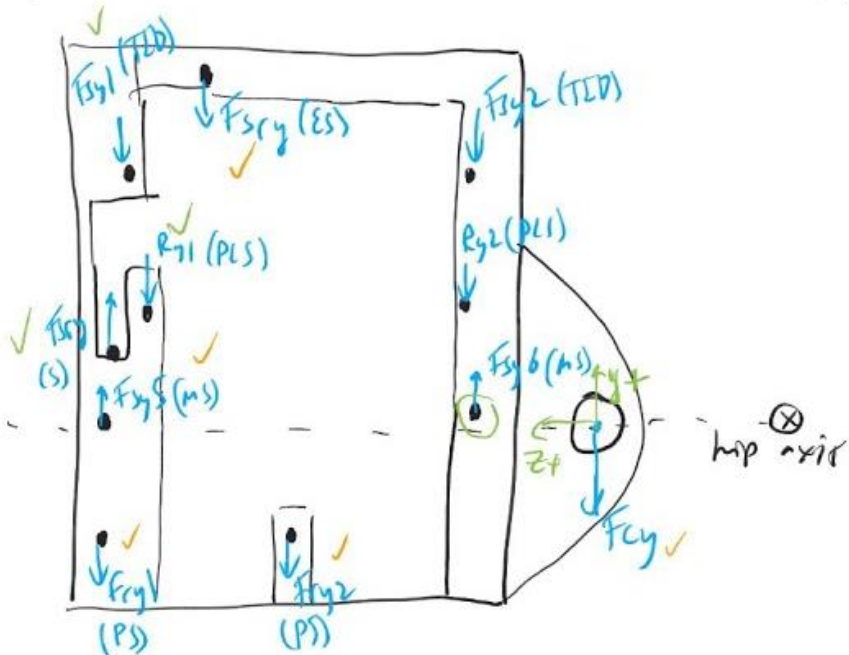
$$\begin{aligned} M: \quad & M_{kip} - \Delta y^t F_{kpx} \\ & - \Delta x^t F_{kpy} - M_{khe} \\ & - \Delta y''^t F_{kex} - \Delta x''^t F_{key} \\ & - F_t H_b = I_{H_b} \alpha_{H_b} \end{aligned}$$

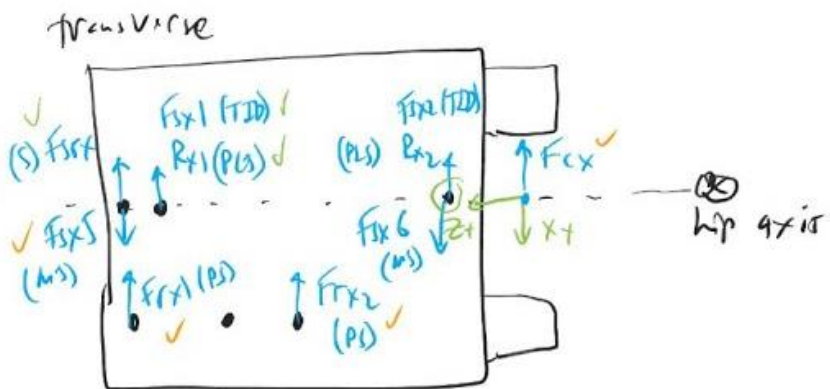
CASE





frontal





\leftarrow Case - F_{cx} - fix munggah ✓
 \downarrow Case - F_{cy} - fix munggah ✓
 \Rightarrow Case - M_c - tetapnya ✓

summat:

$$\begin{aligned}
 X: & -F_{cx} - \underbrace{F_{sx1} + F_{sx2}}_{(TDD)} - \underbrace{R_{x1} + R_{x2}}_{(PLS)} \\
 & -F_{sr_x} + F_{sx5} + F_{sx6} - \underbrace{F_{rx1} - F_{rx2}}_{(PS)}
 \end{aligned}$$

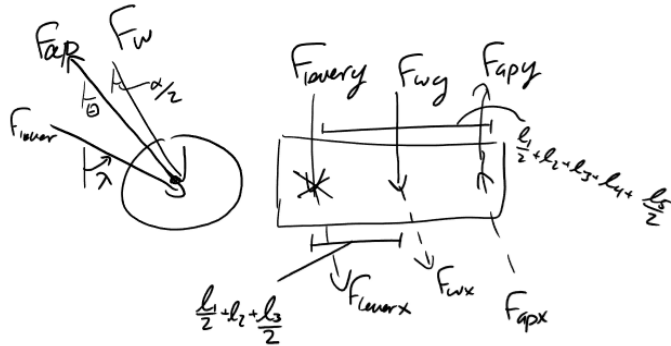
$$\begin{aligned}
 Y: & -F_{cy} - \underbrace{F_{sy1} + F_{sy2}}_{(TDD)} - \underbrace{R_{y1} + R_{y2}}_{(PLS)} \\
 & -F_{sry} + F_{sry} + \underbrace{F_{sy5} + F_{sy6}}_{(+M_{es})} \\
 & -F_{ry1} - F_{ry2} = \underbrace{M_c a_y}_{(+M_{es})} \text{ hip}
 \end{aligned}$$

$\checkmark M:$
 $\checkmark d_{psx} = R_s + R_{spnLg}$
 $\checkmark d_{psy} = R_s + R_{plly}$
 $\checkmark d_{sy} = d_{pm} - d_{sl}$
 $\checkmark d_{pls} = d_{pm}$
 $\checkmark d_{tidy} = d_{pt} + R_{+iA} + R_{e-pl}$
 $\checkmark d_{esx} = d_{psx}$
 $\checkmark d_{isy} = d_{tidy} + R_{+id}$

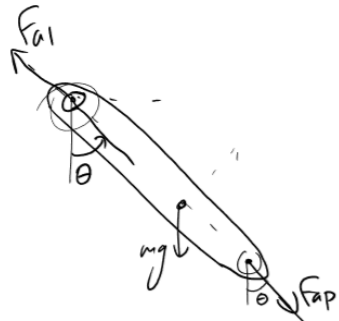
$$\begin{aligned}
 -M_C &= -\underbrace{d_{psx}(F_{ry1} + F_{ry2})}_{(PS)} \checkmark \\
 &\quad -\underbrace{d_{psy}(F_{rx1} + F_{rx2})}_{(PS)} \checkmark \\
 + \mu_{CFS} &+ \underbrace{d_{sy} \cdot F_{srx}}_{(PLS)} \checkmark \\
 &\quad + \underbrace{d_{pls}(R_{x1} + R_{x2})}_{(TID)} \checkmark \\
 &\quad + \underbrace{d_{tidy}(F_{sx1} + F_{sx2})}_{(TID)} \checkmark \\
 &\quad - \underbrace{d_{esx} F_{sm}}_{(ES)} \checkmark \\
 &= 0
 \end{aligned}$$

Timing Pin (two views) and Timing Pin Arm.

TIMINGPIN

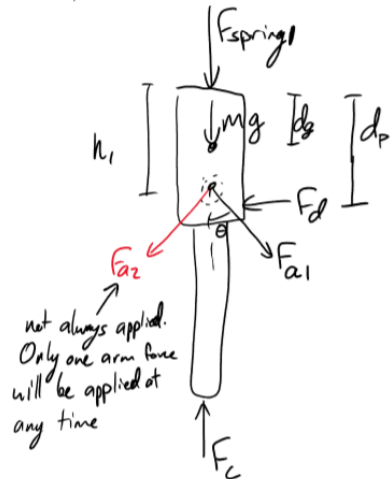


TIMING PIN ARM

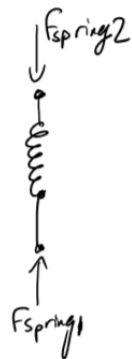


Timing Cam Follower and Timing Cam Spring

TIMINGCAMFOLLOWER

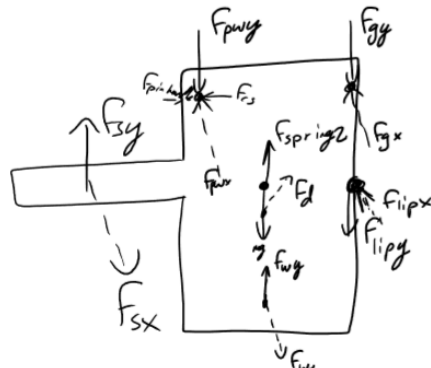
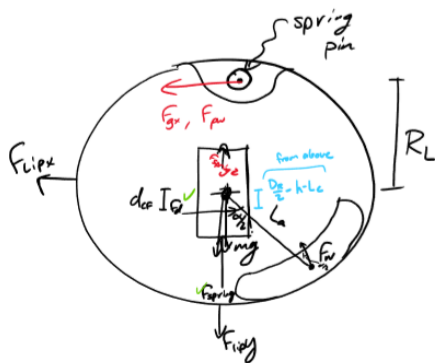


TIMING CAM SPRING



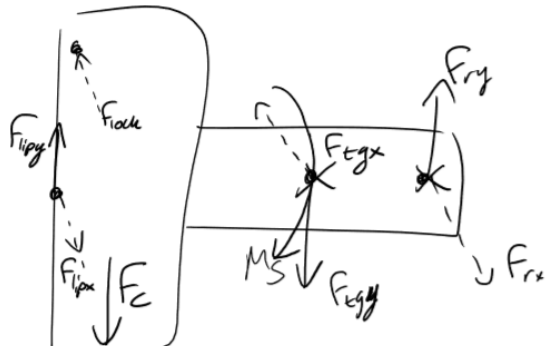
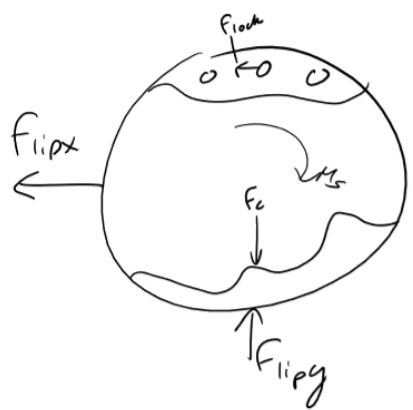
Timing Pin Disk (two views)

TIMING PINDISK



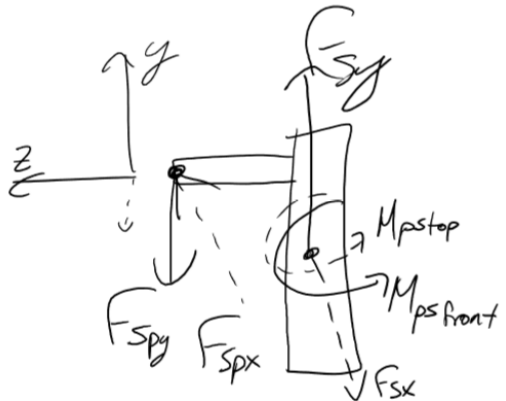
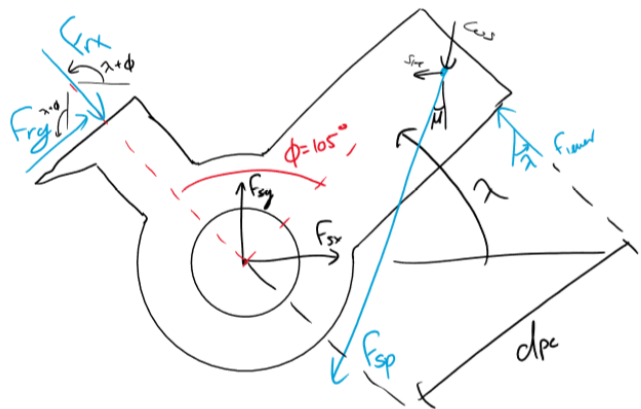
Timing Cam Disk and Timing Belt Gear

TIMING CAM DISK



Timing PawLever (two views)

TIMING PAWLEVER

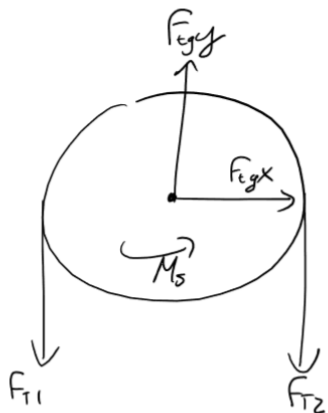


Timing Paw Spring and Timing Belt Gear

TIMING PAW SPRING

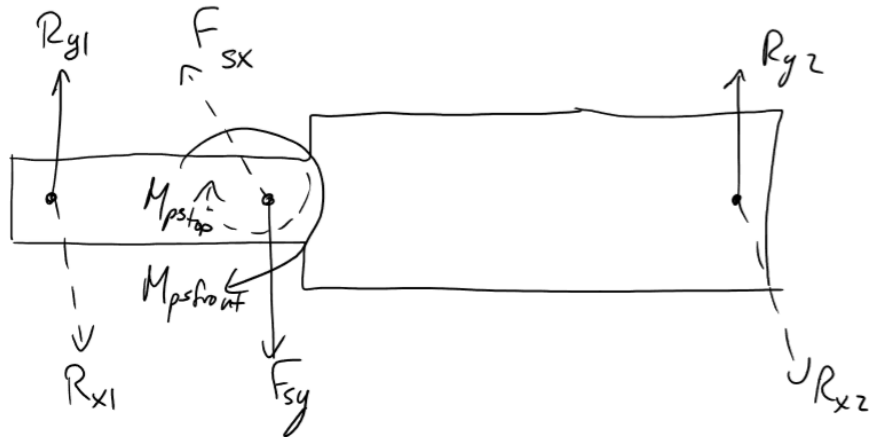


TIMING BELT GEAR



Timing Paw Shaft

TIMING PAW SHAFT



TIMING PIN

$$\sum F_x = F_{lever} \sin \alpha + F_w \sin \left(\frac{\alpha}{2}\right) - F_{ap} \sin \theta$$

$$\sum F_y = -F_{lever} \cos \alpha + F_w \cos \left(\frac{\alpha}{2}\right) + F_{ap} \cos \theta$$

Around lever: $\sum M_{ant} = -F_w \cos \frac{\alpha}{2} \left(\frac{L_1}{2} + L_2 + L_{lever} + \frac{L_2}{2} \right) + F_{ap} \cos \theta \left(\frac{L_1}{2} + L_2 + L_{lever} + L_2 \right)$

$$\sum M_{ap} = F_w \sin \frac{\alpha}{2} \left(\frac{L_1}{2} + L_2 + \frac{L_2}{2} \right) - F_{ap} \sin \theta \left(\frac{L_1}{2} + L_2 + L_{lever} + L_2 \right)$$

TIMING PIN ARM

$$\sum F_x = F_{ap} \sin \theta - F_{ai} \sin \theta$$

$$\sum F_y = -F_{ap} \cos \theta + F_{ai} \cos \theta$$

TIMING CAM FOLLOWER

$$\sum F_x = F_{ai} \sin \theta - F_d$$

$$\sum F_y = -F_{ai} \cos \theta - F_{spring1} + F_c$$

TIMING PINDISK

$$\sum F_z = F_{pinhole} - F_{cs}$$

$$\sum F_x = -F_w \sin \left(\frac{\alpha}{2}\right) + F_d + F_{sx} - F_{px} - F_{gx} - F_{ipx}$$

$$\sum F_y = F_w \cos \left(\frac{\alpha}{2}\right) + F_{spring2} - F_{pg} + F_{sy} - F_{pwg} - F_{gy} - F_{ipy}$$

$$\sum M_{ag} = \left(\frac{D}{2} - h - L_c\right) F_d - F_{pn} \cdot R_L - F_{gx} \cdot R_L$$

$$\sum M_{Ant} = -F_{sy} (L_s + T_{D2}) + F_{pwg} \cdot (T_{D2}) - F_{gy} (T_{D2}) - F_{ipy} (T_{D2})$$

$$\sum M_{Top} = F_{sx} (L_s + T_{D2}) - F_{px} (T_{D2}) + F_{gx} (T_{D2}) - F_{ipx} (T_{D2})$$

TIMING CAM SPRING

$$\sum F_y = F_{spring1} - F_{spring2}$$

shaft guide

TIMINGCAMDISK

$$\sum F_x = F_{lipx} - F_{lach} - F_{tgc} + F_{rx}$$

$$\sum F_y = F_{ly} - F_c - F_{tgy} + F_{ry}$$

$$\sum M_z = F_{lach} \cdot R_L - M_s$$

$$\sum M_{front} = -F_{lipy}(T_0 + T_{g2}) + F_c(T_{g2} + T_{g3}) + F_{ry}(L_s + T_{g2} + T_c)$$

$$\sum M_{top} = -F_{lipy}(T_0 + T_{g3}) - F_{lach}(T_0 + T_{g2}) - F_{rx}(L_s + T_{g2} + T_c)$$

TIMING BELT GEAR

$$\sum F_x = F_{tgy}$$

$$\sum F_y = F_{tgy} - F_{T1} - F_{T2}$$

$$\sum M = M_s + F_{T1} \cdot \frac{D_o}{2} - F_{T2} \cdot \frac{D_o}{2}$$

TIMING PAWLEVER

$$\sum F_x = -F_{rx} \cdot \cos(\lambda + \phi) - F_y \sin(\lambda + \phi) + F_{sx} - F_{sp} \sin \mu - F_{lever} \sin \lambda$$

$$\sum F_y = -F_{rx} \cdot \sin(\lambda + \phi) - F_y \cos(\lambda + \phi) + F_{sg} - F_{sp} \cos \mu + F_{lever} \cdot \cos \lambda$$

$$\sum M_{sg} = -F_y \cdot L_p + F_{sp} \sin \mu L_p - F_{sp} \cos \mu L_p + F_{lever} \cdot d_p$$

$$\sum M_{front} = M_{psfront} - F_{sp}(L_{sp} + T_2)$$

$$\sum M_{top} = M_{pstop} - F_{sp}(L_{sp} + T_2)$$

TIMING PAW SPRING

$$\sum F_x = F_{sp} \sin \mu - F_{sr} \sin \mu$$

$$\sum F_y = F_{sp} \cos \mu - F_{sr} \cos \mu$$

TIMING PAW SHAFT

$$\sum F_x = R_{x1} + R_{xz} - F_{sx}$$

$$\sum F_y = R_{y1} + R_{yz} - F_{sy}$$

$$\sum M_{front} = -M_{psfront} - R_{y1}(L_{s2} + \frac{L_b}{2} + L_c) + R_{yz}(L_{s1} + \frac{L_b}{2})$$

$$\sum M_{top} = -M_{pstop} + R_{x1}(L_{s2} + \frac{L_b}{2} + L_c) - R_{xz}(L_{s1} + \frac{L_b}{2})$$

Appendix I Gears

The following is a list of assumptions made during gear stress analysis:

- The gear-tooth surface temperatures are always below 120°C (250°F).
- The surface fatigue endurance limit can be calculated from the surface hardness alone.
- The surface fatigue stress is a maximum at the pitch point (line).
- The manufacturing quality of the gears corresponds to the linear curve D in Figure 15.24 with a slope of $1/960\pi$.
- The output gear experiences moderate torsional shock.
- The characteristics of support include accurate mounting, uniform gears, and contact across the full face.
- The tooth profiles of the gears are standard involutes. The contact surfaces at the pitch point can be approximated by cylinders.
- The gears are mounted to mesh at the pitch circles.
- The effects of surface failure from abrasive wear and scoring are eliminated by enclosure and lubrication—only pitting needs consideration.
- The stresses caused by sliding friction can be neglected.
- The contact pressure distribution is unaffected by the lubricant.
- Thermal stresses and residual stresses can be neglected.
- The gear materials are homogeneous, isotropic, and linearly elastic.
- The surface endurance limit and life factor data available are sufficiently accurate.
- The velocity factor Kv, the overload factor Ko, and the mounting factor Km obtained from the available data are reasonably accurate and uniform.
- The material for all gears is steel or aluminum.
- The maximum width of all gears is less than 50mm.
- All gears have a minimum reliability of 99%.
- Bending stress analysis is only affected by bending loads.
- The system does not have any idler gears.
- All gears have a constant pitch angle.
- All gears have a uniform geometry factor.

- The steel material has an ultimate strength of 140 ksi and the aluminum material has an ultimate strength of 40 ksi for the purpose of gear analysis

Table 18 Constant variables and their values. Values sourced from [70]

Symbol	Name	Value			Units	Source
		Steel	Aluminum	Plastic		
C_{Li}	Life Factor	1	1	1	-	Figure 15.27
C_R	Reliability Factor	1	1	1	-	Table 15.6
Bhn	Hardness	280	150	95	Brinell Hardness Number	Figure 3.7 & Appendix AC-7
C_P	Elastic Coefficient	162	145	145	$\sqrt{\text{MPa}}$	Table 15.4b
K_o	Overload Factor	1	1	1	-	Table 15.1
K_m	Mounting Factor	1.3	1.3	1.3	-	Table 15.2
C_L	Load Factor	1	1	1	-	Equation 15.18
C_G	Gradient Factor	0.85	0.85	0.85	-	Equation 15.18
C_s	Surface Factor	0.7	1	1	-	Figure 8.13
K_t	Temperature Factor	1	1	1	-	Equation 15.9
K_{ms}	Mean Stress Factor	1.4	1.4	1.4	-	Section 15.7

θ	Pitch Angle	20	20	20	Degrees	Section 15.7
J	Geometry Factor	0.4	0.4	0.4	-	Figure 15.23

Appendix J Agenda, Minutes, and Gantt

Agenda

Group: 13

Time: 12:00

Date: November 1st, 2019

Location: CBY B109-D

Meeting Chair: Michael

Secretary: Philippe

Item #	Agenda Item	Reference	Responsibility
1	Call to order		Michael
2	Approval of agenda		All
3	Discuss what went right with the working analysis		All
4	Discuss what went wrong and points for improvement		All
5	Adjust project scope		All
6	Come up with a schedule for remaining work		All
7	Attendance		All
8	Update TO-DO list		All
9	Adjournment		Michael

Agenda

Group: 13

Time: 9:00

Date: Nov. 5th, 2019

Location: CBY B-109D

Meeting Chair: Yousef

Secretary: Michael

Item #	Agenda Item	Reference	Responsibility
1	Call to order		Yousef
2	Automate shaft stress analysis code	Capstone project report	Yousef and Michael
3	Add waist components equilibrium equations in MATLAB	Capstone project report	Dmitry
4	Obtain missing gait data	Capstone project report	Michael
5	Plan frontal plane analysis	Capstone project report	All
6	Start SolidWorks for simple parts (if there's time)	Capstone project report	All
7	Note absences		All
8	Adjournment		Yousef

Agenda

Group: 13

Time: 1:00 PM

Date: Nov. 8th, 2019

Location: CBY B-109D

Meeting Chair: Dmytro

Secretary: Yousef

Item #	Agenda Item	Reference	Responsibility
1	Call to order		Dmytro
2	Continue to add waist components equilibrium equations in MATLAB	Capstone project report	Dmytro and Yousef

3	Prepare equations for simplified frontal plane analysis	Capstone project report	Michael
4	Continue SolidWorks modelling	Capstone project report	Michael
5	Find an alternative to Winter 1990 for elderly flat walking (also need GRFs)	Capstone project report	All
6	Note absences		All
7	Adjournment		Dmytro

Agenda

Group: 13

Time: 10:00

Date: Nov. 12th, 2019

Location: CBY B-109D

Meeting Chair: Dymtro

Secretary: Yousef

Item #	Agenda Item	Reference	Responsibility
1	Call to order		Dmitry
2	Create frontal plane analysis code	Capstone project report	Michael
3	Run various simulations and fix errors produced	Capstone project report	Dmitry and Yousef
4	Continue planning GUI and coding	Capstone project report	Yousef
5	Continue creating Solidworks files	Capstone project report	All
6	Fix errors in shear analysis code	Capstone project report	Yousef
7	Note absences		All

8	Adjournment		Dmitry
---	-------------	--	--------

Agenda

Group: 13

Time: 1:00 PM

Date: Nov. 14th, 2019

Location: CBY B-109D

Meeting Chair: Yousef

Secretary: Dmytro

Item #	Agenda Item	Reference	Responsibility
1	Call to order		Yousef
2	Update simulation and shaft analysis code to accept new design of main shaft	Capstone project report	Dmytro and Yousef
3	Test output of secondary shaft analysis	Capstone project report	Dmitry
4	Present frontal plane analysis code to group	Capstone project report	Michael
5	Start running dimensioning algorithms to approximate default dimensions	Capstone project report	All
6	Note absences		All
7	Adjournment		Yousef

Agenda

Group: 13

Time: 1:00 PM

Date: Nov. 15th, 2019

Location: CBY B-109D

Meeting Chair: Michael

Secretary: Philippe

Item #	Agenda Item	Reference	Responsibility
1	Call to order		Michael
2	Continue making parametrized stress analysis code <ul style="list-style-type: none"> • Impact loading of timing pin • Timing pin/camdisk shafts • Gears • Bolts - thighbar, gears - iterative solutions • Thighbar 	Capstone project report	Dmitry
3	Adjust gear analysis code	Capstone project report	Phil
4	Adjust frontal plane analysis code	Capstone project report	Michael
5	SolidWorks <ul style="list-style-type: none"> • Pindisk/camdisk • Thighbar • Waist components 	Capstone project report	Michael, Yousef, Dmitry
6	Note absences		All
7	Adjournment		Michael

Agenda

Group: 13

Time: 10:30

Date: November 19th, 2019

Location: CBY B-109D

Meeting Chair: Yousef

Secretary: Michael

Item #	Agenda Item	Reference	Responsibility
1	Call to order		Yousef
2	Plan 3d printing	Capstone project report	All

3	Continue SolidWorks	Capstone project report	All
4	Fix frontal plane MATLAB analysis	Capstone project report	All
5	Stress + fatigue analysis in MATLAB for thigh components	Capstone project report	All
6	Notes absences		All
7	Adjournment		Yousef

Agenda

Group: 13

Time: 15:00

Date: November 20th, 2019

Location: CBY B-109D

Meeting Chair: Michael

Secretary: Dmytro

Item #	Agenda Item	Reference	Responsibility
1	Call to order		Michael
2	Continue SolidWorks	Capstone project report	All
3	Fix frontal plane MATLAB analysis	Capstone project report	All
4	Stress + fatigue analysis in MATLAB for thigh components	Capstone project report	All
5	Continue automation of all of MATLAB stress analysis	Capstone project report	All
6	Notes absences		All

7	Adjournment		Michael
---	-------------	--	---------

Agenda

Group: 13

Time: 12:00

Date: November 21st, 2019

Location: CBY B-109D

Meeting Chair: Dmytro

Secretary: Yousef

Item #	Agenda Item	Reference	Responsibility
1	Call to order		Dmytro
2	Complete analytic stress + fatigue analysis in MATLAB	Capstone project report	All
3	Initiate Solidworks FEA analysis of some complex parts	Capstone project report	All
4	Continue automation of all of MATLAB stress analysis and parameter export to SolidWorks	Capstone project report	All
5	Note absences		All
6	Adjournment		Dmytro

Agenda

Group: 13

Time: 12:00

Date: November 22nd, 2019

Location: CBY B-109D

Meeting Chair: Michael

Secretary: Dmitry

Item #	Agenda Item	Reference	Responsibility

1	Call to order		Michael
2	Continue SolidWorks and add spline dimensions	Capstone project report	All
3	Implement stability analysis in MATLAB	Capstone project report	All
4	Complete analytic stress + fatigue analysis in MATLAB	Capstone project report	All
5	Initiate Solidworks FEA analysis of some complex parts	Capstone project report	All
6	Continue automation of all of MATLAB stress analysis and parameter export to SolidWorks	Capstone project report	All
7	Note absences		All
8	Adjournment		Michael

Agenda

Group: 13

Time: 12:00

Date: November 24th, 2019

Location: CBY B-109D

Meeting Chair: Phil

Secretary: Michael

Item #	Agenda Item	Reference	Responsibility
1	Call to order		Phil
2	Continue SolidWorks - finish components, put into assembly <ul style="list-style-type: none"> • All parts to be done and connected to text files • Assign materials for rendering 	Capstone project report	Yousef and Michael
3	Implement stability analysis in MATLAB	Capstone project report	Phil

4	Initiate Solidworks FEA analysis of some complex parts	Capstone project report	Dmitry
5	Continue automation of all of MATLAB parameter synchronization and export to SolidWorks <ul style="list-style-type: none"> • link GUI to analysis code and SolidWorks 	Capstone project report	Yousef, Dmitry and Michael
6	Choose parameters for 3D print <ul style="list-style-type: none"> • Add tolerances • Pick parts to print 	Capstone project presentation	Yousef and Dmitry
7	Note absences		All
8	Adjournment		Phil

Agenda

Group: 13

Time: 11:00

Date: November 26th, 2019

Location: CBY B-109D

Meeting Chair: Dmitry

Secretary: Yousef

Item #	Agenda Item	Reference	Responsibility
1	Call to order		Dmitry
2	Status update: what is the current status of the project	Capstone project report	All
3	Prepare next batch of parts for 3D printing	Capstone project report	Dmitry and Yousef
4	Integrate stability analysis check code into GUI	Capstone project report	Yousef
5	Finalize frontal plane analysis and integrate it into the GUI	Capstone project report	Michael and Dmitry
6	Start writing final report	Capstone project report	All
7	Start organizing final presentation	Final presentation	All

	<ul style="list-style-type: none"> Determine group expectations (dress code, etc...) 		
8	Notes absences		All
9	Adjournment		Dmitry

Agenda

Group: 13

Time: 14:30

Date: November 27th, 2019

Location: CBY B-109D

Meeting Chair: Michael

Secretary: Dmitry

Item #	Agenda Item	Reference	Responsibility
1	Call to order		Michael
2	Status update: what is the current status of the project	Capstone project report	All
3	Prepare next batch of parts for 3D printing	Capstone project report	Dmitry and Yousef
4	SolidWorks (tweak global variables and do as much assembly as possible)	Capstone project report	Michael and Dmitry
5	Meet with Prof to obtain clarification	Capstone project report	All
6	Plan SolidWorks drawings	Capstone project report	All
7	Finalize frontal plane analysis and integrate it into the GUI	Capstone project report	Michael and Dmitry
8	Continue writing final report	Capstone project report	All
9	Notes absences		All
10	Adjournment		Michael

Agenda

Group: 13

Time: 12:00

Date: November 28th, 2019

Location: CBY B-109D

Meeting Chair: Yousef

Secretary: Michael

Item #	Agenda Item	Reference	Responsibility
1	Call to order		Yousef
2	Add frontal analysis to GUI	Capstone project report	All
3	Make case	Capstone project report	All
4	FEA studies on case	Capstone project report	All
5	Continue working on report	Capstone project report	All
6	Notes absences		All
7	Adjournment		Yousef

Agenda

Group: 13

Time: 12:00

Date: November 29th, 2019

Location: CBY B-109D

Meeting Chair: Dmitry

Secretary: Yousef

Item #	Agenda Item	Reference	Responsibility
1	Call to order		Dmitry
2	Finish cleaning up case	Capstone project report	All
3	Run FEA on case	Capstone project report	All

4	Continue working on report	Capstone project report	All
5	Notes absences		All
6	Adjournment		Dmitry

Agenda

Group: 13

Time: 12:00

Date: November 30th, 2019

Location: CBY B-109D

Meeting Chair: Philippe

Secretary: Michael

Item #	Agenda Item	Reference	Responsibility
1	Call to order		Yousef
2	Finish debugging code	Capstone project report	All
3	Make case	Capstone project report	All
4	FEA studies on case	Capstone project report	All
5	Continue working on report	Capstone project report	All
6	Notes absences		All
7	Adjournment		Yousef

Agenda

Group: 13

Time: 12:00

Date: December 1st, 2019

Location: CBY B-109D

Meeting Chair: Yousef

Secretary: Philippe

Item #	Agenda Item	Reference	Responsibility
1	Call to order		Yousef
2	Finish 3D printing case	Capstone project report	All
3	Finalize FEA	Capstone project report	All
4	Work on presentation	Capstone project report	All
5	Continue working on report	Capstone project report	All
6	Notes absences		All
7	Adjournment		Yousef

Minutes of Meeting

October 28th, 2019

(Group13_Week09_minutes)

Present: Yousef, Michael, and Dmytro (secretary), Philippe (chair)

Absent: None

Observer: Nobody

Item #	Agenda Item	Action
1	Call to order: 12:00 pm	Philippe
2	Approval of agenda <ul style="list-style-type: none"> • Agenda was approved by all members 	All
3	Complete remaining stress analysis on shafts <ul style="list-style-type: none"> • Stress analysis of main shaft, pulley shaft, timing cam shaft, and timing pin shaft is complete. 	Michael
4	Double check spring stress analysis	Yousef

	<ul style="list-style-type: none"> Double check is complete, some errors were found and fixed. 	
5	Complete gear analysis	Phil
6	Bearing analysis <ul style="list-style-type: none"> Bearing analysis is completed by hand, no MATLAB code was created. 	Dmitry
7	Finish energy diagrams with and without device assist <ul style="list-style-type: none"> Energy diagrams are complete and show device effect on gait. 	Dmitry
8	Type up the report <ul style="list-style-type: none"> Introduction is complete System changes section done Spring analysis is complete Bearing analysis is good enough Inverse dynamics started Gear analysis needs equations Energy analysis 	All
9	Update TO-DO list <ul style="list-style-type: none"> Blown up drawing needs to be done Gear analysis needs to be typed up Inverse dynamics section needs to be typed up Assumptions need to be thrown into the appendix 	All
10	Adjournment: 9:00 pm	Philippe

Minutes of Meeting

November 1st, 2019

(Group13_Week09_minutes)

Present: Yousef, Michael (Chair), and Dmytro, Philippe (Secretary)

Absent: None

Observer: Nobody

Item #	Agenda Item	Action
1	Call to order: 1:00 pm	Michael
2	Approval of agenda <ul style="list-style-type: none"> Agenda was approved by all members 	All
3	Discuss what went right with the working analysis <ul style="list-style-type: none"> Systems of equations program Stress equations and programs 	All
4	Discuss what went wrong and points for improvement <ul style="list-style-type: none"> Some code needs to be more automated 	All

	<ul style="list-style-type: none"> ○ Bolts ○ Springs ○ Shafts ○ Matrix for all forces and moments ● Parametrization happened too early (should have been done after FBDs) ● Could have had a more realistic timeline ● Neglected hip attachment analysis (lack of time) ● Overlapping roles 	
5	<p>Adjust project scope</p> <ul style="list-style-type: none"> ● Combing inverse dynamics to sum of forces of mech. comp. (if time) ● SolidWorks stress analysis (for parts undoable by hand) <ul style="list-style-type: none"> ○ Ratchet gear and pawl lever ○ Timing disks ● 3d printed parts with owned printers ● Final report content decided two weeks before final deadline 	All
6	<p>Come up with a schedule for remaining work</p> <ul style="list-style-type: none"> ● Schedule made for tasks and people responsible 	All
7	<p>Class attendance:</p> <ul style="list-style-type: none"> ● All attended this week's CAD classes 	All
8	<p>Update TO-DO list</p> <ul style="list-style-type: none"> ● Updated 	All
9	<p>Adjournment: 2:30 pm</p>	Michael

Minutes of Meeting

Nov. 5th, 2019

(Group13_Week10_minutes)

Present: Yousef (chair), Michael (secretary) and Dmitry

Absent: Philippe

Observer: None

Item #	Agenda Item	Action
1	Call to order: 9:00 am	Yousef
2	<p>Automate shaft stress analysis code</p> <ul style="list-style-type: none"> ● Loading diagrams code and fatigue stress code are now more automated 	Yousef and Michael
3	Add waist components equilibrium equations in MATLAB: in progress	Dmitry
4	Obtain missing data	Michael

	Digitized and ready-to-use elderly data: <ul style="list-style-type: none">• Reid 2010 - stairs up for static analysis• Vickers 2008 - incline up 5 deg. for static and dynamic analyses• Winter 1990 (Biomechanical Walking Pattern Changes) - flat walking for static and dynamic analyses	
5	Plan frontal plane analysis <ul style="list-style-type: none">• Identified device interference issue that hinders the placement of the frontal plane damper• Removing this damper is being considered	All
6	Start SolidWorks for simple parts (if there's time) Modeled parts: <ul style="list-style-type: none">• Thigh belt gear• Spring belt gear• Main shaft	All
7	Note absences <ul style="list-style-type: none">• Phil was absent to the lab on Tuesday, Nov. 5th, 2019	All
8	Adjournment: 5:20 pm	Yousef

Minutes of Meeting

Nov. 5th, 2019

(Group13_Week10_minutes)

Present: Yousef (secretary), Michael, and Dmitry (chair)

Absent: Philippe

Observer: None

Item #	Agenda Item	Action
1	Call to order: 1:00 pm	Dmytro
2	Continue to add waist components equilibrium equations in MATLAB <ul style="list-style-type: none">• MATLAB system has been completed and tested. It correctly simulates test frames from flat ground gait.• Needs to be refined.• GUI interface to MATLAB code was started.	Dmytro and Yousef
3	Prepare equations for simplified frontal plane analysis <ul style="list-style-type: none">• Equations for frontal plane damping were started, MATLAB implementation was also started	Michael
4	Continue SolidWorks modelling <ul style="list-style-type: none">• Was put on hold while frontal plane equation modelling is being completed	Michael

5	Find an alternative to Winter 1990 for elderly flat walking (also need GRFs) <ul style="list-style-type: none"> • Group decision to use young walking data due to lack of flat walking elderly GRF data 	All
6	Note absences <ul style="list-style-type: none"> • Philippe was absent due to a family emergency 	All
7	Adjournment: 8:00 pm	Dmytro

Minutes of Meeting

Nov. 12th, 2019

(Group13_Week11_minutes)

Present: Yousef (secretary), Michael, and Dmitry (chair)

Absent: Philippe

Observer: None

Item #	Agenda Item	Action
1	Call to order: 10:00 am	Dmitry
2	Create frontal plane analysis code <ul style="list-style-type: none"> • Temporary code created, will be presented to group next meeting 	Michael
3	Run various simulations and fix errors produced <ul style="list-style-type: none"> • Many errors were fixed, new graphs were produced to show device effectiveness 	Dmitry and Yousef
4	Continue planning GUI and coding <ul style="list-style-type: none"> • General GUI input options are complete • Planning started for output display format 	Yousef
5	Continue creating Solidworks files <ul style="list-style-type: none"> • More solidworks files complete 	All
6	Fix errors in shear analysis code <ul style="list-style-type: none"> • Several errors were found and fixed, resulting in shear and bending diagrams identical to those generated manually 	Yousef
7	Note absences <ul style="list-style-type: none"> • Philippe was absent 	All
8	Adjournment: 4:00 pm	Dmitry

Minutes of Meeting

Nov. 14th, 2019

(Group13_Week11_minutes)

Present: Yousef (chair), Michael, and Dmitry (secretary)

Absent: Philippe

Observer: None

Item #	Agenda Item	Action
1	Call to order: 12:00 pm	Yousef
2	Update simulation and shaft analysis code to accept new design of main shaft <ul style="list-style-type: none">• Code updated, simulation produces expected results, shear and bending diagrams match expectations	Dmytro and Yousef
3	Test output of secondary shaft analysis <ul style="list-style-type: none">• Secondary shaft analysis needs some fixing due to odd bugs	Dmitry
4	Present frontal plane analysis code to group <ul style="list-style-type: none">• Analysis methodology was simplified	Michael
5	Start running dimensioning algorithms to approximate default dimensions <ul style="list-style-type: none">• Some placeholder dimensions were calculated for several parts. Will be used as default output values if no input parameters are changed	All
6	Note absences <ul style="list-style-type: none">• Philippe was absent	All
7	Adjournment: 5:30 pm	Yousef

Minutes of Meeting

Nov. 15th, 2019

(Group13_Week11_minutes)

Present: Yousef, Michael (chair), and Dmitry, Philippe (secretary)

Absent: None

Observer: None

Item #	Agenda Item	Action
1	Call to order: 1:00 pm	Michael
2	Continue making parametrized stress analysis code <ul style="list-style-type: none">• Impact loading of timing pin: done• Timing pin/camdisk shafts: done• Gears: in progress	Dmitry

	<ul style="list-style-type: none"> • Bolts - thighbar, gears - iterative solutions: in progress • Thighbar: in progress 	
3	Adjust gear analysis code <ul style="list-style-type: none"> • Started readjustment to make the code output gear diameters for a given safety factor, and a log file of calculation steps 	Phil
4	Adjust frontal plane analysis code <ul style="list-style-type: none"> • Changed to output moment contribution of damping pads given material properties instead of the other way around 	Michael
5	SolidWorks <ul style="list-style-type: none"> • Pindisk/camdisk: in progress • Thighbar: not started yet • Waist components: not started yet 	Michael, Yousef, Dmitry
6	Note absences: none	All
7	Adjournment: 7 pm	Michael

Minutes of Meeting

(November 19th, 2019)

(Group13_Week12_minutes)

Present: Yousef (chair), Michael (secretary), Dmitry

Observer: None

Item #	Agenda Item	Action
1	Call to order: 11:00 am	Yousef
2	Plan 3d printing Decided on parts that will be printed: <ul style="list-style-type: none"> • Thigh bar • All main parts • All timing parts 	Michael Yousef Dmitry
3	Continue SolidWorks <ul style="list-style-type: none"> • Belt gears corrected • Tigh bar and waist dimensions adjusted in parametrization tables 	Michael Yousef Dmitry
4	Fix frontal plane MATLAB analysis <ul style="list-style-type: none"> • Not started yet 	Michael
5	Stress + fatigue analysis in MATLAB for thigh components <ul style="list-style-type: none"> • Not started yet 	Dmitry

6	Noted absences <ul style="list-style-type: none"> • Phil absent for family reasons 	All
7	Adjournment: 4 pm	Yousef

Minutes of Meeting

(November 20th, 2019)

(Group13_Week12_minutes)

Present: Michael (chair), Dmitry (secretary), Yousef

Observer: None

Item #	Agenda Item	Action
1	Call to order 14:30	Michael
2	Continue SolidWorks <ul style="list-style-type: none"> • DISKLOCKHANDLE • THIGH BAR • Corrections to other parts 	Michael Yousef
3	Fix frontal plane MATLAB analysis <ul style="list-style-type: none"> • Not done yet 	Michael
4	Stress + fatigue analysis in MATLAB <ul style="list-style-type: none"> • Added more components with parameters • Remaining - thighbar, thighbeltattachment, thighrigidsupport, waiststuff 	Dmitry Yousef
5	Continue automation of all of MATLAB stress analysis <ul style="list-style-type: none"> • Dimensional equivalencies started and many done • Automated export of solidworks parameter text files • Fixed parameter naming inconsistencies • Fixed default parameter values that made no sense 	Dmitry Yousef
6	Noted absences <ul style="list-style-type: none"> • Phil absent due to family reasons 	All
7	Adjournment: 19:00	Michael

Minutes of Meeting

(November 21th, 2019)

(Group13_Week12_minutes)

Present: Dmytro(chair), Yousef(secretary)

Observer: None

Item #	Agenda Item	Action
1	Call to order 12:30	Dmitry
2	Stress + fatigue analysis in MATLAB <ul style="list-style-type: none">• Added parametrized thigh component analysis• Changed materials and component property computations to account for material changes• Parametrized additional springs• Reworked some iterative scripts	Dmitry Yousef
3	Continue automation of all of MATLAB stress analysis <ul style="list-style-type: none">• More dimensional equivalencies done	Dmitry Yousef
4	Noted absences - not expected to come today: <ul style="list-style-type: none">• Phil• Michael	All
7	Adjournment: 17:00	Dmitry

Minutes of Meeting

(November 22nd, 2019)

(Group13_Week12_minutes)

Present: Michael (chair), Dmitry (secretary), Yousef, Phil

Observer: None

Item #	Agenda Item	Action
1	Call to order 13:00	Michael
2	Continue SolidWorks and add spline dimensions: done	Michael
3	Implement stability analysis in MATLAB: in progress	Phil
4	Complete analytic stress + fatigue analysis in MATLAB	Dmitry

	<ul style="list-style-type: none"> Analytic component analyses completed 	Yousef
5	Initiate Solidworks FEA analysis of some complex parts <ul style="list-style-type: none"> Not started Pending complex geometry components: Waist component, Timing disks, full geometry thighbar 	Dmitry
6	Continue automation of all of MATLAB stress analysis and parameter export to SolidWorks <ul style="list-style-type: none"> Fixed parametrization code More dimensional equivalencies GUI linkage of force and stress solver - to do 	Yousef Dmitry
7	Noted absences <ul style="list-style-type: none"> None 	All
8	Adjournment: 19:00	Michael

Minutes of Meeting

(November 24th, 2019)

(Group13_Week12_minutes)

Present: Phil (chair), Michael (secretary), Yousef, Dmitry

Observer: None

Item #	Agenda Item	Action
1	Call to order 13:00	Phil
2	Continue SolidWorks - finish components, put into assembly <ul style="list-style-type: none"> Many parts connected to text files from MATLAB Many parts assigned materials Fixed sizing parameters and synchronization in MATLAB Subassemblies mostly done: energy, timing, pulley, thighbar subsystems 	Michael Yousef
3	Implement stability analysis in MATLAB <ul style="list-style-type: none"> in progress 	Phil
4	Analytic stress + fatigue analysis in MATLAB <ul style="list-style-type: none"> Fixed a few issues 	Dmitry Yousef
5	Initiate SolidWorks FEA analysis of some complex parts <ul style="list-style-type: none"> Not started, awaiting full SolidWorks component synchronization with MATLAB 	Dmitry

	<ul style="list-style-type: none"> Pending complex geometry components: Waist component, Timing disks, full geometry thighbar 	
6	<p>Continue automation of all of MATLAB stress analysis and parameter export to SolidWorks</p> <ul style="list-style-type: none"> Fixed parametrization code More dimensional equivalencies GUI linkage of force and stress solver - to do 	Yousef Dmitry
7	<p>Choose parameters for 3D print</p> <ul style="list-style-type: none"> Awaiting full SolidWorks component synchronization with MATLAB 	All
8	<p>Noted absences</p> <ul style="list-style-type: none"> None 	All
9	Adjournment: 20:00	Phil

Minutes of Meeting

(November 26th, 2019)

(Group13_Week13_minutes)

Present: Yousef (chair), Michael (secretary), Dmitry, Phil

Observer: None

Item #	Agenda Item	Action
1	Call to order: 11:10 am	Yousef
2	<p>Status update</p> <ul style="list-style-type: none"> GUI is done Waist and hip stuff not done, but coming along Stability analysis implemented Equivalences are all set up excluding waist/hip/case Renders have been started Main assembly components have been printed, timing components for tomorrow Report and presentation need to be worked on 	All
3	Prepare next batch of parts for 3D printing	All
4	<p>Integrate stability analysis check code into GUI</p> <ul style="list-style-type: none"> Completed and tested 	Yousef/Dmitry
5	<p>Finalize frontal plane analysis and integrate it into the GUI</p> <ul style="list-style-type: none"> Put on hold due to time constraints, 	Michael and Dmitry

6	Start writing final report <ul style="list-style-type: none"> Phil has started typing his related parts. General structure has been discussed 	All
7	Start organizing final presentation <ul style="list-style-type: none"> Presentation content/structure has been decided 	All
8	Notes absences <ul style="list-style-type: none"> Phil and Michael absent 	All
9	Adjournment: 5:30 pm	Yousef

Minutes of Meeting

(November 27th, 2019)

(Group13_Week13_minutes)

Present: Yousef, Michael (chair), Dmitry (secretary), Philippe

Observer: None

Item #	Agenda Item	Reference	Responsibility
1	Call to order		Michael
2	Status update: what is the current status of the project	Capstone project report	All
3	Prepare next batch of parts for 3D printing <ul style="list-style-type: none"> Next set of parts and reprints was completed and ready for reprinting 	Capstone project report	Dmitry and Yousef
4	SolidWorks (tweak global variables and do as much assembly as possible) <ul style="list-style-type: none"> Stuff was made more generic for better parametrization 	Capstone project report	Michael and Dmitry
5	Meet with Prof to obtain clarification <ul style="list-style-type: none"> Talked to Curtis to clarify some topics for final report 	Capstone project report	All
6	Plan SolidWorks drawings <ul style="list-style-type: none"> Not worked on 	Capstone project report	All
7	Finalize frontal plane analysis and integrate it into the GUI	Capstone project report	Michael and Dmitry

	<ul style="list-style-type: none"> Frontal plane analysis finalized, not integrated into GUI yet 		
8	Continue writing final report <ul style="list-style-type: none"> Lit review added to final report, topics from conceptual design were started 	Capstone project report	All
9	Notes absences <ul style="list-style-type: none"> None 		All
10	Adjournment		Michael

Minutes of Meeting

(November 28th, 2019)

(Group13_Week13_minutes)

Present: Yousef (chair), Dmitry (secretary)

Observer: None

Item #	Agenda Item	Action
1	Call to order: 12:00 am	Yousef
2	Add frontal analysis to GUI <ul style="list-style-type: none"> Frontal plane analysis successfully added to incline and stair gait tabs in GUI 	All
3	Make case <ul style="list-style-type: none"> Case mainly done, need to run FEA to see if it is feasible. 	All
4	FEA studies on case <ul style="list-style-type: none"> Not done, will be done tomorrow 	All
5	Continue working on report <ul style="list-style-type: none"> Relevant sections from conceptual report added, system flow diagrams redone to fit new design. Subsystem descriptions started 	All
6	Notes absences <ul style="list-style-type: none"> Phil and Michael absent - other coursework 	All
7	Adjournment: 10:00 pm	Yousef

Minutes of Meeting

(November 29th, 2019)

(Group13_Week13_minutes)

Present: Dmitry (chair), Yousef (secretary), Michael

Observer: None

Item #	Agenda Item	Action
1	Call to order: 12:00 am	Dmitry
2	Finish cleaning up case	All
3	Run FEA on case	All
4	Report <ul style="list-style-type: none">• Intro done• Litreview• Gait section• Systems/subsystems in progress	All
6	Notes absences <ul style="list-style-type: none">• Phil - working on another assignment	All
7	Adjournment: 10:00 pm	Dmitry

Minutes of Meeting

(November 30th, 2019)

(Group13_Week13_minutes)

Present: Dmitry, Yousef, Michael (secretary), Philippe (chair)

Observer: None

Item #	Agenda Item	Action
1	Call to order: 12:00 am	Dmitry
2	Finish cleaning up case	All
3	Start building presentation	All
4	Report <ul style="list-style-type: none">• Intro done• Litreview done• Gait section done• Systems/subsystems in progress	All

5	Notes absences • None	All
6	Adjournment: 9:00 pm	Dmitry

Minutes of Meeting

(December 1st, 2019)

(Group13_Week13_minutes)

Present: Dmitry, Yousef (chair), Michael, Philippe (secretary)

Observer: None

Item #	Agenda Item	Action
1	Call to order: 12:00 am	Yousef
2	Finish all 3D components of case	All
3	Complete all renders	All
4	Finish building presentation	All
5	Report <ul style="list-style-type: none"> • Intro done • Litreview done • Gait section done • Systems/subsystems still in progress • Additional SolidWorks stress analysis in progress • Image rendering 	All
6	Notes absences <ul style="list-style-type: none"> • None 	All
7	Adjournment: 8:30 pm	Yousef

Gantt Chart

Group: 13

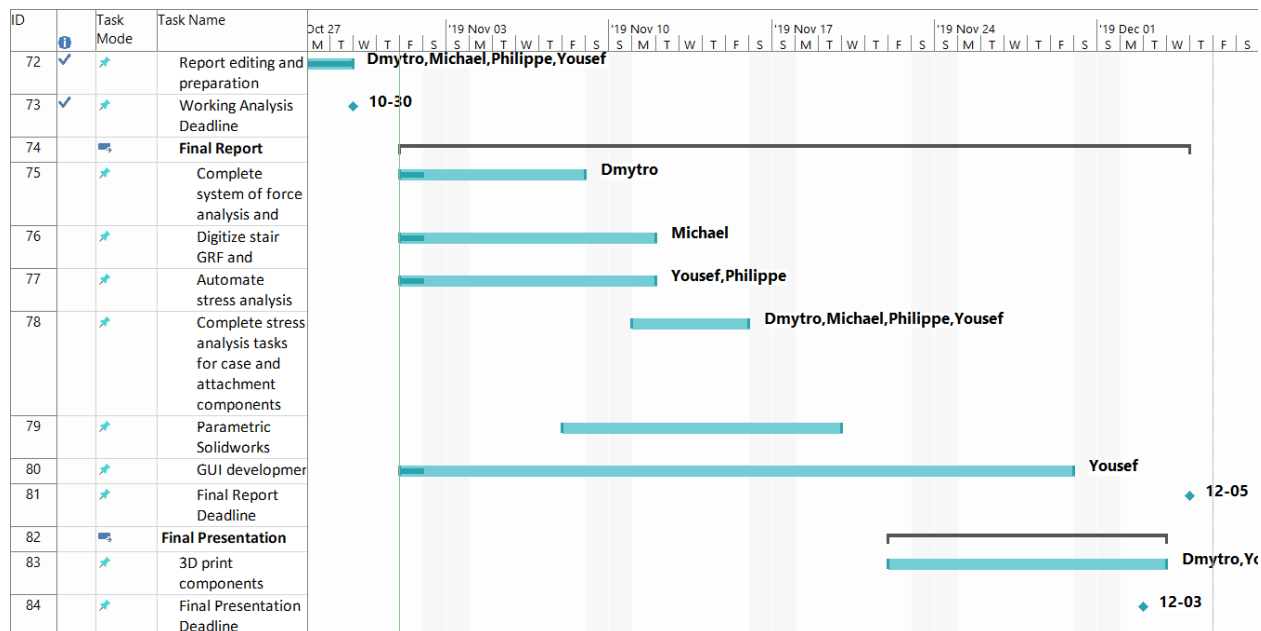
Time: 13:00

Date: 01/Nov/19

Location: CBY B-109D

Meeting Chair: Michael Botros

Secretary: Philippe Shouldice



Gantt Chart

Group: 13

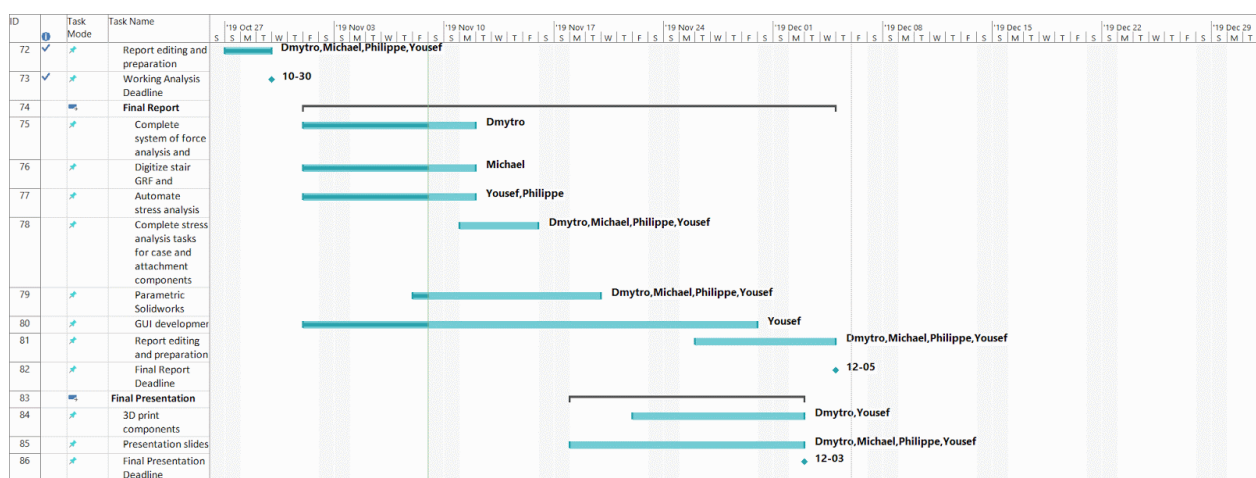
Time: 13:00

Date: 08/Nov/19

Location: CBY B-109D

Meeting Chair: Dmytro Lomovtsev

Secretary: Yousef Bader



Gantt Chart

Group: 13

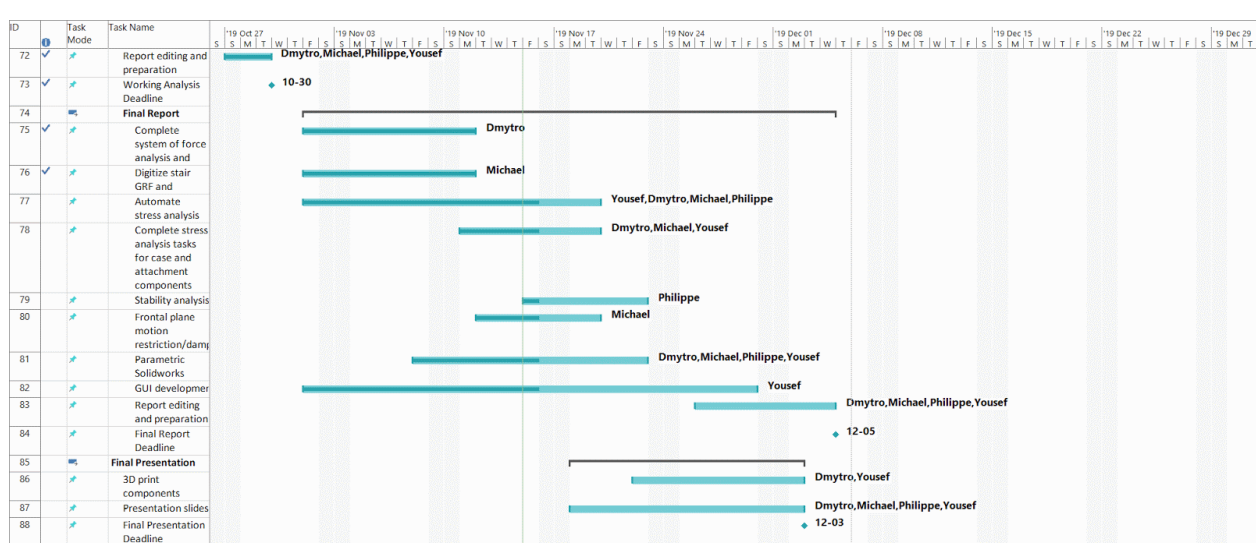
Time: 13:00

Date: 15/Nov/19

Location: CBY B-109D

Meeting Chair: Michael

Secretary: Philippe



Gantt Chart

Group: 13

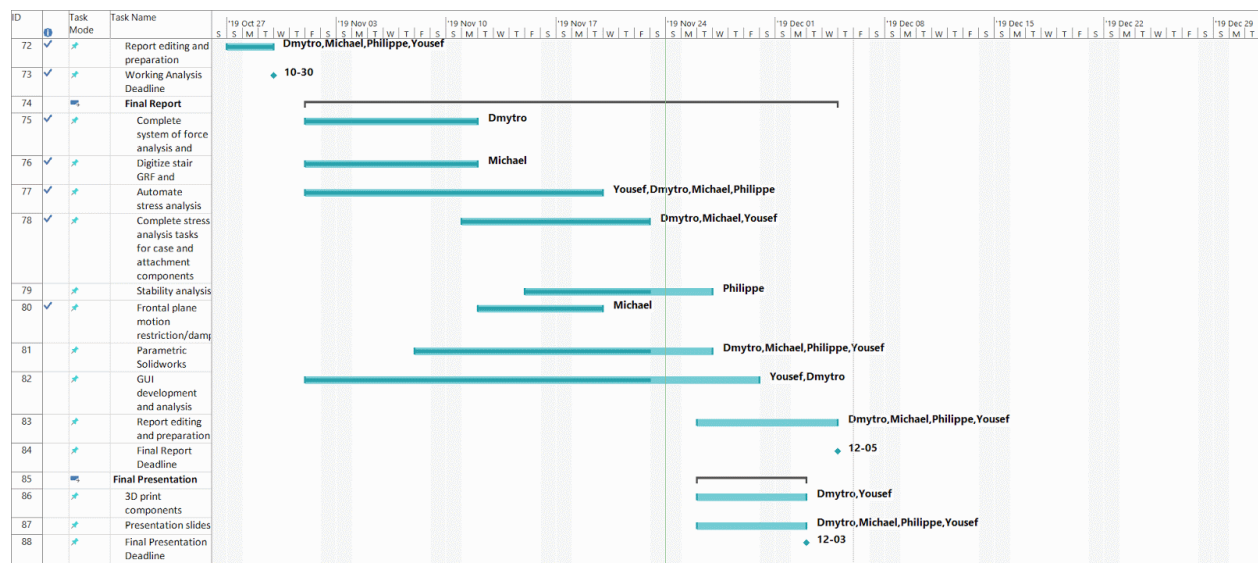
Time: 13:00

Date: 22/Nov/19

Location: CBY B-109D

Meeting Chair: Michael

Secretary: Dmitry



Gantt Chart

Group: 13

Time: 13:00

Date: 01/Dec/19

Location: CBY B-109D

Meeting Chair: Yousef

Secretary: Phil

